Rotational polarisation effects in the inelastic collisions of NO(X) and Ar

A thesis submitted for the degree of Doctor of Philosophy

Balázs Hornung

Jesus College, University of Oxford

Trinity Term, 2013

Investigation of Rotational Polarisation Effects In the Inelastic Collisions of NO(X) and Ar

Balázs Hornung, Jesus College
A thesis submitted for the degree of Doctor of Philosophy
Trinity Term, 2013

Abstract

Rotational polarisation effects have been investigated in the rotationally inelastic collisions of NO(X) and Ar by means of theoretical and experimental methods. Rotational polarisation describes the correlation between the $\boldsymbol{k} - \boldsymbol{k'} - \boldsymbol{j'}$ vectors, that is the initial and final relative velocities of the colliding partners and the final rotational angular momentum of the diatom, respectively. The simplest types of polarisation are the rotational orientation, or preferred sense of rotation, and the rotational alignment, or preferred plane of rotation. They are quantified by the renormalised polarisation dependent differential cross sections (PDDCSs)

In this thesis the theoretical methods included exact quantum mechanical, quasi-classical trajectory and Monte Carlo classical hard shell calculations. Various features of the interaction potential influence differently the polarisation dynamics. The effects of attraction and soft repulsion were elucidated employing a number of differently modified potentials. The rotational alignment is primarily determined by a classical impulsive, or hard shell mechanism at a collision energy of 66 meV. The attractive and soft repulsive forces only perturb this underlying mechanism. On the other hand, the parity dependent oscillations of the open shell alignment moments are due to differences between the quantum mechanical differential cross sections. It has been shown the bigger the well depth compared to the collision energy, the less applicable becomes the classical hard shell model to describe rotational alignment.

The quantum mechanical rotational alignment in the collisions of hard shells was also calculated. The classical and quantum mechanical hard shell models predict different rotational alignment. Nevertheless, the classical alignment is a good approximation to the exact quantum mechanical results.

The rotational orientation is much more sensitive to the details of the interaction potential. It does not exist in the classical description of hard shell collisions, if the system exhibits certain symmetry properties. The attraction and finite range repulsion break this symmetry and leads to the molecule having a preferred sense of rotation. In general there is non-vanishing rotational orientation in the collisions of a hard shell in the framework of quantum mechanics. This is due to the finite spatial and temporal interaction of the colliding partners. Quantum mechanical interference effects also play an important role in this phenomenon.

The rotational alignment was experimentally determined in the collisions of NO(X) and Ar at collision energy of 66 meV with a hexapole state selective ion-imaging apparatus. An algorithm was developed based on the Fourier moment analysis to extract rotational polarisation information from the experimental ion images. It is fast and robust and can also be of used to simulate experimental images. This algorithm was used to retrieve the experimental renormalised PDDCSs ion images. The measurements confirmed that a classical, impulsive dynamics is mainly responsible for the rotational alignment in these collisions.

Publications

1. Fully lambda-doublet resolved state-to-state differential cross-sections for the inelastic scattering of NO(X) with Ar

C.J. Eyles , M. Brouard, H. Chadwick, B. Hornung, B. Nichols, C.-H. Yang, J. Klos, F.J. Aoiz, A. Gijsbertsen, A.E. Wiskerke and S. Stolte *Phys. Chem. Chem. Phys.* **14**, 5403, (2012).

2. Rotational alignment effects in NO(X) + Ar inelastic collisions: An experimental study

M. Brouard, H. Chadwick, C.J. Eyles, B. Hornung, B. Nichols, F.J. Aoiz, P.G. Jambrina, and S. Stolte *J. Chem. Phys.* **138**, 104310, (2013).

3. Rotational alignment effects in NO(X) + Ar inelastic collisions: A theoretical study

M. Brouard, H. Chadwick, C.J. Eyles, B. Hornung, B. Nichols, F.J. Aoiz, P.G. Jambrina, S. Stolte, and M.P. de Miranda *J. Chem. Phys.* **138**, 104309, (2013).

4. The fully quantum state-resolved inelastic scattering of NO(X) + Ne: experiment and theory

M. Brouard, H. Chadwick, C. J. Eyles, Hornung, B. Nichols, J. M. Scott, F. J. Aoiz, J. Klos, S. Stolte, and X. Zhang *Mol. Phys.* **111**, 1759, (2013)

Future Publications

The origin of the collision induced rotational orientation – The role of symmetry

M. Brouard, B. Hornung

Alignment over the rainbow

M. Brouard, H. Chadwick, S. D. S. Gordon, B. Hornung, B. Nichols, F.J. Aoiz, S. Stolte, M. H. Alexander

Rotationally inelastic collisions of NO(X)+Kr

M. Brouard, H. Chadwick, S. D. S. Gordon, B. Hornung, B. Nichols, F.J. Aoiz, S. Stolte

Acknowledgements

First and foremost I would like to thank my supervisor, Professor Mark Brouard for all of his help, guidance and support during the course of my doctoral studies. I cannot express enough my appreciation for his scientific eagerness, accurate and insightful thoughts without which it would have been impossible to accomplish this work.

I would like say thank you for all the present and past members of the Brouard group, all of whom I am wholeheartedly glad to know. They made my time eventful and joyful both inside and outside of the Chemistry Department. I am especially thankful to Dr. Chris Eyles and Dr. Helen Chadwick for introducing various theoretical and practical aspects of inelastic scattering to me. They were always ready to answer any question of mine even though they were just about simple rotations.

I also acknowledge that the experimental ion-images were collected by Dr. Helen Chadwick and Bethan Nichols.

Many long discussion have deepened my knowledge on stereochemistry with Prof. Javier Aoiz, Prof. Marcelo de Miranda, Prof. Steven Stolte and Dr. Pablo Jambrina, for which I feel fortunate, and owe them thanks.

I completed my studies as a Marie Curie fellow as a part of the ICONIC (Imaging and Control in Chemistry) network within the seventh Initial Training Network of the European Union. The joint effort of Professor David Parker and Dr. Andre Eppink, along with many scientists, resulted in setting up this network. In addition to making it possible to pursue my studies, the regular meetings have provided excellent occasions to share and discuss our results and problems with fellow young and experienced scientists from every part of Europe. Andreas, Aneta, Ben, Chandan, David, Dimitrios, Eduardo, Gloria, Jaro, Martin, Mikael, Mohammad, Ondřej, Orla, Pavle, it has been my greatest pleasure to know you and learn about the fascinating variety of your cultures.

Finally, I would like to thank the support of my family and friends. My parents and grandparents, my idols, have always supported me and helped me to achieve my aims.

Contents

Chapter 1

Introduction

The immense variety of chemical processes spans complexities ranging from unimolecular gas phase reactions to biochemical systems embedded in living cells. Investigating what enables, initiates and governs these reactions is the primary concern of chemical dynamics. Depending on its complexity, each of these reactions demands different aspects and methods by means of which it can optimally be investigated. It is often useful to model a system with a simpler one that can be described in much more detail and with greater accuracy. The interactions of small, usually diatomic or triatomic molecules and atoms are the main interest of reaction dynamics. Despite consisting of few atoms these systems often impose considerable theoretical and experimental challenges. Nevertheless, the extent to which these systems allow rigorous comparison of theory and experiments is unique. Atom–diatom collisions can thus serve as a basis for the investigation of systems comprising a greater numbers of atoms. Ground state nitric oxide, NO(X), and Ar is one of these prototype systems. The present thesis focusses on the rotationally inelastic collisions of this system.

1.1 Atom–diatomic molecule collisions

The term 'collision' refers to an event where the colliding partners approach each other so closely that some of their chemical or physical properties may change. A collision is

considered inelastic, if the quantum state of at least one of the partners changes, otherwise it is called elastic. The vector properties, such as relative velocity, $\boldsymbol{k}$, and rotational angular momentum, $\boldsymbol{j}$, can also change during the course of the collision [1]. Looking at how these vectors are correlated as a function of the change in the quantum state reveals detailed information on the interaction pertaining to the system.

In addition to deepening the fundamental knowledge on scattering processes, these studies have practical implications. For instance, if rotational or vibrational excitation may remove some energy, which would otherwise result in chemical reaction. This process has importance in combustion chemistry, where the exact knowledge of rate constants is needed in order to predict the products of the combustion process.

On the other hand, it could be that vibrational mode-specific excitation of an internal degree of freedom enhances a certain reaction [1, 2], as in the case of K+HCl [3] or CH_3D dissociation reactions [2]. The initial rotational state can also affect a reaction. The probability of the Cl+HF reaction strongly depends on the initial j state of the diatomic collision partner [4]. This effect has also been seen in the Be+HCl reaction [5].

1.2 Potential energy surfaces

A central notion of the atom–diatom scattering theory is that of the potential energy surface, PES [1, 6]. It corresponds classically to an energy hypersurface on which the interacting particles move. This concept is helpful to quantify and ascertain the role of various features of the interaction potential, *e.g.*, attractive or repulsive nature, steepness, anisotropy. A number of assumptions have to be made in order to derive the PES from the exact quantum mechanical description of molecular systems.

The total Hamiltonian of the system can be factored into terms which correspond to the electron–electron, electron–nucleus and nucleus–nucleus interactions and the kinetic

energy terms of the electrons and the nuclei. The Hamiltonian in atomic units is given by:

$$\begin{aligned} \hat{\mathcal{H}}(\boldsymbol{r},\boldsymbol{R}) &= -\frac{1}{2}\sum_{i}\nabla_{\mathrm{i}}^{2} - \sum_{\mathrm{i<j}}\frac{1}{r_{\mathrm{ij}}}\sum_{\mathrm{A<B}}\frac{z_{\mathrm{A}}z_{\mathrm{B}}}{r_{\mathrm{AB}}} - \frac{1}{2}\sum_{A}\nabla_{\mathrm{A}}^{2} \\ &\equiv \hat{\mathcal{T}}_{\mathrm{e}}(\boldsymbol{r}) + \hat{\mathcal{V}}(\boldsymbol{r},\boldsymbol{R}) + \hat{\mathcal{T}}_{\mathrm{N}}(\boldsymbol{R})\,, \end{aligned} \tag{1.1}$$

where r_{ij} is the electron–electron distance, R_{ij} is the nuclei–nuclei distance. It is readily seen that the total wavefunction is not separable, because the potential term, $\hat{\mathcal{V}}(\boldsymbol{r},\boldsymbol{R})$, contains both the electronic, $\boldsymbol{r}$, and nuclear, $\boldsymbol{R}$, coordinates.

The Born–Oppenheimer approximation assumes that the kinetic energy is equally partitioned among the particles. The electrons move much faster than the nuclei do, because their masses are at least three orders of magnitude smaller than that of the heavier nuclei. The electrons thus instantaneously follow the nuclei whenever they move, which serves as the basis of the adiabatic approximation. The total wavefunction is thus separable for a fixed configuration of the nuclei:

$$\psi(\boldsymbol{r},\boldsymbol{R}) = \psi(\boldsymbol{r};\boldsymbol{R})\psi(\boldsymbol{R})\,, \tag{1.2}$$

where the coordinates of the nuclei appear as parameters in the electronic wavefunction. If the Hamiltonian is solved for a certain nuclear configuration, the energy is obtained, $E = E(\boldsymbol{r};\boldsymbol{R})$, which depends parametrically on $\boldsymbol{R}$. By gradually changing $\boldsymbol{R}$, it is possible to construct a map of the energy as a function of the relative positions of the atoms. This function is called the potential energy surface.

If the electrons and the other particles have similar masses, or very precise energies are needed, the Born-Oppenheimer approximation should be replaced by a more accurate approximation. This approximation also breaks down when coupled potential energy surfaces are involved in the scattering process [1, 6], for instance, relaxations through a conical intersection [1, 7, 8], or spin–orbit changing transitions of open shell molecules [9].

1.3 Vector correlations

Classically, four vectors are sufficient to fully specify the initial and final translational and rotational motion of the diatom, these are the initial and final relative velocities and initial and final rotational angular momenta $\boldsymbol{k}$, $\boldsymbol{k'}$, $\boldsymbol{j}$ and $\boldsymbol{j'}$, respectively [10, 11]. One can also choose the initial and final bond axis orientations, $\boldsymbol{r}$, $\boldsymbol{r'}$ instead of the rotational angular momenta.

The lowest order correlation is that of two vectors [10, 11]. The correlation between the initial and final relative velocities is the most extensively investigated one. It shows in what direction the products most likely depart with respect to the initial velocity. The angle between $\boldsymbol{k}$ and $\boldsymbol{k'}$ is called the scattering angle, θ [12, 13]. The probability that a particle is scattered through an angle, θ is proportional to the differential cross section, DCS, which is one of the most fundamental experimental observables. The DCS provides valuable information both on the classical and quantum mechanism of the collision. Many properties of the interaction potential can also be deduced from the differential cross sections [14].

If the distribution of $\boldsymbol{j'}$ is unpolarised after a particular collision, then $\boldsymbol{j'}$ points at every point with uniform probability. If the distribution is not uniform, the ensemble is called rotationally polarised [10]. The degree of the rotational polarisation may depend on the scattering angle, and is quantified by the polarisation dependent differential cross section [15–17]. This is a third order vector correlation, since it establishes relationships between the initial and the final relative velocities, and the final rotational angular momentum [15, 16]. This angular dependence provides uniquely detailed information on the mechanism of the collisions [11].

The experimentally determined rotational polarisation in atom–diatom collisions has mainly been interpreted in terms of various hard shell models [18–21]. Chandler *et al.* used classical hard shell models to rationalise the rotational orientation in the NO(X)–Ar collision [18]. This model was also used to interpret the observed rotational alignment in

the same system [19].

The kinematic apse model (AM) will play a central role in the present thesis. It states that the projection of the rotational angular momentum onto the kinematic apse is conserved throughout the collision, which is true in the case of a classical impulsive collisions [22, 23]. The kinematic apse, $\hat{\boldsymbol{a}}$, is the unit vector pointing in the direction of the momentum transfer. In case of non-reactive collisions it is given as

$$\hat{\boldsymbol{a}} = \frac{\hat{\boldsymbol{k}}' - \hat{\boldsymbol{k}}}{|\hat{\boldsymbol{k}}' - \hat{\boldsymbol{k}}|}\,. \tag{1.3}$$

Meyer found that the rotational alignment predicted by the kinematic apse model rotational alignment was in good agreement with the experimentally observed data in the collisions of NH_3 and Ar [24]. However, only a limited number of studies have considered the role of the entire potential energy surface as opposed to treating the system as a hard shell. Marinakis [25] *et al.* presented exact quantum mechanical, quasi classical trajectory and kinematic apse model calculations for the NO(X)–Kr system. It was found that the exact quantum mechanical calculations deviate considerably from the apse model results, especially at low scattering angles and for low Δj transitions, where the attractive part of the potential is expected to play a more important role.

More recently, a careful theoretical and experimental study compared the kinematic apse model, exact quantum mechanical and experimental polarisation parameters in the inelastic collisions of NO(A) and Ne [26]. The AM results reproduces the general trend of the exact QM and experimental data, but not their detailed angular dependence. It was ascribed to the possible inaccuracies of the potential energy surface. Also, the real interaction potential has a finite range which may cause the exact QM polarisation moments to deviate from the AM ones, which assumes an infinitely steep interaction potential [26].

Other vector correlations include the $\boldsymbol{j}$–$\boldsymbol{j}'$ correlation, which measures the collisional depolarisation [27–29]. It helps to ascertain the factors that determine how an initially polarised distribution of $\boldsymbol{j}$ becomes isotropic due to collisions [30]. The comparison between

different theoretical models and experiments, reveals detailed information on the atom–diatom interaction of interest [31, 32]. For instance, the total depolarisation cross sections were measured for the NO(A)+Kr and OH(A)+Kr systems. The classical calculations agreed with the experimental results in the first case, but not in the collisions of OH(A) and Kr, due to the importance of non-adiabatic electronic processes [33]. Paterson *et. al.* investigated the collisional depolarisation of NO(X) caused by Ar [34]. They concluded that the polarisation of the open shell NO(X) is less efficient *via* elastic collisions than in case of OH(X) and Ar, which possesses a more anisotropic and attractive PES.

1.4 Theoretical methods

Molecular collisions can be treated in several theoretical frameworks. Each of them has its own merits in elucidating a particular aspect of the complex interaction. The main three branches of theory are classical mechanics, quantum mechanics and semiclassical mechanics.

Classical mechanics provides a mechanistic and conceptually simple view of the collision event, since it allows infinite resolution in position and momenta, time and energy simultaneously. Its principal notion is that of the trajectory which is the trace of the particle in the spatio-temporal continuum, or in other suitable space such as the Hamiltonian phase space. The initial conditions of the particles are accurately defined, and evolve under the influence of the potential energy surface according to the the rules of classical mechanics. Each trajectory could traverse a different path on the PES, such that various mechanisms can be discerned depending on which regions of the interaction potential are sampled. In order to get a reliable answer a vast number of trajectories have to be evaluated, each of which is initialised according to the nature of the problem [14, 35]. The integral and differential cross sections as well as the higher order vector correlations are obtained from statistical analysis of the trajectories.

This method has long been applied in the field of molecular scattering studies. The

first calculations considered reactive collisions of hydrogen atoms restricted to a colinear geometry [36, 37], then in three dimensions [38]. Later on, these methods were extended to the rotationally and vibrationally inelastic collisions of atoms and diatomic molecules [39–41]. Quasi-classical trajectory (QCT) calculations have been used to study many more complicated systems in the past decades, including reactive scattering, due to the continuously increasing computing power [42, 43]. The first quasi-classical trajectory studies of the NO(X)–Ar collisions were carried out by Aoiz *et al.* [44]. Since these methods provide a full characterisation of the final products they can be used to calculate high order vector correlations [10, 11, 45].

The classical methods which employ a manifold of surfaces, such as surface hopping QCT calculations, are not considered in this work [1, 46, 47].

Quasi-classical methods cannot account for such quantal effects as quantisation, the Heisenberg Uncertainty Principle, tunneling and selection rules [48]. An exact quantum mechanical treatment should be able to fulfil these requirements, however, there are two major shortcomings in doing so. Firstly, accurate quantum mechanical calculations are time-demanding, this time constraint often being prohibitive even in the case of small systems. Secondly, the classical notion of a mechanism is not strictly applicable in interpreting quantum mechanical results, and the mechanistic view is lost. However, quantum mechanics calculations can accurately reproduce the quantal effects which may be crucial to understand the behaviour of open shell systems.

Quantum mechanical calculations can be divided into two major groups. The first is where the time dependence of the scattering process is treated explicitly, or alternatively, where only the time points infinitely before and after the collision are considered [1, 49]. A central notion of the time-dependent scattering theory is the wave packet, the evolution of which on the potential energy surface determines the outcome of the collision [1]. These methods are primarily used to model reactive or photodissociation scattering events.

The present thesis focusses exclusively on the application of time independent methods to the investigation of nonreactive molecular scattering processes. There are only two dis-

tinguished points in time one placed infinitely removed before and an other infinitely posed after the collision. As opposed to letting the Hamiltonian propagate the wavefunction, all of its effects are virtually contained within the scattering or transition operators which transform the initial wavefunctions to the final one, as such it eliminates the explicit time dependence [12, 13]. Determining the outcome of the scattering event is thus equivalent to finding the correct scattering matrix.

The standard way to determine the scattering matrix for atom–diatom collisions is to formulate the problem as a set of differential matrix equations. These are the so-called close-coupled equations, first introduced by Arthurs and Dalgarno in the case of closed shell interactions [50]. The formalism was then extended to treat open shell systems by Alexander [9]. However, the solution of these equations is very time consuming and prone to numerical errors. A number of numerical algorithms were developed in order to overcome these issues. One major group, known as the approximate potential method, approximates the interaction potential locally, to which it finds the exact solution. The methods which approximate the solution whilst retaining the exact potential consist of two major groups. The solution following methods are best employed when the potential varies slowly[51]. The invariant imbedding approach gives accurate results even if the potential varies rapidly, examples of which are the amplitude density method [52] and the log-derivative method [53]. The breakthrough was the introduction of the modified log-derivative method of Manolopoulos [54] which is fast and accurate at short interparticle separations. Most of the available quantum mechanical scattering codes combine the log-derivative and solution following procedures, and are capable of handling open shell systems, such as Hibridon[55] and MolScat[56]. These computer codes are routinely used to solve scattering problems relating to closed shell and open shell systems [25, 31].

Due to the Heisenberg Uncertainty Principle, the incident wave function has to be expanded in terms of partial waves. Each partial wave contributes to the scattering in the entire scattering angle region, giving rise to interference effects [12], which are absent from the classical description. Also quantum mechanical parity heavily influences the outcome

of a collision [9, 57, 58], which also has to be accounted for in determining the scattering matrix.

Another fundamental difference between classical and quantum mechanics is that the continuous probability functions of classical mechanics have to be replaced by density matrices.

Semiclassical methods attempt to simultaneously retain the mechanistic insight of classical methods, but also embody quantum effects [59]. There are numerous ways to implement this idea. The most widespread is to construct the scattering matrix as a sum of 'paths' using semiclassical phase shifts, which forms the basis of the semiclassical S-matrix theory [60–62]. In this method, the phase shifts are calculated along the classical trajectories which the particle might take, if it were driven by classical forces only [12, 59]. It is also possible to use the close-coupled equations or a suitable approximation to those, but the exact phase shifts are replaced by the semiclassical ones. This results in an enormous increase in computing speed, and can highlight quantum effects such as interference [63–66]. Semiclassical methods are successful in reproducing most of the qualitative and quantitative features of the differential cross section and other related physical quantities. However, their exactness is limited [67].

1.5 Experimental methods

Theoretical methods provide perfect state selection and control over interacting species. The results of these calculations have to be compared to experimental ones to test their accuracy. However, experiments only have finite resolution. In order to maximise the amount of information obtained from an experiment, it is desirable to have the greatest possible control over the system and process of interest.

The initial relative velocity is the easiest vector property to have a handle on. By means of molecular beams, the molecules' mean velocity, velocity spread, rotational and vibrational temperature can be controlled [68–71]. Therefore crossed molecular beam ex-

periments are widely used in the study of vector correlations. The polarisation of the initial bond axis can also be prepared. Strong electric fields are capable of aligning the bond axis if the molecule has a dipole moment [72–74]. It is possible to orient the molecule, such that a particular end preferably points parallel to the relative velocity.

The initial quantum state of an open shell molecule can be selected using electric fields. A hexapole electric field combined with supersonic molecular beam expansions has been used to fully prepare the initial state of the NO(X) molecule [73, 75]. The prepared beam is intersected by the beam of the collision partner. In general, a range of scattered products are formed in the collisions, which have to be state selectively detected. This can be achieved using resonantly enhanced multiphoton ionisation (REMPI) [76] to selectively ionise a particular quantum state. Additionally, the excitation step in a REMPI ionisation can be used to probe the direction of the rotational angular momentum, making use of the correlation between the transition dipole moment and the rotational angular momentum [15]. The transition strength depends on the square modulus of the overlap of the electric field vector, $\hat{\boldsymbol{\epsilon}}$, and transition dipole moment, $\hat{\boldsymbol{\mu}}$, according to:

$$I \propto |\langle \hat{\boldsymbol{\epsilon}} \cdot \hat{\boldsymbol{\mu}} \rangle|^2 . \tag{1.4}$$

For example, in the case of $\Sigma \leftarrow \Pi$ R branch transitions, the transition dipole moment and the rotational angular momentum are perpendicular to each other and to the bond axis. If the lab frame components of the electric vector are known, information can be deduced about the direction of $\hat{\boldsymbol{\mu}}$ and $\boldsymbol{j'}$, *via* Eq. (1.4). Linearly polarised light is sensitive to the rotational alignment,[19, 72, 77], whilst circularly polarised light is sensitive to both rotational alignment and orientation.

The velocity map imaging techniques allow the two dimensional detection of the ions, according to their relative velocity. Velocity map imaging combined with a REMPI detection scheme allows the direct measurement of the $\boldsymbol{k}-\boldsymbol{k'}-\boldsymbol{j'}$ three vector correlation[18, 19].

In the case of the laser induced fluorescence (LIF) detection scheme, the polarised

ensemble is excited with an appropriate laser scheme. The subsequent fluorescent decay from the excited state is used to retrieve information on rotational polarisation[78–80]. It also provides time resolved results, as such it is suitable to monitor the change in rotational polarisation as a function of time [81, 82]. One of the earliest study concerned with the collisional reorientation of Li_2 by He and Ar [83]. It was widely used to investigate different species present in flames, such as OH(X) [84]. A magnetic field can be applied to rotate the angular momentum distribution which serves the basis of the quantum beat spectroscopy [72, 85, 86].

A novel experimental technique to monitor the change of the polarisation of a molecular ensemble is polarisation spectroscopy [87–90]. In this method, the polarisation is generated by a powerful polarised laser pulse. The ensemble is probed subsequently by a counter or copropagating laser beam having the same or a different colour [89, 90]. The signal copropagates with the probe beam, but it has perpendicular polarisation with respect to the probe beam. This method has been used to investigate the depolarisation of OH(X)–Ar [90]. The collisional evolution of the rotational angular momentum polarisation in the collisions of OH(X) with N_2 and O_2 [91] has also been studied with this method.

1.6 Outline of the Thesis

This thesis is organised as follows: The second chapter presents an overview of the classical and quantum mechanical theories of atom–diatom collisions. It introduces the fundamental notions and relationships upon which the rest of the thesis is built. The details of the quasi-classical trajectory and closed coupled quantum mechanical calculations are discussed. Density matrix theory is briefly introduced. Formulae are derived through which the experimental observables can be calculated.

The third chapter is primarily concerned with the rotational momentum polarisation phenomena in molecular collisions. Rotational polarisation can be quantified in terms of probability functions in the framework of classical mechanics. These functions in turn

can be expanded in terms of polarisation dependent differential cross sections (PDDCSs) which characterise the preferred sense or preferred plane of molecular rotation, which will be the central quantities in this work. As such, their properties are discussed in great detail. The quantum mechanical description of rotational polarisation relies on density matrix theory. The PDDCSs appear as the multipole moments of the density matrices and this relationship is derived in order to establish links among different theoretical models and experimental data in the later chapters of this thesis.

A number of existing theoretical methods were adapted for the present investigation, namely, the classical hard shell and exact quantum mechanical hard shell models. It is possible to assign various effects to different parts, attractive or repulsive, of the potential energy surfaces, by introducing a simple scaling procedure. The differential cross sections obtained with these methods are characterised in order to gain insight on the role of the interaction potential.

The fifth chapter is concerned with the theoretical study of rotational alignment effects. It invokes a variety of models which have been previously introduced. The circumstances under which the rotational alignment conforms to the kinematic apse model are determined. The exact quantum mechanical hard shell and kinematic apse model are compared and the differences are pointed out. The role of the parity and different features of the PES are carefully investigated.

The alignment renormalised PDDCSs are measured experimentally using a hexapole state selective ion-imaging apparatus. The experimental methods used to measured these PDDCS are described in the sixth chapter. These details are necessary to know in order to understand the algorithm by means of which the PDDCSs are extracted from the ion-images. The novel algorithm builds on the Fano–Macek formalism of the line strengths in a polarised medium and on the Fourier moments analysis, both of which are described in detail in the subsequent chapter. The procedure is first introduced step by step. The experimentally determined renormalised PDDCSs are then compared to the theoretically calculated ones.

The rotational orientation is investigated by the same inventory of theoretical methods as in the case of rotational alignment. It is however, useful to extend the definition of the PDDCS and introduce the polarisation dependent opacity functions and partial cross sections. The origin of the classical rotational orientation is accurately identified with a particular emphasis on the the role of symmetry. These phenomena are also investigated from the viewpoint of quantum mechanics.

Upon summarising the presented findings, general conclusions are drawn. These are put in a broader context in the provision of extending the methods employed in this thesis towards being capable describing more complex behaviour of more complicated systems.

Chapter 2

General theory

In this chapter, the theoretical foundations are laid down upon which the main body of the present thesis is built. Firstly, the electronic and angular momentum theory of the electronic ground state of nitric-oxide, NO(X), is reviewed. This is followed by the characterisation of the potential energy surfaces for the NO(X) and rare gas systems. The standard classical and exact quantum mechanical theories of atom–diatom scattering are considered, with a particular emphasis on the similarities and differences between them. Various physical quantities, such as opacity functions, differential cross sections and integral cross sections which are central to this work are derived in the framework of both classical and quantum mechanics. This section also includes the formulation of the so-called close-coupled equations.

2.1 The ground state nitric-oxide molecule

The ground state nitric-oxide, NO(X)molecule, has an unpaired electron, and as such, it is an open shell molecule. Its electronic configuration is

$$1\sigma^2 1\sigma^{*2} 2\sigma^2 2\sigma^{*2} 1\pi^4 3\sigma^2 1\pi^{*1} \,. \tag{2.1}$$

The unpaired electron carries an angular momentum, $\boldsymbol{L} = 1$ with a projection onto the molecular axis, $\Lambda = 1$ [92]. It also has a spin, $\boldsymbol{S} = 1/2$, which projection onto the molecular

axis, Σ, which can take the values of $\pm 1/2$. The coupling of the angular momentum of the molecular framework, $\boldsymbol{R}$, to orbital momentum of the electron and the spin is best described by the Hund's case (a) coupling scheme [92]. $\boldsymbol{R}$ couples to $\Omega = \Lambda + \Sigma$, that is to the sum of the projections of electronic and spin angular momenta. The resultant vector is called rotational angular momentum and denoted by $\boldsymbol{j}$. Because $\overline{\Omega}$ can take two values, namely $\overline{\Omega} = 0.5$ and $\overline{\Omega} = 1.5$, there are two separate series of j, each of which correspond to a particular spin–orbit manifold.

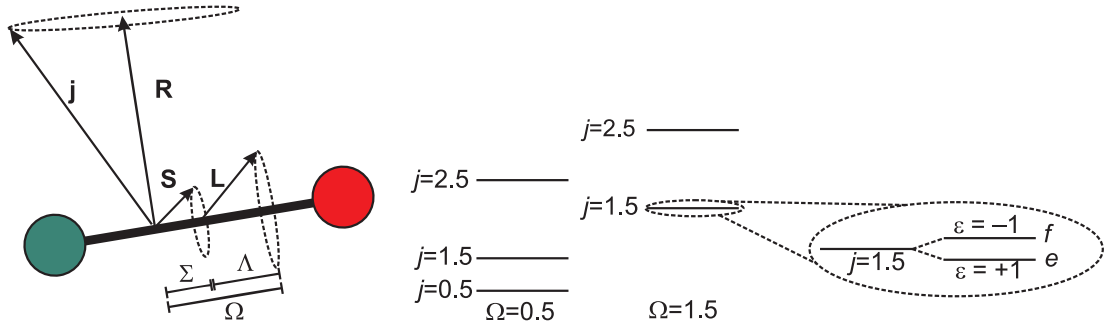

Figure 2.1: The diagram of the Hund's case (a) coupling scheme (left panel). The projection of the electronic angular momentum, Ω couples to the angular momentum of the molecular framework, $\boldsymbol{R}$, resulting in the total rotational angular momentum, $\boldsymbol{j}$. The rotational energy levels in Hund's case (a) coupling scheme (middle panel). There are two spin–orbit manifolds corresponding to $\overline{\Omega} = 0.5$ and $\overline{\Omega} = 1.5$. Each rotational level splits into two sub-levels due to Λ-doubling.

Neglecting Λ-doubling, the Hamiltonian of the rotating system can be factored into two terms according to Eq. (2.2) [93]. The first term, $\hat{\mathcal{H}}_{\rm rot}$, corresponds to the rotation of the molecular frame, having the argument $\boldsymbol{R} = \boldsymbol{j} - \boldsymbol{L} - \boldsymbol{S}$. The total energy also depends on whether the projections of the electronic spin $\boldsymbol{S}$ and the electronic orbital angular momentum $\boldsymbol{L}$ couple in a parallel or antiparallel way [92]. This is represented by the second term, $\hat{\mathcal{H}}_{\rm SO}$:

$$\hat{\mathcal{H}} = \hat{\mathcal{H}}_{\rm rot} + \hat{\mathcal{H}}_{\rm SO} \, . \tag{2.2}$$

Then the total energy is given by Eq. (2.3) [93]:

$$E(j) = B_0 \left[(j - 0.5)(j + 1.5) \pm 0.5X \right] \, , \tag{2.3}$$

where

$$X = \sqrt{4(j-0.5)(j+1.5)+(Y-2)^2} = \sqrt{4(j+0.5)^2+Y(Y-4)}\,, \tag{2.4}$$

and

$$Y = \frac{A_0}{B_0}\,, \tag{2.5}$$

where $A_0 = 123.13\,\mathrm{cm}^{-1}$ is the spin–orbit coupling constant [94]. $B_0 = 1.6961\,\mathrm{cm}^{-1}$ is the rotational constant of the NO(X) molecule [94]. Each of the spin–orbit manifolds, denoted by F_1 and F_2, arises from the '$-$' or '$+$' sign of the $0.5X$ coupling term in Eq. (2.3), which correspond to the $\overline{\Omega} = 0.5$ and $\overline{\Omega} = 1.5$ projections, respectively. The electronic states are denoted as $^2\Pi_{1/2}$ and $^2\Pi_{3/2}$.

In addition to spin–orbit coupling, there exists another coupling in Hund's case (a) and Hund's case (b), namely Λ-doubling. The electronic orbital angular momentum, $\boldsymbol{L}$, interacts with the rotation of the nuclei, resulting in each j level splitting into two sub-levels. Usually the energy difference between the Λ-doublet levels is less than $1\,\mathrm{cm}^{-1}$ [92]. However, the splitting increases linearly with j for $^2\Pi_{1/2}$ states, and it is proportional to the third power of j for the $^2\Pi_{3/2}$ manifold [92]. It increases from $0.01188\,\mathrm{cm}^{-1}$ to $0.1767\,\mathrm{cm}^{-1}$ between the rotational levels $j = 0.5$ and $j = 16.5$ for the $\overline{\Omega} = 0.5$ manifold of the NO(X) molecule [94, 95]. In case of the $\overline{\Omega} = 1.5$ manifold, it ranges between $4 \times 10^{-5}\,\mathrm{cm}^{-1}$ and $0.016\,\mathrm{cm}^{-1}$ as the rotational level state increases from $j = 0.5$ to $j = 13.5$ [96]. $j = 16.5$ and $j = 13.5$ are the highest achievable rotational states in the spin–orbit conserving and changing energy ladders at the highest collision energy considered in this work. The two Λ-doublet levels are usually denoted by $\epsilon = \pm 1$ or equivalently $\epsilon = e, f$ [92, 97]. They correspond to the following physical picture. The unpaired electron can either reside in the π^* orbital which is out of the plane of molecular rotation, labeled as A'' according to its symmetry, or it can be in the π^* orbital which is confined in the plane of molecular rotation, labeled as A' in the high j limit [98]. Obviously, if the molecule does not rotate

and in the absence of any external field or particles, the Λ-levels are degenerate.

In the Hund's case (a) coupling scheme, the rotational wave function only consists of terms from a particular spin–orbit manifold. The individual $|j, m, \overline{\Omega}\rangle$ wave function does not possess the required symmetry properties with respect to inversion through the plane of rotation, as such, they are not correct wave functions of the molecular Hamiltonian. However, the symmetric and antisymmetric combinations of them are eigenfunctions of the inversion operator and are thus proper wave functions [93]. These can be written as

$$|j, m, \Omega, \epsilon\rangle \equiv \frac{1}{\sqrt{2}} \left[|j, m, \overline{\Omega}\rangle + \epsilon |j, m, -\overline{\Omega}\rangle \right] , \tag{2.6}$$

where

$$|j, m, \overline{\Omega}\rangle = \sqrt{\frac{2j+1}{4\pi}} D^{j}_{m,\overline{\Omega}} (\theta, \phi, 0)^{*} , \tag{2.7}$$

and ϵ is the Λ-doublet index. Thus the molecular rotational wave functions are linear combinations of the Wigner D-matrices [99]. It is possible to prove these functions are indeed eigenfunctions of the inversion operator with an eigenvalue of $p = (-1)^{j-\epsilon/2}$ which is called parity [92].

The Hund's case (a) coupling scheme is exact only for $j = 0.5$. As j increases, it gradually becomes a less good approximation [93, 100]. The interaction between the various angular momenta is more accurately described by an intermediate Hund's case (a) and Hund's case (b) scheme. As such, Ω is no longer an appropriate quantum number, and the proper wave function gradually becomes a linear combination of the $\overline{\Omega} = 0.5$ and $\overline{\Omega} = 1.5$ wave functions:

$$|F_1, \rangle = a|j, m, \overline{\Omega} = 0.5, \epsilon\rangle + b|j, m, \overline{\Omega} = 1.5, \epsilon\rangle \tag{2.8}$$

$$|F_2, \rangle = a|j, m, \overline{\Omega} = 1.5, \epsilon\rangle - b|j, m, \overline{\Omega} = 0.5, \epsilon\rangle , \tag{2.9}$$

where the mixing coefficients, a and b are defined as

$$a \equiv \sqrt{\frac{X + (Y-2)}{2X}} \tag{2.10}$$

$$b \equiv \sqrt{\frac{X - (Y-2)}{2X}}\,. \tag{2.11}$$

X and Y were defined in Eqs. (2.4) and (2.5). The degree of mixing of different manifolds increases with j. a ranges between $a = 1$ and $a = 0.975$, whilst b takes the values between $b = 0$ and $b = 0.222$ as j increases from $j = 0.5$ to $j = 16.5$. Since the A_0/B_0 ratio is small for NO(X) the mixing of the Hund's case (a) and Hund's case (b) wave functions is negligible to a good approximation for all of the states considered in this work.

The NO(X) molecule belongs to the $C_{\infty v}$ point group, however this symmetry is reduced, if an atom approaches the molecule in a non-linear geometry. The triatomic ensemble has C_s symmetry. Apart from identity, the only symmetry operation is the reflection in the plane containing the three atoms. As such, the electronic states are labeled as A' and A'' depending on whether they change sign or not under reflection, respectively [9]. A number of potential energy surfaces (PESs) of various accuracy have been constructed for the NO(X)–Ar system [98, 101] in the past few decades. The potential energy surfaces of Alexander were employed in the present study [102]. They were obtained using coupled cluster singles and doubles with perturbative triples (CCSD(T)) level of theory [103]. More recently Sumiyoshi obtained PESs from partially spin-restricted CCSD(T) (RCCSD(T))[103] calculations employing a large basis set [104]. It has been shown that both the details of the PESs and the scattering calculations performed on them are practically identical [105]. The interatomic distance between the N and O atoms was kept fixed at the equilibrium bond length, $r_{\mathrm{e}} = 2.175\,\mathrm{bohr}$ [102]. Therefore the vibrational motion of the NO(X) molecule was ignored during both the electronic structure calculations and the scattering calculations of this work. There are two degrees of freedom, which are conveniently chosen to describe the system. These are the distance between the centre of mass of the diatom and the atom, $\boldsymbol{R}$; and the angle, γ, which $\boldsymbol{R}$ makes with the bond

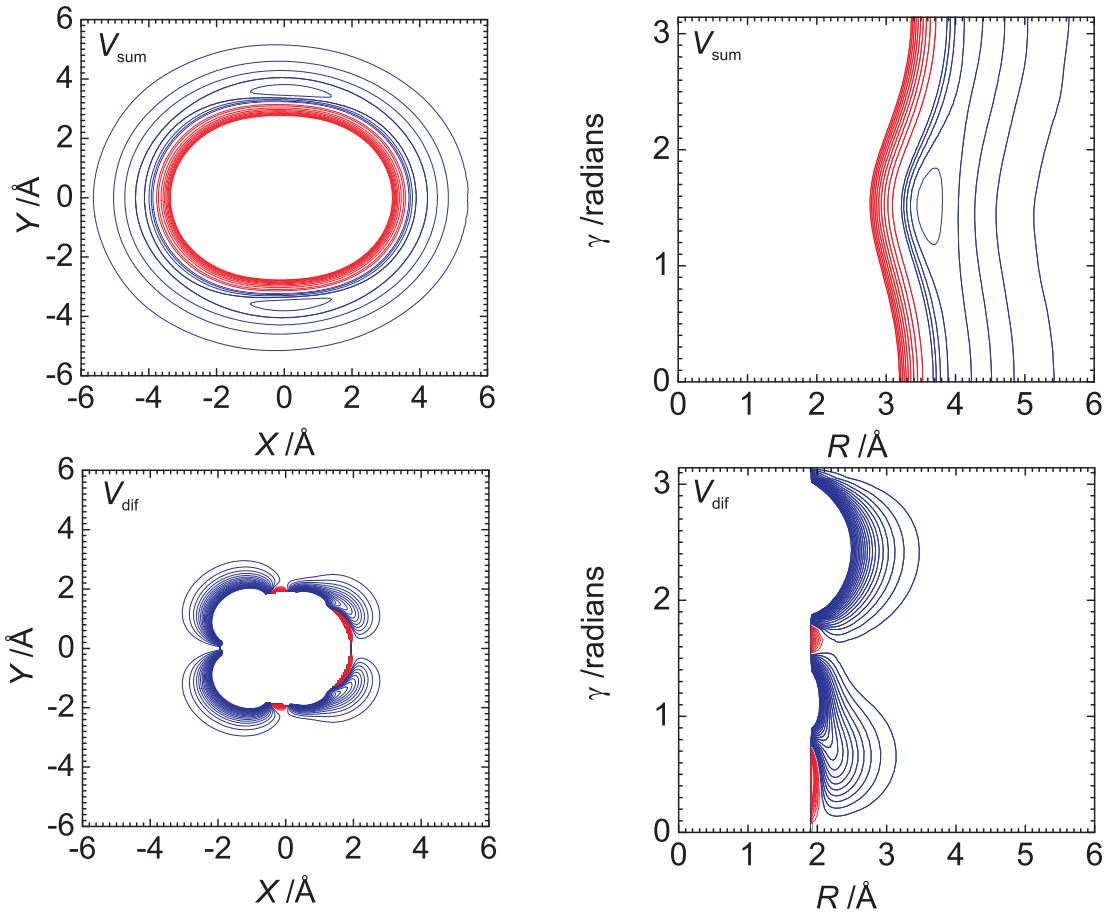

Figure 2.2: The Cartesian (left column) and polar plots (right column) of the NO(X)–Ar $V_{\rm sum}$ and $V_{\rm dif}$ potential energy surfaces are presented in the top and bottom rows, respectively. The red contours represent 100 cm^{-1} separation on each plot. The blue contours correspond to 25 cm^{-1} on the $V_{\rm sum}$ and 100 cm^{-1} energy differences of the $V_{\rm sum}$ and $V_{\rm dif}$ PESs.

axis, $\boldsymbol{r}$. These are the so-called Jacobi co-ordinates, γ being the Jacobi angle [1, 106]. The A' and A'' surfaces are repulsive at short atom–diatom distances and have a shallow attractive well at larger inter-particle separations. The $V_{A'}$ PES of A' symmetry has a global minimum of $-116\,\mathrm{cm}^{-1}$ at $\gamma = 95°$ and $R = 6.8\,\mathrm{bohr}$. The global minimum of the $V_{A''}$ surface is located at $\gamma = 70°$, $R = 6.8\,\mathrm{bohr}$ and has a well depth of $-111\,\mathrm{cm}^{-1}$ [102]. Thus the most attraction is experienced by the Ar atom when it approaches the NO(X) molecule in a 'T'-shaped geometry.

Inelastic collisions of NO(X) with a rare gas simultaneously take place on both $V_{A'}$ and $V_{A''}$ surfaces [9]. In the theoretical treatment of these collisions, it is customary to introduce the linear combinations of these surfaces defined in Eq. (2.12). The half sum

and half difference potentials can be given in terms of a series expansion, where the basis functions are the small (or reduced) Wigner d-matrix elements, $d^l_{\lambda 0}(\gamma)$, [99], and the radial dependent expansion coefficients are denoted as $V_{l0}(R)$ and $V_{l2}(R)$:

$$V_{\rm sum}\left(R,\gamma\right) = \frac{1}{2}[V_{A''}\left(R,\gamma\right) + V_{A'}\left(R,\gamma\right)] = \sum_l V_{l0}(R) d^l_{00}(\gamma) \tag{2.12}$$

$$V_{\rm dif}\left(R,\gamma\right) = \frac{1}{2}[V_{A''}\left(R,\gamma\right) - V_{A'}\left(R,\gamma\right)] = \sum_l V_{l2}(R) d^l_{20}(\gamma)\,. \tag{2.13}$$

In the Hund's case (a) limit, the spin–orbit conserving collisions take place on the $V_{\rm sum}\left(R,\gamma\right)$ potential, whereas the spin–orbit changing collisions sample the $V_{\rm dif}\left(R,\gamma\right)$ potential [9]. That is to say, the potential matrix elements, defined later in Eq.(2.41), will only contain terms from the $V_{\rm sum}\left(R,\gamma\right)$ potential, if spin–orbit conserving transitions are considered. On the other hand, the spin–orbit changing transitions will only be coupled by terms from the $V_{\rm dif}\left(R,\gamma\right)$ potential [9]. The $V_{\rm sum}\left(R,\gamma\right)$ PES is strongly repulsive. There is an attractive well at larger atom–diatom distances having a minimum of about $-110\,{\rm cm}^{-1}$. At shorter distances a repulsive wall steeply builds up. The $V_{\rm dif}\left(R,\gamma\right)$ PES is strongly attractive. Both PESs are asymmetric with respect to the plane perpendicularly halving the bond axis which is due to the heteronuclear nature of the molecule, though the $V_{\rm dif}\left(R,\gamma\right)$ more markedly deviates from $C_{\infty v}$ PES symmetry.

2.2 Scattering theory

The classical and quantum mechanical theories of atom–diatom molecule scattering are discussed in this section. The description of the atom–diatom scattering will be developed on the basis of Newtonian or, equivalently, Hamiltonian mechanics. Its key concept is that of the trajectory, where the spatial coordinates and momenta of a particle are exactly known during the entire course of the collision. Based on these assumptions the observable quantities, such as integral and differential cross sections, are derived. However, classical mechanics can only serve as an approximate description, since it is incapable of handling

quantum mechanical effects, whose consequences are indeed observed in experiments. Despite its shortfalls it has proven to be extremely useful by the virtue of giving simple, mechanical 'interpretation' of the dynamics. It is also helpful in discerning classical and quantum mechanical effects. Quantum mechanics provides a more accurate description of the scattering events, however, at the expense of losing the mechanical insight to some extent. This description exactly treats quantum effects, such as the uncertainty principle or interferences. It will be highlighted how these phenomena manifest themselves in deriving the observable quantities, which will be compared to those obtained classically. The differences which are inherent in the principles of quantum mechanics will be addressed.

2.2.1 Quasi-classical trajectory calculations

The method of quasi classical trajectory calculations (QCT) rely on the classical solution of the atom–molecule scattering problem. Analytical solutions only exist for a number of simple potentials *e.g.*, spherical hard shell potential, Lennard–Jones's *6-12* potential and *exp-6* potential [12]. If the potential describing the interaction between the particle has a more complicated form, it is usually not possible to present the deflection functions or the differential cross section in a closed form [12]. Nevertheless, it is still possible to obtain these quantities by means of numerical methods. The quasi-classical trajectory calculations assume that the trajectory of each particle, or path in other words, is fully determined by the classical laws of motion on the PES [107]. Thus the final position and momenta of the diatom and atom can be calculated from the initial ones by propagating the interacting particles between appropriate time bounds. The phase space or probability density is the fundamental notion in Hamiltonian mechanics, therefore a multitude of trajectories are required to establish the classical solution as opposed to a single one. These mechanistic details of the QCT calculations are discussed in the following section [108, 109].

The atom–diatomic molecule system consists of three atoms, as such nine pairs of coordinates and momenta describe their motion. The Hamiltonian of the system is expressed

in terms of Cartesian coordinates as follows [106]:

$$\mathcal{H} = \sum_{i=1}^{3} \frac{p_{x_i}^2}{2m_A} + \sum_{i=4}^{6} \frac{p_{x_i}^2}{2m_B} + \sum_{i=7}^{9} \frac{p_{x_i}^2}{2m_C} + V(x_1, x_2, ..., x_9), \tag{2.14}$$

where the atom is labeled by 'A' having a mass of m_A, the atoms constituting the molecule are denoted by 'B' and 'C' having masses m_B and m_C. x_i and p_{x_i} are the coordinates and linear momenta of the atom for $i = 1, 2, 3$. The coordinates and momenta of atom 'B' and 'C' are indexed by $i = 4, 5, 6$ and $7, 8, 9$, respectively. The first three sums describe the kinetic energy of the system, whereas $V(x_1, x_2, ..., x_9)$ is the potential energy of the system in Eq. (2.14). This equation contains the motion of the centre of mass. It is thus straightforward to separate that from the internal motion of the system. This is equivalent to running the calculations in a space fixed frame as shown in Figure 2.3. If the origin is placed in the centre of mass of the diatom, only six pairs of coordinates and momenta are needed to describe the motion of the system. The Hamiltonian can then be parametrised in terms of Jacobi coordinates, all of which have a well defined and relevant physical meaning. The coordinates q_1, q_2 and q_3 are the relative position of atom 'C' with respect to atom 'B'. Intuitively, these correspond to the bond vector, $\boldsymbol{r}$, of the molecule. q_4, q_5 and q_6 specify the position of atom 'A' relative to the centre of mass of the B–C moiety, which is equivalent to the atom–diatom distance in the scattering picture. The conjugate momenta are denoted by p_{q_i} for $i = 1, 2, ..., 6$. There is an important derived coordinate, γ, which is the angle between $\boldsymbol{r}$ and $\boldsymbol{R}$, calculated by forming the dot product of $\boldsymbol{r}$ and $\boldsymbol{R}$:

$$\cos(\gamma) = \frac{R_x r_x + R_y r_y + R_z r_z}{|\boldsymbol{R}||\boldsymbol{r}|} = \frac{q_1 q_4 + q_2 q_5 + q_3 q_6}{\sqrt{q_1^2 + q_2^2 + q_3^2}\sqrt{q_4^2 + q_5^2 + q_6^2}}. \tag{2.15}$$

Then the Hamiltonian of the system in Jacobi coordinates is given as

$$\mathcal{H} = \sum_{i=1}^{3} \frac{p_{q_i}^2}{2\mu_{BC}} + \sum_{i=4}^{6} \frac{p_{q_i}^2}{2\mu_{A,BC}} + V\left(\boldsymbol{R}, \boldsymbol{r}, \gamma\right), \tag{2.16}$$

where μ_{BC} is the reduced mass of the diatom, and $\mu_{A,BC}$ is the reduced mass of the atom

and diatom together. The first term expresses the kinetic energy associated with the motion of the molecule, the second is the kinetic energy term of the relative motion of atom 'A' with respect to the molecule. The potential energy term $V(\boldsymbol{R}, \boldsymbol{r}, \gamma)$ expresses the interaction potential persisting between the atoms, and it also includes the effect of the external field, if any acts on the atoms.

The trajectories are generated on the potential energy surface by solving Hamilton's equations of motion according to Eqs. (2.17) and (2.18):

$$\frac{\mathrm{d}q_i}{\mathrm{d}t} = \frac{\partial \mathcal{H}}{\partial p_i} = \frac{\partial \mathcal{T}}{\partial p_i} \tag{2.17}$$

$$\frac{\mathrm{d}p_i}{\mathrm{d}t} = -\frac{\partial \mathcal{H}}{\partial p_i} = -\frac{\partial \mathcal{V}}{\partial p_i} = -\left(\frac{\partial V}{\partial R}\frac{\partial R}{\partial q_i} + \frac{\partial V}{\partial r}\frac{\partial r}{\partial q_i} + \frac{\partial V}{\partial \cos\gamma}\frac{\partial \cos\gamma}{\partial q_i}\,.\right) \tag{2.18}$$

The propagation of the equations should, in theory start, in time and space infinitely before the particle reaches the turning point, and should continue to a point infinitely removed in time and space afterwards [12]. Practically, the starting point is positioned at a distance from the centre of mass at which the interaction between the atom and the molecule is negligible, so that the derivative of the potential energy is practically zero. The propagation is terminated when the atom is beyond the interaction region, so that its momenta are no longer affected by the molecule. The starting distance, R_0, is determined by running small batches of trajectories, making sure that increasing R_0 does not change the outcome of the calculation, so that the derivative of the potential energy is practically zero [110]. In the case of the NO(X)–Ar system this corresponds to vanishingly small interaction energy at large atom–diatom separations. The equations which describe spatial-temporal evolution of the system are solved by numerical methods, namely by the fourth order Runge–Kutta method [111] followed by Hammond's predictor corrector algorithm [112]. These explicitly propagate the atom on the potential energy surface by solving Eqs. (2.17) and (2.18). The bond length of the molecule is kept fixed at its equilibrium value of by means of Lagrangian multipliers [113].

The space fixed frame in which the trajectories were initialised and propagated is shown

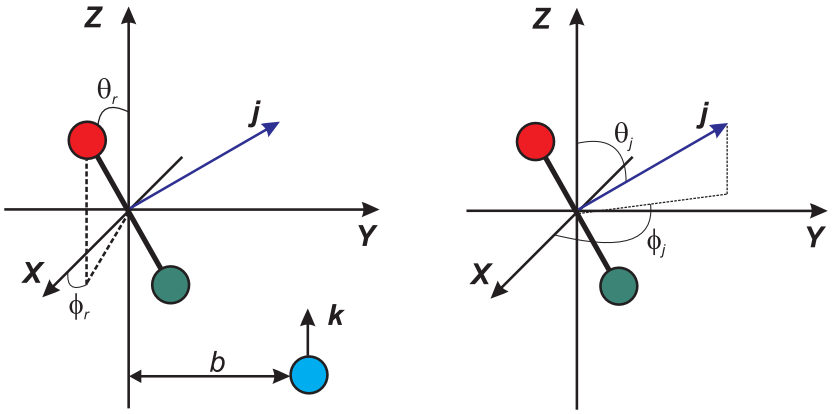

Figure 2.3: The space fixed frame in which the QCT and hard shell calculations are carried out (left panel). The incoming particle initially resides in the $+Y - Z$ quadrant at a distance of b from the Z axis. The initial orientation of the molecule is specified by angles θ_r and ϕ_r. θ_j the polar and ϕ_j the azimuthal angles of $\boldsymbol{j}$ are shown in the right panel of the figure.

in Figure 2.3. The origin of the space fixed frame is placed at the centre of mass of the diatom. Its principal axis, Z, is parallel to the initial relative velocity, $\boldsymbol{k}$. The incoming particle always initially reside in the $+Y - Z$ quadrant. The third axis, X, is chosen in order that the frame is righthanded. The details of the calculations are as follows:

- Owing to the statistical nature of QCT calculations a *great number* of trajectories are required to obtain reliable results. Usually the number of trajectories has to be in the order of 10^5–10^6 depending on how good statistics are needed for physical quantities to be determined. The initial conditions are chosen from a distribution defined so as to correctly model the actual physical system of interest.

- *Total energy* or *collision energy* is one of the most important quantities in inelastic scattering. Its magnitude determines the possible degrees of the rotational and vibrational excitation. Its relative magnitude compared to the different features of the PES is crucial in governing the dynamics of the collisions. As such, it is important that it is set correctly. It can be kept fixed for all of the trajectories, the method which was used in this study, or varied between pre-defined limits according to a particular distribution, for instance a Boltzmann distribution.

- *Impact parameter*, b, is the distance between the initial position of the atom and

the Z axis. It is continuously sampled between zero and a positive value which is large enough to keep the atom at a distance at which the interaction between the atom and the molecule is minimal. Since it is allowed to take any values between the above limits, the initial orbital angular momentum, $\boldsymbol{\ell}$ is not quantised.

- The *initial bond axis orientation* is defined by two angles, θ_r and ϕ_r. ϕ_r is the azimuth of the bond axis, θ_r is the polar angle. It is here where we define that $\theta_r = 0$ refers to a molecular configuration when the O-end of the molecule points towards the $+Z$ direction, that is the bond axis vector, $\boldsymbol{r}$, is drawn from the N-end of the molecule to the O-end. θ_r varies between 0 and π radians, and ϕ_r is sampled in the $[0, 2\pi)$ interval.

- *Initial rotational angular momentum of the molecule*, $\boldsymbol{j}$. The angular momentum, in general, is continuous in classical mechanics. However, if one wishes to compare the QCT results to quantum mechanical ones, where j is quantised, it is necessary to quantise the classical angular momentum. It is usually done by equating the modulus of the classical and quantum mechanical angular momenta, $|\boldsymbol{j}| = \hbar\sqrt{j(j+1)}$, then j is rounded to the nearest integer. A collision is considered as elastic, if the initial and final rotational quantum numbers do not differ by more than ± 0.5, that is $j' = j \pm 0.5$. The initial rotational angular momentum can only take certain values according to which initial quantum state is considered. Despite j being initially restricted it is allowed to vary continuously during the course of the propagation, for it is permitted by the laws of classical mechanics. The final rotational quantum number, j', then has to be binned to an integer value, as shown above. If $\boldsymbol{j} = 0$ the molecule initially does not rotate, otherwise the molecule has a non-zero angular momentum whose magnitude and direction have to be assigned. The direction of $\boldsymbol{j}$ is specified the polar and azimuth angle, θ_j and ϕ_j, respectively, in the space fixed frame. Since $\boldsymbol{j}$ is perpendicular to the molecular axis, its distribution is in part determined by the molecular axis distribution. If both θ_j and ϕ_j are uniformly distributed, the

rotational motion of the molecule is not polarised. Confining these two angles to a particular non-uniform distribution means that the molecule preferentially rotates in a particular sense, or has a preferred plane of rotation.

The above parametrisation is necessary and sufficient to fully specify the initial conditions of the triatomic system. It is worth noting this information can be provided in a number of ways. Most importantly the action angle variables [106] have proven to be especially useful in the semi-classical formulation of molecular scattering theory.

Classical hard shell calculations

A further step to simplify the scattering problem is achieved by replacing the $V_{\text{sum}}(R, \gamma)$ PES on which the QCT trajectories run by a hard shell potential [114–116]. The hard shell potential is infinite within a certain boundary and is zero outside of it [116]. This method does not require the explicit propagation of trajectories, and provides an almost analytical insight into the collision dynamics. As such, it will be discussed in Chapter 4.

2.2.2 Classical differential and integral cross sections

Analytical formulae of the classical differential and integral cross sections only exist for a small number of simple systems [12]. For more complex problems, these quantities have to be derived from the multitude of the trajectories by using statistical methods. Since the hard shell model is essentially a quasi-classical trajectory method, in which the special form of the potential makes the explicit propagation unnecessary, the following discussion is equally valid for both the QCT and classical hard shell calculations.

The atom is initially positioned at a distance b, from the Z axis of the collision frame. Depending on the impact parameter, b the atom is likely to experience different parts of the potential, at least at the beginning of its path, according to our classical picture. As a consequence, the probability of the system ending up in a particular final state is expected to be a function of the impact parameter. The probability of the transition from the initial state 'i' to final state 'f' for a particular impact parameter, b, is quantified by the classical

opacity function:

$$P_{f\leftarrow i}(b) = \frac{N_{f\leftarrow i}(b)}{N_i(b)}, \tag{2.19}$$

where $N_{f\leftarrow i}(b)$ is the number of particles going through the specified transition and $N_i(b)$ the total number of particles starting in the initial with a particular impact parameter b. The classical partial cross section defined in Eq. (2.20) is the differential cross section of the $(b, b + \mathrm{d}b)$ annulus [1]:

$$\sigma_{f\leftarrow i}(b) = 2\pi b P_{f\leftarrow i}(b)\,. \tag{2.20}$$

The total cross section is the integral of the partial cross section from zero impact parameter to infinity, hence it is called the integral cross section (ICS). In practice, there is an upper limit for the integration, a maximum impact parameter, $b_{\max}$, beyond which the probability of the transition of interest vanishes [1]. The integral represent a summation of the transition probability of each and every annulus:

$$\sigma_{f\leftarrow i} = \int_0^{b_{\max}} \sigma_{f\leftarrow i}(b)\mathrm{d}b\,. \tag{2.21}$$

The integral cross section is the effective area that the incoming particle needs to encounter in order to induce the $f \leftarrow i$ transition. It is worth noting that while it is possible to determine $b_{\max}$ for an inelastic collision, *i.e.* to find the maximum impact parameter beyond which the interaction is not sufficient to induce inelastic transitions, no such boundary exists in the case of elastic collisions. The elastic opacity function becomes unity at a sufficiently large impact parameter where the inelastic transition probability vanishes. As a consequence the elastic cross section diverges to infinity.

From the point of view of the experiments presented in this thesis, it is more convenient to quantify the transition probability as a function of, θ, the angle between the initial and final relative velocities. This angle is called the scattering angle [12]. This scattering angle

dependent function is the differential cross section, DCS, and is defined as

$$\frac{\mathrm{d}\sigma_{f\leftarrow i}}{\mathrm{d}\omega} = \frac{1}{\sin\theta}\frac{\mathrm{d}^2\sigma_{f\leftarrow i}}{\mathrm{d}\theta\mathrm{d}\phi}\,, \tag{2.22}$$

which is the cross section for scattering into a conical solid angle $\mathrm{d}\omega = \sin\theta\mathrm{d}\theta\mathrm{d}\phi$. The ICS is the integral of the DCS over 4π solid angle:

$$\sigma_{f\leftarrow i} = \int_0^{2\pi}\int_0^{\pi} \frac{\mathrm{d}\sigma_{f\leftarrow i}}{\mathrm{d}\omega}\sin\theta\mathrm{d}\theta\mathrm{d}\phi\,. \tag{2.23}$$

Both the ICSs and the DCSs are the central physical quantities of scattering theory and experiments. The ICS indicates how favoured a particular transition is. The differential cross section provides detailed information about the mechanism of collisions. For instance, it will have a particular shape, if it is associated with impulsive collisions, which is markedly different to that due to a deflective collision induced by long range attractive forces.

The DCS is obtained from the QCT trajectories by binning the number of particles that underwent the $f \leftarrow i$ transition into a $(\theta, \theta+\Delta\theta)$ bin. This method is called histogram binning and the exact expression of the DCS is given by

$$\frac{\mathrm{d}\sigma_{f\leftarrow i}}{\mathrm{d}\omega} = \frac{1}{2\pi\Delta\cos\theta}b_{\max}^2\pi\frac{N_{f\leftarrow i}(\theta+\Delta\theta)}{N_i(\theta+\Delta\theta)}\,. \tag{2.24}$$

The drawback of this method is that a very large number of trajectories are required for each final state to have reliable statistics for even moderate angular resolution. A more feasible way to generate DCSs of sufficient angular resolution is to expand them in terms of Legendre polynomials [112] as shown in Eq. (2.25). The $c_{k,f\leftarrow i}$ expansion coefficients

in Eq. (2.25) are the expectation values of the corresponding P_k Legendre polynomials:

$$\frac{\mathrm{d}\sigma_{f\leftarrow i}}{\mathrm{d}\omega} = \frac{\sigma_{f\leftarrow i}}{4\pi}\sum_{k=0} c_{k,f\leftarrow i} P_k\left(\cos\theta\right) \tag{2.25}$$

$$\begin{aligned} c_{k,f\leftarrow i} &= \left\langle P_k\left(\cos\theta\right)\right\rangle_{f\leftarrow i} \\ &= \frac{1}{N_{f\leftarrow i}}\sum_{n=1}^{N_{f\leftarrow i}} P_k\left(\theta_{n,f\leftarrow i}\right)\,. \end{aligned} \tag{2.26}$$

Usually, a reasonably low number of trajectories is sufficient to obtain smooth and continuous DCSs.

2.2.3 Quantum mechanical theory of atom–molecule scattering

In the following section, the time-independent quantum mechanical theory of atom–diatomic molecule scattering is reviewed. Firstly, the solution of the Schrödinger equation of elastic scattering by a central force is discussed. The concepts of phase shifts and scattering amplitudes are introduced. These two quantities are subsequently related by the partial wave expansion technique. The elastic phase shifts are then generalised for inelastic scattering by introducing the concepts of scattering and transition matrices. The atom–molecule scattering problem is cast in the mathematical form of the so-called close–coupled equations. Their solution along with scattering matrix theory serve as a basis to derive the observable quantities. The features particular to quantum mechanics will be addressed at each point throughout the discussion outlined above.

Elastic scattering from a central potential

The Schrödinger equation of a particle scattering from a central force is written as

$$\left[-\frac{\hbar^2}{2\mu}\nabla^2 + V(R)\right]\Psi(r) = E\Psi(R)\,, \tag{2.27}$$

where μ is the reduced mass of the system and $V(R)$ is the interaction potential which asymptotically goes to zero, that is $V(R\rightarrow\infty) = 0$. The asymptotic solution of Eq. (2.27)

assumes the form of Eq. (2.28), where the first exponential term represents the unperturbed incoming plane wave, the second term is the scattered spherical wave. $f(\theta)$ is the scattering amplitude the square modulus of which is proportional to the differential cross section [12]:

$$\Psi(R) \underset{R\to\infty}{\sim} \mathrm{e}^{+ikz} + \frac{\mathrm{e}^{+ikR}}{R} f\left(\theta\right) . \tag{2.28}$$

On the other hand the Schrödinger equation of Eq. (2.27) can be written as

$$\left[\frac{\mathrm{d}^2}{\mathrm{d}R^2} + k^2 - U_\ell(R)\right] \psi_\ell(R) = 0\,, \tag{2.29}$$

where the square of the wavenumber $k^2 = 2\mu E/\hbar^2$ and the effective potential $U_\ell(R) = [V(R) + \ell(\ell+1)/R^2]2\mu/\hbar^2$. It is possible to show that the general asymptotic solution of this equation is

$$\psi_\ell(R) \sim \sin(kR - \ell\pi/2 + \eta_\ell)\,. \tag{2.30}$$

The $\ell\pi/2$ factor accounts for the centrifugal barrier. The η_ℓ term is called the phase shift. This is due to the presence of the $U_l(R)$ potential which perturbs the wave function. Since in the absence of the $U(R)$ potential the phase shift is zero, the effect of the potential manifests itself in η_ℓ. The relationship between scattering amplitudes of Eq. (2.28) and the phase shifts in Eq. (2.30) can be established by using the partial wave expansion of the exponential function [12]:

$$\mathrm{e}^{+ikz} = \sum_{l=0}^{\infty} (2\ell+1) i^l j_\ell(kr) P_\ell\left(\cos\theta\right) , \tag{2.31}$$

where j_ℓ are the Bessel functions of the first kind [111], and P_ℓ are the Legendre polynomials. The elastic scattering amplitude can then be written as

$$f(\theta) = \frac{1}{2ik} \sum_{\ell=0}^{\infty} (2\ell+1)(\mathrm{e}^{i2\eta_\ell} - 1) P_\ell(\cos\theta)\,. \tag{2.32}$$

Classically, it is possible to simultaneously define the exact position and momentum of the incoming particle. This is no longer possible in quantum mechanics due to the Heisenberg Uncertainty Principle. Roughly speaking, since the linear momentum of the incoming particle is well defined in the direction of propagation, its wave function has to spread over the entire plane perpendicular to this direction. The uncertainty of the scattering angle and that of the impact parameter is also interrelated by the Heisenberg Uncertainty Principle, so that $\Delta\theta = \Delta p_\perp/(mv) = \hbar/(mv\Delta b)$, where $p_\perp$ is the component of $\boldsymbol{p}$ perpendicular to the propagation direction. If the scattering angle is perfectly defined, the impact parameter, or more precisely ℓ, should extend to infinity, which is actually the basis of the partial wave expansion. As a consequence, each partial wave contributes to all scattering angles. On the contrary, in the classical picture, the deflection function restricts the values of b which lead to a particular scattering angle [12].

Let us rewrite Eq. (2.32)

$$f(\theta) = \frac{1}{2ik}\sum_{\ell=0}^{\infty}(2\ell+1)(S_\ell - 1)P_\ell(\cos\theta)\,, \tag{2.33}$$

where $S_\ell = \mathrm{e}^{i2\eta_\ell}$ is the scattering matrix. It is possible to generalise the S-matrix to describe multichannel and inelastic scattering. It will be shown that the S-matrix and the closely related T-matrix determine the relationship between the initial and final waves in inelastic and non-central collisions which are dealt with in the following section.

Close-coupled equations

The exact mathematical formulation of the atom–diatomic molecule scattering problem was first developed by Arthurs and Dalgarno [50]. The key steps of their procedure lay in expressing the system's wave function by coupling the rotational and orbital angular momenta, and in constructing a set of equations by forming the matrix representation of the Schrödinger equation. The Hamiltonian can then be parametrised by the Jacobi coordinates; such as $\boldsymbol{r}$, the atom–atom separation in the molecule, $\boldsymbol{R}$, the distance be-

tween the baricentre of the diatom and the atom and γ, the Jacobi angle, which is well suited to handle atom–molecule collisions as were shown in Section 2.2.1. Ignoring the molecules vibrational motion, the total Hamiltonian of the atom–molecule system is given by Eq. (2.34):

$$\mathcal{H} = \mathcal{H}_{\text{rot}} - \frac{\hbar^2}{2\mu}\nabla_R^2 + \frac{\hbar^2}{2\mu R^2}\ell(\ell+1) + V(R,\gamma)\,, \tag{2.34}$$

where μ is the reduced mass of the system. Since $\boldsymbol{r}$ is kept fixed at the equilibrium bond length, the Hamiltonian of the above form will be considered. However, the derivation can be extended to treat vibrationally inelastic collisions [12]. The Hamiltonian is factored into four terms, each representing a particular type of contribution to the total energy. The first term, $\mathcal{H}_{\text{rot}}$, is the rotational Hamiltonian of the diatomic molecule:

$$\hat{\mathcal{H}}_{\text{rot}} Y_j^{m_j}(\hat{\boldsymbol{r}}) = \frac{\hbar^2}{2I} j(j+1) Y_j^{m_j}(\hat{\boldsymbol{r}})\,, \tag{2.35}$$

where j is the rotational angular momentum quantum number and m_j its projection quantum number onto a particular axis. I is the moment of inertia of the diatom. The translational energy contribution of the atom is represented by the second term in Eq. (2.34). The angular motion of the atom is given by the third term in Eq. (2.34), where ℓ is the orbital angular momentum quantum number which has a projection of m_l and whose eigenfunctions are the spherical harmonics, $Y_\ell^m(\hat{\boldsymbol{R}})$. The potential energy term, $V(R,\gamma)$, represents the interaction between the atom and the molecule.

If the collision energy is denoted by E_{coll} then the total energy, E_j, of the system for the j-th rotational state is

$$E_j = E_{\text{coll}} + \frac{\hbar^2}{2I} j(j+1)\,. \tag{2.36}$$

The correct total eigenfunction of this Hamiltonian should be an eigenfunction of the radial motion of the atom, the rotational motion of the molecule and the rotational motion of the atom with respect to the molecule at the same time [12]. The system also has a total angular momentum denoted by $\boldsymbol{J}$ which results from the coupling of the rotational

angular momentum and orbital angular momentum, that is to say $\boldsymbol{J} = \boldsymbol{j} + \boldsymbol{\ell}$. Therefore the angular part of the total wavefunction is an eigenfunction of $\hat{\boldsymbol{J}}$. The coupling of the orbital and rotational wavefunctions is carried out according to Eq. (2.37):

$$\mathcal{Y}_{j\ell}^{JM}(\boldsymbol{R}, \hat{\boldsymbol{r}}) = \sum_{m_j, m_l} Y_{m_j}^{j}(\hat{\boldsymbol{r}}) Y_{m_\ell}^{\ell}(\hat{\boldsymbol{R}}) \langle j m_j, j m_\ell | J M \rangle \,, \tag{2.37}$$

where $\langle j m_j, j m_\ell | J M \rangle$ is the Clebsch–Gordan or vector-coupling coefficient [93, 99, 117] and M is the projection quantum number of $\boldsymbol{J}$. The total eigenfunction, $\Psi_{j\ell}^{JM}(\hat{\boldsymbol{R}}, \hat{\boldsymbol{r}})$ assumes a form of an expansion in the coupled representation:

$$\Psi_{j\ell}^{JM}(\boldsymbol{R}, \hat{\boldsymbol{r}}) = \sum_{j', \ell'} \frac{u_{j\ell j'\ell'}^{JM}(R)}{R} \mathcal{Y}_{j,\ell'}^{JM} \,. \tag{2.38}$$

The radial dependent expansion coefficients, $u_{j\ell j',\ell'}^{JM}(R)$, specify the form of the wave function at all distances. The determination of these coefficients is equivalent to solving the scattering problem. If the matrix elements of the Hamiltonian in Eq. (2.34) are formed between two eigenstates, the values of $u_{j'\ell'}^{JM}(R)$ can be ascertained from solving the following set of equations at any particular distance [50]:

$$\frac{\hbar^2}{2\mu} \left[-\frac{\mathrm{d}^2}{\mathrm{d}R^2} + \frac{\ell'(\ell'+1)}{R^2} - k_{j',j}^2 \right] u_{jj'\ell\ell'}^{JM}(R) + \sum_{j'', \ell''} \langle j''\ell'', JM | V | JM, j'\ell' \rangle u_{j\ell j''\ell''}^{JM}(R) = 0 \,. \tag{2.39}$$

The wavenumber $k_{j',j}$ embodies the energy differences between the entrance (initial) and exit (final) channels:

$$k_{j,j'} = \frac{2\mu}{\hbar^2} \left[E_{\mathrm{coll}} + \frac{\hbar^2}{2I} j(j+1) - \frac{\hbar^2}{2I} j'(j'+1) \right] . \tag{2.40}$$

The potential matrix elements are defined as

$$\langle j''\ell'', JM | V(R) | JM, j'\ell' \rangle = \int\int \mathcal{Y}_{j''\ell''}^{JM*} V \mathcal{Y}_{j'\ell'}^{JM} \mathrm{d}\hat{\boldsymbol{r}} \mathrm{d}\hat{\boldsymbol{R}}. \tag{2.41}$$

The various (j, ℓ) channels are coupled by the potential matrix elements, hence the common name 'coupling matrix'. The possible internal electronic structure of the molecule and the atom were ignored in the above derivation. It is possible to extend this formalism to include the effects arising from the possible open shell nature of the diatom, such as spin–orbit coupling, Λ-doubling [9, 100, 118]. Solving the close-coupled equation often imposes considerable mathematical difficulties. An important family of methods to solve this set of second order differential equations are the propagation methods [119], among other ones which are chosen according to the characteristics particular to the system investigated [14].

The complexity of the close-coupled equation can be much reduced by decoupling the various channels from each other. This is equivalent with making some of the summations vanish in Eq. (2.39) [14]. One can substitute the set of orbital angular quantum numbers, ℓ, by a single value, $\overline{\ell}$ which is the key step in deriving the so-called coupled-states (CS) equations [120–122]. The underlying physical picture corresponds to a collision in which the collision energy is so large that the precise value of the centrifugal barrier is unimportant. This approximation is expected to return good results when the potential is purely repulsive and it is in general less reliable in the case of attractive potentials [123]. The infinite order sudden (IOS) approximation further eases the mathematical burden of solving the coupled equations. It is assumed that all of the channels have the same energy, that is to say only one rotational quantum number, j, is included. Thus the IOS approximation can be perceived as the energy sudden approximation to the CS approximation [14, 124]. Close energy spacings of the energy levels is required to ensure the validity of the approximation $k_j \approx k_i \; i \neq j$ [121]. There exist numerous other decoupling schemes [14], however, only the IOS approximation will be used in the present work.

Scattering and transition matrices

The notion of the scattering matrix introduced during the discussion of elastic scattering in Eq.(2.33) is now generalised to inelastic collisions in the following paragraphs. The scattering operator, $\hat{S}$, by definition transforms the ingoing wave to the outgoing wave.

The transitions between different waves are obtained as a difference of the outgoing and ingoing waves. The relationship between them is traditionally represented by the transition operator, $\hat{T}$, as given in Eq. (2.43). The matrix elements of these operators are calculated over the basis of the eigenfunctions in Eq. (2.38). These matrices are referred to as scattering, or S-matrix, and transition, or T-matrix. The operators, or equivalently the matrices, contain all the knowledge about the system which can possibly be gained. Once they have been determined, all of the physical quantities of the scattering system can be derived:

$$\hat{S}|^{\rm in}\Psi\rangle = |^{\rm out}\Psi\rangle \tag{2.42}$$

$$\hat{T}|^{\rm in}\Psi\rangle = (\hat{S} - i\hat{I})|^{\rm in}\Psi\rangle\,. \tag{2.43}$$

It has been shown that the solution of the close coupled equations Eq. (2.39), the $u^{JM}_{j\ell,j'\ell'}$ expansion coefficients fully determine the outgoing wavefunction. All of the information on the scattering process is contained in the S-matrix. Thus an equivalence relation should exist between the two formalisms. This relationship can be established by investigating the asymptotic form of the radial part of the total wavefunction in the $R \to \infty$ limit. Let us consider an arbitrary transition from the $|JMj\ell\rangle$ initial state to the $|J'M'j'\ell'\rangle$ final state [50]:

$$u^{JM}_{j\ell,j'\ell'}(R) \sim \delta_{jj'}\delta_{\ell\ell'}{\rm e}^{-i(k_{jj}R-\frac{1}{2}\ell\pi)} - \sqrt{\frac{k_{jj}}{k_{j'j}}}S^{JM}_{j\ell,j'\ell'}{\rm e}^{+i(k_{j'j}R-\frac{1}{2}\ell'\pi)}\,. \tag{2.44}$$

The first exponential term in Eq. (2.44) is the asymptotic form of the ingoing wave, whilst the second belongs to the outgoing wave in Eq. (2.44). The S-matrix elements, $S^{JM}_{j\ell,j'\ell'}$, are chosen so that the sum of these two waves is proportional to the expansion coefficients $u^{JM}_{j\ell,j'\ell'}$. The S-matrix elements can then be expressed as:

$$S^{JM}_{j\ell,j'\ell'} = \sqrt{k_{j'j}}\frac{u^{JM}_{j\ell,j'\ell'}(R) - \delta_{jj'}\delta_{\ell\ell'}{\rm e}^{-i(k_{jj}R-\frac{1}{2}\ell\pi)}}{{\rm e}^{+i(k_{j'j}R-\frac{1}{2}\ell'\pi)}}\,. \tag{2.45}$$

Since the total angular momentum must be conserved during the collision, the S-matrix is diagonal with respect to J. Also the S-matrix is independent of M.

2.2.4 Observable quantities

The probabilistic nature of the quantum mechanical processes becomes more apparent, if the physically observable quantities, such as differential and integral cross sections are derived on the basis of the S-matrix theory. Let us consider an initial wavefunction for a particular total angular quantum number, J. This, in general, is a superposition of wavefunctions according to Eq. (2.46) where the n superindex stands for the j, ℓ pair of indices:

$$|^{\text{in}}\Psi^J\rangle = \sum_n c_n |\Psi_n^J\rangle \,. \tag{2.46}$$

This wave function has to be normalised to unity which is equivalent with requiring that

$$\sum_n |c_n|^2 = 1 \,,$$

where the square modulus of the expansion coefficient c_n is the probability of the finding the system in the $|\Psi_n^J\rangle$ state. Let us assume the system initially resides in a single $|\Psi_i^J\rangle$ state. Due to the interactions persisting in the system, this initial wavefunction evolves to the final state $|^{\text{out}}\Psi^J\rangle$, which is symbolically expressed by letting $\hat{S}^J$ operate on the initial state, $|^{\text{in}}\Psi^J\rangle$ as in Eq. (2.47):

$$|^{\text{out}}\Psi^J\rangle \;\; = \;\; \hat{S}^J |\Psi_i^J\rangle \,. \tag{2.47}$$

The probability of the $f \leftarrow i$ transition is equal to the square modulus of the T-matrix element [12]:

$$P_{f\leftarrow i}(J) = |T_{f\leftarrow i}|^2 \,, \tag{2.48}$$

where $P_{f\leftarrow i}(J)$ is the quantum mechanical opacity function. The probability of an inelastic collision is given by

$$P_{f\leftarrow i}(J) = |c_f|^2, \quad f \neq i\,. \tag{2.49}$$

That is, the probability of finding the system in the f state is equal to the probability of inducing the $f \leftarrow i$ particular transition. The elastic opacity function is

$$P_{f\leftarrow i}(J) = 1 + |c_f|^2 - 2\Re(c_i), \quad f = i\,. \tag{2.50}$$

The transition probability is no longer equal to the square modulus of Ψ_i^J's expansion coefficient in the outgoing wavefunction. Since the ingoing and outgoing waves are identical apart from the phase shift induced by the interaction potential, they can interfere with each other. This may lead to enhancing or reducing the transition probability depending on whether the interference is constructive or destructive, respectively.

The quantum mechanical partial cross section is derived from the opacity function of Eq. (2.48) according to Eq. (2.51):

$$\sigma_{f\leftarrow i}^J = \frac{\pi}{k^2}\frac{2J+1}{2j+1}\left[2\min(J,j)+1\right]P_{f\leftarrow i}(J)\,, \tag{2.51}$$

where k is the wave number and j is the rotational quantum number of state f. $\sigma_{f\leftarrow i}^J$ corresponds to a cross section which would be measured in a hypothetical experiment in which only one partial wave contributes to the scattering. Nevertheless, there is a correspondence relation between J and the classical impact parameter b. By the virtue of the approximation $J \approx \ell \approx kb$, the different partial waves can be linked to various impact parameters.

The quantum mechanical integral cross section is the sum of the partial cross sections:

$$\sigma_{f\leftarrow i} \;=\; \sum_{J=0}^{\infty}\sigma_{f\leftarrow i}^J = \sum_{J=0}^{\infty}\frac{\pi}{k^2}\frac{2J+1}{2j+1}\left[2\min(J,j)+1\right]P_{f\leftarrow i}(J) \tag{2.52}$$

In theory the summation is infinite. In practice, it can be truncated at a sufficiently large

J value, at which the partial cross section vanishes. The classical mechanical equivalent is the termination of the integral over at a maximum impact parameter, $b_{\max}$, in Eq. (2.20).

The differential cross section uncovers the scattering angle dependence of the integral cross section. As such, its notional definition is provided in Eq. (2.22). In terms of quantum mechanics the DCS is equal to the the square modulus of the scattering amplitude. The scattering amplitude in turn can again be expressed in terms of the T-matrix elements:

$$f_{f\leftarrow i}(\theta) = \frac{1}{2ik}\sum_{J}\frac{2J+1}{2j+1}\left[2\min(J,j)+1\right]P_J\left(\cos\theta\right)T_{fi}\,. \tag{2.53}$$

Thus the differential cross section can be written as

$$\begin{aligned}\frac{\mathrm{d}\sigma_{f\leftarrow i}}{\mathrm{d}\omega} &= \frac{1}{4k^2}\sum_{J,J'}\frac{2J+1}{2j+1}\frac{2J'+1}{2j+1}\left[2\min(J,j)+1\right]\left[2\min(J',j)+1\right] \\ &\times\ T^{J}_{fi}T^{J*}_{fi}P_J\left(\cos\theta\right)P_{J'}\left(\cos\theta\right)\,.\end{aligned} \tag{2.54}$$

The DCS in Eq. (2.54) can be viewed as a summation over the elements of a matrix. The diagonal elements contain the contributions from identical partial waves. The off-diagonal elements – with respect to the total angular momentum – are the interference terms between different partial waves. Each partial wave contributes to the scattering intensity for every scattering angle. Classically, this would correspond to a situation where the deflection function maps the whole impact parameter regime to each scattering angle.

2.3 Summary

The classical and quantum mechanical theories of atom–diatom collisions were reviewed. The fundamental notions, such as angular momenta, coupling phenomena, and potential energy surfaces relevant to the NO(X)–Ar scattering were discussed. Methods were provided to calculate various classical and quantum mechanical physical quantities, such as opacity functions, differential cross sections and integral cross sections. This includes an overview of the scattering or S-matrix theory, and the formulation of the so-called

close-coupled equations. The following chapter builds further on this overview, where the classical and quantum mechanical theories of rotational angular momentum polarisation will be discussed.

Chapter 3

Theory of angular momentum polarisation

The rotational motion of a scattered molecule is not usually random. The non-uniformity of the molecular rotation is described by the rotational polarisation. It is possible to use rotational polarisation to gain detailed information about the mechanism of the scattering process. The classical rotational angular momentum, $\boldsymbol{j}$, is a continuous variable which can be directed towards any arbitrary point in space. Thus the probability that $\boldsymbol{j}$ points in a certain direction is best described by a continuous probability distribution function [11]. This distribution fully characterises the rotational motion of the molecule; as such, it describes both the rotational orientation, the sense of rotation, and the rotational alignment, the plane of rotation. These quantities in turn are quantified by the polarisation moments and the scattering angle resolved polarisation dependent differential cross sections (PDDCSs), all of which are defined along with discussion of their exact meaning in this chapter.

The quantum mechanical rotational angular momentum is quantised, and its directional interpretation is not as straightforward as in classical mechanics due to the Heisenberg Uncertainty Principle. The polarisation can instead be interpreted as the coherence between different rotational magnetic sublevels of the system. This will be formulated on the basis of the density matrix and the closely related state multipole theories. The quantum mechanical polarisation moments and PDDCSs will also be derived. The working equations will be developed by means of which the polarisation moments can conveniently

be obtained from quasi-classical and quantum mechanical calculations. The correspondence relations between the classical and quantum mechanical theories will be highlighted throughout this chapter.

3.1 Classical mechanical theory of angular momentum polarisation

3.1.1 The scattering frame

When dealing with vectors, it is usual to establish a frame in which their direction can be defined. It is often convenient to choose the so-called scattering frame as the principal frame in particle–particle scattering experiments. The scattering frame is defined as follows: by considering a collision where the colliding partners' initial relative velocity is denoted by $\boldsymbol{k}$. The $\hat{\boldsymbol{z}}$ axis of the scattering frame is parallel to $\boldsymbol{k}$. The particle is always scattered to the $+zx$ half of the plane with a relative velocity of $\boldsymbol{k'}$ which determines the direction of the second axis, $\hat{\boldsymbol{x}}$. The third axis, $\hat{\boldsymbol{y}}$, is chosen so as to render the frame to be righthanded as shown in the left panel of Figure 3.1. Therefore, the final relative velocities of the scattering partners fully define the scattering frame.

3.1.2 Classical probability distribution functions

The classical rotational angular momentum, $\boldsymbol{j}$, can have a well defined direction. This is given by the angles (θ_j, ϕ_j), where θ_j is the polar angle of $\boldsymbol{j}$ and ϕ_j is the azimuth. Both angles are defined in the scattering frame as depicted in the right panel of Figure 3.1. The probability that the particle is scattered through a scattering angle, θ, and that the final rotational angular momentum, $\boldsymbol{j'}$ points in the direction $(\theta_{j'}, \phi_{j'})$ is given by the $P(\theta, \theta_{j'}, \phi_{j'})$ probability distribution function [10, 11, 16, 44]. This function should be

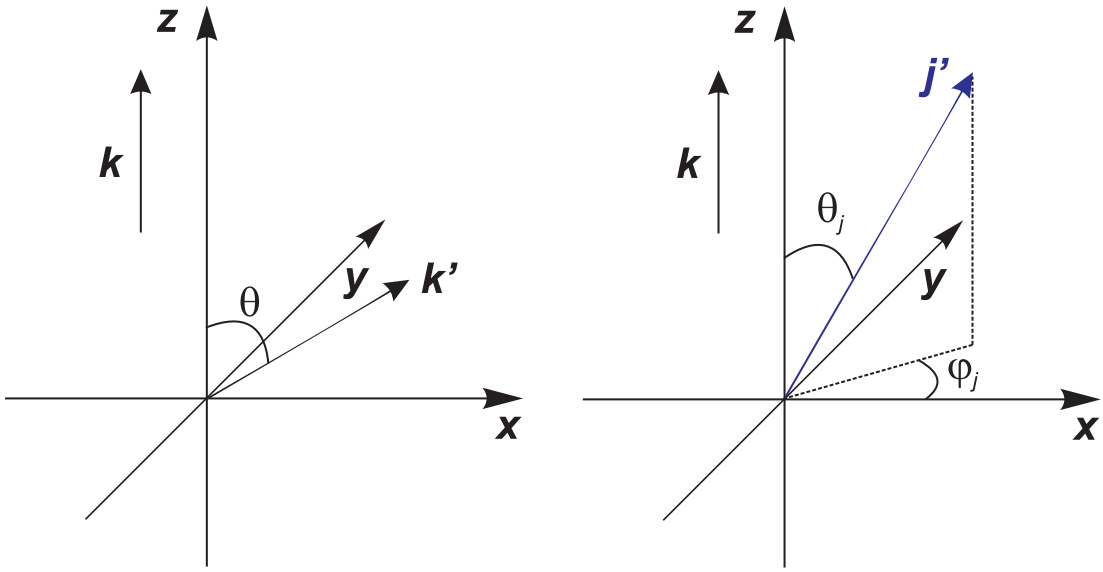

Figure 3.1: The principal axis, $\hat{\boldsymbol{z}}$, of the scattering frame is parallel to the initial relative velocity, $\boldsymbol{k}$. The atom is always scattered to the $+xz$ half-plane (left panel). The polar angle, $\theta_{j'}$, and the azimuth, $\phi_{j'}$, of $\boldsymbol{j'}$ are parametrised in the scattering frame (right panel).

normalised to unity:

$$\int_0^{\pi}\int_0^{\pi}\int_0^{2\pi} P\left(\theta,\theta_{j'},\phi_{j'}\right)\sin\theta \mathrm{d}\theta\sin(\theta_{j'})\mathrm{d}\theta_{j'}\mathrm{d}\phi_{j'} = 1. \tag{3.1}$$

This distribution can be expanded in terms of the complex conjugates of the modified spherical harmonics, $C_{kq}(\theta_{j'},\phi_{j'})$ [16, 117]:

$$P\left(\theta,\theta_{j'},\phi_{j'}\right) = \frac{1}{4\pi}\sum_{k=0}^{\infty}\sum_{q=-k}^{k}(2k+1)\left(\frac{2\pi}{\sigma}\frac{\mathrm{d}\sigma_q^{(k)}}{\mathrm{d}\omega}\right)C_{kq}^{*}\left(\theta_{j'},\phi_{j'}\right), \tag{3.2}$$

where σ is the integral cross section defined in Eq. (2.23). The scattering angle dependent expansion coefficients are called the normalised polarisation dependent differential cross sections (PDDCSs). They are the expectation values of the modified spherical harmonics over the $P\left(\theta,\theta_{j'},\phi_{j'}\right)$ distribution at a particular scattering angle, which can be shown by inverting Eq. (3.2) and using the orthogonality properties of the modified spherical

harmonics:

$$\left(\frac{2\pi}{\sigma}\frac{\mathrm{d}\sigma_q^{(k)}}{\mathrm{d}\omega}\right) = \int_0^{\pi}\int_0^{2\pi} P\left(\theta,\theta_{j'},\phi_{j'}\right) C_{kq}^{*}(\theta_{j'},\phi_{j'}) \sin\theta_{j'}\mathrm{d}\theta_{j'}\mathrm{d}\phi_{j'} \quad (3.3)$$
$$= \langle C_{kq}^{*}(\theta_{j'},\phi_{j'})\rangle \,.$$

As such, each PDDCS measures the corresponding multipolar contribution to the whole $P\left(\theta,\theta_{j'},\phi_{j'}\right)$ distribution [11, 15]. For instance, the angular distribution function is equivalent to the $k = 0$, $q = 0$ PDDCS:

$$\int_0^{\pi}\int_0^{2\pi} P\left(\theta,\theta_{j'},\phi_{j'}\right)\sin\theta_{j'}\mathrm{d}\theta_{j'}\mathrm{d}\phi_{j'} = \frac{2\pi}{\sigma}\frac{\mathrm{d}\sigma_0^{(0)}}{\mathrm{d}\omega} = P(\cos\theta) = \frac{2\pi}{\sigma}\frac{\mathrm{d}\sigma}{\mathrm{d}\omega}. \quad (3.4)$$

The average polarisation of the full ensemble is recovered if $P\left(\theta,\theta_{j'},\phi_{j'}\right)$ is integrated over the entire scattering angle region as in Eq. (3.5),

$$P\left(\theta_{j'},\phi_{j'}\right) = \int_0^{\pi} P\left(\theta,\theta_{j'},\phi_{j'}\right)\sin\theta\mathrm{d}\theta \,. \quad (3.5)$$

This probability function, $P\left(\theta_{j'},\phi_{j'}\right)$, can again be given in terms of a series expansion according to Eq. (3.6):

$$P\left(\theta_j,\phi_j\right) = \frac{1}{4\pi}\sum_0^k (2k+1)\sum_{q=-k}^{k} a_q^{(k)} C_{kq}^{*}(\theta_{j'},\phi_{j'}) \,, \quad (3.6)$$

where the $a_q^{(k)}$ expansion coefficients are the polarisation moments. They are the expectation values of $C_{kq}^{*}(\theta_{j'},\phi_{j'})$ spherical harmonics calculated according to Eq. (3.7). The $a_q^{(k)}$ moments can be viewed as the multipole contributions to the $P\left(\theta_{j'},\phi_{j'}\right)$ distribution function. They also quantify the overall polarisation of the whole scattered ensemble,

$$a_q^{(k)} = \int_0^{\pi}\left(\frac{2\pi}{\sigma}\frac{\mathrm{d}\sigma_q^{(k)}}{\mathrm{d}\omega}\right)\sin\theta\mathrm{d}\theta = \langle C_{kq}^{*}(\theta_{j'},\phi_{j'})\rangle \,, \quad (3.7)$$

where the integrand is the normalised PDDCS in Eq. (3.3):

$$n_q^{(k)}(\theta) = \frac{2\pi}{\sigma}\frac{\mathrm{d}\sigma_q^{(k)}}{\mathrm{d}\omega}. \tag{3.8}$$

$P(\theta, \theta_{j'}, \phi_{j'})$ is a joint probability, such that it simultaneously measures the probability of a particle being scattered at a particular angle, if $\boldsymbol{j'}$ points in a certain direction. However, it is possible to define the conditional probability which only depends on the distribution of $\boldsymbol{j'}$ and is independent of the actual scattering intensity as shown in Eq. (3.9) [10]:

$$P(\theta_j, \phi_j|\theta) = \frac{P(\theta_j, \phi_j, \theta)}{P(\theta)}\,. \tag{3.9}$$

If the numerator, the angular distribution function, is expressed with the aid of Eq. (3.2), and the angular distribution function is substituted by Eq. (3.4) in the denominator, we arrive at the formula:

$$P(\theta_{j'}, \phi_{j'}|\theta) = \frac{1}{4\pi}\sum_{k=0}^{\infty}(2k+1)\sum_{q=-k}^{k}\left(\frac{\mathrm{d}\sigma_q^{(k)}/\mathrm{d}\omega}{\mathrm{d}\sigma_0^{(0)}/\mathrm{d}\omega}\right)C_{kq}^*(\theta_{j'}, \phi_{j'})\,. \tag{3.10}$$

The expansion coefficients in the parenthesis are the renormalised polarisation dependent differential cross sections. They are the conditional expectation values of the complex conjugate of the modified spherical harmonics, $C_{kq}^*(\theta_{j'}, \phi_{j'})$ at the scattering angle θ, and express the (k, q) multipole contribution to the $\boldsymbol{j'}$ probability distribution function at that angle [10, 11, 16]:

$$\rho_q^{(k)}(\theta) \equiv \left(\frac{\mathrm{d}\sigma_q^{(k)}/\mathrm{d}\omega}{\mathrm{d}\sigma_0^{(0)}/\mathrm{d}\omega}\right) = \int_0^{\pi}\int_0^{2\pi} P(\theta_{j'}, \phi_{j'}|\theta)\, C_{kq}^*(\theta_{j'}, \phi_{j'})\,\mathrm{d}\theta_{j'}\sin\theta_{j'}\mathrm{d}\phi_{j'}\,. \tag{3.11}$$

Non-chiral collisions are symmetric with respect to the xz, or scattering plane, which establishes relationships between certain polarisation moments. The probability distribution

function fulfills the following equality:

$$P\left(\theta, \theta_{j'}, \phi_{j'}\right) = P\left(\theta, \pi - \theta_{j'}, \pi - \phi_{j'}\right). \tag{3.12}$$

Along with the symmetry properties of the modified spherical harmonics [117], the complex polarisation moments, and similarly the PDDCSs, are connected by the following equalities [10, 11]:

$$a_q^{(k)} = (-1)^{k+q} a_{-q}^{(k)} = (-1)^k \left[a_q^{(k)}\right]^* . \tag{3.13}$$

These relations in turn impose restrictions on the number of the independent polarisation moments and show which ones should vanish in the case of non-chiral collisions. If k is odd, $a_q^{(k)}$ is purely imaginary and will vanish, if q even. If k is even, then $a_q^{(k)}$ is purely real.

The above defined polarisation moments and various PDDCS are in general complex. These quantities ought to be combined into real ones in order to link a physical meaning to them. In doing so, the real polarisation moments become expectation values of real modified spherical harmonics. As such, they embody directional information of the $\boldsymbol{j'}$ distribution, because the spherical harmonics are the functions of the orientation angles $\theta_{j'}$ and $\phi_{j'}$. Hertel and Stoll derived normalisation formulae for Wigner's rotation matrices which can be applied to other tensorial quantities to remove their imaginary part [125]. The Hertel–Stoll normalised modified spherical harmonics are defined in Eqs. (3.14)–(3.16):

$$C_0^{\{k\}}(\theta_{j'}, \phi_{j'}) = C_0^{(k)}(\theta_{j'}, \phi_{j'}) \tag{3.14}$$

$$C_{q+}^{\{k\}}(\theta_{j'}, \phi_{j'}) = \frac{1}{\sqrt{2}} \left[(-1)^q C_{+q}^{(k)}(\theta_{j'}, \phi_{j'}) + C_{-q}^{(k)}(\theta_{j'}, \phi_{j'})\right], \quad 1 \le q \le k \tag{3.15}$$

$$C_{q-}^{\{k\}}(\theta_{j'}, \phi_{j'}) = \frac{1}{\sqrt{2}i} \left[(-1)^q C_{+q}^{(k)}(\theta_{j'}, \phi_j) - C_{-q}^{(k)}(\theta_{j'}, \phi_{j'})\right], \quad 1 \le q \le k. \tag{3.16}$$

If these real functions are used in Eq. (3.7), the real Hertel–Stoll normalised polarisation

moments, $a_{q\pm}^{\{k\}}$, are obtained. They can alternatively be given by Eqs. (3.17)–(3.19):

$$a_0^{\{k\}} = a_0^{(k)} \tag{3.17}$$

$$a_{q+}^{\{k\}} = \frac{1}{\sqrt{2}}\left[(-1)^q a_{+q}^{(k)} + a_{-q}^{(k)}\right], \quad 1 \leq q \leq k \tag{3.18}$$

$$a_{q-}^{\{k\}} = \frac{1}{\sqrt{2}i}\left[(-1)^q a_{+q}^{(k)} - a_{-q}^{(k)}\right], \quad 1 \leq q \leq k\,. \tag{3.19}$$

Similar formulae can be derived for the PDDCSs, normalised PDDCSs and renormalised PDDCSs. The real quantities are discerned from the complex ones by using the superscript '$\{k\}$' and subscript '$q\pm$' throughout the present work [11, 15, 126]. The selection rules that govern which real moments should disappear can be deduced from Eqs. (3.13) and (3.17)–(3.19). If k is even, then only the q zero or positive moments do not vanish. If k is odd, only the q negative moments persist [11, 72].

Calculation of the classical polarisation moments and PDDCSs

So far we have only been concerned with the definition and characteristics of the classical polarisation phenomena. Formulae are provided in this section by means of which the polarisation moments and polarisation dependent differential cross sections can be obtained from quasi-classical calculations. The quasi-classical trajectory (QCT) or classical hard shell calculations enable us to ascertain the exact final coordinates and momenta of the atom and the diatom as discussed in Section 2.2.1. Thus, both the scattering frame and the orientation angles, $(\theta_{j'}, \phi_{j'})$, of $\boldsymbol{j'}$ are known for each and every trajectory. A possible way to obtain the quantities of interest would be to calculate the respective $C_{q\pm}^{\{k\}}(\theta_{j'}, \phi_{j'})$ values for each trajectory and generate the PDDCSs with histogram binning in the same manner as in Eq. (2.24). However, the scattering angle resolved functions will be smoother and continuous, if they are constructed in terms of a series expansion [10, 11]. The Hertel–Stoll normalised, normalised PDDCSs are given as a series of modified spherical harmonics in Eq. (3.20) [10]:

$$n_{q\pm}^{\{k\}}(\theta) = \frac{1}{2}\sum_{k_1 \geq q}^{\infty}(2k_1+1)s_{q\pm,k_1}^{\{k\}}C_{k_1,-q}(\theta,0)\,. \tag{3.20}$$

The $s^{\{k\}}_{q\pm,k_1}$ expansion coefficients are obtained as the following expectation values:

$$
\begin{aligned}
s^{\{k\}}_{q+,k_1} &= \sqrt{2}\langle C_{k_1 q}(\theta,0) C_{kq}(\theta_{j'},0)\cos(q\phi_{j'})\rangle && (3.21)\\
&= \sqrt{2}\frac{1}{N_{j'}}\sum_{n=1}^{N_{j'}} C_{k_1 q}(\theta^{(n)},0) C_{kq}(\theta^{(n)}_{j'},0)\cos(q\phi^{(n)}_{j'}) \\
s^{\{k\}}_{q-,k_1} &= \sqrt{2}\langle C_{k_1 q}(\theta,0) C_{kq}(\theta_{j'},0)\sin(q\phi_{j'})\rangle && (3.22)\\
&= \sqrt{2}\frac{1}{N_{j'}}\sum_{n=1}^{N_{j'}} C_{k_1 q}(\theta^{(n)},0) C_{kq}(\theta^{(n)}_{j'},0)\sin(q\phi^{(n)}_{j'}) \\
s^{\{k\}}_{0,k_1} &= \langle P_{k_1}(\cos\theta)\, P_k(\cos\theta_{j'})\rangle && (3.23)\\
&= \frac{1}{N_{j'}}\sum_{n=1}^{N_{j'}} P_{k_1}\left(\cos\theta^{(n)}\right) P_k\left(\cos\theta^{(n)}_{j'}\right).
\end{aligned}
$$

The trajectories which end in the final rotational state j' are labeled by (n) and their total number is $N_{j'}$. The nonvanishing real polarisation moments are calculated as the expectation values over all trajectories that end up in the final state j' according to Eqs. (3.24)–(3.26) [10]:

$$
\begin{aligned}
a^{\{k\}}_{q+} &= (-1)^q\sqrt{2}\langle C_{k|q|}(\theta_{j'},0)\cos(q\phi_{j'})\rangle && (3.24)\\
a^{\{k\}}_{q-} &= (-1)^q\sqrt{2}\langle C_{k|q|}(\theta_{j'},0)\sin(q\phi_{j'})\rangle && (3.25)\\
a^{\{0\}}_{0} &= \langle P_k(\cos\theta_{j'})\rangle\,. && (3.26)
\end{aligned}
$$

3.1.3 Directional meaning of the polarisation moments

The conditional probability distribution of Eq. (3.3) can now be re-expanded in terms of the real renormalised PDDCSs according to Eq. (3.27),

$$
\begin{aligned}
P(\theta_{j'},\phi_{j'}|\theta) &= && (3.27)\\
&\sum_{k=0}^{\infty}\frac{2k+1}{4\pi}\Big[\rho^{\{k\}}_0(\theta) C^{\{k\}*}_0(\theta_{j'},\phi_{j'}) \\
&+ \sum_{q=1}^{k}\left(\rho^{\{k\}}_{q+}(\theta) C^{\{k\}*}_{q+}(\theta_{j'},\phi_{j'}) + \rho^{\{k\}}_{q-}(\theta) C^{\{k\}*}_{q+}(\theta_{j'},\phi_{j'})\right)\Big]\,,
\end{aligned}
$$

where each term carries physical information about the polarisation of $\boldsymbol{j'}$. The directional meaning of the renormalised PDDCSs and polarisation moments are defined in Table 3.1. If the expansion in Eq. (3.27) only contains the $k = 0$, $q = 0$ term, the distribution of $\boldsymbol{j'}$ is isotropic, that is to say $\boldsymbol{j'}$ points towards every angle with uniform probability.

The $k = 1$ rank moments are called orientation moments. The orientation quantifies whether a set of vectors is parallel or antiparallel to a reference axis. Therefore the orientation of the rotational angular momentum vector describes the sense of rotation. Positive and negative values indicate counterclockwise or clockwise rotation with respect to the reference axis, respectively. Any value between these limits indicates non-perfect orientation with respect to the reference axis.

The $k = 2$ rank moments are called alignment moments. A set of vectors is aligned with respect to a reference vector, if they are arranged along that vector. Their direction can either be parallel or antiparallel, the alignment is not affected. It is insensitive to and independent of the orientation. The alignment moments of $\boldsymbol{j'}$ define the plane of rotation. Positive values indicate parallel alignment while negative values refer to perpendicular alignment with respect to the reference axis.

k	q	Spherical harmonics	positive	negative
1	1-	$\langle \sin\theta_{j'} \sin\phi_{j'} \rangle$	orientation parallel to $\hat{\boldsymbol{y}}$	orientation antiparallel to $\hat{\boldsymbol{y}}$
1	0	$\langle \cos\theta_{j'} \cos\theta_{j'} \rangle$	orientation parallel to $\hat{\boldsymbol{z}}$	orientation antiparallel to $\hat{\boldsymbol{z}}$
1	1+	$\langle \cos\theta_{j'} \rangle$	orientation parallel to $\hat{\boldsymbol{x}}$	orientation antiparallel to $\hat{\boldsymbol{x}}$
2	2-	$\frac{\sqrt{3}}{2}\langle \sin^2\theta_{j'} \sin 2\phi_{j'} \rangle$	alignment along $\hat{\boldsymbol{x}} + \hat{\boldsymbol{y}}$	alignment along $\hat{\boldsymbol{x}} - \hat{\boldsymbol{y}}$
2	1-	$\sqrt{3}\langle \cos\theta_{j'} \sin\theta_{j'} \sin\phi_{j'} \rangle$	alignment along $\hat{\boldsymbol{y}} + \hat{\boldsymbol{z}}$	alignment along $\hat{\boldsymbol{y}} - \hat{\boldsymbol{z}}$
2	0	$\frac{1}{2}\langle 3\cos^2\theta_{j'} - 1 \rangle$	alignment along $\hat{\boldsymbol{z}}$	alignment perpendicular to $\hat{\boldsymbol{z}}$
2	1+	$\sqrt{3}\langle \cos\theta_{j'} \sin\theta_{j'} \cos\phi_{j'} \rangle$	alignment along $\hat{\boldsymbol{x}} + \hat{\boldsymbol{z}}$	alignment along $\hat{\boldsymbol{x}} - \hat{\boldsymbol{z}}$
2	2+	$\frac{\sqrt{3}}{2}\langle \sin^2\theta_{j'} \cos 2\phi_{j'} \rangle$	alignment along $\hat{\boldsymbol{x}}$	alignment along $\hat{\boldsymbol{y}}$

Table 3.1: The definitions of the classical polarisation moments. The directional meaning is shown in the right column [11].

In order to illustrate the somewhat abstract theory of classical angular momentum polarisation, it might be instructive to consider three types of collisions. Let us assume that every molecule rotates exactly in the scattering plane and the sense of rotation is

anti-clockwise which will be case (a). In the second example, case (b), the molecules still rotate in the scattering plane but the probability of anti-clockwise and clockwise rotation is equal. Finally, in case (c), it is only required that the rotation is perpendicular to the xy plane and cylindrically symmetric around the $\hat{\boldsymbol{z}}$ axis. The three molecular ensembles are illustrated in the top panels of Figure 3.2. The corresponding $P(\theta_j, \phi_j)$ probability distribution functions are shown in the bottom panels of Figure 3.2. In case (a) every $\boldsymbol{j'}$ points at the $-\hat{\boldsymbol{y}}$ direction thus the distribution function is a Dirac delta, therefore $\boldsymbol{j'}$ is oriented antiparallel to $\hat{\boldsymbol{y}}$. In case (b), $\boldsymbol{j'}$ is either directed towards $+\hat{\boldsymbol{y}}$ or $-\hat{\boldsymbol{y}}$ which is equivalent with a sum of two Dirac delta functions making the angle π with each other. There are two oriented sub-ensembles with equal weight, such that the whole set of molecules is not oriented. However, it is aligned along the $\hat{\boldsymbol{y}}$ axis. There is no particular vector with respect to which the $\boldsymbol{j'}$ vectors are oriented in the last example, but there is a plane, namely the xy plane in which they reside, thus the system is aligned perpendicularly with respect to $\hat{\boldsymbol{z}}$ axis. This information is readily obtained if the overlap between the

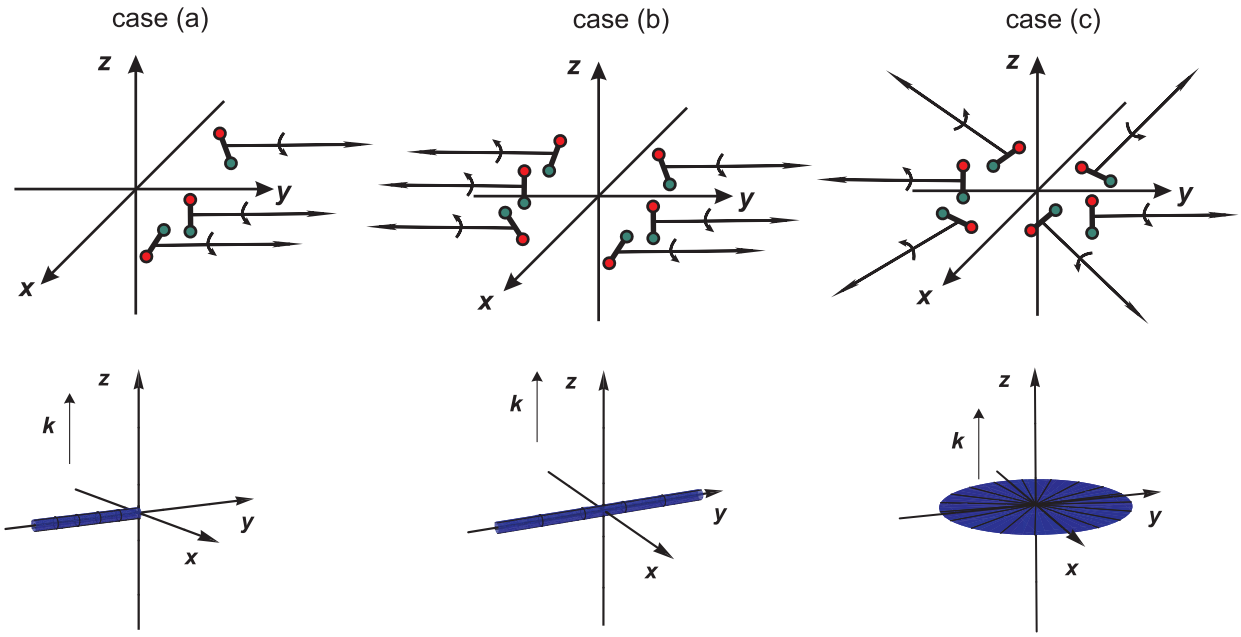

Figure 3.2: The example molecular ensembles (top row). Case (a): every molecule rotates in the xz plane in anticlockwise sense (left panel), equal number of molecules rotates clockwise and anti-clockwise sense in the in the xz plane (middle panel). The molecules are equally distributed and rotate in the xy plane. The $P(\theta_j, \phi_j)$ distribution functions in the same frame in the bottom row, only show orientation in case (a), though, all of them are aligned.

probability distribution functions in Eqs. (3.28)–(3.30) and the real spherical harmonics are calculated:

$$P(\theta_j, \phi_j) = \delta(\pi/2 - \theta_j)\delta(\pi/2 - \phi_j) \tag{3.28}$$

$$P(\theta_j, \phi_j) = \frac{1}{2}\left[\delta(\pi/2 - \theta_j)\delta(\pi/2 - \phi_j) + \delta(-\pi/2 - \theta_j)\delta(\pi/2 - \phi_j)\right] \tag{3.29}$$

$$P(\theta_j, \phi_j) = \frac{1}{2\pi}\delta(\pi/2 - \theta_j)\,. \tag{3.30}$$

The $a_{1-}^{\{1\}}$ moments all vanish, except in case (a), where it has a value of unity. Its value is zero in case (b), where the two contributions along the $\hat{\boldsymbol{y}}$ axis cancel each each other, likewise in case (c), the overlap between the $C_{1-}^{\{1\}}(\theta_{j'}, \phi_{j'})$ function and the probability distribution of $\boldsymbol{j'}$ is zero. The $a_0^{\{2\}}$ moment takes its lower limiting value of -0.5 in all three cases, since $\boldsymbol{j}$ is perpendicular to the z axis. The $a_{1+}^{\{2\}}$ moment is zero for all arrangements, since none of them are aligned along the $\hat{\boldsymbol{x}} \pm \hat{\boldsymbol{z}}$ vectors. In case (a), $\boldsymbol{j'}$ is oriented thus aligned along the $\hat{\boldsymbol{y}}$ axis, thus $a_{2+}^{\{2\}}$ is equal to $+1$. Despite the lack of orientation with respect to the $\hat{\boldsymbol{y}}$ axis, the ensemble is still aligned to the maximum possible extent with respect to the $\hat{\boldsymbol{y}}$ axis in case (b). Due to the axial symmetry around the $\hat{\boldsymbol{z}}$ axis this moment vanishes in case (c).

3.2 Quantum mechanical theory of angular momentum polarisation

Quantum mechanically, the direction of the angular momentum cannot be determined with arbitrary precision due to the uncertainty principle. The system is best described by a mixture of different quantum states, each being a magnetic sublevel of j. The weights of these states and the coherences between them are contained in the quantum mechanical density matrix, ρ [72]. This density matrix can be expanded in terms of the so-called state multipoles. The expansion coefficients are related to the quantum mechanical polarisation moments and they are proportional to the expectation values of the components of the

spherical tensor operator of $\hat{j}$ [72].

3.2.1 Density matrix theory

Let us consider a system in a certain state, $|\Psi_n\rangle$, which can be expanded using the orthonormal and complete set of the system's eigenfunctions, $\{\psi\}$, according to Eq. (3.31) [72]. The states which can be characterised by the wavefunctions of this form are referred to as pure states,

$$|\Psi_n\rangle = \sum_m a_m^{(n)} |\psi_m\rangle \,. \tag{3.31}$$

It is, however, not always possible to prepare systems which reside in a pure state. It may occur that only the probability of the system being in a certain pure state is known, that is to say the actual state is a statistical mixture of the pure states with the weights, W_n. These states are called mixed states. The density operator, $\hat{\rho}$, defined in (3.32) fully characterises the system:

$$\hat{\rho} = |\Psi\rangle\langle\Psi| = \sum_n W_n |\Psi_n\rangle\langle\Psi_n| \,. \tag{3.32}$$

Using the orthonormality of the eigenvectors and inserting Eq. (3.31) into Eq. (3.32) the matrix elements between the states $\langle\psi_i|$ and $|\psi_j\rangle$ are evaluated as

$$\rho_{ij} \equiv \langle\psi_i|\rho|\psi_j\rangle = \sum_n W_n a_i^{(n)} a_j^{(n)}. \tag{3.33}$$

The matrix constructed by the above elements is called the density matrix in the $|\psi\rangle$ representation. The following properties of the density are important to be considered:

It is Hermitian which follows from Eq. (3.33).

The diagonal elements express the probability that the system is in a particular basis state:

$$\rho_{mm} = \sum_n W_n |a_m^{(n)}|^2 \,. \tag{3.34}$$

The trace of the density matrix is the sum of the W_n weights, such that it is independent

of the representation and is equal to the total population:

$$\mathrm{tr}(\rho) = \sum_n \sum_i W_n |a_i|^2 \,. = \sum_n W_n \tag{3.35}$$

The off-diagonal matrix elements represent the coherences between different $|\psi_i\rangle$ states. The system is said to be incoherent, if all of the off-diagonal elements vanish.

The expectation value of any $\hat{Q}$ operator can be expressed as the trace of the matrix of the product operator $\hat{\rho}\hat{Q}$:

$$\begin{aligned} \langle \hat{Q} \rangle &= \frac{\sum\limits_n W_n \langle \Psi_n | \hat{Q} | \Psi_n \rangle}{\sum\limits_n W_n} = \frac{1}{\sum\limits_n W_n} \sum_n W_n \sum_{ij} a_i^{(n)*} a_j^{(n)} \langle \psi_i | \hat{Q} | \psi_j \rangle \\ &= \frac{1}{\sum\limits_n W_n} \sum_{ij} \langle \psi_i | \hat{Q} | \psi_j \rangle \langle \psi_j | \hat{\rho} | \psi_i \rangle = \frac{\mathrm{tr}\,(\rho Q)}{\mathrm{tr}(\rho)}. \end{aligned} \tag{3.36}$$

If the population is unity, the denominator, $\mathrm{tr}(\rho)$ can be omitted from the above expression.

3.2.2 Tensor operators and state multipoles

The density operator defined in Eq. (3.32) can be expanded in terms of tensor operators. The expansion coefficients are the so-called state multipoles [72]. Both of these quantities have a clear physical meaning charecterising the quantum mechanical polarisation state of the system.

Let us consider a system in a sharp rotational angular momentum state, j. Two angular momenta with projections m and m'can then be coupled to the total angular momentum, k, which has a projection q:

$$|kq\rangle = \sum_{m,m'} \langle jm', jm | kq \rangle | jm' \rangle | jm \rangle. \tag{3.37}$$

The coupled projection operator is constructed from the individual projection operators,

$|jm'\rangle\langle jm|$ in the same manner:

$$\hat{T}_q^{(k)}(j) = \sum_{m'm} (-1)^{j-m} \langle jm', j-m|kq\rangle |jm'\rangle\langle jm|. \tag{3.38}$$

The elements of the density operator are obtained if the equation above is inverted:

$$|jm'\rangle\langle jm| = (-1)^{j-m} \langle jm', jm|kq\rangle \hat{T}_q^{(k)}(j)\,. \tag{3.39}$$

The $\hat{T}_q^{(k)}(j)$ operator behaves as a tensorial quantity under rotations as shown in Eq. (3.40) [72, 99], hence it is called a tensor operator:

$$\hat{T}_q^{(k)}(j)' = \sum_{p=-k}^{k} D_{pq}^k(\Omega) \hat{T}_p^{(k)}(j)\,, \tag{3.40}$$

where $D_{pq}^k(\Omega)$ is the Wigner D-matrix and $\Omega = (\alpha, \beta, \gamma)$ are the angles of rotation. It is useful to know the relationships between the adjoint operators and matrix elements which are given below [72]:

$$\hat{T}_q^{(k)}(j)^\dagger = (-1)^q \hat{T}_q^{(k)}(j) \tag{3.41}$$

$$\langle jm|\hat{T}_q^{(k)}(j)^\dagger|jm'\rangle = \langle jm'|\hat{T}_q^{(k)}(j)^\dagger|jm\rangle\,. \tag{3.42}$$

The matrix elements of the tensor operator can easily be calculated by virtue of the Wigner–Eckart theorem as shown in Eq. (3.43), where $\langle j||T^{(k)}||j\rangle$ is the reduced matrix element of $\hat{T}_q^{(k)}$ [72, 99]:

$$\begin{aligned} \langle jm'|\hat{T}_q^{(k)}(j)^\dagger|jm\rangle &= (-1)^{j-m'} \begin{pmatrix} j & k & j \\ -m' & q & m \end{pmatrix} \langle j||T^{(k)}||j\rangle \\ &= (-1)^{j-m'} \begin{pmatrix} j & k & j \\ -m' & q & m \end{pmatrix} (2k+1)^{1/2}, \end{aligned} \tag{3.43}$$

where the quantities in the brackets:

$$\begin{pmatrix} j & k & j \\ -m' & q & m \end{pmatrix} \tag{3.44}$$

are the so-called $3j$-symbols defined in [99]. The tensor operators are constructed as the combination of $\hat{\boldsymbol{j}}$ and its components $\hat{j}_x, \hat{j}_y, \hat{j}_z$ and they have well defined, transparent physical meanings [72, 93]. For instance, the zeroth rank operator is the identity operator normalised to unity:

$$\hat{T}_0^{(0)}(j) = \frac{1}{2j+1} \sum_{m=-j}^{j} |jm\rangle\langle jm| = \frac{1}{2j+1}\hat{I}\,. \tag{3.45}$$

The spherical components of the angular momentum operator are proportional to the components of the first rank tensor operator:

$$\begin{aligned} \hat{T}_1^{(0)}(j) &= \hat{j}_0 = \hat{j}_z & (3.46)\\ \hat{T}_{\pm q}^{(1)}(j) &= \left[\frac{3}{(2j+1)(j+1)j}\right]^{1/2} \hat{j}_{\pm q} \quad q = 1 & (3.47)\\ &= \left[\frac{3}{(2j+1)(j+1)j}\right]^{1/2} \mp \frac{1}{\sqrt{2}}\left(\hat{j}_x \pm i\hat{j}_y\right)\,. \end{aligned}$$

The density operator can be reconstructed on the basis of the tensor operators, if the projection operators are substituted by the tensor operators of Eq.(3.48) and the relationship between the Clebsch–Gordan coefficients and $3j$-symbols is used [72, 117]:

$$\begin{aligned} \hat{\rho} &= \sum_{m',m} |jm'\rangle\langle jm| & (3.48)\\ &= \sum_{k,q}\left[\sum_{m'm}\langle jm'|\rho|jm\rangle(-1)^{j-m}(2k+1)^{1/2}\begin{pmatrix} j & k & j \\ -m' & q & m \end{pmatrix}\right]\hat{T}_q^{(k)}(j)\\ &= \sum_{k,q}\langle \hat{T}_q^{(k)}(j)^\dagger\rangle \hat{T}_q^{(k)}(j). \end{aligned}$$

The factors in the square brackets, denoted by $\langle \hat{T}_q^{(k)}(j)^\dagger \rangle$ are the state multipoles:

$$\langle \hat{T}_q^{(k)}(j)^\dagger \rangle \equiv \sum_{m,m'} \langle jm'|\rho|jm\rangle (-1)^{j-m} (2k+1)^{1/2} \begin{pmatrix} j & k & j \\ -m' & q & m \end{pmatrix} . \tag{3.49}$$

It can be shown that the state multipoles are the trace of the matrix of the $\hat{\rho}\hat{T}_q^{(k)}(j)^\dagger$ product operator. As such, they are the values of the respective tensor operators, justifying the use of the angle brackets [72]:

$$\langle \hat{T}_q^{(k)}(j)^\dagger \rangle = \mathrm{tr}\left(\rho T_q^{(k)}(j)^\dagger\right) . \tag{3.50}$$

The equivalent of Eq. (3.48) in terms of matrix elements is shown in Eq. (3.51). The density matrix and state multipole descriptions are equivalent. Both contain the same information, which is sufficient to fully characterise the system of interest. Since the state multipoles are proportional to expectation values of the angular momentum tensor operators and to the quantum mechanical polarisation moments, in some cases it could be more insightful to employ them to describe the system:

$$\langle jm'|\hat{\rho}|jm\rangle = (-1)^{j-m'} \sum_{k,q} (2k+1)^{1/2} \begin{pmatrix} j & k & j \\ m' & -q & -m \end{pmatrix} \langle \hat{T}_q^{(k)}(j)^\dagger \rangle . \tag{3.51}$$

3.2.3 Quantum mechanical polarisation moments

The quantum mechanical polarisation moments or parameters have been defined in a number of ways [11, 15, 77]. Every definition is associated with the notion of the state multipoles introduced in Eqs. (3.48)–(3.49), though the normalisations employed might be different. This issue will addressed in Appendix C. The complex polarisation moments used throughout the present work are defined in Eq. (3.52) [11, 126],

$$a_q^{(k)} = (-1)^q \sqrt{\frac{2j+1}{2k+1}} \langle T_{-q}^{(k)}(j)^\dagger \rangle . \tag{3.52}$$

If the state multipoles are substituted by the polarisation moments in Eq. (3.51), the density matrix elements can be constructed in terms of a series expansion, where the coefficients are the polarisation moments,

$$\langle jm'|\hat{\rho}|jm\rangle = \sum_{k=0}^{2j}\sum_{q=-k}^{k}\frac{2k+1}{2j+1}a_q^{(k)}\langle jm', kq|jm\rangle\,. \tag{3.53}$$

The analogous expression for the polarisation moments is given in Eq. (3.54), which is equivalent to Eq. (3.49). Therefore, the information contained in the set of the polarisation moments is sufficient to fully characterise the system,

$$a_q^{(k)} = \sum_{m=-j}^{j}\sum_{m'=-j}^{j}\langle jm'|\hat{\rho}|jm\rangle\langle jm', kq|jm\rangle\,. \tag{3.54}$$

An important relationship between a polarisation moment and its complex conjugate immediately follows from Eq. (3.52):

$$a_q^{(k)*} = (-1)^q a_{-q}^{(k)}\,. \tag{3.55}$$

Polarisation moments in symmetric systems

The planar symmetry of the scattering events established a connection between different components of the same rank classical polarisation moments and PDDCSs, as discussed in section 3.1.2. It also determined the criteria for which moments should vanish. The symmetry of the quantum mechanical systems also has implications on the possible values of the moments. Three types of symmetry have particular importance to the molecular collisions considered in this work, namely axial, planar and total symmetry.

In *axially symmetric* systems, there exists at least one particular axis about which a rotation by an arbitrary angle leaves the system unchanged. For instance, if a molecular ensemble is excited by a circularly polarised laser pulse, then this axis is parallel to the propogation direction of the laser. When linearly polarised laser is used, the axis of symmetry is parallel to the electric vector of the laser light. These observations will be

exploited to facilitate the calculation of line strength factors in Appendix C. It is customary to choose the symmetry axis as the $\hat{\boldsymbol{Z}}$ axis of the frame. Any physical quantity should be identical in the rotated and in the non-rotated systems including the state multipoles. This requirement can be expressed in mathematical terms using the rotation rules of Eq. (3.40):

$$\begin{aligned}\langle \hat{T}^{(k)}_q(j)^\dagger \rangle &= \langle \hat{T}^{(k)}_q(j)^\dagger \rangle_{\rm rot} = \sum_{p=-k}^{k} D^k_{pq}(0,0,\gamma)\langle \hat{T}^{(k)}_p(j)^\dagger \rangle \\ &= \sum_{p=-k}^{k} {\rm e}^{-ip\gamma}\delta_{qp}\langle \hat{T}^{(k)}_p(j)^\dagger \rangle \\ &= {\rm e}^{-iq\gamma}\langle \hat{T}^{(k)}_q(j)^\dagger \rangle \,. \end{aligned} \tag{3.56}$$

The equality in the bottom line of Eq. (3.56) should hold for any γ angle, which can only be fulfilled if $q = 0$. Thus only the $q = 0$ state multipoles and polarisation moments do not vanish in an axially symmetric system if the axis of quantisation is identical to the symmetry axis.

Non-chiral collisions are symmetric with respect to reflections in the xz plane (scattering plane), thus this *planar symmetry* is mirrored in the relationships between the polarisation moments. The reflection in the xz plane can be decomposed into a sequence of two symmetry operations, namely that of a rotation about the $\hat{\boldsymbol{y}}$ axis by π and an inversion through the origin [127]. The inversion does not change the components of $\boldsymbol{j}$, or equivalently the density matrix elements. Therefore it is sufficient to investigate the effect of rotation. The rotated and non-rotated polarisation moments should be identical:

$$a^{(k)}_q = \sum_{p=-k}^{k} D^k_{pq}\,(0,\pi,0)\,a^{(k)}_p \tag{3.57}$$

$$= \sum_{p=-k}^{k} (-1)^{k+p}\delta_{pq}a^{(k)}_p$$

$$= (-1)^{k+q}a^{(k)}_q. \tag{3.58}$$

This requirement along with that of Eq. (3.55) establishes the relationships between the polarisation moments, similar to those observed in the classical case. These are given by

Eq. (3.13):

$$a_q^{(k)} = (-1)^{k+q} a_{-q}^{(k)} = (-1)^k \left[a_q^{(k)}\right]^* . \tag{3.59}$$

The system is said to be *unpolarised*, if all of its vectorial properties are uniformly distributed in the three dimensional space, or equivalently, it is invariant under any rotations about any arbitrary axis. As a consequence each $\langle \hat{T}_q^{(k)}(j)^\dagger \rangle$, or equivalently the $\hat{j}_q^{(k)}$ spherical operators should be equal to each other irrespective of the axis of quantisation. This is only possible, if all of them vanish apart from the $k = 0$, $q = 0$ one. In mathematical terms, the system is axially symmetric and every $|jm\rangle$ level is equally populated. Only the $q = 0$ state multipoles do not vanish (cf. Eq. (3.56)). The diagonal elements of the density matrix can be factored out from Eq. (3.48) and using the sum rule of Clebsch–Gordan coefficients stated in Eq. 8.7.1.(1) of [117]. Only the $\langle \hat{T}_0^{(0)}(j)^\dagger \rangle$ do not disappear and the density matrix can be written as

$$\hat{\rho} = \hat{T}_0^{(0)}(j) \langle \hat{T}_0^{(0)}(j)^\dagger \rangle = \frac{1}{2j+1} \hat{I} . \tag{3.60}$$

This result is similar to that of the classical case when the expansion of an isotropic system in Eq. (3.4) is terminated after the first term.

Renormalised polarisation parameters

If a subset of molecules scattered through a particular angle, θ, is considered, the angular resolved polarisation moments will be called polarisation dependent cross sections, PDDCSs, in analogy with the terminology introduced in Section 3.1.2. The q-th component of the k-th rank PDDCS thus is defined as:

$$\frac{\mathrm{d}\sigma_q^{(k)}}{\mathrm{d}\omega} \equiv \sum_{m'=-j}^{j} \equiv \sum_{m=-j}^{j} \langle jm', kq | jm \rangle \langle jm' | \hat{\rho}(\theta) | jm \rangle , \tag{3.61}$$

or equivalently

$$\langle jm'|\hat{\rho}(\theta)jm\rangle = \frac{1}{2j+1}\sum_{k=0}^{2j}\sum_{q=-k}^{k}(2k+1)\frac{\mathrm{d}\sigma_q^{(k)}}{\mathrm{d}\omega}\langle jm', kq|jm\rangle\,, \tag{3.62}$$

where $\hat{\rho}(\theta)$ is the scattering angle resolved density operator. The trace of the density matrix is equal to the probability of finding the system in the rotational angular momentum state, j, which is related to the integral cross section, σ, and the differential cross section by Eq. (3.63) [11],

$$\frac{2\pi}{\sigma}\frac{\mathrm{d}\sigma_0^{(0)}}{\mathrm{d}\omega}\mathrm{tr}\left[\rho(\cos\theta)\right] = \frac{2\pi}{\sigma}\frac{\mathrm{d}\sigma}{\mathrm{d}\omega}\,. \tag{3.63}$$

The density matrix, $\rho_\theta(\theta)$, which only characterises the polarisation state of the ensemble independent of the scattering probability can then be calculated by dividing the density matrix of Eq. (3.62) by its trace according to Eq. (3.64):

$$\rho_\theta(\theta) = \frac{\rho(\theta)}{\mathrm{tr}\left[\rho(\theta)\right]}\,. \tag{3.64}$$

The equivalent classical probability is $P(\theta_{j'}, \phi_{j'}|\theta)$ defined in Eq. (3.27). The expansion of the renormalised density matrix is as follows:

$$\langle jm'|\rho_\theta(\theta)|jm\rangle = \frac{1}{2j+1}\sum_{k=0}^{2j}\sum_{q=-k}^{k}(2k+1)\rho_q^{(k)}(\theta)\langle jm', kq|jm\rangle\,. \tag{3.65}$$

where the scattering angle dependent expansion coefficients are the renormalised polarisation dependent differential cross sections:

$$\rho_q^{(k)}(\theta) \equiv \frac{\mathrm{d}\sigma_q^{(k)}}{\mathrm{d}\omega}\left[\frac{\mathrm{d}\sigma_0^{(0)}}{\mathrm{d}\omega}\right]^{-1}\,. \tag{3.66}$$

The density matrix theory discussed above can be viewed as the quantum mechanical counterpart of the classical formalism discussed in Section 3.1, where the probability distribution function was replaced by the density matrix.

Real polarisation moments and PDDCSs

The renormalised PDDCSs and the polarisation moments contain information about the polarisation state of the system. Their exact physical meaning is explained below. They are proportional to the expectation values of the components of the spherical angular mometum operator [15, 72]. Therefore quantum mechanical polarisation moments are in general complex. They can conveniently be combined into real ones by employing the Hertel–Stoll normalisation introduced in Eqs. (3.14)–(3.16) and Eqs. (3.17)–(3.19), which is valid for all tensorial quantities. The real, Hertel–Stoll normalised, quantities are distinguished from the complex ones by using superscript $\{k\}$ and subscript $q\pm$ in accordance with the notation used previously. The real polarisation moments are proportional to the expectation values of certain combinations of the Cartesian components of the angular momentum operator. The exact expressions are enumerated in Table 3.2. The proportionality

k	q	operator	positive	negative
1	1-	$c_1\langle\hat{j}_y\rangle$	orientation parallel to $\hat{\boldsymbol{y}}$	orientation antiparallel to $\hat{\boldsymbol{y}}$
1	0	$c_1\langle\hat{j}_z\rangle$	orientation parallel to $\hat{\boldsymbol{z}}$	orientation antiparallel to $\hat{\boldsymbol{z}}$
1	1+	$c_1\langle\hat{j}_x\rangle$	orientation parallel to $\hat{\boldsymbol{x}}$	orientation antiparallel to $\hat{\boldsymbol{x}}$
2	2-	$\sqrt{3}c_2\langle\hat{j}_x\hat{j}_y+\hat{j}_y\hat{j}_x\rangle$	alignment along $\hat{\boldsymbol{x}}+\hat{\boldsymbol{y}}$	alignment along $\hat{\boldsymbol{x}}-\hat{\boldsymbol{y}}$
2	1-	$\sqrt{3}c_2\langle\hat{j}_y\hat{j}_z+\hat{j}_z\hat{j}_y\rangle$	alignment along $\hat{\boldsymbol{y}}+\hat{\boldsymbol{z}}$	alignment along $\hat{\boldsymbol{y}}-\hat{\boldsymbol{z}}$
2	0	$c_2\langle 3\hat{j}_z^2-\hat{j}^2\rangle$	alignment along $\hat{\boldsymbol{z}}$	alignment perpendicular to $\hat{\boldsymbol{z}}$
2	1+	$\sqrt{3}c_2\langle\hat{j}_z\hat{j}_x+\hat{j}_x\hat{j}_z\rangle$	alignment along $\hat{\boldsymbol{x}}+\hat{\boldsymbol{z}}$	alignment along $\hat{\boldsymbol{x}}$
2	2+	$\sqrt{3}c_2\langle\hat{j}_x^2+\hat{j}_y^2\rangle$	alignment along $\hat{\boldsymbol{x}}$	alignment along $\hat{\boldsymbol{y}}$

Table 3.2: The quantum mechanical polarisation moments and the associated operators. The directional meaning is shown in the right column [11].

coefficients are defined as

$$c_1 = [j(j+1)]^{-1/2} \tag{3.67}$$

$$c_2 = [j(j+1)(2j+3)(2j-1)]^{-1/2}\,. \tag{3.68}$$

In order to demonstrate a connection to the classical polarisation moments let us consider the $a_0^{\{2\}}$ alignment moment which quantifies the alignment along the $\hat{\boldsymbol{z}}$ axis. The

expectation values can be given in terms of the density matrix,

$$a_0^{\{2\}} = \sum_{m=-j}^{j} \rho_{mm} \frac{3m^2 - j(j+1)}{[j(j+1)(2j+3)(2j-1)]^{1/2}} \,. \tag{3.69}$$

There are two limiting cases. Dealing with only integer angular momenta, if the $m = 0$ state is populated, which has the minimal possible projection onto the z axis, the polarisation moment becomes:

$$a_0^{\{2\}} = \frac{-j(j+1)}{[j(j+1)(2j+3)(2j-1)]^{1/2}} \,. \tag{3.70}$$

corresponding to a perpendicular classical alignment. The value of the associated classical moment is -0.5 which is independent of the actual magnitude of $\boldsymbol{j}$. On the contrary, the limiting values of the quantum mechanical polarisation moments are a function of j due to the uncertainty principle. However, taking the high j limit of Eq. (3.69), the -0.5 value is recovered. The other extreme case of alignment is observed when only the $m = \pm j$ states are occupied. The alignment moment in this case is:

$$a_0^{\{2\}} = \frac{(j+1)^2 - 1}{[j(j+1)(2j+3)(2j-1)]^{1/2}} \,. \tag{3.71}$$

which again assumes the classical value of unity in the high j limit. The exact quantum mechanical limits are conveniently calculated by diagonalising the spherical tensor matrix on the $\{|jm\rangle\}$ basis. The smallest and biggest diagonal elements are the limits of the polarisation moments [128].

Minimum uncertainty states

It is impossible to assign an exact direction to the $\boldsymbol{j'}$ vector in the framework of quantum mechanics, say, specified by the angles $(\theta_{j'}, \phi_{j'})$. As a consequence, the definition of the $P(\theta_{j'}, \phi_{j'})$ function is not allowed. Nevertheless, it is possible to define the minimum uncertainty state, $|\theta_{j'}, \phi_{j'}\rangle$, in which $\boldsymbol{j'}$ is localised around $(\theta_j, \phi_{j'})$ to the greatest possible

extent [129]. This state can be generated by rotating the $|j'j'\rangle$ eigenstate to the $(\theta_{j'}, \phi_{j'})$ direction:

$$\hat{R}(\theta_{j'}, \phi_{j'})|j'j'\rangle = \sum_{m=-j'}^{j'} D^{j'}_{m,j'}(\theta_{j'}, \phi_{j'}, 0)|j'm\rangle \,. \tag{3.72}$$

The elements of the normalised density matrix between the minimum uncertainty states are given by Eq. (3.73). Using standard angular momentum algebra, this expression can be cast in a series expansion in which the expansion coefficients are proportional to the polarisation moments:

$$\begin{aligned} Q(\theta_{j'}, \phi_{j'}) &= \frac{\langle \theta_{j'}, \phi_{j'}|\hat{\rho}|\theta_{j'}, \phi_{j'}\rangle}{\mathrm{tr}\rho} \\ &= \sum_{k=0}^{k=2j'} (2k+1) \sum_{q=0}^{k} \langle j'j', k0|j'j'\rangle C^*_{kq}\left(\theta_{j'}, \phi_{j'}\right) a^{(k)}_q \,. \end{aligned} \tag{3.73}$$

$Q(\theta_{j'}, \phi_{j'})$ is the probability that $\boldsymbol{j'}$ is localised to the maximum possible extent about the direction of $(\theta_{j'}, \phi_{j'})$, hence it is called the minimum uncertainty state. This expansion is almost identical to its classical counterpart in Eq. (3.6), apart from the Clebsch–Gordan coefficients which account for the quantum mechanical uncertainty. This corresponds to the physical picture of $\boldsymbol{j'}$ being localised in a finite volume, as opposed to a Dirac delta function of the classical case. The Clebsch–Gordan coefficients approach unity in the high j limit, revealing the correspondence between the quantum and classical mechanical descriptions.

3.2.4 Calculation of the quantum mechanical polarisation moments

In the last section of the theoretical chapters, the formulae for the quantum mechanical polarisation moments and polarisation dependent cross sections are derived.. The scattering matrix formalism which was discussed in Chapter 2 and the density matrix theory will be linked together in order to achieve this goal.

The diagonal elements of the density matrix express the probability of finding the

system in a particular state. As such, they are equal to the square modulus of the scattering amplitudes defined in Eq. (2.32) [13, 72]. The off-diagonal elements are equal to the cross products of the scattering amplitudes. The density matrix elements can then be expressed in terms of the scattering amplitudes [72] and the polarisation moments or PDDCSs can subsequently be calculated:

$$\langle jm'|\hat{\rho}(\theta)|jm\rangle = f_{jm'}(\theta)^* f_{jm}(\theta). \tag{3.74}$$

However, it is more convenient to use the helicity representation of the scattering amplitudes, reducing the number of required summations [11, 130]:

$$\begin{aligned} \frac{\mathrm{d}\sigma_q^{(k)}}{\mathrm{d}\omega}(\theta) &= \frac{1}{N}(-1)^{k-q} \sum_{\Omega,\Omega_1,\Omega_2} \langle j\Omega_1, kq|j\Omega_2\rangle \\ &\times \left[(2J+1)d^J_{\Omega\Omega_1}(\theta)S^J_{j'\Omega_1,j\Omega}\right]\left[(2J+1)d^J_{\Omega\Omega_2}(\theta)S^J_{j'\Omega_2,j\Omega}\right]^* . \end{aligned} \tag{3.75}$$

where the N normalisation factor is defined as

$$\sum_J (2J+1)|S^J_{j'\Omega',j\Omega}|^2. \tag{3.76}$$

The renormalised PDDCSs, $\rho_q^{(k)}(\theta)$, are calculated from the PDDCSs by dividing them with the zeroth rank PDDCS. It is worth pointing out that the equations for calculating DCSs and PDDCSs exhibit analogous structures. The interferences between different partial waves, for example, manifest themselves in the product of the two sums in a way similar to Eq. (2.54). The polarisation moments are functions of the scattering matrix which in turn depends on the interaction potential. It is thus possible to gain knowledge on the role of the potential by investigating the rotational polarisation.

3.3 Summary

In this chapter, the principles of the classical and quantum mechanical theories of angular momentum polarisation were reviewed. The polarisation, or non-uniformity of rotation, was quantified by continuous probability functions in classical mechanics, and by density matrices in quantum mechanics. Both descriptions factor the polarisation into various elementary contributions. The main interest of this thesis lies in the investigation of two of these, namely the orientation and alignment, which are related to the sense and the plane of rotation, respectively. Although there are analogies between the classical and quantum mechanical treatments, they are inherently different. These theories will be invoked to rationalise a variety of rotational angular momentum polarisation effects in the inelastic collisions of NO(X) and Ar. A number of them can at least partially be explained with classical arguments, though, some phenomena demand quantum mechanical arguments to be fully uncovered.

Chapter 4

Modified potential energy surfaces and quantum mechanical hard shell scattering

The theoretical methods adapted and developed as a part of this thesis are introduced and discussed in this chapter. These include the construction of modified coupled potential energy surfaces and the exact quantum mechanical treatment of hard shell scattering.

The main focus of the present thesis is on the polarisation effects in atom–diatom collisions. Nevertheless, the scalar quantities and low order vector correlations, such as integral and differential cross sections, provide valuable information on the collision mechanism, and can be used to elucidate the more complex polarisation phenomena.

4.1 Classical hard shell calculations

The hard shell potential is devised to study the dynamics of perfectly impulsive collisions. The removal of the attractive and soft repulsive features of the PES might lead to the oversimplification of the problem. Nevertheless, valuable insight can be gained on the role of the omitted parts of the potential by comparing the hard shell and QCT results. The term 'QCT' always refers to quasi-classical calculations in which the employed PES is continuous in order to avoid confusion.

In the classical hard shell model, the $V_{\mathrm{sum}}(R,\gamma)$ PES defined in Section 2.1 [102] is replaced by a boundary, $\boldsymbol{R_E}$, inside of which the potential is positive infinite and zero

outside [114–116],

$$V(R,\gamma) = \begin{cases} +\infty & \text{if } R(\gamma) \leq R_{\mathrm{E}}(\gamma) \\ 0 & \text{if } R(\gamma) > R_{\mathrm{E}}(\gamma)\,, \end{cases} \tag{4.1}$$

$$\boldsymbol{R}_{\mathbf{E}} = \boldsymbol{R}_{\mathbf{E}}\left(\gamma,\Delta\right) = R_{\mathrm{E}}\left(\gamma,\Delta\right)\hat{\boldsymbol{R}}_{\mathbf{E}}\,. \tag{4.2}$$

$R_{\mathrm{E}}\left(\gamma,\Delta\right)$ is a function which determines the shape of the hard shell, hence it is called the shape function. The angles γ and Δ specify the relative position of the atom with respect to the bond axis of the molecule. γ is equivalent to the Jacobi angle of Eqs. (2.12) and (2.15). Δ, the azimuth, is redundant as long as the diatomic molecule and its shape function are axially symmetric. The NO(X) molecule belongs to the $C_{\infty v}$ or $D_{\infty h}$ point groups, depending on whether it is treated as a heteronuclear or homonuclear molecule, therefore Δ will be omitted from now on. As a consequence, all the geometrical information is contained in a 2D contour obtained by intersecting the V_{sum} PES with the collision energy. R_{E} is just the mathematical representation of the contour, which can either be an equation of an ellipse, in the homonuclear case, or given in terms of series expansion in both cases according to Eqs. (4.3) and (4.4) [131],

$$R_{\mathrm{E}}(\gamma) = \frac{A}{B}\sqrt{\left(A^2\sin^2(\gamma) + B^2\cos^2(\gamma)\right)} \tag{4.3}$$

$$R_{\mathrm{E}}(\gamma) = \sum_l \frac{2l+1}{2}\Xi_l P_l\left(\cos(\gamma)\right)\,. \tag{4.4}$$

In Eq. (4.3) A and B are the major and minor semiaxes of the ellipse which represents the molecule, respectively. In Eq. (4.4) Ξ_l are the expansion coefficients, $P_l\left(\cos(\gamma)\right)$ is a Legendre polynomial of order l.

Instead of using an ellipse as a homonuclear contour, it was obtained by intersecting the $V_{\mathrm{sum}}(R,\gamma)$ potential, whose odd expansion coefficients in Eq. (2.12) were set to zero, in order cause the least possible distortion of the original contour. Since the contour, or equivalently R_E, is a function of the collision energy, the hard shell model implicitly depends on the collision energy too, as illustrated in the left panel of Figure 4.1. The hard shell contour of the NO(X) molecule is slightly asymmetric as shown in the right panel of

Figure 4.1. The expansion coefficients are listed in Table 4.1. The calculations where the NO(X) molecule was treated as a homonuclear or heteronuclear entity are referred to as classical homonuclear hard shell(C-HOHS) or classical heteronuclear hard shell (C-HEHS) calculations, respectively.

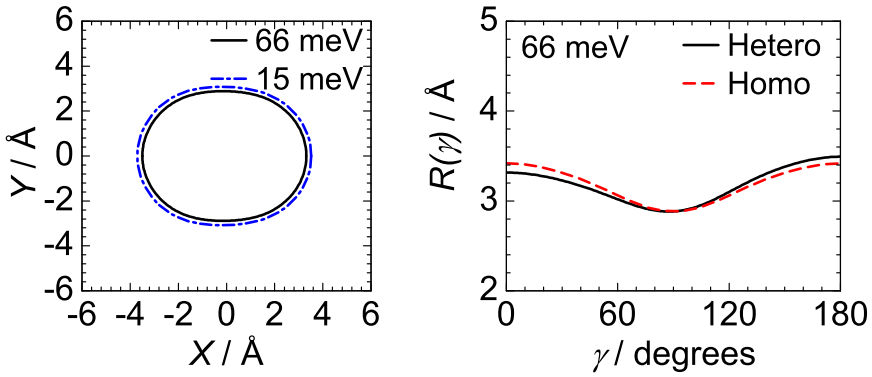

Figure 4.1: The hard shell contours at a collision energy of 66 meV (black solid line) and 15 meV (blue dash-dotted line) (left panel). The comparison of the heteronuclear (black solid line) and homonuclear (red dashed line) contours shows that the NO(X) hard shell is slightly asymmetric at a collision energy of 66 meV (right panel).

l	Ξ_l / Å		
	15 meV	66 meV (hetero)	66 meV (homo)
0	3.4241	3.0855	3.0462
1	−0.1041	−0.0858	0.0000
2	0.3887	0.3586	0.3322
3	0.0054	−0.0049	0.0000
4	−0.0824	−0.0524	0.0275
5	0.0024	0.0042	0.0000
6	0.0186	0.0106	0.0013
7	−0.0024	−0.0018	0.0000
8	0.0008	0.0018	−0.0013

Table 4.1: The expansion coefficients of the NO(X)–Ar hard shell contours used in this work.

In the classical hard shell calculations, the initial and final asymptotes are parametrised and sampled as discussed in Section 2.2.1. Because the atom and the particle only interact in an infinitely short period of time and space, solving the equations of motion does not require the explicit propagation of trajectories. The solution of the scattering problem

is reduced to determining the spatial coordinates where the atom reaches the molecular surface. If the contour is given by an ellipse, the point of contact can be expressed analytically in terms of the initial asymptote, therefore the deflection function has a closed, analytic form too [114, 115]. If an analytic formula is not attainable for the point of contact, it has to be calculated numerically which is often the case when dealing with heteronuclear molecules. In the present study a one dimensional simplex algorithm was employed to find the solution [132]. Once this point is found, the final coordinates and momenta can be calculated according to Eqs. (4.5)–(4.7) [115],

$$\Delta \boldsymbol{j} = \boldsymbol{j'} - \boldsymbol{j} = -\Delta p \, (\boldsymbol{R} \times \hat{\boldsymbol{n}}) \tag{4.5}$$

$$\frac{\Delta p}{p} = -2(\hat{\boldsymbol{n}} \cdot \hat{\boldsymbol{p}}) \frac{1-q}{1 + \frac{\mu_{\mathrm{BC}}}{I} \left(\boldsymbol{R} \times \hat{\boldsymbol{n}}\right)^2} \quad (\hat{\boldsymbol{n}} \cdot \hat{\boldsymbol{p}}) < 0, \tag{4.6}$$

where initial rotation is taken into account by the factor of q defined as

$$q \equiv \frac{j}{I} \frac{\mu_{\mathrm{BC}}}{p} \frac{(\boldsymbol{R} \times \hat{\boldsymbol{n}}) \, \hat{\boldsymbol{j}}}{\hat{\boldsymbol{n}} \cdot \hat{\boldsymbol{p}}}. \tag{4.7}$$

μ_{BC} and I_{BC} are the reduced mass and the moment of inertia of the diatom, respectively. The $\hat{\boldsymbol{n}} \cdot \hat{\boldsymbol{p}} < 0$ criterium ensures the molecular surface is convex at every point. Let us consider an initially non-rotating molecule; both the magnitude and the lab frame direction of the final rotational angular momentum, $\boldsymbol{j'}$, are solely determined by the point of contact, $\boldsymbol{R}$, the surface normal at that point, $\hat{\boldsymbol{n}}$ and the cosine of the angle, β, between $\hat{\boldsymbol{n}}$ and the initial relative momenta, $\boldsymbol{p}$. It worth reminding ourselves the lab frame orientation of $\boldsymbol{j'}$ is insensitive to the handedness of the $\boldsymbol{R}$–$\hat{\boldsymbol{n}}$–$\boldsymbol{p}$ triplet of vectors.

4.1.1 Classical hard shell differential cross sections

The main features of the homonuclear and heteronuclear hard shell differential cross sections are illustrated for the $\Delta j = 3, 7, 10$ and 14 transitions in Figure 4.2. Only the perpendicular component of the initial linear momentum, $\boldsymbol{p}$, can be transferred to the ro-

tational degree of freedom of the molecule. The degree of excitation depends on the angle between the surface normal, $\hat{\boldsymbol{n}}$, and $\boldsymbol{p}$. It has a maximum at a fixed point-of-contact, if $\boldsymbol{p}$ and $\hat{\boldsymbol{n}}$ are antiparallel, in which case the molecule is perfectly backward scattered. Parallel orientation would mean that the molecule is concave. Hence, as the degree of the rotational excitation increases, the collisions are more likely to happen in a geometry where $\hat{\boldsymbol{n}}$ and $\boldsymbol{p}$ are aligned antiparallel, thus the associated scattering angle is larger.

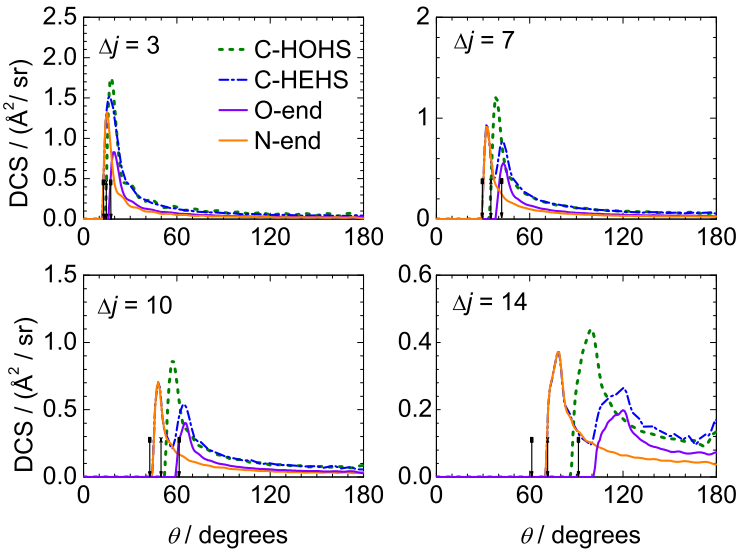

Figure 4.2: The C-HOHS (green dash–dot-dot line) and C-HEHS (blue dash–dot line) DCSs for the $\Delta j = 3, 7, 10$ and 14 transitions are shown in the top left, right and bottom left, right panels, respectively. The C-HEHS DCSs are decomposed according to the ends of the NO(X) molecule. The orange and purple lines represent scattering from the N-end and O-end, respectively. The C-HOHS and C-HEHS IOS rainbow angles are marked with cross- and square-ended arrows, respectively. All the data were obtained at a collision energy of 66 meV.

The final rotational state also depends on the effective impact parameter, $b_n = |\hat{\boldsymbol{n}} \times \boldsymbol{R}|$, [114]. The larger the effective impact parameter, the greater the torque that is exerted on the molecule for a fixed Δp. The effective impact parameter takes the value of zero, if the point-of-contact, $\boldsymbol{R}$, and $\hat{\boldsymbol{n}}$ are parallel, thus the impact of the atom causes no torque. For homonuclear molecules, these configurations are those where the atom hits the pointed end of the molecule, 'head on' collisions, or the intersection of the dihedral mirror plane and the molecular surface. It is maximal for a given distance from

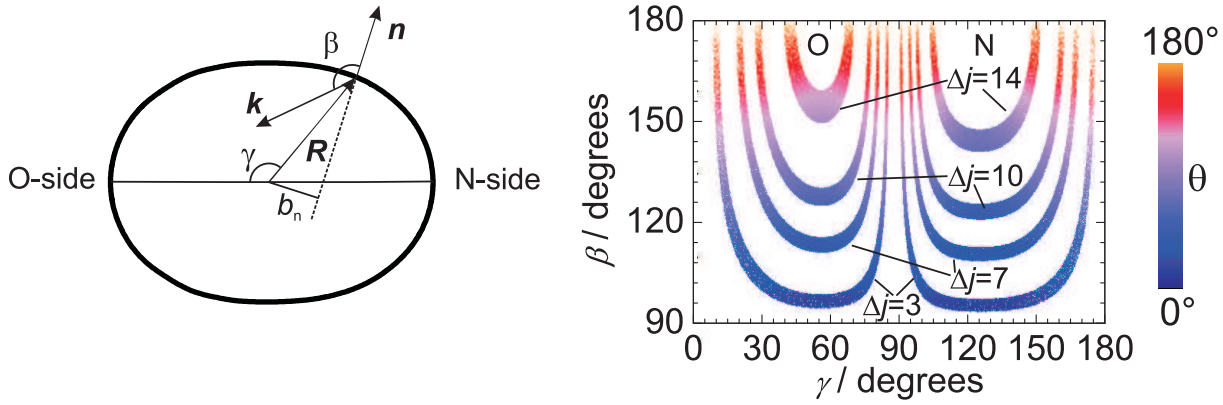

Figure 4.3: (Left panel) The NO(X)–Ar hard shell contour at a collision energy of 66 meV. The vectors which determine the amount of the momentum transferred are shown. (Right panel) The scattering angle as a function of the Jacobi angle, γ, and the apse angle, β, for the $\Delta j = 3, 7, 10$ and 14 transitions

the centre-of-mass of the molecule when the angle between the surface normal and the point-of-contact, is the closest to $\pi/2$ on the molecular surface.

A heteronuclear molecule no longer possesses a mirror plane perpendicular to its symmetry axis, thus it is possible to discern two ends of the molecule, namely the O-end and the N-end. They are separated by the line along which the $\hat{\boldsymbol{n}} \times \boldsymbol{R}$ cross product is zero, that corresponds to a Jacobi angle of about $\pi/2$. The N-end is more pointed and extends farther from the centre-of-mass of the diatom, as compared to the O-end. In the case of homonuclear molecules, the two sides are equivalent.

The homonuclear DCSs are single peaked, whereas the heteronuclear DCSs are double peaked. This is not so apparent for low Δj transitions, since the two peaks overlap. For instance, the second peak only appears as a shoulder for $\Delta j = 3$. As the degree of the rotational excitation increases, the separation between the peaks becomes larger as shown in Figure 4.2. This phenomenon can be explained as follows. In order to transfer enough linear momentum to excite the molecule to a particular final state, the collision ought to happen at specific geometries. If Δj is low, those configurations which lead to the state in question are widely distributed and roughly identical for the two ends of the molecule. As a consequence, scattering from either end of the molecule leads to similar scattering angle distributions.

This phenomenon is illustrated by the right panel of Figure 4.3, where the scattering angle is plotted as a function of the angle between $\hat{\boldsymbol{n}}$ and $\boldsymbol{p}$ and the Jacobi angle for a selection of final states. The two curved bands for the $\Delta j = 3$ transition have similar shape. At higher Δj states, only collisions having certain initial configurations can lead to transitions, because β and b_n have to take specific values to maximise the momentum transfer. Hence the number and positions of these configurations become gradually more restricted. Since the curvatures of the two ends of the molecule are different, the scattering angle distribution will be markedly different, and the gap between the maxima opens up. For instance, the average β angle is bigger on the O-end of the molecule than on the N-end, for scattering to high Δj, as a result the corresponding scattering angles will be larger on this end. Also, the average distance between the centre-of-mass and the molecular surface is smaller on the O-end than that of the N-end. As a result the bands for the $\Delta j = 14$ transition are the most separated and backward scattered.

Since the C-HEHS method is inherently classical, it is possible to label the individual trajectories according to which end of the molecule they are scattered. The differential cross sections resolved with respect to the side of the collision are shown in Figure 4.2. The total DCS is the sum of the two resolved DCSs. Classically, there is no interference between the trajectories arising from N-end and O-end collisions. Both the 'N' and 'O' DCSs are single peaked, the distance between which increases as Δj progresses. The 'O' DCS is more backward scattered which reaffirms the above discussion that it is linked to collisions where the initial linear momentum is preferentially more aligned perpendicularly to the molecular surface.

The rotational rainbow angle, θ_{R}, is the angle at which the transition becomes classically allowed [133]. According to the infinite order sudden (IOS) approximation [63, 134] this angle is given by Eqs. (4.8)–(4.9) for the final state j', if the hard shell potential is approximated by an ellipse whose minor and major semiaxes are denoted by A and B,

respectively:

$$\Delta j_{\max} = k(A - B) \tag{4.8}$$

$$\theta_{\mathrm{R}} = 2\sin^{-1}(j'/\Delta j_{\max})\,, \tag{4.9}$$

where $\Delta j_{\max}$ is the maximum of the classically achievable rotational excitation and $k = p/\hbar$ is the wave number. If the molecule is treated as a homonuclear entity then $A = 3.46\,\text{Å}$ and $B = 2.95\,\text{Å}$. The calculated IOS rainbow angles are marked in Figure 4.2 by red arrows. They agree well with the C-HOHS rainbow angles for low rotational states. For higher j' the agreement breaks down, since the assumption that the rotational levels are degenerate becomes a gradually less exact approximation. It is more appropriate to treat the NO(X) molecule as being heteronuclear, such that it can be described by two ellipses which correspond to each end of the molecule. The two sets of the semiaxes are $A_{\mathrm{N}} = 3.37\,\text{Å}$, $B_{\mathrm{N}} = 2.95\,\text{Å}$ for the O-end and $A_{\mathrm{N}} = 3.53\,\text{Å}$ $B_{\mathrm{N}} = 2.95\,\text{Å}$ for the N-end. The calculated heteronuclear IOS rainbow angles are marked by black arrows in Figure 4.2. They match the classical (C-HEHS) ones when the rotational excitation is low or medium. The agreement is less good in the case of high j' states for the reasons discussed above.

4.2 Modified potential energy surfaces

A transition from a particular initial state to a final state is generally influenced by the entire potential energy surfaces, PESs, on which it takes place. This is especially true in the case of quantum mechanical close-coupled calculations where the scattering wave function is propagated from the classically forbidden region to a point where the interaction potentials vanishes [54, 55]. In the case of quasi-classical trajectory (QCT) calculations, the propagation starts at a distance where the interaction between the particles is negligible and proceeds to the classical turning point, which is situated at smaller interparticle separations. Then it is terminated at large distances, where the interaction is negligible.

In either case, a wider range of potentials is sampled, which can be attractive or repulsive.

In the following, particular attention will be paid to how the repulsive or attractive features of the potential energy surfaces, influence the collision dynamics. Thus it is helpful to introduce the so-called soft potential, where the attractive part of the potential is omitted. QCT calculations were run on the $V_{\mathrm{sum}}(R,\gamma)$ surface, and the spin–orbit conserving transitions primarily take place on this surface in the NO(X)–Ar system and at the collision energies considered in this thesis.

Classically, the soft modified $V_{\mathrm{sum}}(R,\gamma)$ potential, $\widetilde{V}_{\mathrm{sum}}(R,\gamma)$, can be defined as follows:

$$\widetilde{V}_{\mathrm{sum}}(R,\gamma) \equiv \begin{cases} V_{\mathrm{sum}}(R,\gamma) & \text{if } V_{\mathrm{sum}}(R,\gamma) \geq 0 \\ 0 & \text{if } V_{\mathrm{sum}}(R,\gamma) \leq 0\,. \end{cases} \tag{4.10}$$

This transformation simply sets every point of the original $V_{\mathrm{sum}}(R,\gamma)$ PES to zero, if it is negative, and retains it otherwise. The generation of this potential does not require extra computational effort. Eq. 4.10 is evaluated once the unmodified potential is calculated.

The open shell close-coupled quantum mechanical (CC QM) calculations run simultaneously on both the $V_{\mathrm{sum}}(R,\gamma)$ and $V_{\mathrm{dif}}(R,\gamma)$ PESs [9]. As a consequence, damping only the $V_{\mathrm{sum}}(R,\gamma)$ potential violates the requirement of Eq. (2.12), that the $V_{\mathrm{sum}}(R,\gamma)$ and $V_{\mathrm{dif}}(R,\gamma)$ PESs should be the half sum and half difference of the A' and A'' PESs. Nullifying the $V_{\mathrm{dif}}(R,\gamma)$ PES at those (R,γ) points where $V_{\mathrm{sum}}(R,\gamma)$ is set to zero introduces unphysical discontinuities. A possible solution is to find an appropriate function which smoothly scales both PESs to zero in a finite interval. The logistic function smoothly varies between its asymptotic values of 0 and 1 between $-\infty$ and $+\infty$, respectively [111]:

$$f(R) = \frac{1}{1+\exp(-R)}\,. \tag{4.11}$$

We chose to scale the potentials with a parametrised variant of this function:

$$f(R,R_0,R_{\mathrm{shift}},\alpha) = 1 - \frac{1}{1+\exp(-\alpha(R-R_0+R_{\mathrm{shift}})}\,, \text{where } \alpha, R_0, R_{\mathrm{shift}} > 0\,, \tag{4.12}$$

where α determines the steepness of the function. R_{shift} shifts the inflexion point of $f(R, R_0, R_{\text{shift}}, \alpha)$ towards smaller R, so that scaled potentials drops below a pre-defined small value of $\varepsilon \cdot E_{\text{coll}}$ at a distance of R_0. ε was chosen to be 10^{-2}. R_0 is the contour of the $V_{\text{sum}}(R, \gamma)$ PES at zero collision energy. As such it depends on γ, the Jacobi angle. The exact value of α is set such that, R_{E}, the contour of the $\tilde{V}_{\text{sum}}(R, \gamma)$ potential taken at the collision energy, is identical to that of the unmodified sum potential. The values that α and R_{shift} are allowed to take are interrelated and depend on the shape of the unmodified PESs and ε.

α_i were set to about 1.0 bohr^{-1} and 5.0 bohr^{-1} and $R_{\text{shift,i}}$ were set to about 1.0 bohr and 0.50 bohr for the (a) and (b) soft potentials, respectively. The sum and difference PESs can then be written as:

$$\begin{aligned} \widetilde{V}_{\text{sum}}(R, \gamma_i) &= V_{\text{sum}}(R, \gamma_i) f(R_i, R_{0,i}, R_{\text{shift,i}}, \alpha_i) \\ \widetilde{V}_{\text{dif}}(R, \gamma_i) &= V_{\text{dif}}(R, \gamma_i) f(R_i, R_{0,i}, R_{\text{shift,i}}, \alpha_i)\,, \end{aligned} \tag{4.13}$$

where the index, i, runs over the Jacobi angles at which the original A' and A'' PESs were calculated [102]. The number of these angles is small, 9, which restricts the biggest possible value of α. If the modified PESs are too steep the series expansion will result in unphysical oscillations between the expansion points, γ_i.

The contour plots of the modified, or soft NO(X)–Ar sum and difference PESs are shown in Figure 4.4. The attractive parts of the sum potential are removed. The repulsive wall between the $R_0(\gamma)$ and $R_E(\gamma)$ is slightly steeper than that of the unmodified potential. The soft and the unmodified potentials are identical at energies higher than the collision energy. The changes of the $\widetilde{V}_{\text{dif}}(R, \gamma)$ potential are less marked.

The effect of making the $V_{\text{sum}}(R, \gamma)$ potential purely repulsive is best illustrated by a comparison of the DCSs obtained on the unmodified, or full, and soft PESs. The DCSs for the $|0.5, 0.5, -1\rangle \rightarrow |j', 0.5, \pm 1\rangle$, $j' = 3.5, 7.5, 10.5$ and 14.5 are shown in the first and second rows of Figure 4.6. At $\Delta j = 3$, the forward scattered peak is greatly reduced and

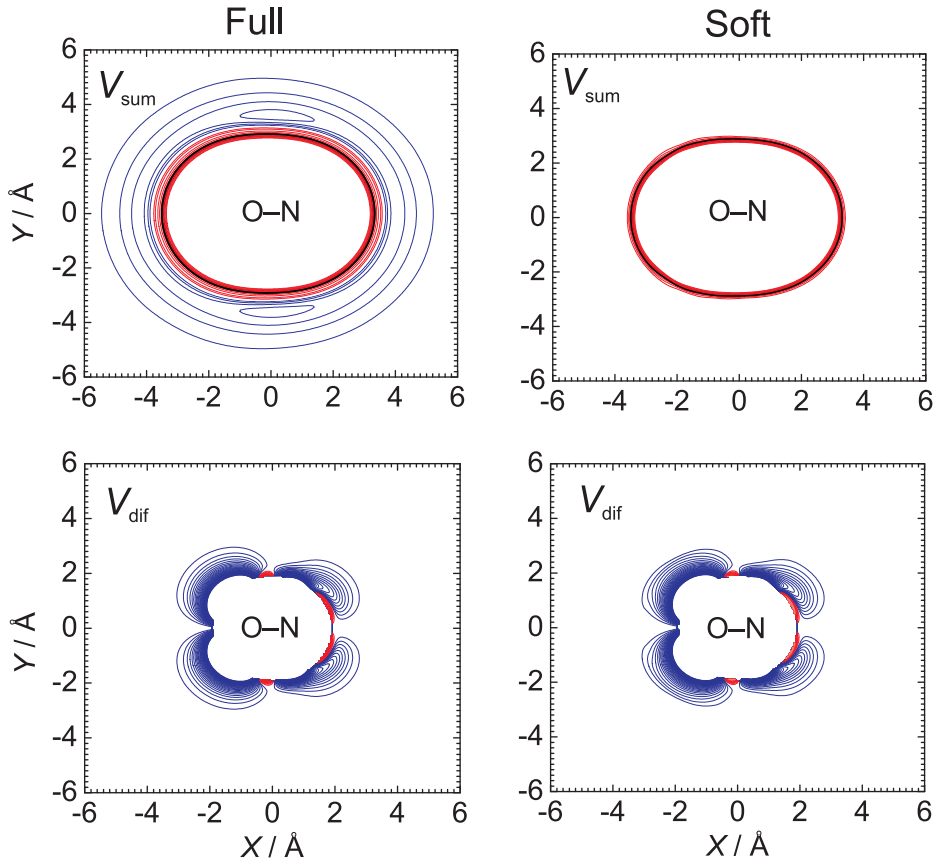

Figure 4.4: Unmodified V_{sum} and V_{dif} PESs (top left and bottom left panels, respectively), the red contours correspond to 100 cm^{-1} spacing. The blue contours represent $-20\,\mathrm{cm}^{-1}$ separation. The modified 'soft' V_{sum} and V_{dif} PESs are shown in top and bottom left hand panels, respectively. The absence of the blue contours in the V_{sum} PES indicates that its attractive part has been removed.

is shifted towards larger scattering angles. For higher Δj, transitions the first maxima of the multiple peaked DCSs are reduced. The peaks in general become more backward scattered, though the difference between the unmodified and soft DCSs are in general less dramatic than in the case of low Δj transitions, where the presence of the attractive forces is more important. For the sake of completeness, the spin–orbit changing DCSs are also shown in the bottom panels of the same figure. The modification of the $V_{\mathrm{dif}}(R, \gamma)$ surface drastically reduced both the $-1 \rightarrow -1$ and $-1 \rightarrow +1$ DCSs at $\Delta j = 3$. The reduction of the attractive potential resulted in making the peaks more prominent in all states.

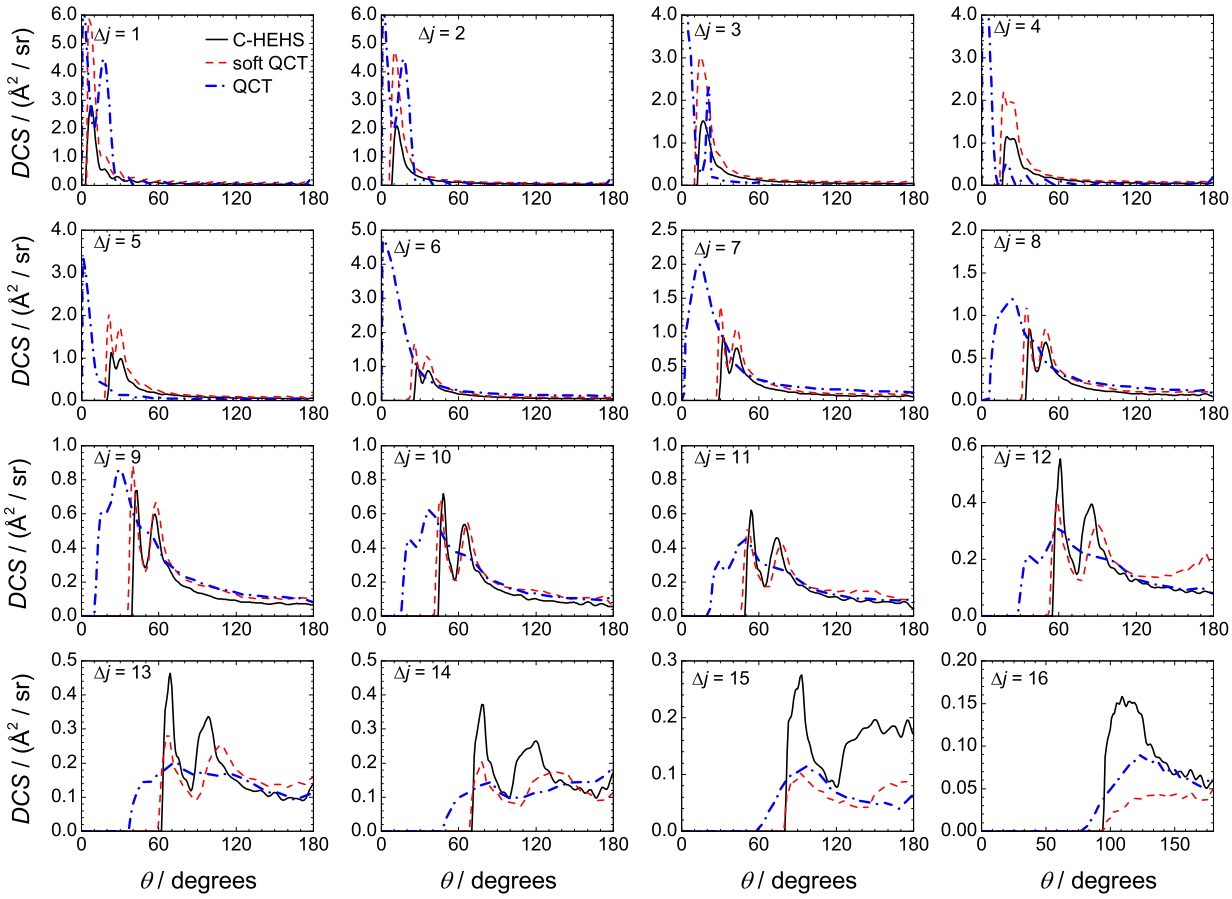

Figure 4.5: The C-HEHS (black solid line) and 'soft' QCT (red dashed line) and full potential QCT DCSs (blue dash-dotted line) for the $\Delta j = 1, ..., 16$ transitions at a collision energy of 66 meV. Note, the QCT DCSs were scaled down with a factor of five in the top row.

4.2.1 Comparison of the classical hard shell and soft potential differential cross sections

The classical hard shell and soft differential cross sections are compared in Figure 4.5. The removal of the attractive part of the potential has drastically changed the differential cross sections compared to the ones obtained on the full $V_{\text{sum}}(R, \gamma)$ surface. The secondary maximum is removed between 10° and 30° at $\Delta j = 3$. The classically forbidden region extends towards larger scattering angles in all states, but still falls slightly short of the hard shell classical limits.

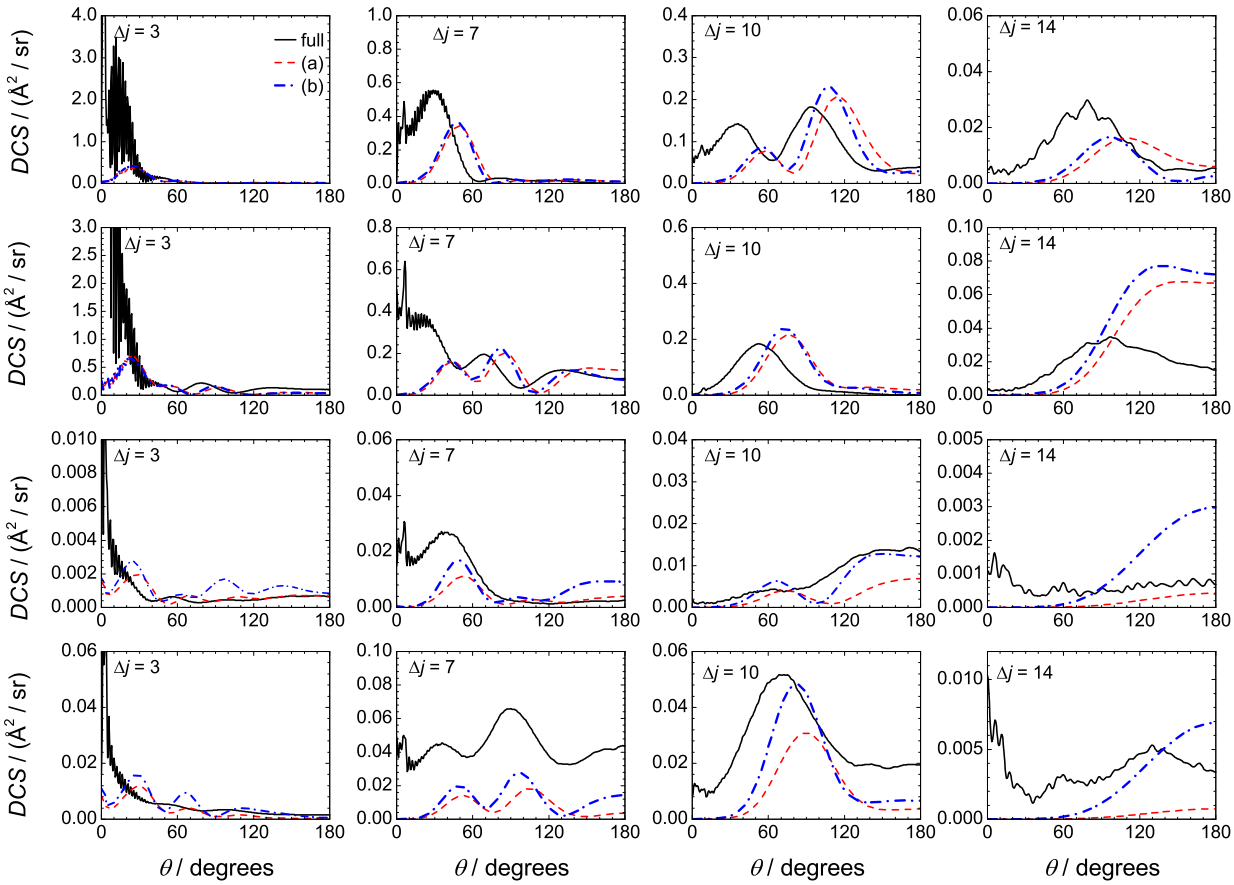

Figure 4.6: The unmodified (black solid line) and the (a) and (b) soft potential (red dashed line and blue dash-dotted lines, respectively) CC QM DCSs for the $|0.5, 0.5, -1\rangle \rightarrow |j', \Omega', \epsilon'\rangle$, $j' = 3.5, 7.5, 10.5$ and 14.5 transitions from left to right. $\epsilon' = -1, \Omega' = 0.5$: top row, $\epsilon' = +1, \Omega' = 0.5$: second row, $\epsilon' = -1, \Omega' = 1.5$: third row, $\epsilon' = +1, \Omega' = 1.5$: bottom row. Note, the full potential $j' = 3.5, \Omega' = 1.5$ DCSs are scaled down by a factor of ten.

At middle Δj transitions, the sharp double peaked structure present in the hard shell and soft QCT data is washed out by attractive forces in the case of full potential DCSs. The presence of a finite range of potential makes the features of soft QCT DCSs smoother than those of the hard shell ones. The agreement is somewhat less good between the soft and C-HEHS data for highly excited states.

It is worth noting the soft DCS are bigger than the hard shell ones at the lower states. This ratio lessens throughout the middle Δj state and is inverted in the case collisions with large energy transfer. The QCT and soft QCT collisions have a bigger cross section than

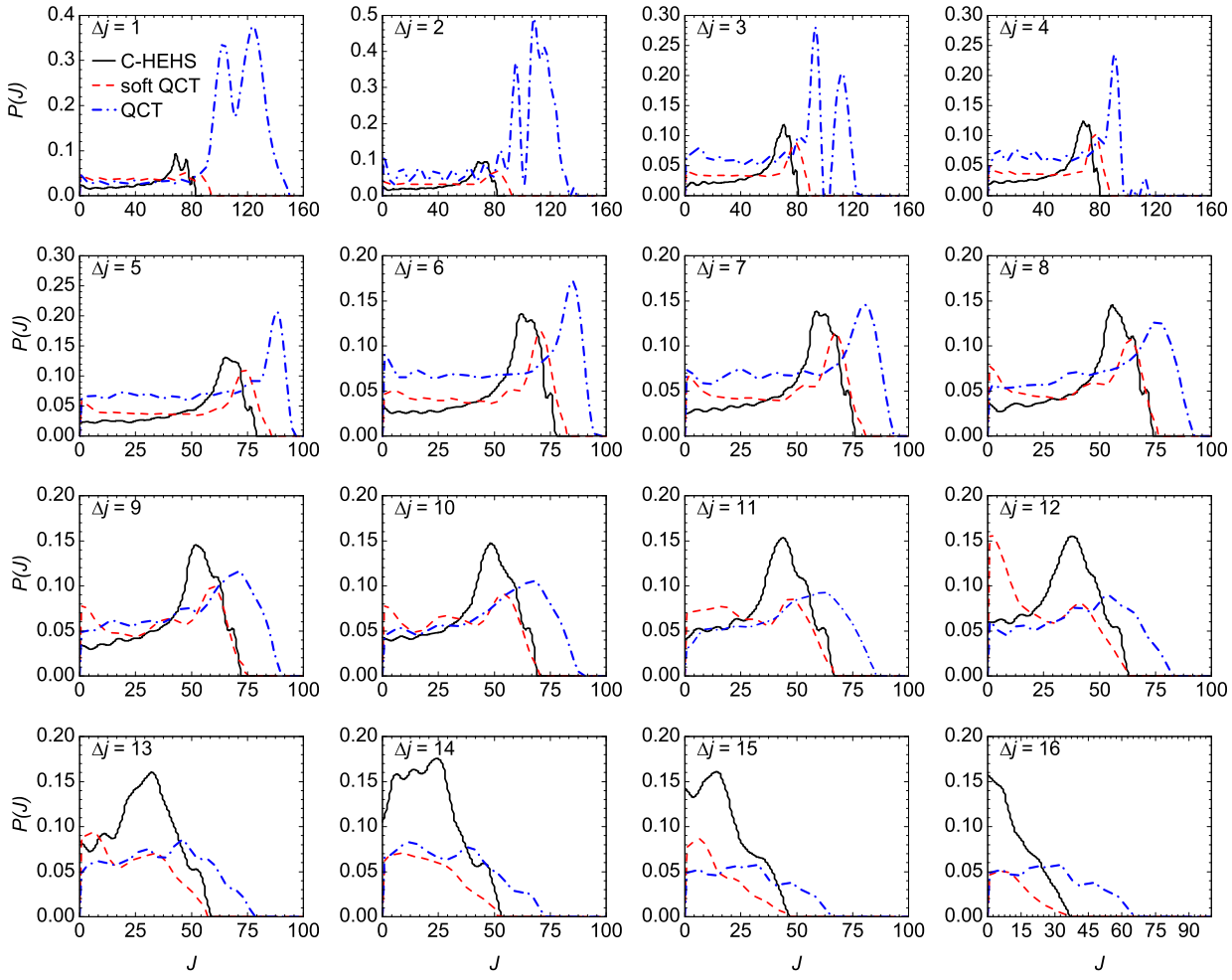

Figure 4.7: The C-HEHS (black solid line) and 'soft' QCT (red dashed line) and full potential QCT opacity functions (blue dash-dotted line) for the $\Delta j = 1, ..., 16$ transitions at a collision energy of 66 meV.

the hard shell collisions at low Δj transitions. This is because sufficient energy transfer can occur at larger distances where the interaction potential is zero in the hard shell case. This, in turn, increases the effective area of the molecule.

At high Δj transitions, the atom has to penetrate deeper into the potential in order to transfer sufficient amounts of energy which decreases the geometric cross section. However, this cannot explain why the soft DCSs are smaller than the hard shell ones, because the hard shell cross section is expected to be the lower limit of the soft shell geometrical cross section. The reason for that will be discussed later in Chapter 8.

The opacity functions embody equivalent information on the scattering dynamics. C-HEHS, soft potential QCT and full potential QCT opacity functions are plotted as a function of total angular momentum J in Figure 4.7. The most remarkable difference can be observed between those obtained on the full potential and the purely repulsive potentials. At low Δj transitions, the secondary lobe is absent from the opacity functions obtained on the purely repulsive potentials at larger impact parameters. The soft opacity functions extend to greater impact parameters than the hard shell ones, because the soft potential goes to zero down at larger atom–diatom distances. The separate maxima at large J of the C-HEHS opacity functions are blurred in their soft counterparts.

4.3 Quantum mechanical hard shell scattering

The quantum mechanical theory of the scattering of a hard shell and a structureless atom was first developed by Bosanac in terms of Jost functions [135]. The problem was later reformulated which resulted in a conceptually simpler solution, employing vanishing integrals of the scattering wavefunctions on the molecular surface [136]. This method was subsequently applied to calculate the differential cross sections in the scattering of D_2 and Ne at a collision energy of 85 meV [136]. Integral cross sections were calculated for the He+HF [137], Xe+HF [138] and Xe+CO_2 [139] systems and compared to those obtained with other theoretical methods. They found that the increasing steepness of a soft potential only results in slow convergence of the ICSs to the exact hard shell quantum mechanical ones in the Xe+HF system [138]. Differential cross section were not published for these or any other systems, and polarisation parameters, such as polarisation dependent differential cross sections and integrated polarisation moments have not been calculated to the best of our knowledge.

The above publications only consider collisions between closed shell molecules and atoms. It is possible to extend the formalism to include collisions between open shell molecules and closed shell atoms. This modification is detailed in Appendix B, though,

only closed shell scattering problems will be investigated.

The quantum mechanical scattering of hard shell atoms and molecules leads to a set of linear equations as derived in Appendix B:

$$-\frac{i(2J+1)}{2k_{j_0\Omega_0\epsilon_0}}X^J_{j'm'\Omega'\epsilon',j_0m_0\Omega_0\epsilon_0} = \sum_{jm} W^J_{j'm'\Omega'\epsilon',jm\Omega\epsilon}F^{Jm_0}_{jm\Omega\epsilon,j_0m_0\Omega_0\epsilon_0}\,. \tag{4.14}$$

The solutions are the partial scattering amplitudes, $F^{Jm_0}_{jm\Omega\epsilon,j_0m_0\Omega_0\epsilon_0}$, which determine the probability of the $|j,\Omega,\epsilon\rangle \rightarrow |j',\Omega',\epsilon'\rangle$ transition as a function of the total angular momentum, J. $W^J_{j'm'\Omega'\epsilon',jm\Omega\epsilon}$ and $X^J_{j'm'\Omega'\epsilon',jm\Omega\epsilon}$ are the 'coupling matrix elements' of the scattered and incident waves, respectively, and are defined in Appendix B. These matrices are the linear combinations of the overlap integrals between the initial and final wavefunctions, $B^{(\ell)}_{jm'\Omega\epsilon,j'm'\Omega'\epsilon'}$:

$$\begin{aligned} B^{(\ell)}_{jm'\Omega\epsilon,j'm'\Omega'\epsilon'} &\equiv \langle j'm'\Omega'\epsilon'|i^l h^{(l)}_{k_{jm\Omega\epsilon}}|jm'\Omega\epsilon\rangle \qquad (4.15)\\ &= \int_0^\pi \sin\gamma \mathrm{d}\gamma \left[d^{j'}_{m'\overline{\Omega}'}(\gamma) + \epsilon' d^{j'}_{m'-\overline{\Omega}'}(\gamma)\right] i^\ell h^{(1)}_\ell(k_j R(\gamma)) \left[d^{j}_{m'\overline{\Omega}}(\gamma) + \epsilon d^{j}_{m'-\overline{\Omega}}(\gamma)\right], \end{aligned}$$

as such they determine the strength of the transition.

4.3.1 Solution of the linear equations

The problem of determining the scattering matrix is thus reduced to solving Eq. (4.14). This seemingly easy task is rather challenging, because the W matrix is ill conditioned. It consists of integrals of Bessel and Hankel functions over several orders, $|J-j| \geq \ell \leq J-j$. Note, the Hankel and Bessel functions with imaginary argument can be expressed in terms of modified Bessel functions of the first and second kind[111]. Their argument, $k_j r$, considerably changes as j increases which makes the functions sample regions where they converge to a finite value or diverges to infinity. In order to overcome this problem, the coupling matrix has to be preconditioned prior to solving the set of linear equations.

Method of least squares with improved convergence properties were chosen to determine the solution, namely the ZGESVX LU-decomposition, and ZGELSS least squares algorithms of the LAPACK [140] linear algebra package.

Partial waves up to $J = 100 - 150$ and rotational states up to $j = 20$ were included in a typical calculation at a collision energy of 66 meV. The convergence as a function of rotational states and the total angular momenta was always checked for every calculation presented in this thesis. The scattering code was written in Fortran90. A typical calculation including 100 partial and a coupling matrix of 500 channel takes approximately 2 minutes using a 2.83 GHz two Quad CPU.

4.3.2 Conservation of diatomic parity

The parity changing collisions are forbidden for a homonuclear molecule. This requirement should be met in any quantum mechanical scattering formalism and is to be tested in the following.

The $|j, m, \Omega, \epsilon\rangle \rightarrow |j', m', \Omega', \epsilon'\rangle$ transition is allowed, if the corresponding $B^{(\ell)}_{jm'\Omega\epsilon,j'm'\Omega'\epsilon'}$ element is non-zero. $|j, m, \Omega, \epsilon\rangle$ has a definite parity with respect to the inversion operator:

$$\hat{i}|j, m, \Omega, \epsilon\rangle = p|j, m, \Omega, \epsilon\rangle = (-1)^{j-\epsilon/2}|j, m, \Omega, \epsilon\rangle \,. \tag{4.16}$$

The integral in Eq. (4.15) contains a product of three functions, namely the initial and final wave functions and a function of the shape function. The shape function belongs to the $D_{\infty h}$ point group for a homonuclear molcule. As a consequence, $h^{(1)}_\ell(k_g R(\gamma, \Delta))$ is also a member of this point group, as it takes its values on the surface. It is symmetric with respect to the inversion operator:

$$\hat{i}h^{(1)}_\ell(k_g R(\gamma, \Delta)) = +1 \cdot h^{(1)}_\ell(R(\gamma, \Delta)) \text{ for all } g \text{ states and order of } \ell \,. \tag{4.17}$$

The product of two functions is symmetric, if both are symmetric or antisymmetric, oth-

erwise it is antisymmetric. The parity of the 'ket' wavefunction is identical to that of the $h_\ell^{(1)}(k_g R(\gamma,\Delta))|j,m,\Omega,\epsilon\rangle\rangle$ product. Thus the integral in Eq. (4.15) vanishes unless $|j,m,\Omega,\epsilon\rangle$ and $|j',m',\Omega',\epsilon'\rangle$ have the same parity. This is the well known selection rule for the rotational transition of the homonuclear molecules. If the molecule is heteronuclear, it belongs to the $C_{\infty v}$ point group, and the shape function no longer has definite parity with respect to inversion. The transitions between states of different parities are not forbidden. Nevertheless, a propensity is still expected to persist for the parity conserving transitions, if the molecule is only slightly heteronuclear.

In the case of closed shell molecules, the integral is over two spherical harmonics. If the molecular contour is an even function of γ the integral obviously vanishes between even and odd spherical harmonics, ensuring the conservation of diatomic parity.

4.3.3 Calculation of the cross sections

The opacity functions can be expressed in terms of the partial scattering amplitudes according to Eq. (4.18) [136]:

$$P_{j_2\leftarrow j_1}(J) \;=\; 4\sum_{\ell_2 m_1}\frac{|f^J_{j_2\ell_2,j_1m_1}|^2}{(2J+1)(2\ell_2+1)}\,, \tag{4.18}$$

where the non-standard normalisation of Bosanac [136] has been taken into account. The $f^J_{j_2\ell_2,j_1m_1}$-s are the partial scattering amplitudes in the (jl,jm) representation [136]. The scattering amplitudes were calculated using a formula provided by Bosanac [136] from which the density matrix was constructed:

$$\begin{aligned} f_{j_2m_2\leftarrow j_1m_1}(\theta,\phi) \;&=\; \sqrt{4\pi}\sum_{J,\ell_2}(2\ell_2+1)^{-1/2} \\ &\quad \langle \ell_2 m_1-m_2, j_2m_2, Jm_1\rangle f^J_{j_2\ell_2|j_1m_1} Y_{\ell_{m_1-m_2}}(\theta,\phi)\;. \end{aligned} \tag{4.19}$$

The differential cross sections and renormalised polarisation dependent cross sections were derived from the density matrix according to the standard equations (3.61)–(3.63) of Chap-

ter 3.

4.3.4 Quantum mechanical hard shell integral and differential cross sections

Quantum mechanical hard shell calculations (HS QM) were carried at collision energies of 15 mev and 66 meV. The hard shell contours were obtained by intersecting the unmodified $V_{\text{sum}}(R, \gamma)$ potential at these collision energies. The contours and the expansion coefficients were shown in Figure 4.1 and Table 4.1. The two contours are almost identical, but the resultant DCSs will turn out to be largely different. This stems from the ratio of the systems de Broglie wavelength and the characteristic size of the scatterer, which is halved at the higher collision energy.

Integral cross sections

The HS QM integral cross sections were compared with closed shell CC QM ones which were obtained employing the steeper modified potential. None of the differential cross sections were scaled. The HS QM and soft CC QM integral cross sections are presented in Figure 4.8. Identical propensity rules apply to both set of ICS. The parity conserving ICSs are larger than the adjacent parity changing ones. Since the moelcule is almost homonuclear the parity changing coupling matrix elements are small, thus the probability of these transition are small [141]. If the molecule is homonuclear, the integral in Eq. (4.15) vanishes, thus these transitions become forbidden, which is confirmed by the right panel of Figure 4.8 in which all of the Δj odd ICSs are zero.

Differential cross sections

The agreement between the HS QM and CC QM data is exceptionally good at a collision energy of 15 meV. The general characteristics, such as the number, the position and the relative magnitude of the peaks tally as testified by Figure 4.9. The minor details, *e.g.*, the phase of the forward scattered oscillations coincide. These findings and the fact that the

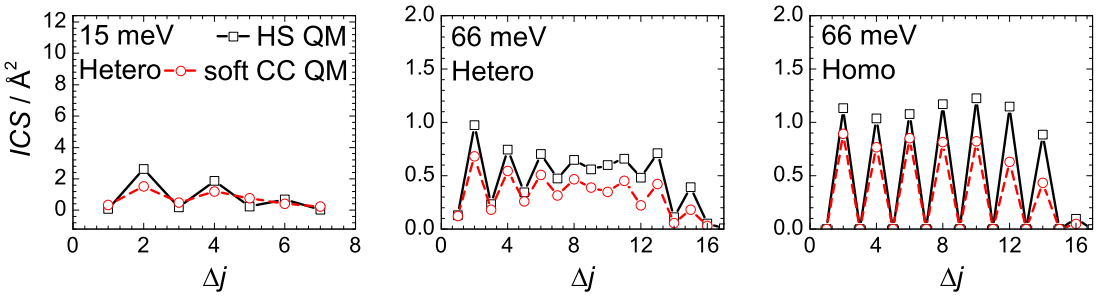

Figure 4.8: The HS QM (black open squares) and 'soft' closed shell CC QM (red open circles) integral cross sections. The parity conserving heteronuclear ICSs have a strong propensity (left panel) at 15 meV and 66 meV collision energies (left and middle panels, respectivel). The homonuclear parity changing ICSs vanish (66 meV, right panel).

absolute magnitude of the DCSs are roughly equal for most of the final states, suggests the soft potential is a good approximation of the exact hard shell potential at this collision energy for this system.

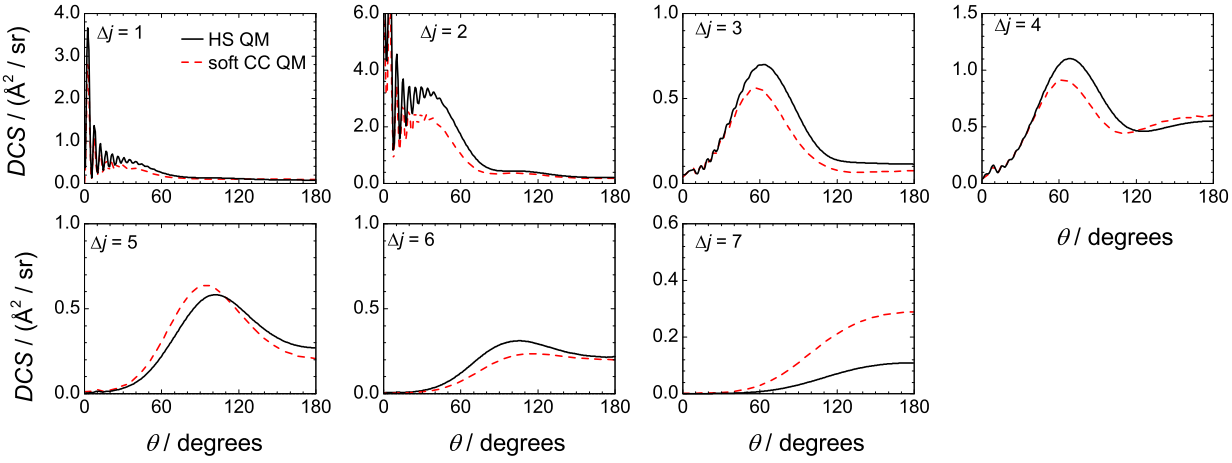

Figure 4.9: The HS QM (black solid line) and 'soft' closed shell CC QM DCSs (red dashed line) for the $\Delta j = 1, ..., 7$ transitions at a collision energy of 15 meV.

The QM HS DCSs are compared to those for the closed shell soft and full potential at a collision energy of 66 meV in Figure 4.10. The forward scattered main peak is missing at low Δj transitions, because of the absence of the attractive forces as was seen previously in the case of open shell DCSs in Figure 4.5. Fast oscillations can still be observed in the forward scattered region, up to $\Delta j = 4$. The amplitude of these oscillations decreases with increasing degree of rotational excitation. The agreement between the HS QM and

'soft' CC QM DCSs is good. The exact hard shell data are slightly shifted towards larger scattering angles. The number, the position, the relative magnitude of the peaks are matched. The structures of the parity conserving, even Δj, and parity conserving, odd Δj, DCSs are more distinct than at 15 meV. The hard shell data gradually become bigger than their CC QM counterparts with increasing Δj.

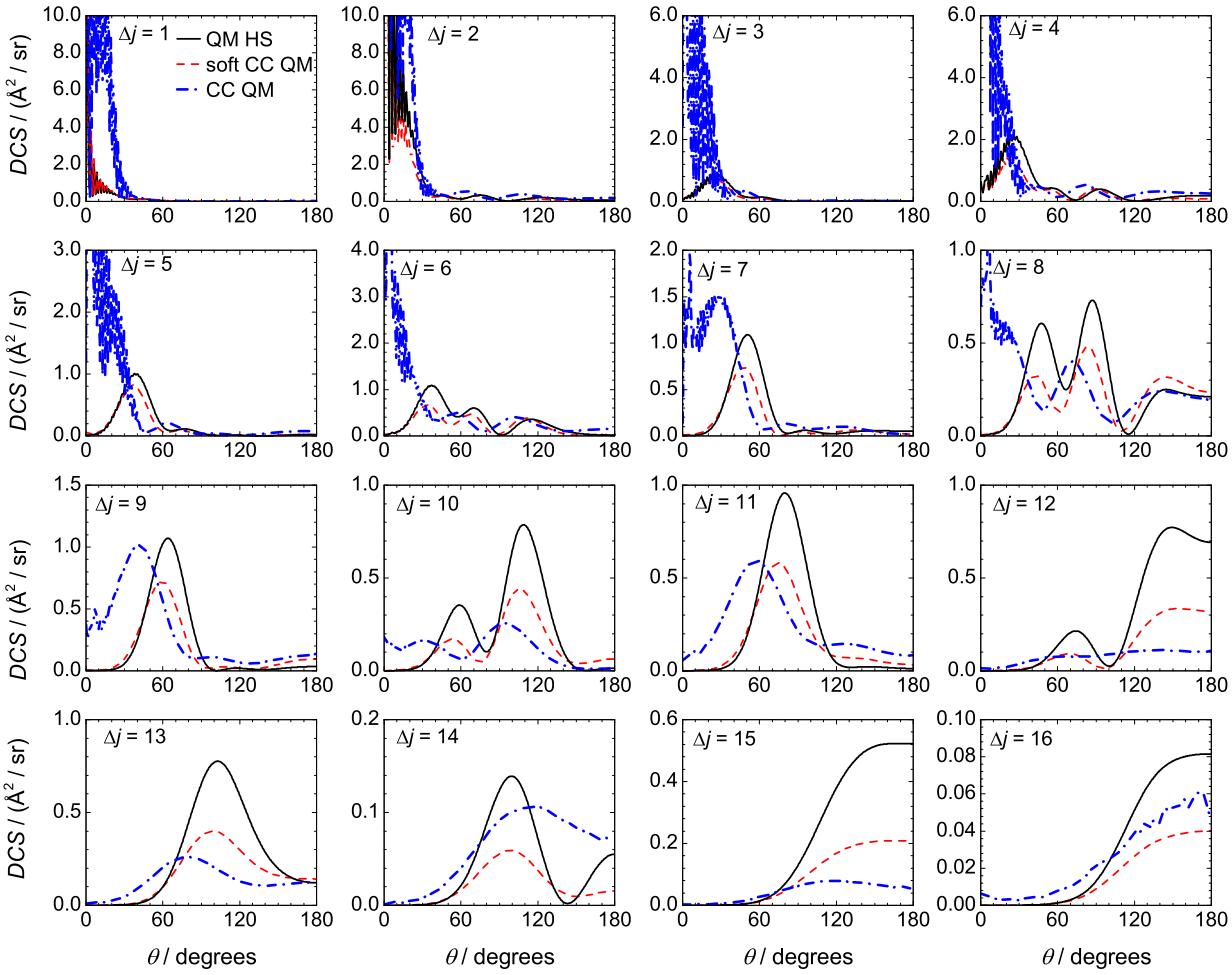

Figure 4.10: The HS QM (black solid line) and 'soft' closed shell CC QM (red dashed line) and full potential closed shell CC QM DCSs (blue dash-dotted line) for the $\Delta j = 1, ..., 16$ transitions at a collision energy of 66 meV.

4.3.5 Quantum mechanical hard shell opacity functions

The opacity functions further highlight the role of the attractive and repulsive ranges of the potentials. If the attractive part is removed the lobe at large J values disappear at low Δj transitions, as illustrated in the top panels of Figure 4.11. The maxima of the soft potential opacity functions are moved towards smaller J values as compared to the full potential opacity functions. The QM HS peaks are positioned to the left of the corresponding soft potential ones, reflecting the exclusion of the attractive and soft repulsive forces. The harder the potential, the more reduced the rightmost maxima of the opacity functions.

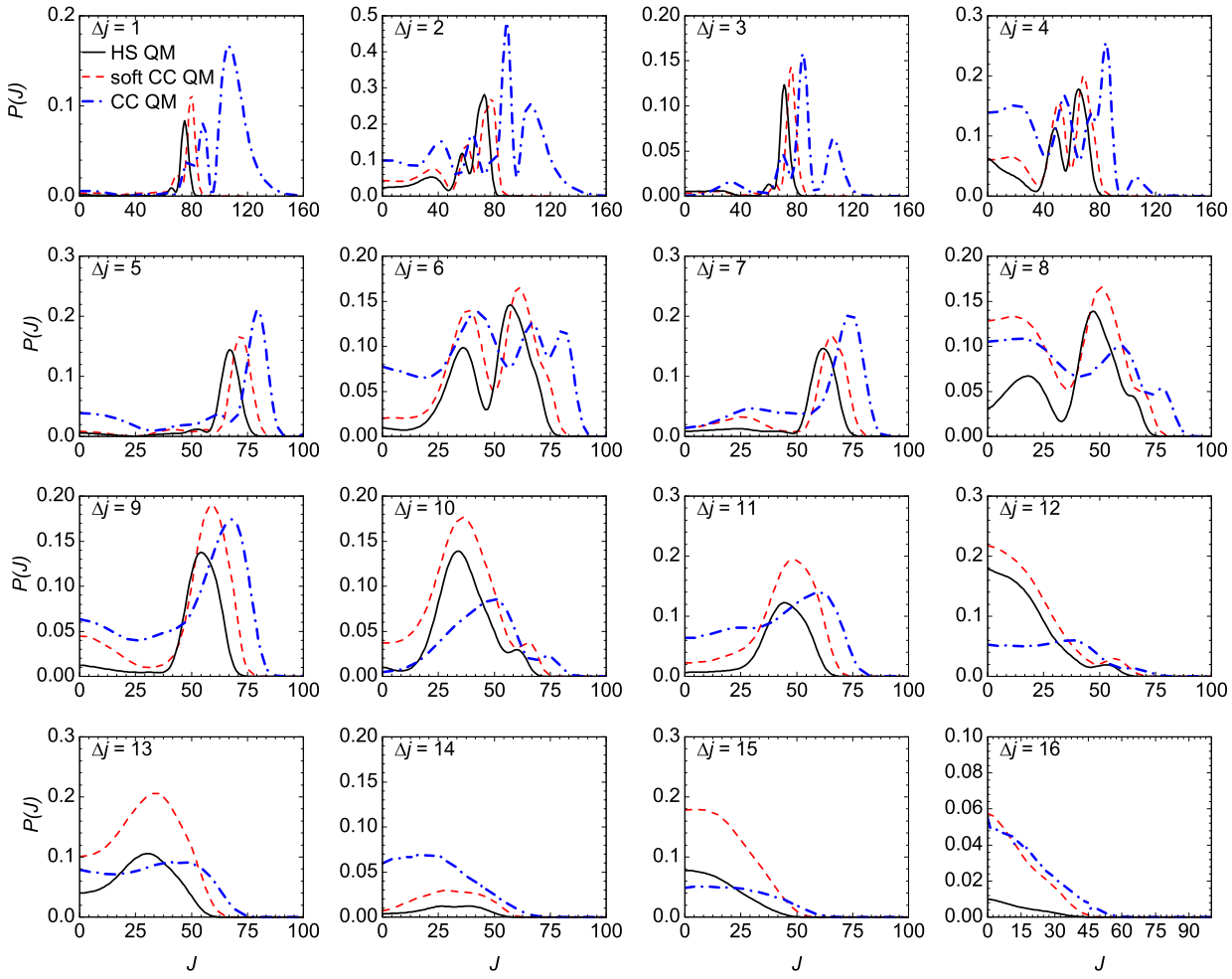

Figure 4.11: The HS QM (black solid line) and 'soft' closed shell CC QM (red dashed line) and full potential closed shell CC QM opacity functions (blue dash-dotted line) for the $\Delta j = 1, ..., 16$ transitions at a collision energy of 66 meV.

The separate peak of the full potential opacity function is only recognised as a small plateau or as a shoulder in the soft and QM HS data, respectively, at $\Delta j = 6$ and 8. It holds for all three type of opacity functions that the parity conserving ones have more maxima than the parity changing ones except for high Δj transitions. For instance, there are three peaks and a shoulder at large impact parameters at $\Delta j = 6$ transition. In constrast, in the case of the $\Delta j = 7$ transition, there are one pronounced maximum at about J=75, and a much less prominent secondary maximum about $J = 25$.

4.3.6 Comparison of the classical and quantum mechanical hard shell DCSs and opacity functions

The number and the degree of the separation of the peaks of the DCSs are purely determined by kinematic requirements in the case of classical collisions, as discussed above. If $\Delta j \geq 4$, there are always two peaks, each corresponding to the different ends of the molecule. In contrast, the number of maxima depends on whether the parity is conserved in quantum mechanical collisions. The main maxima of the classical DCSs coincides with the first maximum of their QM counterparts as shown in Figure 4.12. For instance, the classical double peak is enveloped by the broad peak of the QM DCSs between $\theta = 20^\circ$ and $\theta = 60^\circ$ at $\Delta j = 6, 7$ and 8. The latter exhibit additional peaks in the backward scattered region, where the classical DCSs monotonically decay.

It is also remarkable, that the HS QM opacity functions, shown in Figure 4.13 are multiple-peaked, except for high Δj transitions, whereas the classical ones only have a single main peak with multiple, unresolved shoulders in the high J region, which correspond to scattering from either end of the molecule. The total classical DCSs are the sum of the trajectories which end up in a particular j' state, because there is no interference between different trajectories.

In contrast, the partial waves may interfere with each other in the case of quantum mechanical scattering. In order to ascertain the role of this interference, series of DCSs were calculated for various total angular momentum intervals, *e.g.*, $0 \leq J \leq 20, 21 \leq J \leq 40, ...$

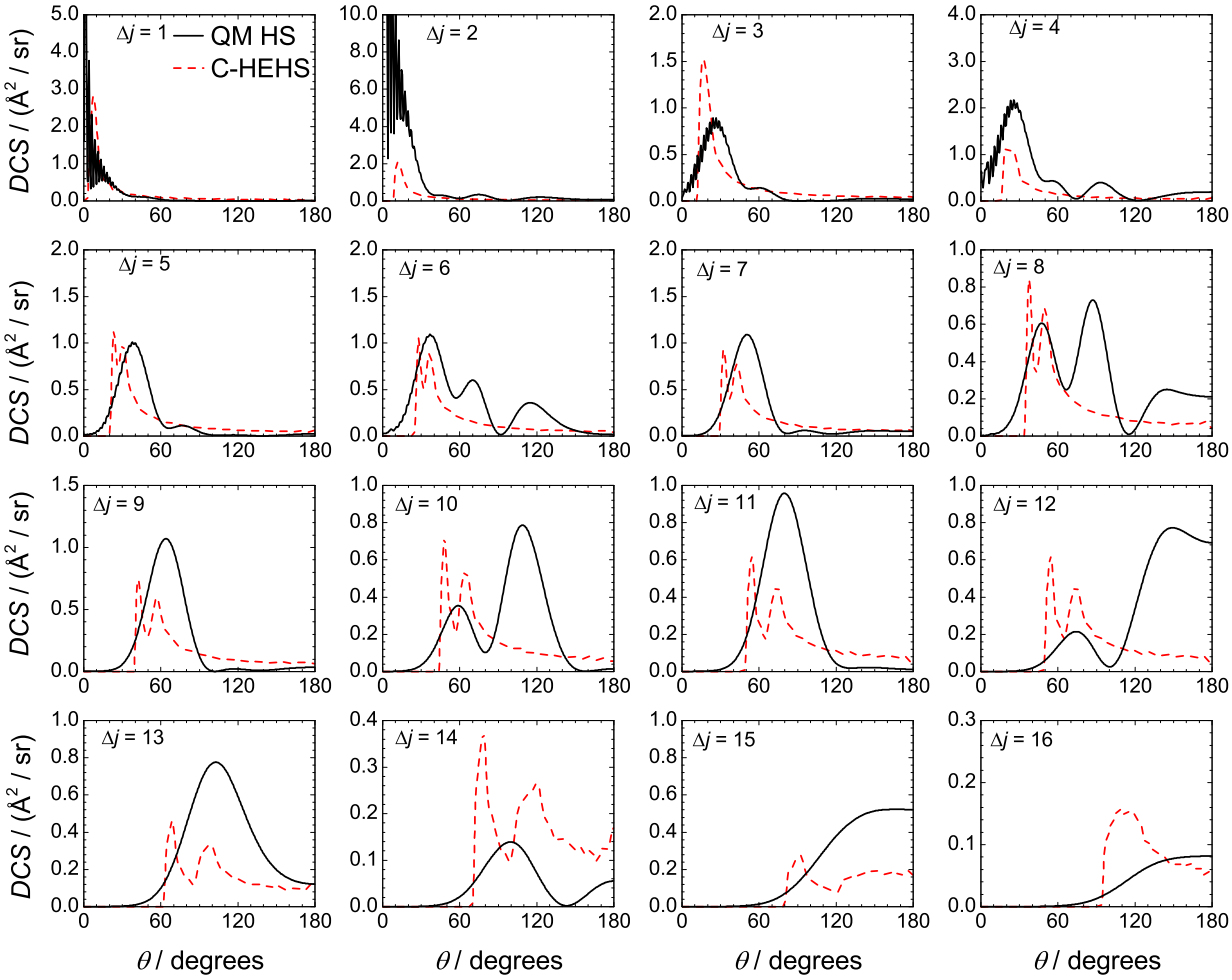

Figure 4.12: The HS QM (black solid line) and the classical hard shell, C-HEHS, (red dashed line) DCSs for the $\Delta j = 1, ..., 16$ transitions at a collision energy of 66 meV.

The total differential cross section was then constructed as an incoherent sum of these DCSs which are shown in Figure 4.14.

A certain region of an opacity function contributes mainly to a certain part of the DCS. For instance, at $\Delta j = 8$, each lobe of the opacity function can be assigned to a maximum of the corresponding DCS. The $J = 0 - 30$ and $J = 30 - 55$ lobes contribute to the peaks centered around $\theta = 120°$ and $\theta = 80°$, respectively at $\Delta j = 8$. The shoulder at around $J = 55 - 70$ is recognised as the peak at $\theta = 30°$ of the DCS. However, if all the partial waves are incoherently summed up, a symmetric DCS is obtained, which bears little resemblance to the fully coherent one, as shown in the right panel of Figure 4.14.

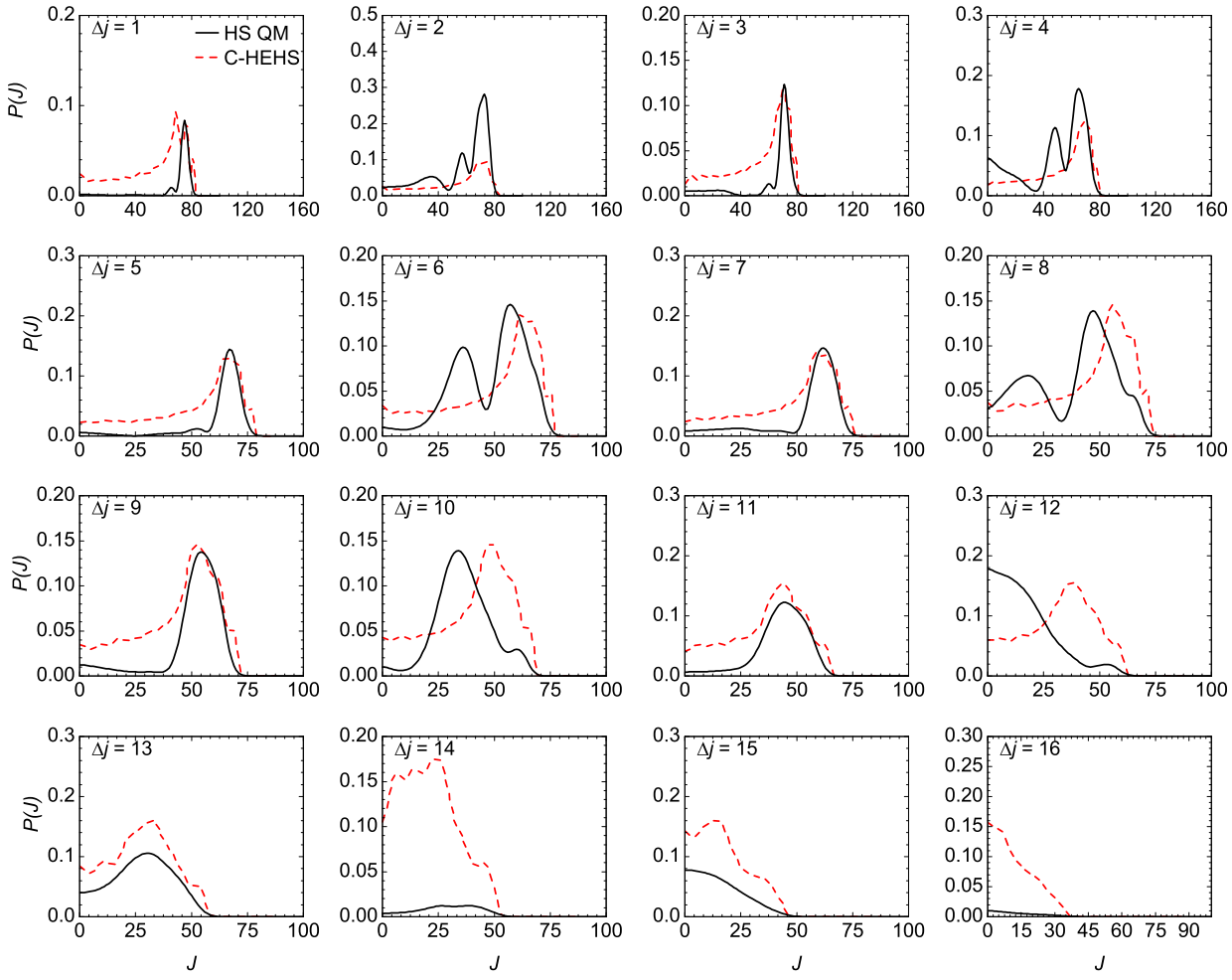

Figure 4.13: The HS QM (black solid line) and the classical hard shell, C-HEHS, (red dashed line) opacity functions for the $\Delta j = 1, ..., 16$ transitions at a collision energy of 66 meV.

If the DCSs calculated for twenty adjacent partial waves summed up, the original DCS is roughly, though, not exactly, recovered. This implies that there is only considerable interference between near partial waves.

Quantum mechanics thus manifests itself in a twofold way. Firstly, for a single partial wave, that is the QM opacity is small or big at a particular J for parity changing or conserving transitions. This is in line with the findings of the previous semiclassical studies, which showed that the interference between the paths scattered from the different ends of the molecule are responsible for the multiple peaked structure. Secondly, the interference

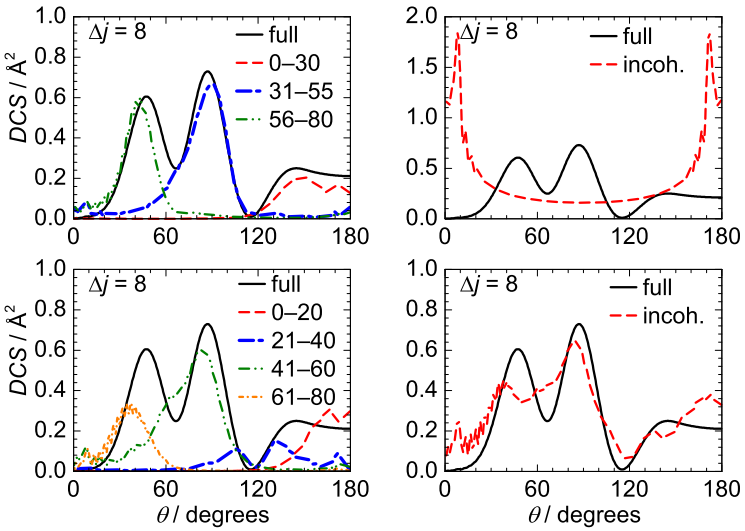

Figure 4.14: The full (black solid line in all panels), $J = 0 - 30$ (red dashed line), $J = 31 - 55$ (blue dash-dotted line) and $J = 36 - 80$ (green short dash line) DCS for the $\Delta j = 8$ transition (top left panel). The incoherent DCS (red dashed line) barely recovers the full DCS (top right panel). If the DCS is calculated for subsets of J, their incoherent sum approximates well the full DCS (bottom panels). All calculations were carried out at a collision energy of 66 meV.

between adjacent partial waves is important which is illustrated by Figure 4.14.

4.4 Comparison of the C-HEHS, QCT and averaged CC QM Differential cross sections

Finally it is helpful to compare the C-HEHS, quasi-classical trajectory and averaged close coupled quantum mechanical (CC QM) differential cross sections obtained on the unmodified potentials. Doing this once again provides insight into what ways the full classical potential and the quantum effects manifest themselves in the collision dynamics. The QCT and averaged CC QM DCSs are greater than the C-HEHS ones for low Δj as shown in the top left panel of Figure 4.15. This is due to the attractive forces which are responsible for the deflective collision, which in turn have a considerable contribution to the total inelastic collisions [44]. As Δj increases the various DCSs become more similar with respect to their magnitude, which reflects the fact the collision dynamics is increasingly dominated by the

repulsive forces. For $\Delta j = 14$ and above the C-HEHS DCSs are bigger than the QCT and averaged CC QM ones. The classically forbidden region is reduced towards smaller scattering angles for the QCT DCSs when compared to the impulsive model. This is due to the attractive and soft repulsive features of the potential which allow sufficient linear momentum to be transferred at lower scattering angles. The QCT DCS has two maxima for $\Delta j = 3$. The one at the smaller scattering angles is caused by the attractive forces. Although the QCT DCSs exhibit a weak doubled peaked structure, especially for high Δj, as shown in the bottom row of Figure 4.15, they are generally single peaked for the medium Δj, transitions,[44, 126].

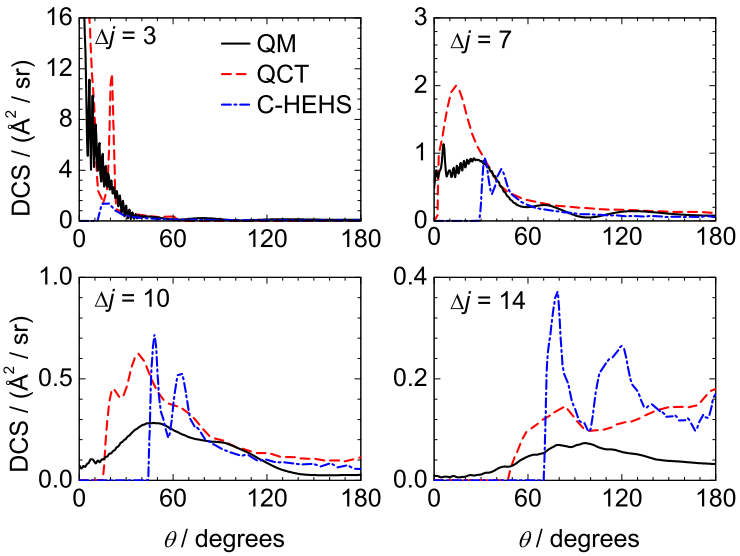

Figure 4.15: The averaged CC QM (black solid line), QCT (red dashed line) and C-HEHS (blue dash–dot line) DCSs for the $\Delta j = 3, 7, 10$ and 14 transitions are shown in the top left and right and bottom left, right panels, respectively. All the data were obtained at a collision energy of 66 meV.

At low Δj, the forward scattered part of the averaged CC QM DCSs are characterised by rapid oscillations which arise from quantum interference effects, [134] which are absent from both the C-HEHS and QCT data. The agreement between the averaged CC QM and QCT DCSs is reasonably good as discussed previously [44, 110]. As for the rotational alignment, it is thus might be expected that the full potential has the most distorting effect on the pure C-HEHS collision mechanism at low j' final states. On the other hand,

less perturbation might be brought about by the attractive and soft features of the full potential if Δj is high. It is also inferred that the QCT results in general are closer to the averaged QM ones for every final state.

4.5 Summary

The theoretical methods adapted and developed as a part of this work were reviewed in this chapter. These were the modification of coupled potential energy surfaces, and exact quantum mechanical hard shell calculations. The resultant opacity functions and differential cross sections were characterised and compared. This enabled us to ascertain what role the different parts of the interaction potential play in the collisions. The removal of the attractive part of the V_{sum} potential drastically changes the angular dependence of the scattering probability, especially at low Δj transitions. Calculations using a purely repulsive soft potential and the infinitely repulsive hard shell potential helped to discern between effects arising from the finite range and hard shell repulsion.

Chapter 5

Theoretical study of the rotational alignment effects in the inelastic collisions of NO(X) and Ar

In this chapter, the rotational angular momentum alignment effects are investigated for the rotationally inelastic collisions of NO(X) and Ar. The theoretical background including the relevant physical quantities and the methods applied here have been introduced in Chapters 2, 3 and 4.

A hierarchy of theoretical models of increasing complexity has been employed in order to ascertain the origin of the various features of the rotational alignment. In the classical Monte Carlo hard shell calculations, the full interaction potential is replaced by a hard shell potential. As such, it only reproduces those effects which arise from a purely impulsive classical mechanism. The quasi-classical trajectory calculations assume that the system is governed by classical attractive and soft repulsive forces. Results from this model provide a basis for comparison to those from the exact close coupled quantum mechanical calculations employing two adiabatic potential energy surfaces (PESs). It has been found that the rotational alignment is primarily due to a classical impulsive mechanism at a collision energy of 66 meV, which is roughly equal to the collision energy of the experiments presented in this thesis. However, at lower collision energies the attractive part of the interaction potential plays an important role in governing the alignment dynamics.

The quantum mechanical rotational alignment in the collisions of hard shells is also presented and investigated for the first time.

5.1 Overview

Much of the theoretical work on the inelastic collisions of NO(X)–Ar has been directed towards the investigation of the integral cross sections and differential cross sections. Accurate potential energy surfaces have been constructed [102, 104], on which exact scattering calculations have been carried out. It has been found that the integral cross sections (ICSs) exhibit parity dependent oscillations, such that the magnitude of the ICSs for parity conserving transitions are, in general, greater than those belonging to parity changing collisions [102], where the parity of the NO(X) molecule is defined as $p = (-1)^{j-\epsilon/2}$ according to [57]. This stems from the parity dependence of the modulus of the potential, or equivalently, coupling matrix elements [9, 98]. The structure of the fully state resolved differential cross sections (DCSs) depends on the parity conserving or changing nature of the transitions [66, 134, 142]. This phenomenon was rationalised as an interference effect between the matter waves scattered from different parts of the interaction potential [134].

The number of studies addressing the rotational polarisation, or alignment effects is markedly smaller. The kinematic apse, $\hat{\boldsymbol{a}}$, will be a central quantity in the further discussion [22]. It is defined as the unit momentum transfer vector:

$$\hat{\boldsymbol{a}} = \frac{\boldsymbol{p'} - \boldsymbol{p}}{|\boldsymbol{p'} - \boldsymbol{p}|}\,, \tag{5.1}$$

where $\boldsymbol{p}$ and $\boldsymbol{p'}$ are the initial and final relative momenta, respectively. In the case of non-reactive collisions, $\boldsymbol{p}$ and $\boldsymbol{p'}$ can be substituted by the initial, $\boldsymbol{k}$, and final relative velocities, $\boldsymbol{k'}$. In the case of sudden collisions, where the molecular axis is unchanged during the course of the interaction, the projections of the initial and final rotational angular momenta, $\boldsymbol{j}$ and $\boldsymbol{j'}$, onto the kinematic apse are equal [23, 143]. This condition is rigorously satisfied in the classical collisions between rigid shells [23, 143]. This conservation law will

serve as a basis for the kinematic apse model (AM) [24]. The geometric apse is defined as

$$\hat{\boldsymbol{a}} = \hat{\boldsymbol{p}}' - \hat{\boldsymbol{p}}\,, \tag{5.2}$$

which is equivalent to the kinematic apse in the case of elastic collisions [64, 144]. The kinematic apse model has been used to correct experimental ion-images for collision induced alignment effects [66, 134, 145], though its applicability has not been rigourously tested. Alexander *et al.* investigated the propensity rules of conservation of the apse frame magnetic level population. His calculations involved a small basis set and the reduced mass of the system was somewhat smaller than the exact value. It was concluded that the apse frame population is only conserved at the backward scattered region, based on coupled states calculations at a collision energy of 35 meV [144]. Aoiz *et al.* investigated the rotational polarisation effects by means of quasi-classical trajectory (QCT) calculations [44]. The role of the correlation between the orbital angular momentum and the rotational angular momentum was found to be a key factor in the polarisation dynamics. They extended the definition of chattering or secondary [116] collisions where the final rotational state is lower than the maximum achieved during the course of the collision due to a prolonged interaction time. These collisions tend to reduce the degree of rotational polarisation [44].

More recently Lemeshko *et. al.* [146, 147] extended the molecular Fraunhofer model of Faubel [148] to handle collisions of open shell molecules with structureless atoms. The Fraunhofer model treats the collision as diffraction of matter waves from an impenetrable object. As such, it is an inherently hard shell description. It is also an infinite order sudden approximation, therefore it is expected that it gives more accurate results for lower final j' states [146]. According to this model, the rapid oscillations of the renormalised PDDCSs originate from diffraction effects in the forward scattered region [147, 149]. The phase of the oscillations are accurately captured, especially at very low scattering angles. At higher scattering angles, it seems to slightly overestimate the amplitude of the oscillations of the renormalised PDDCSs. However, this model is only applicable for forward scattering to

low j' final states.

Most recently, Jambrina *et al.* have analysed the rotational polarisation effects in terms of a canonical scattering mechanism [150], though their main interest laid in uncovering the origin of the rotational orientation. In their description, the overall polarisation is a result of a balance between $1 \min(j, j') + 1$ orthogonal collision mechanisms which lead to different elementary polarisations [150].

Chandler *et al.* experimentally determined the rotational alignment resolved in final Λ-doublet levels [19] at a mean collision energy of 66 meV, results of which will be discussed in Chaper 7. The results of their measurements were compared to those from simple hard ellipse calculations and found to be in relatively good agreement. However, it might be worth noting it is perhaps unclear whether they employed a 2D or a 3D model. Also the axes of the ellipse are given as 2.63 Å, and 3.5 Å, and these data should refer to the semiaxes of the employed model instead.

Meyer *et al.* calculated the geometric apse model and kinematic apse model $k = 2$, $q = 0$ scattering angle dependent polarisation parameter for the NO(X)+Ne system at a collision energy of 131 meV [24]. They were subsequently compared to their experimental results and a good agreement was found[24, 151]. Marinakis [25] presented the full state resolved alignment CC QM renormalised PDDCSs for the NO(X)–Kr collisions at a collision energy of 500 meV. The theoretical data showed a slight dependence on the parity conserving/changing nature of the collisions.

5.2 Classical hard shell calculations

The NO(X)–Ar system can be described by two potential energy surfaces (PESs)[102] according to Eq. (2.12) and as shown in Figure 2.2. The spin–orbit conserving transitions primarily sample the V_{sum} PES, whilst the spin–orbit changing transitions occur on the V_{dif} PES in the Hund's case (a) limit.

A general transition of the NO(X) molecule is represented by Eq. (5.3),

$$|j, \Omega, \epsilon\rangle \rightarrow |j', \Omega', \epsilon'\rangle \,, \tag{5.3}$$

where j is the rotational angular momentum, Ω denotes the spin–orbit manifold, and the Λ-doublet level is referred to by ϵ. The primed symbols represent quantities in the final state. The spin–orbit manifolds and the Λ-doublet levels are undefined in classical mechanics, and they cannot even approximately be taken into account when dealing with molecules with Hund's case (a) coupling. Therefore the quasi-classical and classical hard shell calculations are carried out using the V_{sum} potential energy surface. Whilst the V_{diff} surface is attractive, the V_{sum} surface is strongly repulsive. It has a slightly asymmetric, $C_{\infty v}$, shape and an attractive well with a depth of $110\,\text{cm}^{-1}$.

It is thus expected that the repulsive forces play a substantial role in the collision dynamics. In order to test to what extent the collision can be described by a purely impulsive mechanism, the full V_{sum} PES was replaced by a hard shell potential, inside of which the potential is infinite, whilst outside it is zero. The exact shape of the shell was obtained by taking the contour of the V_{sum} PES at the actual collision energy. Two types of classical hard shell calculations were carried out as described in Section 4.1. In the case of classical homonuclear hard shell calculations (C-HOHS), the odd expansion coefficients were set to zero in Eq. 4.4 thus the potential had $D_{\infty h}$ symmetry, corresponding to a homonuclear molecule. In the case of the classical heteronuclear hard shell (C-HEHS) calculations, the odd expansion coefficients were not excluded, resulting in an egg-shaped, $C_{\infty v}$, potential. The kinematic and dynamical properties of the collision system were calculated as described in Section 2.2.1.

5.2.1 Alignment in classical hard shell collisions

The rotational alignment in the collisions of a classical hard shell is entirely determined by the fact that the projection of the rotational angular momentum onto the kinematic apse

has to be conserved. It is thus useful to introduce the so-called apse frame. Its principal axis, $\hat{\boldsymbol{z}}_{\mathrm{a}}$, is parallel to the kinematic apse. Its second axis, $\hat{\boldsymbol{y}}_{\mathrm{a}}$, is parallel to that of the scattering frame, $\hat{\boldsymbol{y}}$. The first axis, $\hat{\boldsymbol{x}}_{\mathrm{a}}$ is chosen so that the apse frame is right handed. The apse angle is the angle between $\hat{\boldsymbol{a}}$ and $\boldsymbol{k}$ and is denoted by β. The two frames are related by a rotation by an angle of $-\beta$ about the $\hat{\boldsymbol{y}}$ axis. Since only initially non-rotating molecules will be considered, the initial rotational angular momentum is zero, so must have zero projection onto the kinematic apse. The final rotational angular momentum, $\boldsymbol{j'}$, should also have zero projection onto the kinematic apse, and therefore should be perfectly perpendicular to the the kinematic apse irrespective of scattering angle and final state. The apse frame polarisation moment, $a_0^{\{2\}\mathrm{a}}$, and renormalised PDDCSs $\rho_0^{\{2\}\mathrm{a}}(\theta)$, take their lower limiting value of -0.5. Since $\boldsymbol{j'}$ is perpendicular to $\hat{\boldsymbol{a}}$ it cannot be aligned with respect to $\hat{\boldsymbol{z}}_{\mathrm{a}} + \hat{\boldsymbol{x}}_{\mathrm{a}}$ or $\hat{\boldsymbol{z}}_{\mathrm{a}} - \hat{\boldsymbol{x}}_{\mathrm{a}}$, therefore $\rho_{1+}^{\{2\}}(\theta)$ vanishes in the apse frame. $\boldsymbol{j'}$ can be aligned with respect to the $\hat{\boldsymbol{x}}_{\mathrm{a}}$ or the $\hat{\boldsymbol{y}}_{\mathrm{a}}$ axis in a single collision. The degree of alignment depends on the relative orientation of the point-of-contact, $\boldsymbol{R}$, the surface normal, $\hat{\boldsymbol{a}}$, and the initial relative velocity, $\boldsymbol{k}$. However, since the system is cylindrically symmetric with respect to the surface normal, the $a_{2+}^{\{2\}\mathrm{a}}$ moment and the corresponding renormalised PDDCSs, $\rho_{2+}^{\{2\}\mathrm{a}}(\theta)$, vanish, if every geometry is sampled with equal weight, which is the case in a classical hard shell calculation. In summary, there is only one non-zero apse frame alignment moment and renormalised PDDCSs, namely $a_0^{\{2\}\mathrm{a}}$ and $\rho_0^{\{2\}\mathrm{a}}(\theta)$ in the case of classical hard shell collisions.

Despite the apse frame $\rho_{q\pm}^{\{2\}}$-s being constants, the scattering frame C-HEHS $\rho_{q\pm}^{\{2\}}$-s vary considerably as a function of the scattering angle as seen in Figure 5.1, which can be explained as follows.

The $\rho_0^{\{2\}}(\theta)$ renormalised PDDCS should take its lower limiting value at perfectly forward and backward scattered angles. If the initial and final relative velocities are aligned parallel, j' has to be aligned perpendicular to both vectors, since $\boldsymbol{j'} = \Delta\boldsymbol{j} = \boldsymbol{\ell'} - \boldsymbol{\ell}$, where $\boldsymbol{\ell}$ and $\boldsymbol{\ell'}$ are the initial and final orbital angular momenta which are always perpendicular to $\boldsymbol{k}$ and $\boldsymbol{k'}$, respectively. This criterion is equivalent to requiring that $\boldsymbol{j'}$ is perpendicular

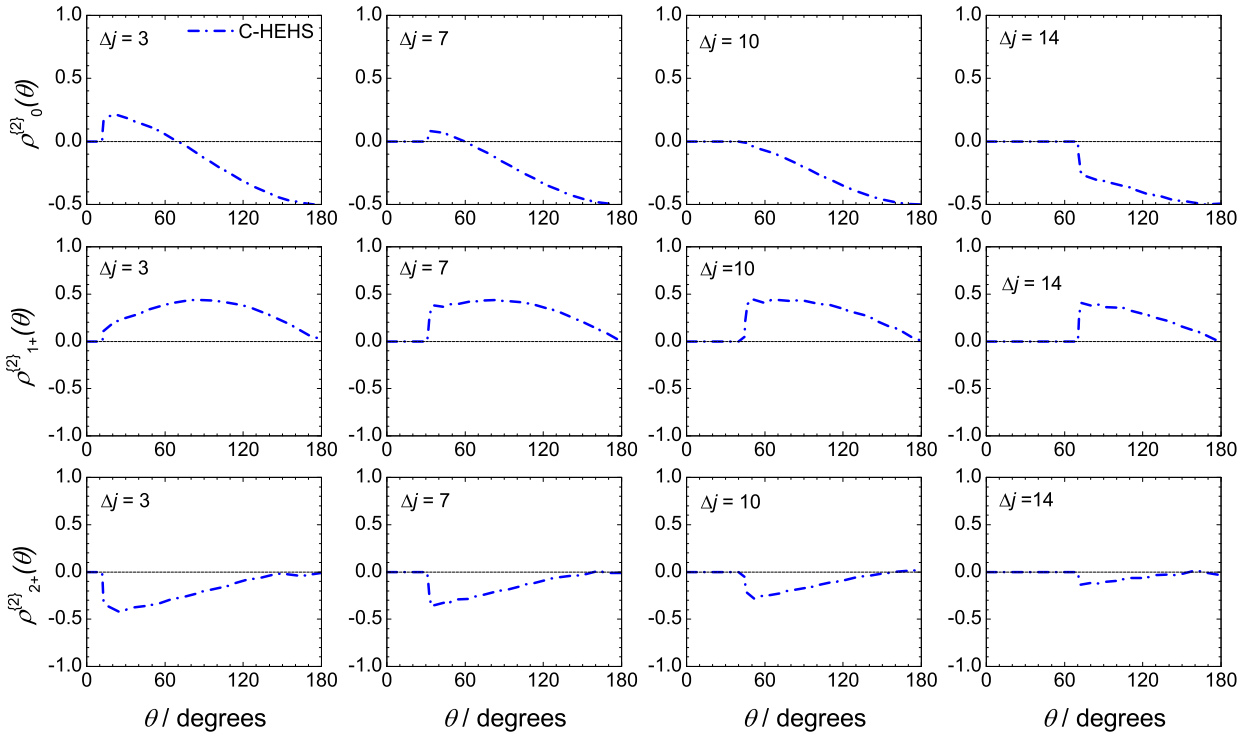

Figure 5.1: C-HEHS (blue dash–dot line) alignment, $\rho_{q\pm}^{\{2\}}(\theta)$, PDDCSs $q = 0$ (top row), $q = 1$ (middle row), $q = 2$ (bottom row), for the $\Delta j = 3, 7, 10$, and 14 from left to right, respectively. All the data were obtained at a collision energy of 66 meV.

to the kinematic apse, which is parallel to the initial relative velocity, when $\theta = 0°$ or $\theta = 180°$.

The $\rho_0^{\{2\}}(\theta)$ renormalised PDDCS exhibits a general decreasing trend as a function of the scattering angle for all Δj transitions. It reaches its lower limiting value at $\theta = 180°$. For low j' final states, it is positive at small scattering angles. As j' increases, the classically forbidden region gradually extends toward bigger scattering angles, thus C-HEHS alignment information on the forward scattered molecules is fully lost and it is partially hidden for sideways scattered products. As a consequence, the behaviour of the backward scattered products can only be investigated. Comparing, the renormalised PDDCSs in this scattering angle interval, it is noticeable that they become gradually more negative as Δj increases; taking value 0, -0.05, -0.1 and -0.3 at an angle about of 70° for $\Delta j = 3, 7, 10$ and 14, respectively. This can be explained as follows. The angle between

the kinematic apse and the relative velocity can take the smallest possible values, if only a small amount of energy is required by the transition. This angle will be the closest to 90° when the initial and final relative velocities make a small angle with each other, that is when the scattering angle is small. Because $\boldsymbol{j'}$ is aligned perpendicularly to the kinematic apse, it will be aligned roughly parallel to $\boldsymbol{k}$ in these cases making $\rho_0^{\{2\}}(\theta)$ positive. As the amount of the required energy increases, the minimum possible value of β increases, thus the maximum extent to which $\boldsymbol{j'}$ can be aligned parallel to $\boldsymbol{k}$ decreases. In addition, the angle at which $\boldsymbol{j'}$ is the least perpendicular to $\boldsymbol{k}$ is shifted towards bigger scattering angles.

Based on Meyer [24] the following relationship can be worked out between the scattering angle and the apse angle:

$$\cos\beta = \frac{D - \cos(\theta)}{\sqrt{D^2 + 1 - 2D\cos(\theta)}}\,, \tag{5.4}$$

where $D = (E_{\text{coll}} - \Delta E)/E_{\text{coll}}$. Differentiating Eq. (5.4) with respect to θ results in an expression for the scattering angle, θ_{a}, at which the apse angle, β_{a}, is minimal:

$$\cos(\theta_{\text{a}}) = D = \sqrt{1 + \frac{k^2 - k'^2}{k^2}} \tag{5.5}$$

$$\beta_{\text{a}} = -\sqrt{1 - D^2} = -\frac{\sqrt{k^2 - k'^2}}{k}\,. \tag{5.6}$$

It is also possible to obtain this result based on simple geometrical considerations as shown in Figure 5.2.

Let $\boldsymbol{k}$ point from O to I. $\boldsymbol{k'}$ is a vector drawn from point O to point F which always resides on circle f, because of the conservation of energy. The kinematic apse then points from I to F. The apse angle, β, is minimal, if the $\overline{IF}$ line is tangent to the circle f. Let us denote the kinematic apse with $\overline{IF'}$, which is not a tangent and is bigger than $\overline{IF}$, then $\gamma = 180° - \beta$ is smaller than β_{a} because of the cosine theorem. This also holds for the OIF'' triangle where, F'' is the other intersection of IF' with the f circle. $\overline{IF''}$ is shorter

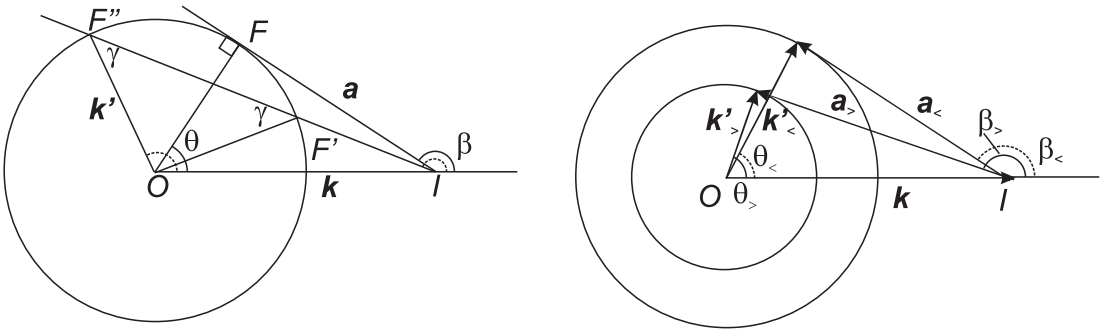

Figure 5.2: Newton diagrams of inelastic scattering. The apse angle, β, is minimal if the kinematic apse, $\overline{IF}$, makes a right angle with the final velocity, $\overline{OF}$ (left panel). Increasing rotational excitation increases the minimum of the apse angle (right panel).

than $\overline{IF}$ by the virtue of the cosine theorem, thus β indeed has a maximum when $\overline{IF}$ is a tangent to f. Since the angle that $\overline{IF}$ makes with $\overline{OF}$ is a right angle, the cosine of β_{a} is given by:

$$\cos\beta_{\mathrm{a}} = -\frac{\overline{IF}}{\overline{IO}} = -\frac{\sqrt{k^2 - k'^2}}{k} \tag{5.7}$$

From Eqs. (5.5)–(5.6), the previous qualitative arguments regarding the behaviour of β_{a} are readily justified. The behaviour of the apse angle as a function of the scattering angle is shown in the left panel of Figure 5.3. The explicit rotation formulae used to transform the apse frame renormalised PDDCSs to the scattering frame will be provided in Section 5.3.2, though some general observations can now be made. Since β_{a} changes inversely with Δj, the maximum extent of $\boldsymbol{j'}$ being aligned parallel to $\boldsymbol{k}$ reduces with increasing Δj. The alignment has a maximum at β_{a}.

The $\rho_{1+}^{\{2\}}(\theta)$ renormalised PDDCS measures the alignment with respect to the $\hat{\boldsymbol{z}} + \hat{\boldsymbol{x}}$ and $\hat{\boldsymbol{z}} - \hat{\boldsymbol{x}}$ axes [11], as shown in the third panel of Figure 5.3. Since $\boldsymbol{j'}$ is perpendicular to $\hat{\boldsymbol{a}}$, and the apse angle is restricted to take values from the interval $[\pi/2, \pi]$, the C-HEHS $\rho_{1+}^{\{2\}}(\theta)$ renormalised PDDCS is always positive apart from the perfectly forward and backward scattered directions. Its variation is roughly the negative of that of the apse angle. However, it does not change monotonically with β, because the frame transformation is not a monotonic function of β.

Since $\hat{\boldsymbol{a}}$ is confined in the xz plane, the distribution of $\boldsymbol{j'}$ is shrunk along the $\hat{\boldsymbol{x}}$ axis, if it is looked at from the $+\hat{\boldsymbol{z}}$ direction. In other words, the projection of $\boldsymbol{j'}$-s onto the xy

plane is always reduced in the x direction, so that $\boldsymbol{j'}$ is aligned with respect to the $\hat{\boldsymbol{y}}$ axis, as illustrated in the fourth panel of Figure 5.3. Thus the C-HEHS $\rho_{2+}^{\{2\}}(\theta)$ renormalised PDDCS is always negative except for $\theta = 0°$ and $\theta = 180°$. Roughly speaking, the bigger the apse angle, the more $\boldsymbol{j'}$ is aligned along $\hat{\boldsymbol{y}}$. However, the exact relationship between β and $\rho_{2+}^{\{2\}}(\theta)$ is again determined by the transformation formulae.

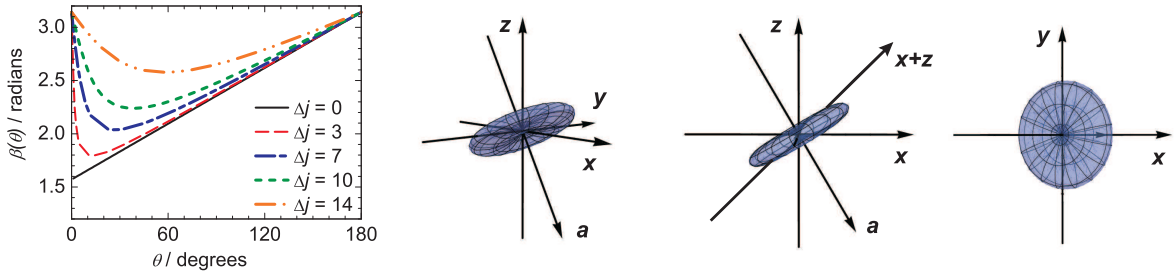

Figure 5.3: The apse angle, $\beta(\theta)$, for the $\Delta j = 0, 3, 7, 10$ and 14 transitions are represented by the black solid, red dashed, blue dash-dot, green dotted, orange dash-dot-dot lines, respectively. In panels 2–4, the minimum uncertainty distributions are shown for the $\Delta j = 3$ transition using full expansion according to Eq. (3.73) at the scattering angle of 90°.

It is now possible to conclude that the scattering frame structure of the renormalised PDDCSs stems from the fact that the projection of $\boldsymbol{j'}$ onto $\hat{\boldsymbol{a}}$ should be conserved, thus it reflects the transformation from the apse frame to the scattering frame, which will be exactly shown in Section 5.3.2.

5.2.2 Comparison of QM, quasi-classical trajectory and C-HEHS alignment renormalised PDDCSs

The effects of attractive and soft repulsive features of the potential on the rotational alignment are examined in this section. The inclusion of these forces is expected to complicate the simple hard shell collision dynamics. In addition, the averaged quantum mechanical results are presented in order to ascertain exactly how the quantum mechanical effects manifest themselves in rotational alignment phenomena. The C-HEHS, QCT and averaged CC QM alignment renormalised PDDCSs are shown in Figure 5.4 for the $\Delta j = 3, 7, 10$ and 14 transitions at a collision energy of 66 meV. The three sets of data are, in general,

in good agreement for all of the states. The deviation between the C-HEHS and QCT renormalised PDDCSs is the most pronounced at small scattering angles for low Δj transitions, as illustrated by the top left panel of Figure 5.4. However, the C-HEHS and QCT renormalised PDDCSs agree well at higher scattering angles, and the full potential appears to only add a perturbation to the hard shell data. For highly excited states, the C-HEHS and QCT second rank renormalised PDDCSs coincide, especially at larger scattering angles. In these cases, the Ar atom has to penetrate to the hard core of the potential, which results in collision dynamics similar to that of pure classical hard shells.

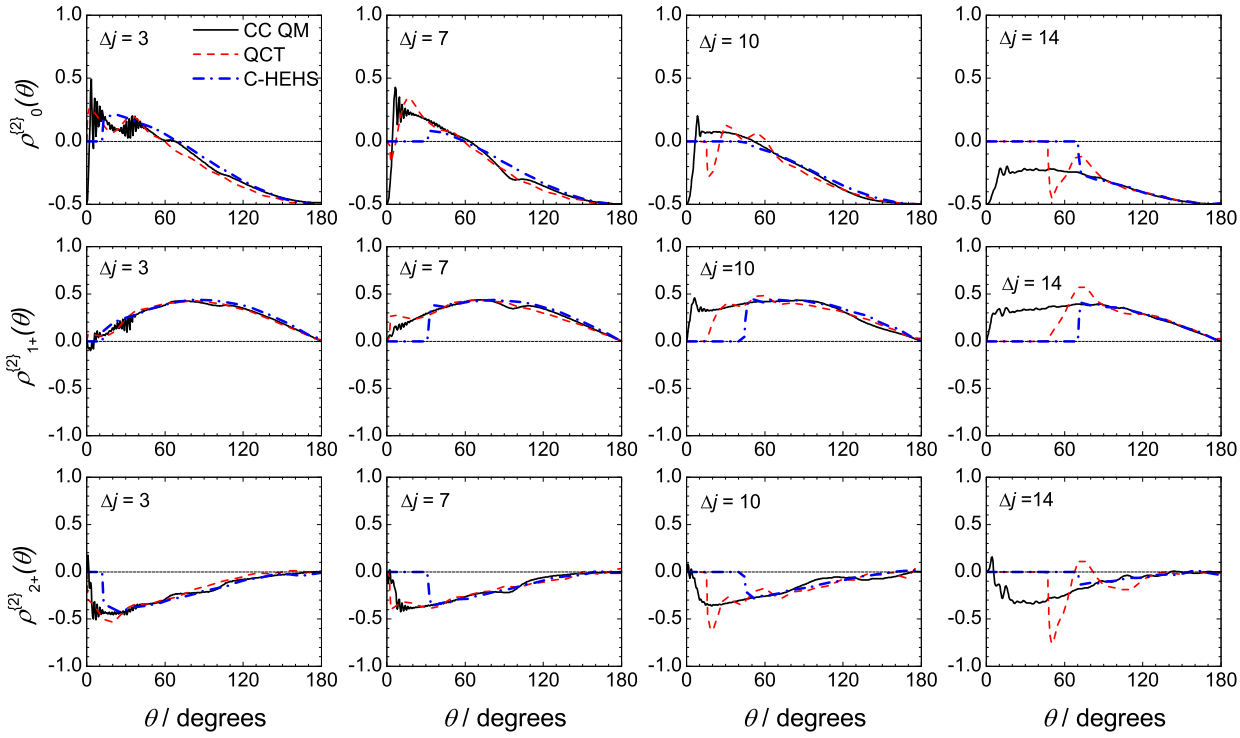

Figure 5.4: The averaged CC QM (black solid line), QCT (red dashed line) and C-HEHS (blue dash–dot line) alignment, $\rho^{\{2\}}_{q\pm}(\theta)$, PDDCSs $q = 0$ (top row), $q = 1$ (middle row), $q = 2$ (bottom row), for the $\Delta j = 3, 7, 10$ and 14 transitions from left to right, respectively. All the data were obtained at a collision energy of 66 meV.

The second rank averaged quantum mechanical renormalised PDDCSs are in remarkably good agreement with their QCT and the C-HEHS counterparts in the classically allowed region. The agreement is especially good between the QCT and the averaged CC

QM parameters, even in the forward scattered region for low Δj transitions. For instance, the averaged CC QM $\rho_0^{\{2\}}(\theta)$ and $\rho_{1+}^{\{2\}}(\theta)$ also have local minima between $\theta = 10^\circ$ and $\theta = 30^\circ$ with which the QCT $\rho_0^{\{2\}}(\theta)$ coincides. However, the quantum mechanical $\rho_{2+}^{\{2\}}(\theta)$ does not indicate an increase of the alignment between these angles. The finer details of the QM renormalised PDDCSs are not captured by either the classical hard shell or the QCT model, including fast oscillations in the forward scattered region. However, the renormalised PDDCSs obtained from both classical models reproduce the general characteristics of the data from the exact quantum mechanical calculations. Thus the underlying dynamics responsible for the rotational alignment is inherently classical at a collision energy of 66 meV.

5.2.3 Λ-doublet resolved quantum mechanical renormalised PDDCSs

The quantum mechanical renormalised PDDCSs shown so far were averaged over the initial and summed over the final Λ-doublet levels. Therefore, information was lost on how these quantities depend on the parity conserving or changing nature of the transitions. The $|j, 0.5, -1\rangle \rightarrow |j', 0.5, -1\rangle$ and $|j, 0.5, -1\rangle \rightarrow |j', 0.5, +1\rangle$ DCSs and alignment renormalised PDDCSs are shown in Figure 5.5 for the final states, $j' = 3.5, 7.5, 10.5$ and 14.5. The structure of the DCSs strongly depends on the final parity as illustrated in the top row of Figure 5.5. This phenomenon has been extensively investigated [43, 104, 145]. The position and number of the maxima are determined by the interferences between the trajectories arising from different sides of the molecule [66, 142].

For low j' final states and small scattering angles, both the parity changing and parity conserving QM PDDCSs exhibit rapid oscillations. As j' increases, the oscillations vanish more quickly and their amplitude is reduced. This fine structure was shown to be due to an interference effect well described by the Fraunhofer model [105, 147]. Parity dependent undulations can be observed at higher scattering angles. For instance, there is a sudden drop followed by a rise in the parity changing, $|0.5, 0.5, -1\rangle \rightarrow |3.5, 0.5, -1\rangle$, renormalised

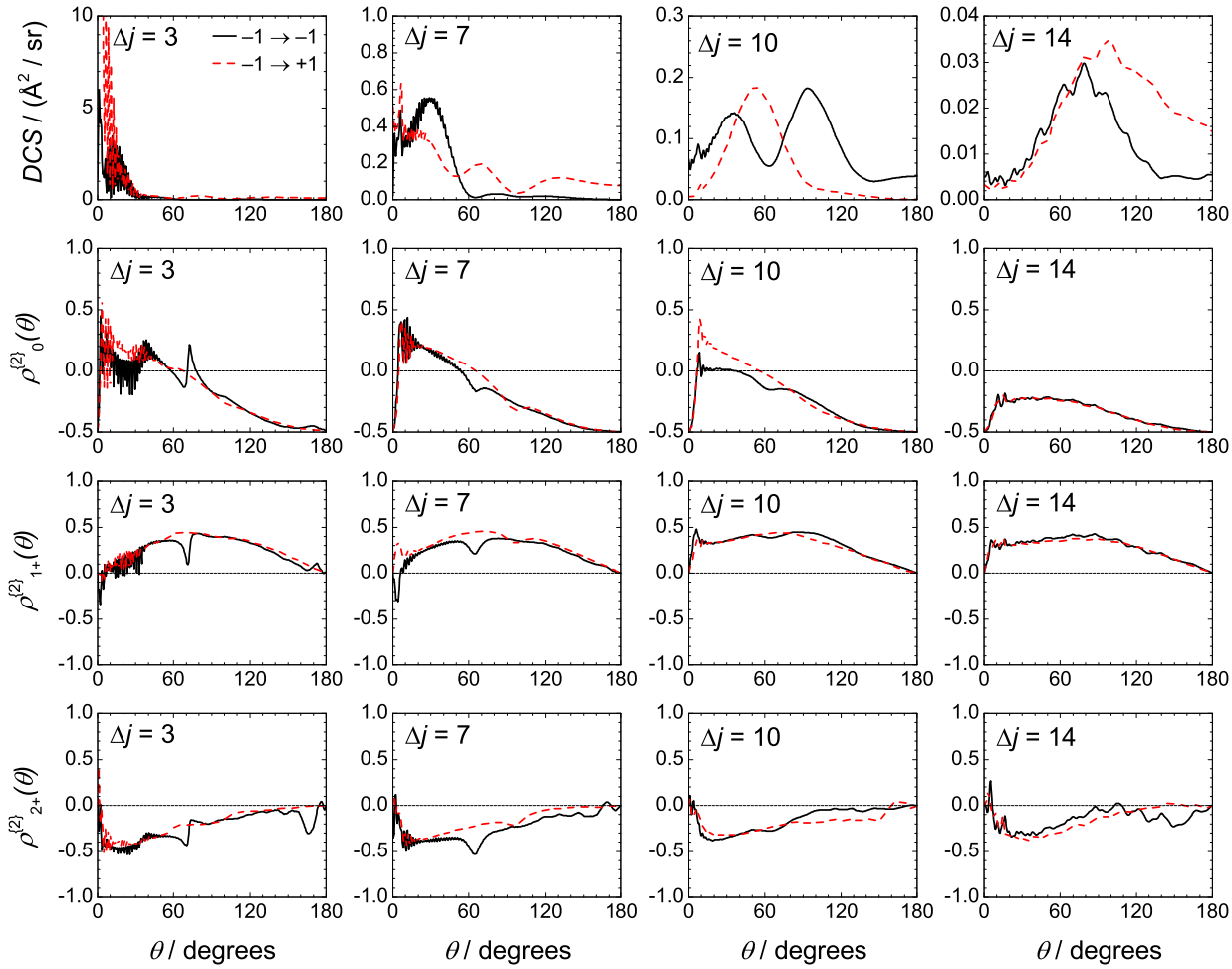

Figure 5.5: The CC QM DCSs (top row) alignment, $\rho^{\{2\}}_{q\pm}(\theta)$, PDDCSs. $q = 0$ (2nd row), $q = 1$ (3rd row), $q = 2$ (bottom row), for the $|0.5, 0.5, -1\rangle \rightarrow |j', 0.5, \epsilon' \rightarrow j' = 3, 7, 10$ and 14 from left to right, respectively. $\epsilon' = -1$: black solid line, $\epsilon' = +1$: red dashed line. All the data were obtained at a collision energy of 66 meV.

PDDCSs between the scattering angles 60° and 80° and at the very backward scattered region between 160° and 180°. The most emphasised deviation between the $|3.5, 0.5, -1\rangle$ and $|3.5, 0.5, +1\rangle$ renormalised PDDCSs can be oberved in the forward scattered region, where the classical attractive forces are dominant. The parity changing renormalised PDDCSs indicate less parallel, or slightly perpendicular alignment of $\boldsymbol{j'}$ to $\boldsymbol{k}$. Besides these points of disagreement, the parity changing and conserving data have overall identical trends. The difference between the renormalised PDDCSs is even smaller for high j' final states. The parity dependent undulations are gradually reduced as illustrated by

the 2nd–4th panels in the middle column of Figure 5.5. The parity changing and parity conserving renormalised PDDCSs are nearly identical at backward scattered angles, when the rotational excitation is high, *e.g.* for $j' = 14$, as seen in the right column of Figure 5.5. However, it is worth pointing out the $\rho_{2+}^{\{2\}}(\theta)$ renormalised PDDCSs deviate to a somewhat greater extent.

5.3 Comparison of C-HEHS, QCT and QM alignment moments

The second rank, or alignment polarisation moments measure the degree of the rotational alignment in the entire molecular ensemble. They are calculated as an integral of the renormalised PDDCSs, weighted with the scattering probability according to Eq. 3.7 over the entire scattering angle region. This is equivalent to the integral of the normalised PDDCSs. As such, the θ dependent information is lost. However, their value depends on the weight with which the renormalised PDDCSs linked to different mechanisms are represented. Thus, they are a measure of the balance of these mechanisms, and signify which one is the most dominant.

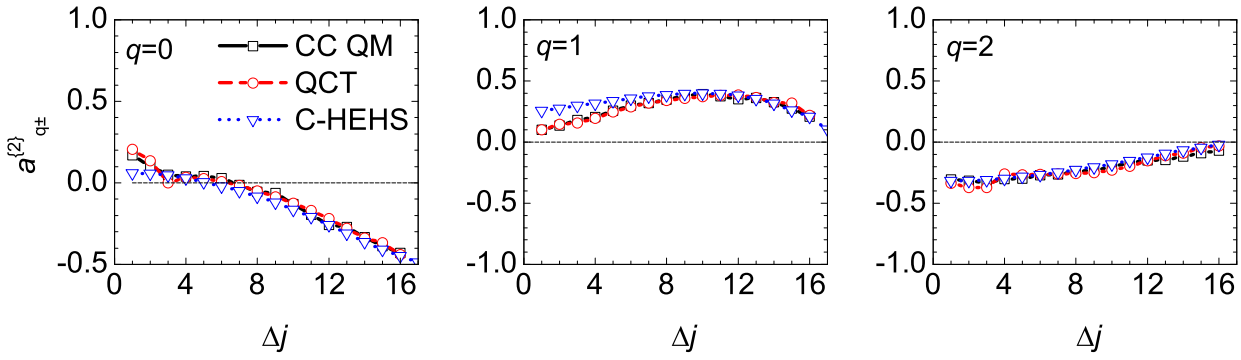

Figure 5.6: The scattering frame averaged CC QM (black open squares), QCT (red open circles) and C-HEHS (blue open triangles) alignment moments, $a_0^{\{2\}}$ (left panel), $a_{1+}^{\{2\}}$ (middle panel), $a_{2+}^{\{2\}}$ (right panel). All the data were obtained at a collision energy of 66 meV.

The averaged CC QM, QCT and C-HEHS alignment moments are shown in Figure 5.6. The general trend of the alignment parameters mirrors that of the corresponding renormalised PDDCSs as function of Δj. This phenomenon stems from the fact that the differential cross sections gradually change from forward to backward scattered as Δj increases. As a consequence, the more backward scattered portions of the renormalised PDDCSs are sampled with greater weight, making a bigger contribution to the final value of the moments.

The $a_0^{\{2\}}$ moment first becomes less positive, then more negative as Δj increases. For low Δj transitions, the moments take a value of around $+0.15$, which indicates slight parallel alignment of $\boldsymbol{j'}$ to the initial relative velocity in the classical case. In the quantum mechanical case $\boldsymbol{j'}$ is slightly more strongly polarised, since the upper limiting value of the QM $a_0^{\{2\}}$ is about $+0.45$ for $j' = 1.5$. This moment gradually approaches its lower limiting value of about -0.5 as Δj increases, which reflects stronger perpendicular alignment of $\boldsymbol{j'}$ with respect to $\boldsymbol{k}$. The $a_{1+}^{\{2\}}$ moment is always positive, revealing that the final rotational angular momentum is preferably aligned parallel to the $\hat{\boldsymbol{x}} + \hat{\boldsymbol{z}}$ axis, especially in the case of medium rotational excitation. On the other hand, the alignment with respect to the $\hat{\boldsymbol{x}}$ or $\hat{\boldsymbol{y}}$ axes, embodied in the $a_{2+}^{\{2\}}$ moments, diminishes as Δj increases. For low Δj transitions, there is a propensity for $\boldsymbol{j'}$ being aligned parallel to the $\hat{\boldsymbol{y}}$ axis as shown by the value of this moment of about -0.4, which approaches zero as Δj increases.

The agreement between the averaged QM and QCT data is remarkable for all final states [44]. The differences between these and the C-HEHS polarisation alignment moments are the most pronounced for the low Δj transitions. The three sets of data almost coincide for $\Delta j \geq 4$. The C-HEHS $a_{1+}^{\{2\}}$ moments deviate the most from their QM and QCT counterparts, especially when $\Delta j < 8$. Both the $a_0^{\{2\}}$ and $a_{2+}^{\{2\}}$ moments agree better with those obtained from calculations using full potentials. More pronounced differences between the C-HEHS and the QM, QCT $a_0^{\{2\}}$ moments can only be observed for $\Delta j = 1, 2$ and 3, where the presence of the attractive forces has previously been found to be important.

The exact effect of the attractive forces can be determined by performing calculations on the soft potentials. The attractive features of the $V_{\rm sum}(R,\gamma)$ PES were excluded according to Eq (4.12), so that it is purely repulsive. In addition, $V_{\rm dif}(R,\gamma)$ was scaled according to Eq. (4.13) in the QM case in order to maintain the relationship in Eq. (2.12) between the two potentials.

The agreement between the three sets of data is even better than that obtained on the unmodified potentials. The 'soft' QM, QCT and the C-HEHS data nearly coincide for low j' final states as shown by Figure 5.7, which reaffirms that attraction only plays a major role at low rotational excitation. This reinforces the fact that the dynamics responsible for the rotational alignment are mainly classical.

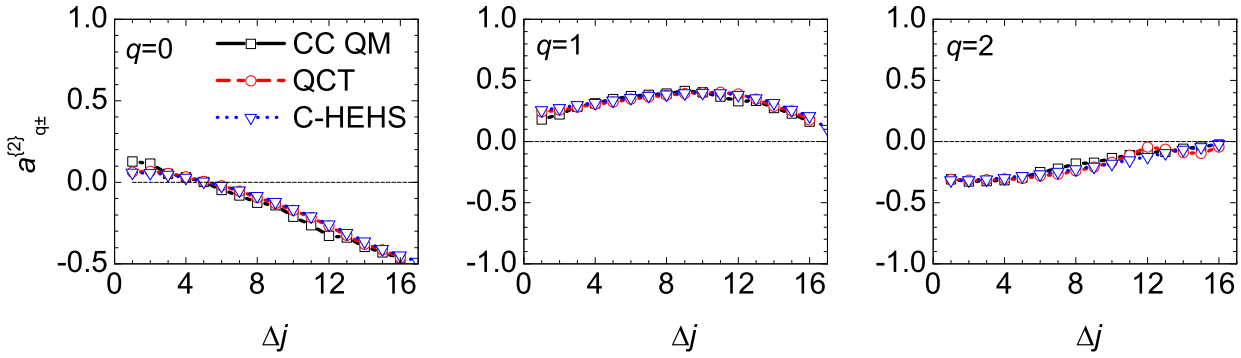

Figure 5.7: The scattering frame averaged CC QM (black open squares), QCT (red open circles) and C-HEHS (blue open triangles) alignment moments, $a_0^{\{2\}}$ (left panel), $a_{1+}^{\{2\}}$ (middle panel), $a_{2+}^{\{2\}}$ (right panel). The CC QM and QCT moments were calculated employing soft potentials defined in Chapter 4. All the data were obtained at a collision energy of 66 meV.

5.3.1 Λ-doublet resolved and hybrid QCT–QM alignment polarisation moments

It has been shown above that the average quantum mechanical behaviour is well described in terms of classical, mainly impulsive, collision dynamics in the case of rotational alignment. The Λ-doublet averaged CC QM alignment renormalised PDDCSs and moments can

be almost exactly approximated by their C-HEHS, or more accurately QCT counterparts. However, the Λ-doublet resolved CC QM alignment moments exhibit parity dependent oscillations superimposed with the general trend as shown in Figure 5.8.

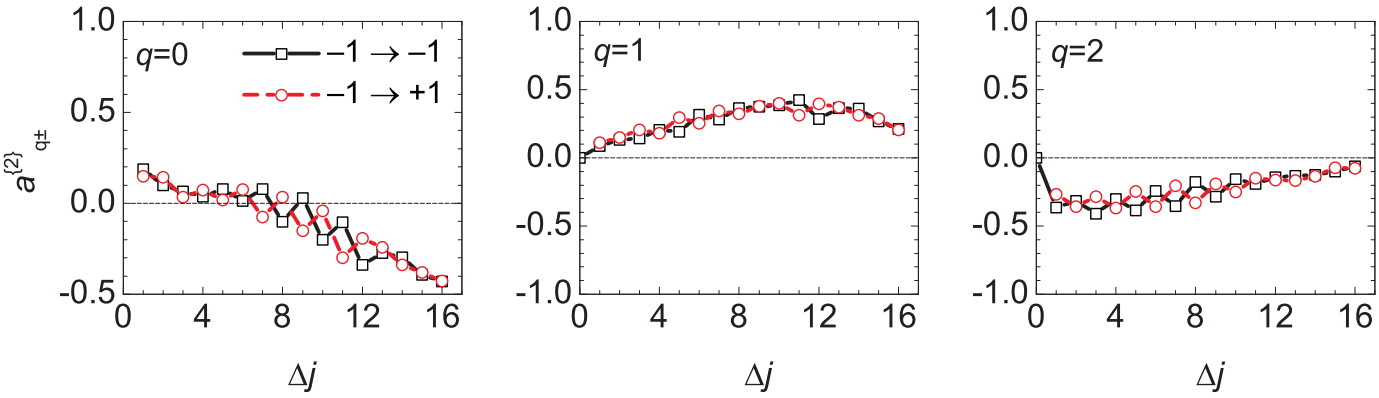

Figure 5.8: The scattering frame averaged CC QM alignment moments, $a_0^{\{2\}}$ (left panel), $a_{1+}^{\{2\}}$ (middle panel), $a_{2+}^{\{2\}}$ (right panel) for the $|0.5, 0.5-1\rangle \rightarrow |j', 0.5, \epsilon'\rangle$ transitions. The moments belonging to the $\epsilon' = -1$ and $\epsilon' = +1$ are marked by black open squares and red open circles, respectively. All the data were obtained at a collision energy of 66 meV.

The $a_0^{\{2\}}$ moments belonging to parity conserving transitions are more positive than the adjacent parity changing moments up to about $\Delta j = 12$. The trend is inverted for the $a_{1+}^{\{2\}}$ and $a_{2+}^{\{2\}}$ moments. For highly excited states, this pattern cannot be clearly observed. These oscillations are not recovered by the classical moments. The presence of the oscillations can either stem from the dependence of the polarisation on the parity as reflected by the renormalised PDDCSs in Figure 5.4 or arise from the differences in the CC QM DCSs belonging to parity conserving and changing transitions, or it can also be a result of both. In order to elucidate the nature of the oscillations it is insightful to introduce the QM–QCT hybrid polarisation moments according to Eq. (5.8):

$$a_{q\pm}^{\{k\},\mathrm{hyb.}}(j\Omega\epsilon \rightarrow j'\Omega'\epsilon') \equiv \int_{-1}^{1} \rho_{q\pm}^{\{k\}\mathrm{QCT}}(\theta; j-0.5 \rightarrow j'-0.5) \left[\frac{2\pi}{\sigma^{\mathrm{QM}}(j\Omega\epsilon \rightarrow j'\Omega'\epsilon')} \frac{\mathrm{d}\sigma^{\mathrm{QM}}(j\Omega\epsilon \rightarrow j'\Omega'\epsilon')}{\mathrm{d}\omega}\right] \mathrm{d}\cos(\theta)\,, \tag{5.8}$$

where the term in the square brackets is the QM DCS for the $|j, \Omega, \epsilon\rangle \rightarrow |j', \Omega', \epsilon'\rangle$ transition and $\rho_{q\pm}^{\{k\}\mathrm{QCT}}(\theta; j \rightarrow j)$ is the QCT renormalised PDDCSs for the $j \rightarrow j'$ transition.

Therefore, the $a_{q\pm}^{\{k\},\mathrm{hyb.}}(j\Omega\epsilon \rightarrow j'\Omega'\epsilon')$ hybrid polarisation moment characterises a hypothetical scattering experiment, where the scattering probability is fully determined by quantum mechanics and the alignment is purely classical.

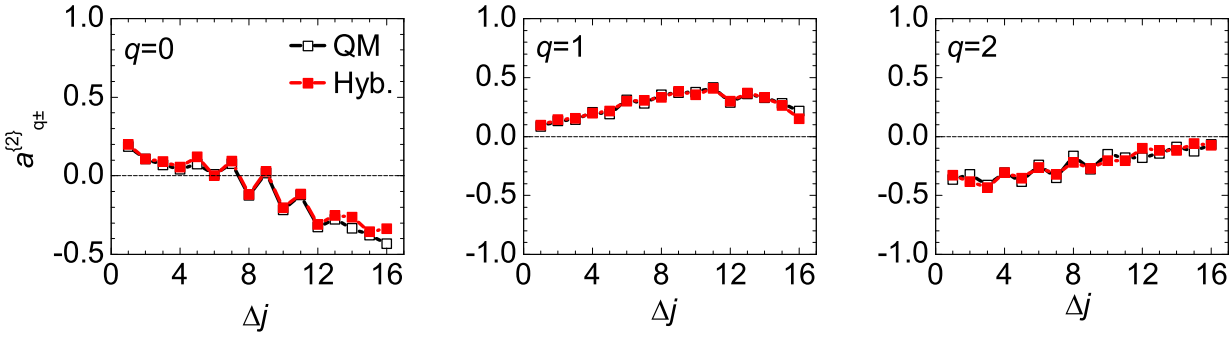

Figure 5.9: The scattering frame CC QM (black open squares) and hybrid (red closed squares) alignment moments, $a_0^{\{2\}}$ (left panel), $a_{1+}^{\{2\}}$ (middle panel), $a_{2+}^{\{2\}}$ (right panel) for the $|0.5, 0.5, -1\rangle \rightarrow |j', 0.5, -1\rangle$ transitions. All the data were obtained at a collision energy of 66 meV.

The QM–QCT hybrid alignment moments are compared to the exact CC QM ones for the $|0.5, 0.5, -1\rangle \rightarrow |j', 0.5, -1\rangle$ transitions in Figure 5.8. Both the general trend and the parity dependent oscillations of the quantum mechanical moments are recovered by the hybrid data. This implies that the dynamics responsible for the rotational alignment is essentially classical even at the quantum mechanical level of the Λ-doublet resolution. The origin of this agreement can be realised by comparing the QCT and QM renormalised and normalised PDDCSs. In the left panel of Figure 5.10 the QCT and CC QM spin–orbit conserving $-1 \rightarrow \pm 1$ renormalised PDDCSs are shown, for $\Delta j = 10$. The renormalised PDDCS for the parity changing transition is more positive than that for the parity conserving transition in the forward scattered region. They are essentially identical in the sideways and backward scattered regions. The QCT renormalised PDDCSs stay between the two CC QM ones and are roughly the average of them. The CC QM and QCT data are almost coincident at high scattering angles. Therefore the Λ-doublet level, or parity resolved renormalised PDDCSs can be well estimated by the quasi-classical ones.

By contrast, the shape of the CC QM DCSs, or equivalently the angular distribution functions depends greatly on whether the transition is parity conserving or parity changing

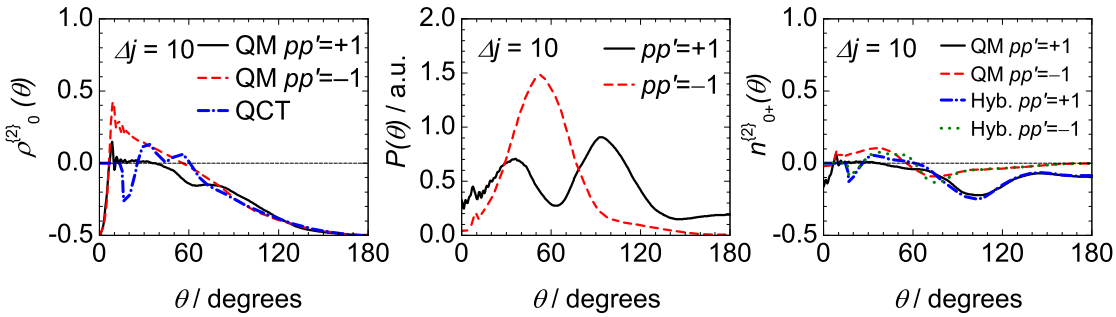

Figure 5.10: The scattering frame $|0.5, 0.5, -1\rangle \rightarrow |10.5, 0.5, -1/+1\rangle$ parity conserving (black solid line) and parity changing (red dashed line) CC QM and $|0\rangle \rightarrow |10\rangle$ (blue dotted line) QCT renormalised PDDCSs, $\rho_0^{\{2\}}(\theta)$, (left panel). The parity conserving (black solid line) and parity changing (red dashed line) angular distributions are shown in the middle panel. The corresponding parity conserving (black solid line) and parity changing (red dashed line) normalised PDDCSs, $n_0^{\{2\}}(\theta)$, and the hybrid normalised PDDCSs (blue dashed line and green dotted line) are shown in the right panel. All the data were obtained at a collision energy of 66 meV.

as shown in the second panel of Figure 5.10. The parity conserving ($\epsilon = -1 \rightarrow \epsilon' = -1$) DCS has two peaks whose maxima are at about 30° and 100°, whereas the parity changing DCS has a single maximum which is centered around 60° [66, 134, 142]. The normalised PDDCS, $n_{q\pm}^{\{2\}}(\theta)$, is the product of the renormalised PDDCS and the angular distribution function. The exact CC QM parity conserving and parity changing $n_{0\pm}^{\{2\}}(\theta)$-s are shown in the right panel of Figure 5.10, along with the QM–QCT hybrid normalised PDDCSs. They were calculated as a product of the QCT renormalised PDDCSs and the CC QM $-1 \rightarrow -1$ or $-1 \rightarrow +1$ angular distribution functions. The exact CC QM and QM–QCT hybrid normalised PDDCSs are very similar throughout the entire classically allowed region. Since the alignment parameters are the integrals of the normalised PDDCSs (*cf.* Eq. (3.7)), the difference between those belonging to parity conserving or changing transitions stems primarily from the differences between the corresponding quantum mechanical differential cross sections. Therefore the rotational alignment can be remarkably well explained in terms of classical mechanics.

5.3.2 Apse model calculations

In the case of classical hard shell collisions, the projection of the rotational angular momentum is conserved onto the kinematic apse. The quantum mechanical kinematic apse model assumes that the projection of $\boldsymbol{j}$ onto the kinematic apse is conserved for any type of collisions [22, 133]. That is to say, the diagonal of the apse frame density matrix is left unchanged during the course of the collision. It is also required that the excitation results in an incoherent mixture of the apse frame magnetic states, m^{a}, hence all of the off-diagonal elements are zero. It has been proven that the coherences between the ± 0.5 states do not affect the polarisation parameters of even rank, omitting this additional requirement does not change the following argument [150]. This is equivalent to requiring that the distribution of $\boldsymbol{j'}$ is cylindrically symmetric about the kinematic apse, thus the system is axially symmetric. If the molecular ensemble initially resides in the $m^{\mathrm{a}} \pm 0.5$ states and is unpolarised, then only the $m^{\mathrm{a}} \pm 0.5$ elements of the density matrix do not vanish after the collision, and they are equal to each other. The apse frame $\rho_q^{(k)\mathrm{a}}(\theta)$ renormalised PDDCSs can be calculated according to Eq. (3.66) [11]:

$$\begin{aligned}
\rho_q^{(k)\mathrm{a}}(\theta) &= \sum_{m_1^{\mathrm{a}}=-j'}^{j} \sum_{m_2^{\mathrm{a}}=-j'}^{j} \langle j' m_1^{\mathrm{a}} | \hat{\rho(\theta)} | j' m_2^{\mathrm{a}} \rangle \langle j' m_1^{\mathrm{a}}, kq | m_2^{\mathrm{a}} \rangle \qquad (5.9) \\
&= \langle j' 0.5 | \hat{\rho(\theta)} | j' 0.5 \rangle \langle j' 0.5, kq | 0.5 \rangle + \langle j' - 0.5 | \hat{\rho(\theta)} | j' - 0.5 \rangle \langle j' - 0.5, kq | - 0.5 \rangle \\
&= \left[1 + (-1)^k \right] \langle j' 0.5 | \hat{\rho(\theta)} | j' 0.5 \rangle = \frac{1}{2} \left[1 + (-1)^k \right] \langle j' 0.5 | \hat{\rho(\theta)} | j' 0.5 \rangle .
\end{aligned}$$

Because of the axial symmetry, only the $k =$ even, $q = 0$ polarisation parameters do not vanish, as it was proven in Eq. (3.56). The $\rho_0^{(2)\mathrm{a}}(\theta)$ parameter takes its lower limiting value for every scattering angle, which indicates perpendicular alignment of $\boldsymbol{j'}$ with respect to $\hat{\boldsymbol{a}}$. The apse frame $\rho_{1+}^{(2)\mathrm{a}}(\theta)$ and $\rho_{2+}^{(2)\mathrm{a}}(\theta)$ can be calculated with the aid of Eqs. (3.66) and (5.9) and both of them are zero. This is in line with the classical hard shell results.

The renormalised PDDCSs of Eq. (5.9) are still in the apse frame, therefore they have to be transformed into the scattering frame. This transformation is carried out by rotating

them through by the apse angle, $-\beta$, about the $\hat{\mathrm{y}}$ axis according to Eq (5.10). The effect of rotation is the mixing of the different components of a renormalised PDDCSs having the same rank. Since only the $q = 0$ components of the apse model renormalised PDDCSs are not zero in the apse frame, the summation over the d-matrix elements collapses. In a general case, all three apse frame components contribute to the scattering frame renormalised PDDCSs:

$$\rho_q^{(2)}(\theta) = \sum_{p=-k}^{k} d_{pq}^k(-\beta)\rho_p^{(2)}(\theta) = d_{0q}^2(-\beta(\theta))\rho_q^{(2)}(\theta)\,. \tag{5.10}$$

Finally, the scattering frame complex renormormalised PDDCSs are combined into real ones in the Hertel–Stoll fashion:

$$\begin{aligned}
\rho_{q+}^{\{k\}}(\theta) &= \rho_q^{\{k\}}(\theta) \quad \text{if } q = 0 && (5.11)\\
\rho_{q+}^{\{k\}}(\theta) &= \frac{1}{\sqrt{2}}\left[(-1)^q\rho_{-q}^{(k)}(\theta) + \rho_{+q}^{(k)}(\theta)\right] && (5.12)\\
&= (-1)^q\frac{1}{\sqrt{2}}\left[1 + (-1)^k\right] d_{0q}^k(-\beta(\theta))\langle j'0.5, k0|j'0.5\rangle \quad \text{if } q > 0 \\
\rho_{q-}^{\{k\}}(\theta) &= 0 \qquad \text{if } q > 0\,. && (5.13)
\end{aligned}$$

It is readily observed there is no rotational orientation in the apse model in any frame. The averaged quantum mechanical, classical hard shell and the apse model alignment renormalised PDDCSs are compared in Figure 5.11. The C-HEHS and AM data are identical in the classically allowed region for Δj transitions apart from a factor of $\langle j'0.5, 2, 0|j'0.5\rangle/0.5$ which goes to unity in the high-j-limit.

The apse model and averaged CC quantum mechanical renormalised PDDCSs are, in general, good agreement. The AM data do not exhibit oscillations in the forward scattered region, and the undulations are not present in the sideways and backward scattered sections. The deviation is most pronounced at small scattering angles where the attractive forces are more dominant. At larger scattering angles the collisions can be characterised by a more impulsive mechanism and as such, for high Δj, the three sets of renormalised

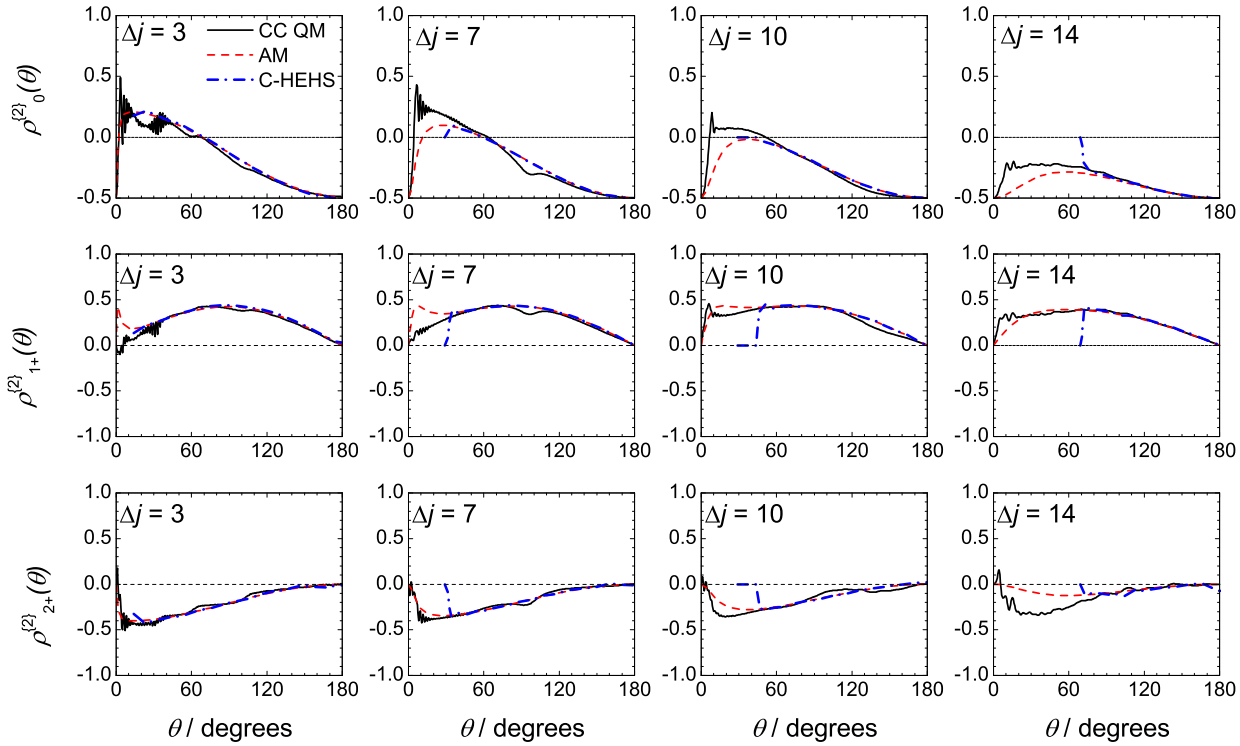

Figure 5.11: The scattering frame averaged CC QM (black solid line), AM (red dashed line) and C-HEHS (blue dash–dot line) alignment, $\rho^{\{2\}}_{q\pm}(\theta)$, PDDCSs $q = 0$ (top row), $q = 1$ (middle row), $q = 2$ (bottom row), for the $\Delta j = 3, 7, 10$ and 14 transitions from left to right, respectively. All the data were obtained at a collision energy of 66 mev.

PDDCSs coincide in this region. However, it is worth noting the deviation between the AM and QM data somewhat gets larger as the degree of rotational excitation increases [152]. This might be explained classically by the fact that the cylindrical symmetry about the kinematic apse is removed because of the surrounding finite range potential, which deflects some of the trajectories (for a more detailed discussion see Chapter 8). This observation will also be recalled when discussing the QM hard shell alignment.

It is now clear that the overall scattering angle dependence of the alignment renormalised PDDCSs stems from the conservation of projection of $\boldsymbol{j}$ onto the kinematic apse. The structure reflects the transformation from the apse frame to the scattering frame. If the apse model is exactly fulfilled, the scattering frame parameter is only a function of a single d^2_{0q}-matrix and the $\rho^{\{2\}a}_0(\theta)$ renormalised PDDCSs as in the case of backward scat-

tering. If it reasonably approximates the full quantum mechanical data, the contribution from the other components of the d^2_{0q}-matrices and second rank renormalised PDDCSs only appear as a minor perturbation for example in the sideways scattered regions of PDDCSs belonging to the medium Δj transitions. The agreement breaks down, again, if the collision is governed by the attractive forces to a greater extent.

5.3.3 Conservation of the projection of j onto the kinematic apse

In this section, it will be quantified to what extent the classical impulsive mechanism is responsible for the rotational alignment. Spin-orbit changing collisions are now included for the sake of better comparison. Spin–orbit conserving and the spin–orbit changing $|0.5, 0.5, -1\rangle|j', \Omega', -1\rangle$, $j' = 3.5, 7.5, 10.5$ and 14.5 transitions are investigated. As has been exhaustively discussed, the projection of the rotational angular momentum onto the kinematic apse is conserved for impulsive (C-HEHS) collisions [22]. The agreement between C-HEHS, QCT and CC QM calculations implies that the underlying dynamics responsible for the rotational alignment are mainly classically impulsive in nature, at least for high j' final states and is a reasonable approximation for low j' and small scattering angles.

If the projection of $\boldsymbol{j'}$ onto $\hat{\boldsymbol{a}}$ is indeed conserved, then only the ± 0.5 magnetic levels are populated in the apse frame when starting from $j = 0.5$. The only non vanishing parameter is $\rho_0^{(2)\mathrm{a}}$, which takes its lower limiting value of about -0.5. In order to test this assumption, the renormalised PDDCSs have to be rotated into the apse frame using Eq. (5.10), but the angle of rotation is β rather than $-\beta$. The scattering frame and apse frame alignment renormalised PDDCSs for the spin–orbit conserving transitions are compared in the top and bottom panels of Figure 5.12, respectively. The scattering frame alignment parameters vary considerably as a function of the scattering angle. The details of this scattering angle and Δj dependent behaviour was detailed in Sections 5.2.2 and 5.2.3. However, when transformed into the apse frame, the structure of the alignment parameters is much simplified. The $\rho_0^{\{2\}\mathrm{a}}(\theta)$ renormalised PDDCSs stay close to their lower

limiting value throughout the whole scattering angle region indicating the conservation of the projection of $\boldsymbol{j'}$ onto the kinematic apse. Significant deviation can only be observed in the forward scattered region, where the attractive forces are more important. In this region, the renormalised PDDCSs are greater then -0.5 and have a sharp maxima taking small positive values. As Δj increases, this peak gradually reduces, at $\Delta j = 10$ it only rises up to -0.2 meaning the alignment of $\boldsymbol{j'}$ with respect to $\hat{\boldsymbol{a}}$ is near perpendicular for the entire scattering angle region. The $\rho_{1+}^{\{2\}\mathrm{a}}(\theta)$ and $\rho_{2+}^{\{2\}\mathrm{a}}(\theta)$ renormalised PDDCSs display similar behaviour. They take values close to zero for the entire scattering angle region, referring to the lack of alignment with respect to the apse frame $\hat{\boldsymbol{x}} \pm \hat{\boldsymbol{z}}$ and $\hat{\boldsymbol{x}}$ or $\hat{\boldsymbol{y}}$ axes. However, the deviation from the theoretically inferred value is somewhat greater than in the case of the $\rho_{0}^{\{2\}\mathrm{a}}(\theta)$ polarisation parameter. At large scattered angles, all of the three parameters closely assume their respective values which are predicted by the kinematic apse model based on the classical impulsive collisions.

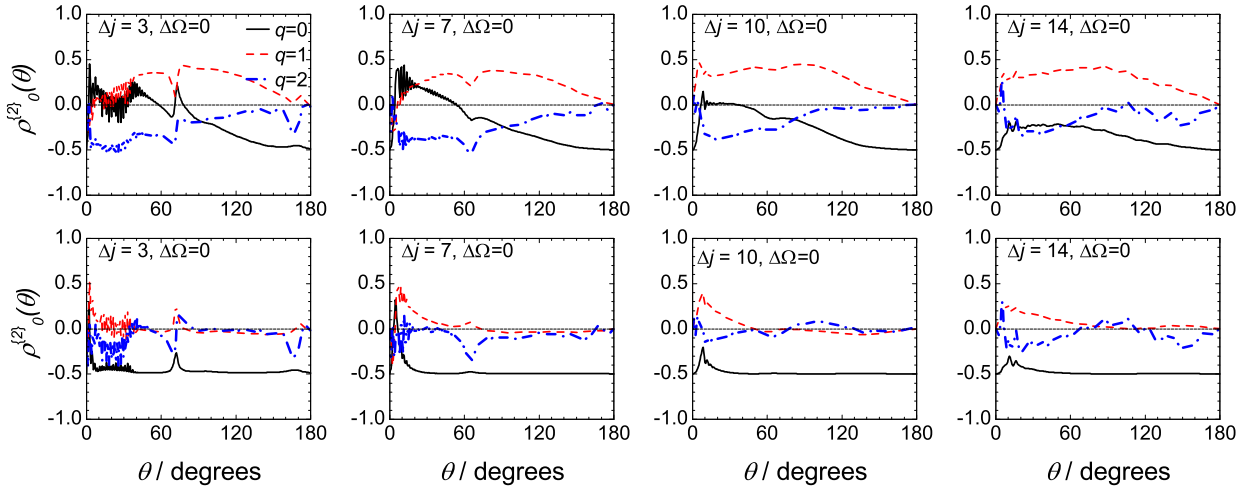

Figure 5.12: The scattering frame CC QM scattering frame alignment, $\rho_{q\pm}^{\{2\}}(\theta)$, PDDCSs $q = 0$ (black solid line), $q = 1$ (red dashed line), $q = 2$ (blue dash-dot line) for the $|0.5, 0.5, -1\rangle \rightarrow |j', 0.5, -1\rangle$ $j' = 4, 7, 10$ and 14 transitions from left to right, respectively, are shown in the top row. The corresponding apse frame data are displayed in the bottom row. All the data were obtained at a collision energy of 66 meV.

The scattering frame spin–orbit changing renormalised PDDCSs are shown in the top

row of Figure 5.13. Their scattering angle dependent structure is roughly similar to that of the spin–orbit conserving ones apart from those belonging to the $\Delta j \leq 4$ transitions. When compared to the spin orbit conserving renormalised PDDCSs, it can be seen that the number of undulations is increased, but the rapid oscillations in the forward scattered direction are reduced in both extension and amplitude. The projection of $\boldsymbol{j'}$ onto the kinematic apse is less well conserved than in the case of spin–orbit conserving transitions, because the spin–orbit changing transitions mainly sample the the attractive V_{dif} potential energy surface [9, 102]. However, the degree of conservation is still remarkable.

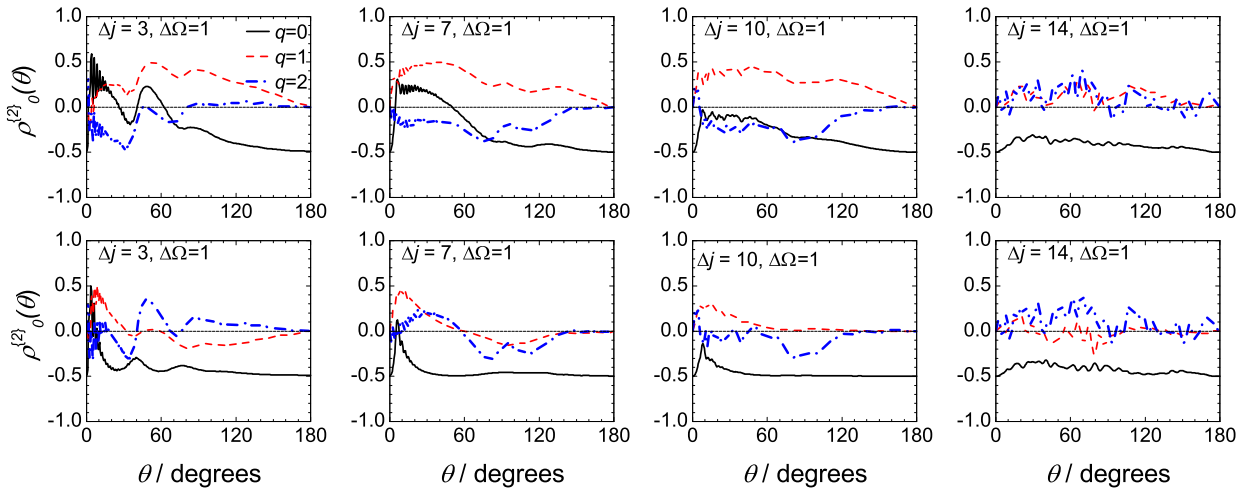

Figure 5.13: The scattering CC frame QM scattering frame alignment, $\rho^{\{2\}}_{q\pm}(\theta)$, PDDCSs $q = 0$ (black solid line), $q = 1$ (red dashed line), $q = 2$ (blue dash-dot line) for the $|0.5, 1.5, -1\rangle \rightarrow |j', 0.5, -1\rangle$ $j' = 4, 7, 10$ and 14 transitions from left to right, respectively, are shown in the top row. The corresponding apse frame data are displayed in the bottom row. All the data were obtained at a collision energy of 66 meV.

The apse frame spin–orbit conserving and spin–orbit changing integrated alignment moments are shown in the left and right panels of Figure 5.14, respectively. The spin–orbit conserving $a_0^{\{2\}\mathrm{a}}$ moments stay close to their lower limiting value of about -0.5 for all Δj transitions. The parity dependent oscillations, which were pronounced in the scattering frame, are absent or greatly reduced in the apse frame. The $a_{1+}^{\{2\}\mathrm{a}}$ and $a_{2+}^{\{2\}\mathrm{a}}$ moments are confined in a narrow interval around zero which indicates that $\boldsymbol{j'}$ is almost perfectly

aligned perpendicularly to the kinematic apse but otherwise it is not aligned with respect to other axes. The $a_{1+}^{\{2\}a}$ and $a_{2+}^{\{2\}a}$ moments exhibit weak parity dependent oscillations but with an amplitude greatly reduced compared to the scattering frame moments. As Δj increases, the moments seem to deviate more from their respective apse model values. However, this deviation is still less than ± 0.1.

The behaviour of the spin–orbit changing alignment moments is illustrated in the right panel of Figure 5.14. The projection of $\boldsymbol{j'}$ onto the kinematic apse is less conserved especially for low Δj transitions. As the degree of the rotational excitation increases, the $a_0^{\{2\}}$ moments approach to their lower limit, again indicating perpendicular alignment of rotational angular momentum with respect to the kinematic apse. The $a_{1+}^{\{2\}}$ and $a_{2+}^{\{2\}}$ moments oscillate around zero. The degree of alignment with respect to the $\hat{\boldsymbol{x}} \pm \hat{\boldsymbol{z}}$ and $\hat{\boldsymbol{x}}$ or $\hat{\boldsymbol{y}}$ axes is greater than in the spin–orbit conserving case.

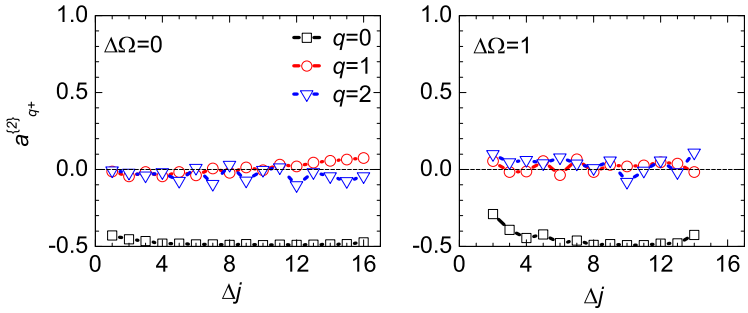

Figure 5.14: The apse frame spin–orbit conserving (left panel) and spin–orbit changing (right panel) CC QM (black open squares) alignment moments, $a_0^{\{2\}}$ (black open squares), $a_{1+}^{\{2\}}$ (red open circles), $a_{2+}^{\{2\}}$ (blue open triangles) for the $|0.5, 0.5, -1\rangle \rightarrow |j', 0.5, -1\rangle$ transitions. All the data were obtained at a collision energy of 66 meV.

5.3.4 The effect of the collision energy on the rotational alignment

The collision energy has been set to 66 meV throughout the entire previous discussion; this collision energy is approximately four times larger than the modulus of the potential well depth of about -15 meV. It has been shown this ratio is sufficient to render the collision

to be inherently impulsive. If the potential well depth is comparable to the collision energy, the attractive forces are expected to play a more important role in the collision dynamics. In order to ascertain their effect, CC QM calculations were carried out at collision energies of 15 meV and 33 meV. The differential cross sections are shown in the

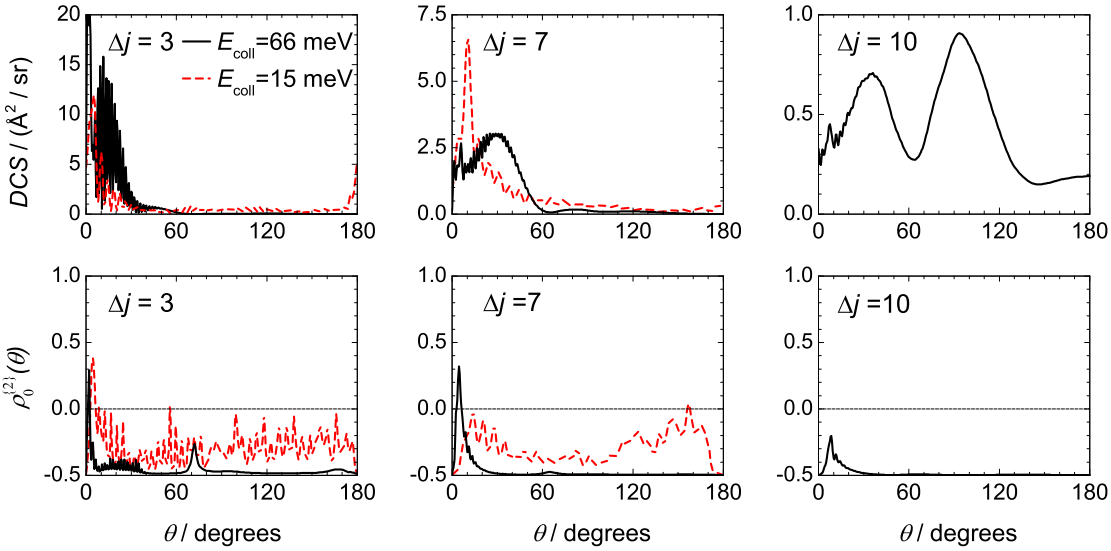

Figure 5.15: The CC QM DCSs for the $|0.5, 0.5, -1\rangle \rightarrow |j', 0.5, j'\rangle$, $j' = 3.5, 7.5$ and 10.5 are shown in the top row from left to right. The collision energy was 66 meV (black solid line) and 15 meV (red dashed line). The corresponding apse frame $\rho_0^{\{2\}}(\theta)$-s are shown in the bottom panels. Note that for 15 meV the $j' = 10.5$ state is not accessible.

top panel of Figure 5.15 for the $|0.5, 0.5, -1\rangle \rightarrow |j', 0.5, -1\rangle$ $\Delta j = 3, 7$ and 10 transitions. As the collision energy decreases the DCSs become more diffuse and less structured. The rapid oscillations which are confined to the forward scattered region at $E_{\text{coll}} = 66$ meV gradually spread out towards larger scattering angles as the collision energy decreases. If the E_{coll} is equal to the modulus of the well depth, the oscillations are present in the entire scattering interval. Their frequency changes inversely with the collision energy which can be rationalised as a decrease in the de Broglie wavelength. The apse frame renormalised PDDCSs, $\rho_0^{\{2\}\text{a}}(\theta)$, are shown in the bottom panel of Figure 5.15. The interference structure dominates the renormalised PDDCSs at the lowest collision energy, whereas it is restricted to forward scattered angles at 66 meV. The $\rho_0^{\{2\}\text{a}}(\theta)$ parameter deviates significantly from

its lower limiting value at the lowest collision energy, which means that the projection of the rotational angular momentum onto the kinematic apse is not conserved. The apse frame renormalised PDDCSs at a collision energy of $E_{\mathrm{col}} = 66\,\mathrm{meV}$ were characterised in Section 5.3.3.

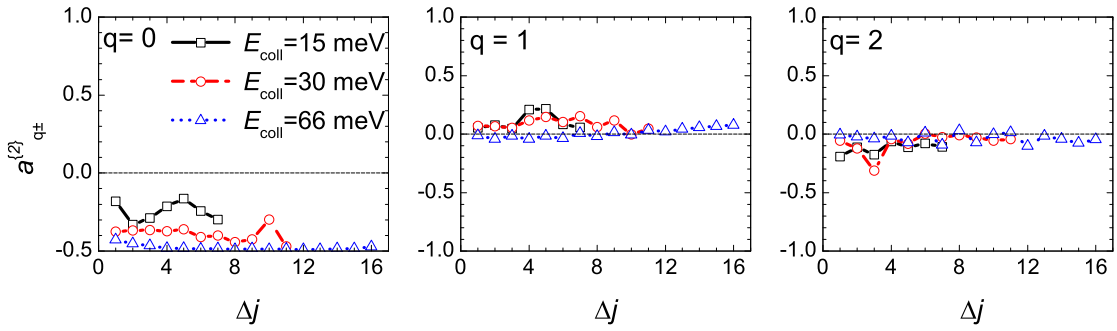

Figure 5.16: The apse frame CC QM $a^{\{2\}}_{q\pm}$ moments $q = 0$ (left panel), $q = 1$ (middle panel), $q = 2$ (right panel), as a function of Δj at collision energies of 15 meV (black open squares), 30 meV (red open circles), 66 meV (blue open triangles) for the $-1 \rightarrow -1$ spin–orbit conserving transitions.

The integrated apse frame alignment moments are shown in Figure 5.16. The $E_{\mathrm{col}} = 15\,\mathrm{meV}$ moments deviate considerably from the values predicted by a hard shell collision. A well defined trend cannot be observed for any q component. The $E_{\mathrm{col}} = 33\,\mathrm{meV}$ data show a better conservation of the projection of $\boldsymbol{j}$ onto the apse. In general, as the collision energy increases the collisions become more impulsive and more dominated by the repulsive core of the potential. Therefore, the rotational alignment can better be approximated by the classical hard shell model where the projection of $\boldsymbol{j}$ onto the kinematic apse is conserved. Highly excited rotational states require the impulsive mechanism, so the integrated alignment moments approach their hard shell limit.

5.3.5 Magnetic level populations in the scattering and apse frame

If a transition starts from $j = 0.5$, only the $m_j = \pm 0.5$ magnetic levels can initially be populated, irrespective of the axis of quantisation. Therefore only the $m_j^{\mathrm{a}} = \pm 0.5$ apse frame levels are occupied with equal weights in the case of an unpolarised non-rotating molecular ensemble. If the apse frame population is conserved during the course of the collision, finally, the only the $m_{j'}^{\mathrm{a}} = \pm 0.5$ levels should be populated.

The diagonal elements of the density matrix describes the population of the magnetic sublevels [72]. As such, investigating the apse frame density matrix should provide yet another way to see whether the projection of the rotational angular momentum is conserved. The density matrix was obtained in terms of the series expansion of Eq. (5.10) where the renormalised PDDCSs were rotated into the apse frame. The scattering frame and apse frame density matrices for the $|0.5, 0.5, -1\rangle \rightarrow |10.5, 0.5, -1\rangle$ transition are shown in the top panel of Figure 5.17. At 0° and 180° when $\boldsymbol{k}$, $\boldsymbol{k'}$ and $\hat{\boldsymbol{a}}$ are parallel and antiparallel, respectively, only the $m_{j'} = \pm 0.5$ states can be populated due to kinematic reasons in any frame. When $\boldsymbol{k}$ is the axis of quantisation, the high $|m_j|$ states are populated in the forward scattered region. As the scattering angle increases the lower levels become more populated. Only the lowest, $|m_j| \leq 2.5$, states are occupied beyond 150°.

Conversely, in the apse frame, the high $m_{j'}^{\mathrm{a}}$ states are only occupied at small scattering angles, $\theta \lesssim 15°$. The tendency of the lowest states being exclusively populated increases in the sideways scattered region as illustrated in the top right panel of Figure 5.17. At angles larger than 30° virtually only the $m_j^{\mathrm{a}} = \pm 0.5$ states are occupied apart from minor undulations. It implies that the projection of the angular momentum onto the kinematic apse is largely conserved. The apse frame population is practically unchanged for low Δj transitions *e.g.* $|0.5, 0.5, -1\rangle \rightarrow |5.5, 0.5, -1\rangle$ at this collision energy as shown in the bottom right panel of Figure 5.17. If the collision energy is comparable to the attractive well depth, there is no propensity for conserving the initial magnetic level population in

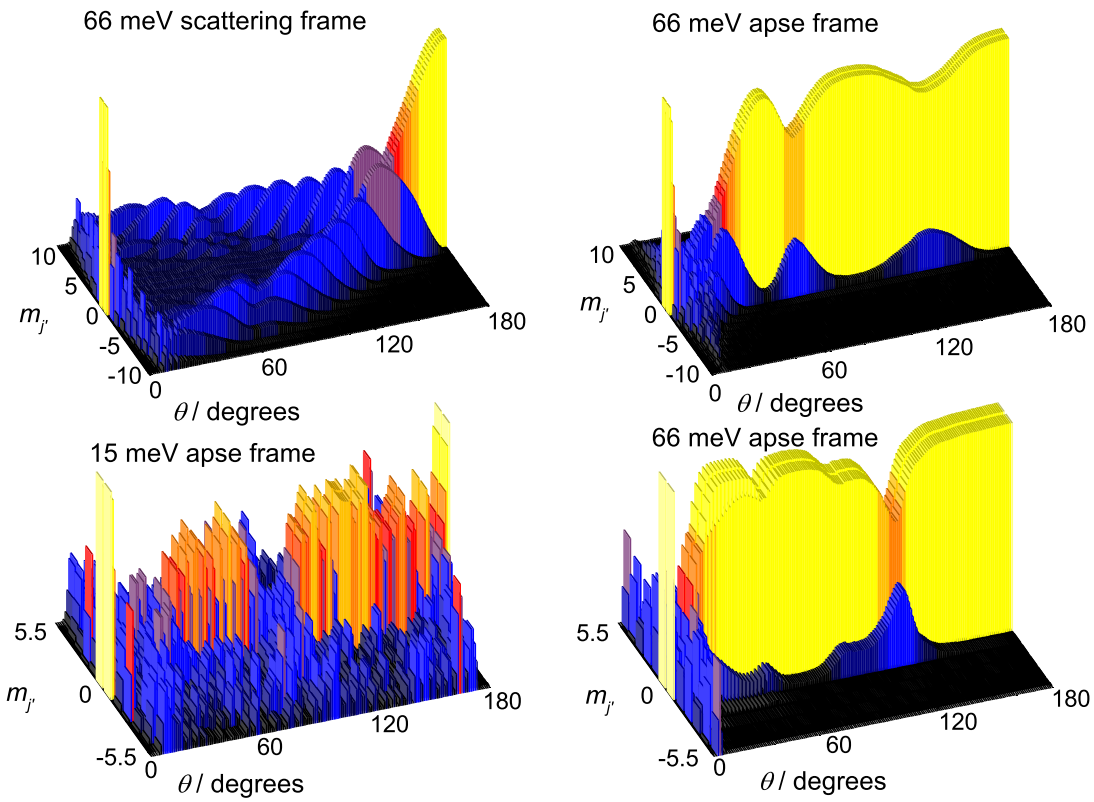

Figure 5.17: The scattering angle resolved CC QM density matrices (black: no population, yellow: 0.5). (Top row) the scattering frame (left panel) and apse frame (right panel) density matrices for the $|0.5, 0.5, -1\rangle \rightarrow |10.5, 0.5, -1\rangle$ transition at a collision energy of 66 meV. (Bottom row) Comparison of the apse frame density matrices for the $|0.5, 0.5, -1\rangle \rightarrow |5.5, 0.5, -1\rangle$ transition at collision energies of 15 meV (left panel) and 66 meV (right panel).

the apse frame. This is exemplified by showing the density matrix for the $|0.5, 0.5, -1\rangle \rightarrow |5.5, 0.5, -1\rangle$ at a collision energy of 15 meV in the bottom left panel of Figure 5.17.

5.4 Quantum mechanical soft potential and hard shell alignment

The exact quantum mechanical hard shell alignment parameters are presented and interpreted for the first time. Using these and the soft potential CC QM results, the exact role of the attractive part of the $V_{\text{sum}}(R, \gamma)$ potential will be examined.

5.4.1 Soft potential alignment parameters

The attractive part of the $V_{\mathrm{sum}}(R,\gamma)$ potential was removed with the log-sigmoid function, which was also used to scale the $V_{\mathrm{dif}}(R,\gamma)$ potential according to Eq. (4.13). The scaling parameters, α, were chosen as 5 bohr^{-1} and 10 bohr^{-1} which required the shift parameter to be set as 1 bohr and 0.5 bohr, respectively. These potentials are referred to as (a) and (b), respectively. The scaled and the full potential $\rho^{\{2\}}_{q+}(\theta)$-s compare well, as illustrated by Figure 5.18 for the $|0.5,0.5,-1\rangle \rightarrow |j',0.5,-1\rangle$, $j' = 3.5, 7.5, 10.5$ and 14.5 transitions.

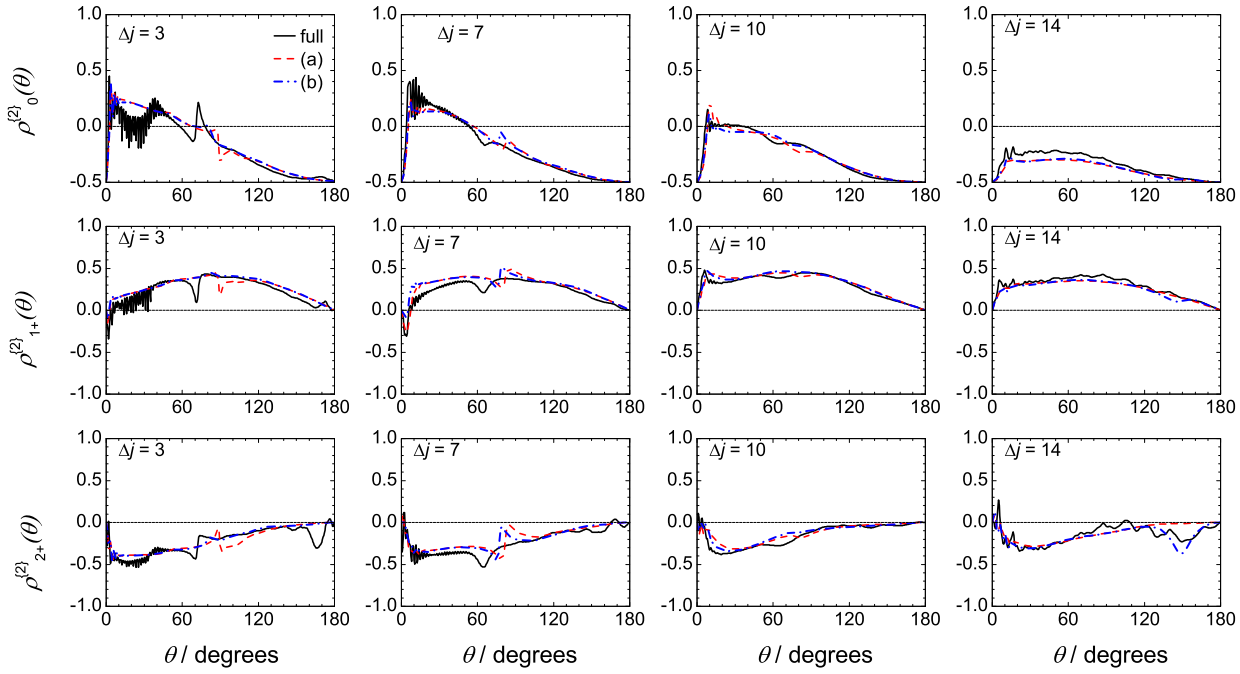

Figure 5.18: The full potential (black solid line) and the soft potential, (a) (red dashed line) and (b) (blue dash-dotted line) alignment renormalised PDDCSs, $\rho^{\{2\}}_{q+}(\theta)$, $q = 0$ (top row), $q = 1$ (middle row), $q = 2$ (bottom row), for the $|0.5,0.5,-1\rangle \rightarrow |j',0.5,-1\rangle$ $j = 3.5, 7.5, 10.5$ and 14.5 transitions. All calculations were carried out at a collision energy of 66 meV

The three sets of data are, in general, good agreement. The most pronounced deviation is observed between $\theta = 10°$ and $\theta = 40°$ scattering angles, at the $\Delta j = 3$ transition. This region coincides with the secondary peak of the corresponding DCS which is due to the long range attraction. This assignment is reaffirmed by the soft potential $\rho^{\{2\}}_{q+}$-s, that lacks the

local maxima between these angles. The full and soft potential alignment renormalised PDDCSs almost overlap at higher states, except that the rapid oscillations are greatly reduced or removed in the forward scattered region, in the case of the soft potential. The undulations are also removed in the sideways scattered region *e.g.* $\Delta j = 7$ and 10 in the middle panels of Figure 5.18. Making the repulsive wall steeper only alters the PDDCSs to a small extent, as revealed by comparing the (a) and (b) soft potential results.

5.4.2 Quantum mechanical hard shell alignment PDDCSs

The kinematic apse model has proven to be an accurate approximation to the alignment dynamics of the NO(X)–Ar collision at $E_{\text{coll}} = 66\,\text{meV}$, where the repulsive forces dominate. However, it has not been confirmed that the exact quantum mechanical description of the hard shell collisions is indeed equivalent to the kinematic apse model. In order to test whether this is indeed the case, exact quantum mechanical hard shell calculations were carried out. The methodology was detailed in Section 4.3.

Renormalised PDDCSs calculated using CC QM on the full and (b) soft potential are compared with the quantum mechanical hard shell (HS QM) calculations in Figure 5.19. The HS QM data are in exceptionally good agreement with those obtained employing the soft V_{sum} potential, confirming that the soft potential is a good approximation to the exact hard shell potential.

The HS QM and CC QM rotational alignment is different, where the role of the attractive forces are dominant, for instance for the scattering angle of $\theta < 40^\circ$ scattering angles at $\Delta j = 3$. At higher states, the three sets of data predicts similar trend of rotational alignment. The agreement between the QM HS and the exact CC QM renormalised PDDCSs does not break down in the forward scattered region at highly excited states, unlike in the case of the AM alignment.

The apse model and the HS QM $\rho_{q+}^{\{2\}}(\theta)$-s agree well at all final states, but they are not identical as shown in Figure 5.20, implying that the apse model is not equivalent to the exact description of the quantum mechanical hard shell collisions. Magnetic states,

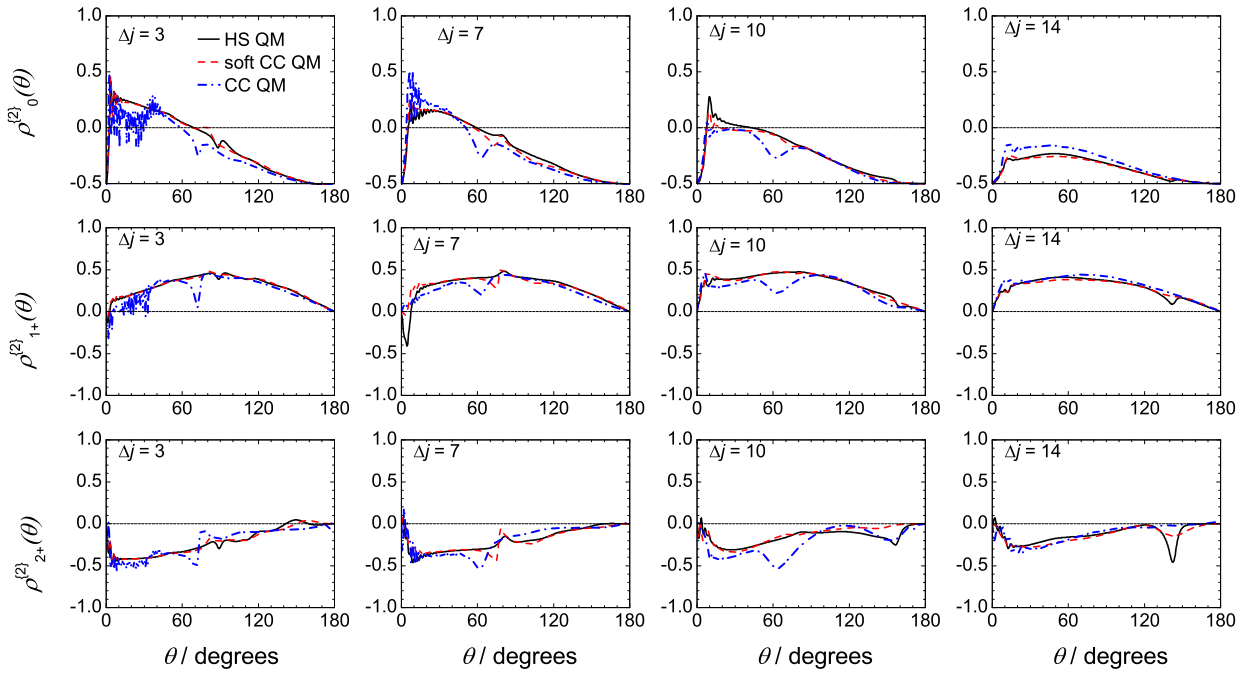

Figure 5.19: The HS QM (black solid line), soft potential (red dashed line) and full potential (blue dash-dotted line) $\rho^{\{2\}}_{q+}(\theta)$, $q = 0$ (top row), $q = 1$ (middle row), $q = 2$ (bottom row), for the $|0.5, 0.5, -1\rangle \rightarrow |j', 0.5, -1\rangle$ $j = 3.5, 7.5, 10.5$ and 14.5 transition.s All calculations were carried out at a collision energy of 66 meV.

different to the lowest apse frame states, can be populated, and the projection of the angular momentum onto the kinematic apse is not, in general conserved, in quantum mechanical hard shell collisions.

The HS QM $\rho^{\{2\}}_{q+}(\theta)$ exhibit rapid oscillations in the forward scattered region which is absent from the simple apse model data which can be realised as an interference pattern in terms of the Fraunhofer model[105].

Naïvely, one would assume the exact hard shell and the apse model would agree at every scattering angle and for all final states. The HS QM and AM renormalised PDDCSs agree less as Δj increases, though, these collision are expected to be more impulsive in a classical sense. The two kind of alignment renormalised PDDCS always disagree to a greater extent in the forward scattered region as shown in Figure 5.20. The key to understand these features is to consider the collision as it evolves in time. The projection

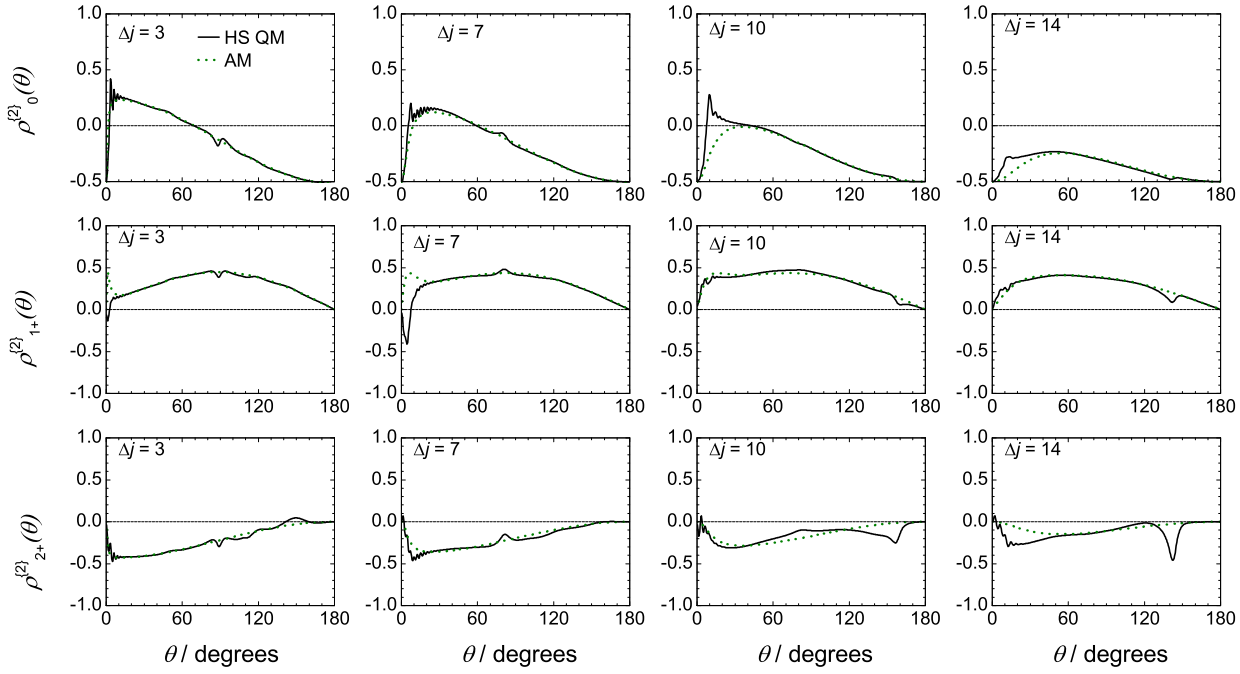

Figure 5.20: The HS QM (black solid line), apse model (green dotted line) $\rho^{\{2\}}_{q+}(\theta)$, $q = 0$ (top row), $q = 1$ (middle row), $q = 2$ (bottom row), for the $|0.5, 0.5, -1\rangle \rightarrow |j', 0.5, -1\rangle$ $j = 3.5, 7.5, 10.5$ and 14.5 transitions. All calculations were carried out at a collision energy of 66 meV.

of $\boldsymbol{j}$ onto $\boldsymbol{a}$ is expected to be best conserved in the energy sudden limit [14, 22, 23], where the molecule does not rotate during the interaction.

At $\Delta j = 1$ and $\Delta j = 16$, the rotational period of the NO(X) molecule is about 7.1×10^{-12} s and 6.1×10^{-13} s, respectively. During this time, the atom can travel 60 Å and 2.0 Å. The major and minor semiaxis of the hard shell are approximately 3.5 Å and 2.95 Å, respectively. At low Δj transitions, the atom, or its wavepacket, departs quickly from the scatterer, thus the initial orientation of the bond axis of the molecule does not change too much. If a larger amount of translational energy is given to the diatom, it rotates faster, and the atom slows down. As a consequence, the interaction is extended in time, during which a wider range of bond axis orientation is sampled.

If the molecule is scattered in the forward direction, its corresponding wavepacket again stays closer to the molecule for a longer time, giving rise to an elongated interaction.

Therefore the projection $\boldsymbol{j}$ onto the kinematic apse is expected to be less conserved at small scattering angles. On the contrary, the backward scattered particle departs faster from the interaction region, thus better conservation of the projection is expected. With increasing Δj, the scattered atom becomes gradually slower, or equivalently, its de Broglie wavelength becomes longer, the deviation between the kinematic apse model and exact HS QM alignment parameters becomes more pronounced in the forward scattered region as shown in Figure 5.20. The smallest non-zero scattering angle at which the two alignment parameters are identical is shifted to higher values, because the slower atom stays close to the scatterer for a longer time, even though it is scattered through larger angles.

As a conclusion, the classical hard shell collision is inherently time independent and restricted to an infinitely reduced point in the space and time. The increased rotational motion of the molecule does not influence the outcome of the scattering event, once the single encounter collision has happened. In contrast, the quantum mechanical collision of hard shells has a finite spread in time and space, and as such it cannot be rigorously 'impulsive' or instantaneous. These findings will have serious consequences on the rotational orientation.

The full CC QM rotational alignment is strictly speaking that of a *quantum mechanical* hard shell collision apart from the perturbing effects of its open shell nature and the attractive and soft repulsive features of the potential. However, the rotational alignment is still dominantly determined by the impulse of the collision, and the quantum effects induce only small deviations from the classical hard shell mechanism at this collision energy.

As a consequence, the kinematic apse model is still a plausible approximation to the QM hard shell, and therefore, to the full potential scattering problem. Marked deviation between the HS QM and AM data is only present at high j' final states.

Scattering frame and apse frame polarisation moments

The scattering frame integrated alignment moments exhibit parity dependent oscillations, most pronounced for the $a_0^{\{2\}}$ moments. The parity conserving, $(-1)^{\Delta j}$ = even, moments reveal stronger perpendicular alignment to $\boldsymbol{k}$ than the adjacent parity changing ones, $(-1)^{\Delta j}$ = odd. $a_{2+}^{\{2\}}$ also oscillates as a function of Δj, though, the difference between adjacent polarisation moments is smaller. In the case of the $a_{1+}^{\{2\}}$ there are no parity dependent oscillations. The parity pair, *e.g.* $\Delta j = 7$ and $\Delta j = 8$, renormalised PDDCSs are almost identical and well approximated by their classical hard shell counterpart PDDCSs. The corresponding DCSs heavily depend on the parity conserving or changing nature of the transition. As a result, the periodic alternation primarily comes from the differences of the DCSs, similar to the full potential CC QM alignment moments. The apse frame

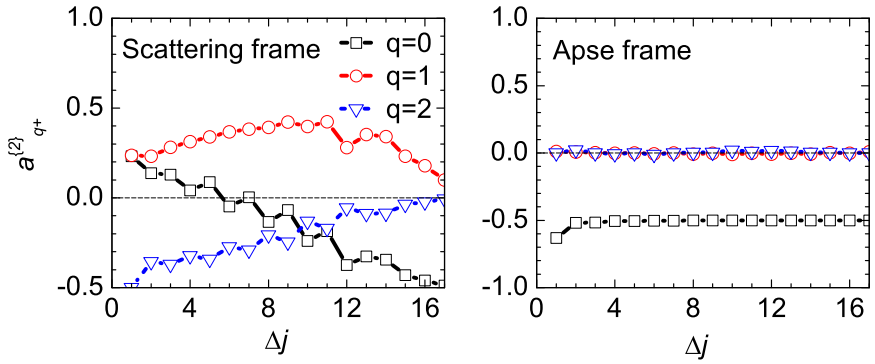

Figure 5.21: The scattering frame HS QM alignment moments, $a_{q\pm}^{\{2\}}$, $q = 0$ (black open squares), $q = 1$ (red open circles), $q = 2$ (blue open triangles) in the scattering frame (left panel). The right panel shows the moments in the apse frame.

moments show a strong conservation of the projection of $\boldsymbol{j'}$ onto the kinematic apse. The apse frame $a_0^{\{2\}}$ moment takes its lower limiting value of -0.63 for $\Delta j = 1$. The propensity is stronger than in the full CC QM case, because they were obtained employing an infinitely repulsive potential. The moments do not deviate from their limiting values at high Δj, because the hard shell DCSs are more backward scattered and therefore weight the region where the apse model would be a good approximation.

5.5 Summary

The rotational alignment effects in the inelastic collisions of NO(X)–Ar have been investigated from a theoretical point of view. Comparison of classical hard shell, quasi-classical and exact quantum mechanical calculations revealed that the dynamics responsible for the rotational alignment in the spin–orbit conserving transitions is mainly classically impulsive, if the attractive well depth of the potential is negligible compared to the collision energy. In a purely impulsive collision, the projection of the rotational angular momentum onto the kinematic apse is conserved. The scattering angle dependence of the alignment renormalised PDDCSs reflects this conservation, on which the attractive features of the potential act as a small perturbation.

It has also been demonstrated that the rotational alignment in the quantum mechanical collisions of hard shells cannot be perfectly described by the kinematic apse model. However, the classical model provides an excellent approximation to the full exact quantum mechanical dynamics.

These theoretical results will be compared to those obtained in experiments in the following chapters.

Chapter 6

Experimental methods

The main focus of the present thesis is on the theoretical aspects of rotational angular momentum polarisation in the collisions of NO(X)–Ar system. However, our findings were tested against experimentally obtained results, to which this chapter is meant to provide a brief introduction. In addition, an algorithm has been developed to extract polarisation data from experimental ion-images. It is thus necessary to overview the experimental methods employed in order to set a background for the next chapter, in which the algorithm is discussed.

A hexapole state selective crossed molecular beam experiment was coupled with velocity mapped ion-imaging to investigate rotational polarisation effects. This experiment provides full initial and final quantum state selection including rotational, vibrational and Λ-doublet states. The initial Λ-doublet selection is achieved by means of the Stark effect, which is generated by a hexapole field through which the molecules have to pass. As a consequence, only those NO(X) molecules that are in their lowest vibrational and rotational states and in the -1 Λ-doublet level are focussed into the scattering chamber. They then undergo collisions with argon atoms, which results in rotational excitation. They are then probed by $(1 + 1')$ resonance enhanced multiphoton ionisation (REMPI), which provides full final state selection. The rotational motion of the scattered molecules is, in general, polarised. The probability of the NO(A $\leftarrow$ X) transition depends on the polarisation state of the NO(X) molecules. Using left and right circularly, or horizontally

and vertically linearly polarised light, the degree of orientation or alignment, respectively, can be measured.

6.1 Hexapole state selection

The hexapole field is generated by six electrodes which are arranged in a hexagonal pattern on the circumference of a cylinder and a non-zero voltage of modulus $|V_0|$ is applied to the electrodes with alternating sign on alternating electrodes. The electronic ground state of NO(X) has two Λ-doublet components which are degenerate in the lowest rotational state as was discussed in Chapter 2 [57]. This degeneracy is removed in the hexapole field where the Hamiltonian of the molecules can be written as [153, 154],

$$\hat{\mathcal{H}} = \hat{\mathcal{H}}_0 + \hat{\mathcal{H}}_Q + \hat{V}_{\text{Stark}}. \tag{6.1}$$

The first term is the field free Hamiltonian of the molecule and it is equivalent to Eq. (2.2) in Chapter 2 [153]. The second term represents the nuclear hyperfine energy contribution which will be neglected in the following discussion. The third term accounts for the Stark effect, the interaction between the molecule's dipole moment, $\boldsymbol{\mu}$, and the electric field, $\boldsymbol{E}$ when the angle between them is $\theta_{\mu E}$. If the field is not too strong, first order perturbation theory results in the following expression for the Stark effect [153, 154]:

$$V_{\text{Stark}} = -\langle \boldsymbol{\mu}.\boldsymbol{E} \rangle = -|\boldsymbol{\mu}||\boldsymbol{E}| \cos(\theta_{\mu E}) = -\epsilon |\boldsymbol{\mu}||\boldsymbol{E}| \frac{|m\Omega|}{j(j+1)}\,, \tag{6.2}$$

where j is the rotational quantum number of NO(X) having the projection quantum number m onto the symmetry axis of the hexapole. Ω denotes the spin–orbit manifold and ϵ is the index of the Λ-doublet level. If the hexapole rods are positioned on the surface of a cylinder which has a radius of r_0, and the potential applied to them is V_0, then the

potential of the ideal field at a point (r, ϕ) is given by

$$V(r) = -V_0 \left(\frac{r}{r_0}\right)^3 \cos(3\phi). \tag{6.3}$$

Thus the magnitude of the electric field at a distance r from the centre of the hexapole is equal to

$$E(r) = V_0 \frac{3r^2}{r_0^3}. \tag{6.4}$$

The force acting on the molecule can then be calculated by combining Eqs. (6.2) and (6.4) as shown in Eq. (6.5),

$$F(r) = \epsilon \frac{|m\Omega|}{j(j+1)} V_0 \frac{6r}{r_0^3}\,. \tag{6.5}$$

The sign of the force depends on the particular Λ-doublet level. If $\epsilon = +1$, as is the case for high-field seeking states, the force is positive and the molecule is propelled out of the hexapole region. On the contrary, if $\epsilon = -1$, as is the case for low-field seeking states, the molecule undergoes harmonic motion down the length of the field. As a consequence, the $\epsilon = -1$ molecules can be selected out of the initial f–e mixture. The extent to which they are separated depends on the strength of the hexapole field and the length of the rods.

6.2 Experimental setup

The experimental apparatus is a crossed molecular beam apparatus in which the NO(X) molecules produced from a molecular beam are state selected by virtue of the Stark effect and intersected by a rare gas beam. The rotationally excited products are probed by a $(1+1')$ REMPI scheme and are velocity mapped on to the detector. The main constituent modules of the apparatus are described in the following.

6.2.1 Molecular beams

16 % NO(X) (BOC) was seeded in Ar at a pressure of 3 bar in order to enhance adiabatic cooling. A General valve was used to produce the molecular beam at a rate of 10 Hz. A

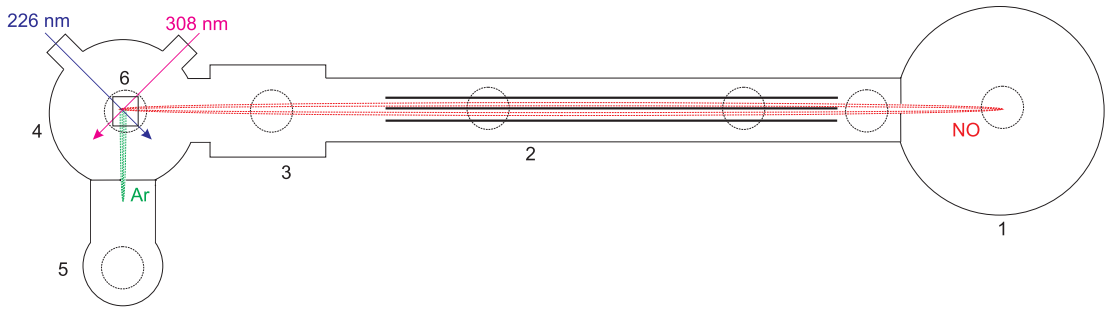

Figure 6.1: The schematic of the hexapole experimental setup where the numbers are: (1) NO source chamber, (2) hexapole section, (3) field free region, (4) scattering chamber, (5) Ar source chamber. The ion optics and the detector are positioned above the area marked by the square (6) in the scattering chamber. The pumps are attached where indicated by the dotted circles.

5 mm skimmer was positioned at a distance of 3 cm from the valve which selects out the rotationally coldest part of the beam. The molecules then travel through the hexapole which selects those residing in the $|j = 0.5, \overline{\Omega} = 0.5, \epsilon = -1\rangle$ state, therefore the molecules which are in another state cannot reach the the field free region after the hexapole. The purity of the molecular beam is at least 99 % [126, 145]. The length of the hexapole and the V_0 field strength in Eq. (6.3) was set so as the molecules were focussed in the centre of the scattering chamber marked by number 6 in Figure 6.1. The secondary beam, which was argon, was also produced by a General valve. The repetition rate was 5 Hz in a two shots on–two shots off pattern, such that it was possible to measure the background signal level simultaneously for both laser polarisations. This beam is skimmed by a 2 mm skimmer and intersects the NO(X) beam at a right angle in the centre of the scattering chamber. The beam velocities had to be determined in order to calculate the exact collision energy. They also have to be known to ascertain the exact orientation of the initial relative velocity, $\boldsymbol{k}$, relative to the collected ion-image. If all of the rotational and vibrational energy of the diatomic molecule is transferred into translational motion, the modulus of its velocity is given by [68, 69]:

$$v = \sqrt{\frac{2k_{\mathrm{B}}T}{m}\frac{\gamma}{\gamma - 1}}\,, \tag{6.6}$$

where k_{B} is the Boltzmann constant, m is the mass of the gas, $\gamma = C_p/C_v$ is the ratio of the constant pressure and constant volume heat capacities, C_p and C_v, respectively. If

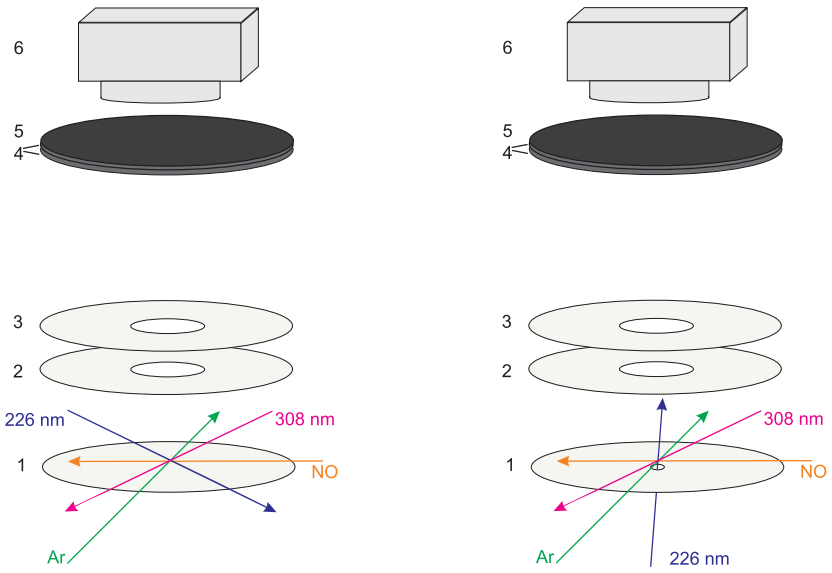

Figure 6.2: The REMPI and detection geometry for collision induced alignment measurements (left panel) and for collision induced orientation measurements (right panel) where the numbers are (1) repellor plate, (2) extractor plate, (3) ground plate, (4) MCP plates, (5) phosphor screen, (6) CCD camera.

T, the absolute temperature of the gas, is taken as 298 K, then velocities are calculated to be 585 ms^{-1} for the NO and 555 ms^{-1} for the argon. This correspond to a collision energy, $E_{\text{coll}} = 470\,\text{cm}^{-1}$. The collision energy as well as the velocity to pixel ratio, p_{vtp}, can be determined from a sequence of ion-images belonging to different final rotational states. The radius, R, of the ion-images is proportional to the modulus of the final relative velocity of the NO molecule, v_{NO}. That is in turn related to the final energy which is a function of the rotational state:

$$R = p_{\text{vtp}} \frac{m_{\text{NO}}}{m_{\text{NO}} + m_{\text{Ar}}} \sqrt{\frac{E_{\text{coll}} - \Delta E_{\text{rot}}(j)}{\mu}} \tag{6.7}$$

where m_{NO}, m_{Ar} are the masses of the Ar atom and the NO(X) molecule and μ is the reduced mass of the system. The change of the rotational energy is approximated by $\Delta E_{\text{rot}}(j) = B_0 j(j+1)$, where B_0 is the rotational constant of the molecule. The collision energy and the pixel to velocity ratio were determined by fitting Eq. (6.7) over a set of experimental images. The fitted collision energy is approximately 66 meV. The velocity of the NO beam has been previously determined to be 625 ms^{-1} [142]. Hence the velocity

of the argon beam is 580 ms^{-1}. These values are somewhat higher than those predicted by Eq. (6.6). If a temperature of 340 K is used instead, both the beam velocities and the collision energy is recovered. This is not unreasonable assumption, as the temperature of the General valves can be higher due to the friction and the current drawn during the continuous operation.

6.2.2 Vacuum system

The compartments of the apparatus have to be under vacuum in order to avoid unwanted collisions and contamination of the crossing molecular beams. The positions of the pumps are indicated by dashed circles in Figure 6.1. The NO source chamber was pumped by a diffusion pump. The diffusion pump was backed by a roots pump which was backed by a rotary vane pump. The pressure was about 1×10^{-6} mbar in this chamber. There is a turbomolecular pump installed after the NO(X) skimmer. The hexapole section and the field free region are pumped by another three turbomolecular pumps. The Ar source chamber and the scattering chamber are also equipped with turbmolecular pumps, all of which are backed by rotary vane pumps. The pressure in the flight path between the source and scattering chambers was of the order of 1×10^{-7} mbar. The pressure in the scattering chamber was around 5×10^{-7} mbar when both beams were on.

6.2.3 Lasers

The $(1 + 1')$ REMPI scheme was formed by the following lasers: the 308 nm output of a EMG 201 MSC XeCl excimer laser was split by a beam splitter. Approximately 90% of the 120 mJ power was used to pump a Lambda Physik FL3002 tunable dye laser. Coumarin 2 was used as a dye in methanol solution which lases at approximately 452 nm. The output of the dye laser was frequency doubled to wavelengths in the region of 226 nm and tuned to the exact value of the NO(A $\leftarrow$ X) rovibrational transition. This was then passed through a Rochon polariser and photoelastic modulator. For the collision induced alignment linearly polarised light was used. The electric vector of the laser was either

parallel or perpendicular to the plane of the molecular beams in the case of horizontal and vertical polarisations, respectively. The laser beam was confined in the plane of the molecular beams and intersected those at an angle of 45° degrees for both polarisations. The other beam path was defined by the remaining 10% of the excimer's beam, which was used to ionise the excited NO(A) molecules. This was also coplanar with the molecular beams and the dye laser, with which it made a right angle. The two laser beams overlapped in the centre of the scattering chamber. The spatial dimension of the detection volume was approximately $1.5\,\mathrm{mm} \times 1.5\,\mathrm{mm} \times 3.5\,\mathrm{mm}$. The polarisation of the dye laser was flipped from vertical to horizontal between subsequent shots, thus the electric vector of the laser $\hat{\boldsymbol{\epsilon}}$ changed shot by shot.

For the rotational orientation measurements a quarter wave plate was mounted after the photoelastic modulator, which enabled the dye laser to be alternated between left and right circularly polarised. In order to maximise the effect of the rotational orientation, the dye laser has to propagate perpendicular to the plane of the molecular beams. For this end, the light was guided through a set of mirrors, and a hole of 5 mm diameter was drilled in the repeller electrode, through which the laser shone upwards intersecting the interaction volume, as shown in Figure 6.2. The laser propagation axis was slightly tilted in order to avoid the detector. The configuration of the excimer laser was unchanged with respect to the geometry employed to measure rotational alignment.

6.2.4 Detection

Using a $(1 + 1')$ REMPI scheme, the rotationally excited NO(X) molecules are excited to the A state by the dye laser. The exact wavelength is chosen according to the particular $\mathrm{A}^2\Sigma^+(j', \Omega', \epsilon') \leftarrow \mathrm{X}^2\Pi(j, \Omega, \epsilon)$ transition of interest. The excimer was used to ionise the excited molecules in the NO(A) state. This scheme makes it possible to keep the power of the dye laser low in order to minimise saturation which reduces the sensitivity of the experiment to the polarisation effects. A single laser shot produced 2–5 ions on average.

Velocity mapped ion-imaging is employed to detect the ionised NO molecules [142, 155].

The interaction volume is positioned between two electrodes, namely between the repeller and the extractor. Voltages of 1000 V and 1500 V are applied to them in order to maintain an inhomogeneous electric field which extracts the ions towards the detector. A ground electrode is placed after the extractor in order to create a field free flight path which extends to the detector. The ions impact on a pair of microchannel plates (MCPs) which results in an avalanche of electrons. The front plate of the MCPs is charged to approximately −920 V and it was pulsed to minimise background. The back plate of the MCPs was charged to 920 V. A P43 phosphor screen was positioned after the back MCP plate which emits light upon electron impact. This light is recorded by a charge coupled device (CCD) camera and it is also monitored by the photoelectron multiplier. Usually 5-10 sets of images for each polarisation were collected to construct a normalised difference image. An individual H or V ion-image is a result of approximately 20,000 laser shots.

6.2.5 Detection probability

The intensity at a certain (x, y) point on the detector is determined by a multitude of factors which represents both the intrinsic properties of the chemical system of interest and the actual–extrinsic–characteristics of the experimental apparatus. They can be grouped into three main components. Firstly, the scattering intensity $P_{f\leftarrow i}(\theta)$ where θ is the scattering angle, that is the angle between the initial and final relative velocities. The $f \leftarrow i$ notation stands for $|j, \Omega, \epsilon\rangle \rightarrow |j', \Omega', \epsilon'\rangle$ transition, but for the sake of brevity this will be abbreviated as $j \rightarrow j'$. The transition probability also depends on the collision induced alignment represented by the term $P_{\mathrm{V/H}}(\theta, \Gamma_{\mathrm{V/H}}; j', j^*)$ where $\Gamma_{\mathrm{V/H}}$ stands for the Euler angles which relate the scattering frame to the laser frame which will be discussed later in Chapter 7. The polarisation dependent differential cross sections (PDDCSs) determine the exact behaviour of $P_{\mathrm{V/H}}(\theta, \Gamma_{\mathrm{V/H}}; j', j^*)$, which were introduced in Chapter 2. j^* is the rotational state to which the dye laser excites the NO(X) molecule after the collision with the Ar atom. The apparatus function, $z(x, y, j, j', j^*, \Gamma_{\mathrm{V/H}})$, expresses the probability that a molecule undergoing the $|j\rangle \rightarrow |j'\rangle$ transition is detected at the position (x, y) on the

detector.

Since velocity map imaging is applied, every ionised particle having the velocity (v_x, v_y, v_z) is projected onto the same (x, y) point on the detector to a good approximation. The interaction region is defined by the intersection of the molecular beams. Both of them have a finite spatial spread leading to a finite interaction region, whose points are related to its origin by the position vector $\boldsymbol{r}_{\mathrm{det}}$. The velocities of the NO and argon, 'Ar', beams are denoted by $\boldsymbol{v}_{\mathrm{NO}}$ and $\boldsymbol{v}_{\mathrm{Ar}}$, respectively. Their moduli vary according to the $f_{t_{\mathrm{NO}}}(v_{\mathrm{NO}})$ and $f_{t_{\mathrm{Ar}}}(v_{\mathrm{Ar}})$ normalised probability distribution functions.

The NO molecules originate from a position, $\boldsymbol{r}_{\mathrm{NO}}$, in the plane which separates the skimmer from the scattering chamber. $\boldsymbol{r}_{\mathrm{NO}}$ expresses the change in number density perpendicular to the main direction of the propagation across the molecular beam. The molecules travel towards the centre of the scattering chamber with a velocity, $\boldsymbol{v}_{\mathrm{NO}}$, which has a finite spread. Thus their number density depends on both their origin and velocity which is represented by $n(\boldsymbol{r}_{\mathrm{NO}}, \boldsymbol{v}_{\mathrm{NO}}, t_{\mathrm{NO}})$ at a time t_{NO}. It is assumed the lengths of the laser pulses are much shorter than that of the molecular beam pulse, so that the molecules are excited and ionised instantaneously. This is in fact true, since the duration of a laser pulse is of the order of 10 ns while the beam pulse is approximately 180 μs long. Likewise, the number density of the rare gas atoms is given by $n(\boldsymbol{r}_{\mathrm{Ar}}, \boldsymbol{v}_{\mathrm{Ar}}, t_{\mathrm{Ar}})$.

The $(1 + 1')$ REMPI requires sufficient power from both of the laser beams. As a consequence, the probabilities of the A $\leftarrow$ X transition and the subsequent ionisation depend on the profile of the laser beams as well as on their spatial position and the time at which the laser fires. This probability is accounted for by the $P(\boldsymbol{r}_{\mathrm{det}})$ factor. The total intensity will thus be the integral over the velocity distributions, the initial number densities, the scattering probability and the transition probability over the whole

interaction region and the entire interaction time:

$$
\begin{aligned}
I(x,y) &= \int\int\int\int\int\int\int n_{\mathrm{NO}}\left(\boldsymbol{r}_{\mathrm{NO}},\boldsymbol{v}_{\mathrm{NO}},t'_{\mathrm{NO}}\right) n_{\mathrm{Ar}}\left(\boldsymbol{r}_{\mathrm{Ar}},\boldsymbol{v}_{\mathrm{Ar}},t'_{\mathrm{rg}}\right) \\
&\times f_{t_{\mathrm{NO}}}(v_{\mathrm{NO}}) f_{t_{\mathrm{Ar}}}(v_{\mathrm{Ar}}) \frac{v_{\mathrm{rel}}}{v'_{\mathrm{NO}}} \sigma_{f\leftarrow i}(v_{\mathrm{rel}}) P(\boldsymbol{r}_{\mathrm{det}}) P_{\mathrm{scat}}(\theta) P_{\mathrm{V/H}}\left(\Gamma_{\mathrm{V/H}}\right) \\
&\times \delta\left(t_{\mathrm{NO}}-t'_{\mathrm{NO}}\right)\delta\left(t_{\mathrm{Ar}}-t'_{\mathrm{Ar}}\right)\mathrm{d}t'_{\mathrm{NO}}\mathrm{d}t'_{\mathrm{Ar}}\mathrm{d}v_{\mathrm{NO}}\mathrm{d}v_{\mathrm{Ar}}\mathrm{d}t_{\mathrm{coll}}\mathrm{d}\boldsymbol{r}_{\mathrm{coll}}\mathrm{d}\boldsymbol{r}_{\mathrm{det}}.
\end{aligned}
\tag{6.8}
$$

The two Dirac delta functions ensure that both particles are at a position, $\boldsymbol{r}_{\mathrm{det}}$ at the time of the collision t_{coll}. The total cross section $\sigma_{f\leftarrow i}$ expresses the transition probability from the initial state j to the final state j'. $\frac{v_{\mathrm{rel}}}{v'_{\mathrm{NO}}}$ is the ratio of the final velocity of the NO molecule and the initial relative velocity which is needed to obtain the correct flux of the scattered molecules.

6.2.6 Determination of the apparatus function

In order to calculate the apparatus function, the velocity spreads, the laser time delay and the laser spatial intensity profiles have to be known. The determination of these factors has been previously discussed in [142, 156]. The moduli of the NO and Ar beam velocities were calculated using Eq. (6.6) and they were 625 ms^{-1} for the NO and 580 ms^{-1} for the Ar. The velocity distribution of the beams can be estimated by taking velocity mapped ion-images of unscattered beams. The Ar beam has to be seeded with a small amount of nitric oxide in order to image it. The mass of the NO is lower than that of the Ar thus the velocity distribution is slightly changed. However, the amount of the NO was kept minimal, so it is plausible to assume it had negligible effect. The intensity distribution of the beam on the detector can be linked to the velocity distribution, which is approximated by a Gaussian function. If the velocity to pixel ratio is known, the full width at half maximum of the velocity distribution can be read and calculated from the image as shown in the left panel of Figure 6.3. The time profile of a beam can be measured by changing the time delay of the laser with respect to the firing time of the beam in question. Scanning over a sufficiently long period of time allows the full temporal profile of the beam to be drawn

by measuring the total light intensity from the phosphor screen. This can then be fitted by a Gaussian function from which the full width at half maximum is retrieved.

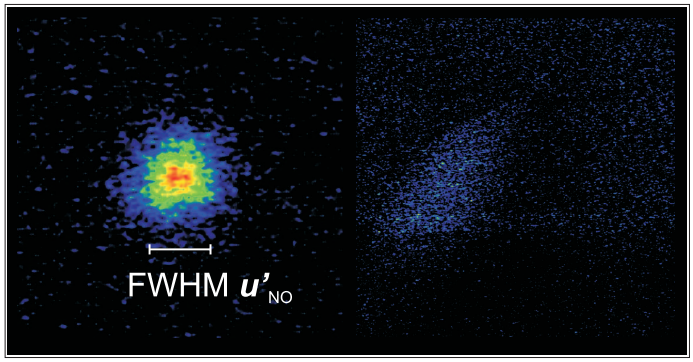

Figure 6.3: The velocity mapped image of the state selected $|0.5, 1/2, -1\rangle$ NO(X) beam (left panel). The intensity distribution can be approximated by a 2D Gaussian function. The full width at half maximum, FWHM, of the NO(X) beam's velocity is indicated by the white bar. The spatial image of the detection volume (right panel).

The detection volume is defined as the spatial overlap of the excimer and dye lasers. This can be determined by taking a spatial image of the ionised NO beam. The dimensions of the laser beams can be inferred from the intensity pattern of the image similar to that shown in the right panel of Figure 6.3. The molecules which are in the most intense regions of the laser overlap are most likely to be ionised, thus various parts of the interaction region are sampled with non uniform probability. Since the detection volume is smaller than the interaction region, the position of the laser beams is important to maximise the signal intensity and to reproduce the apparatus function correctly. In an idealised scattering experiment the apparatus function is uniform such that it is a projection of a sphere onto a plane. In the case of an idealised experiment, the spatial and temporal spreads of the molecular and laser beams are infinitely short and the beams themselves are confined to the same place. As a consequence, all scattering events happen in the shortest possible time exactly in the same pointlike interaction region. As such, it is axially symmetric and the intensity is greatest around the rim due to the Abel transform [157] as shown in the left panel of Figure 6.4. An apparatus function characteristic to the experiments is shown in the second panel of Figure 6.4. The initial relative velocity, $\boldsymbol{k}$, points from the bottom right to the top left. The apparatus function is asymmetric with respect to $\boldsymbol{k}$.

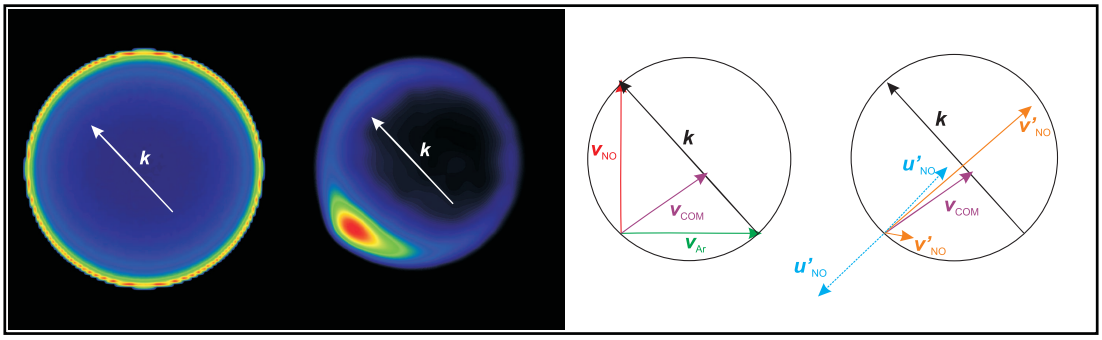

Figure 6.4: An ideal apparatus function (left panel), apparatus function for the $|0.5, 1/2, -1\rangle \rightarrow |8.5, 1/2, -1\rangle$ transition (second panel). The lab frame and centre of mass velocities are shown in the third panel, which explains the origin of the slow and fast lab frame velocities in the right panel. The lab frame and centre-of-mass velocities are denoted by $\boldsymbol{v}$ and $\boldsymbol{u}$, respectively.

The intensity enhancement in the bottom diagonal of the image implies a molecule is more likely to be detected if its final relative velocity, $\boldsymbol{k'}$, makes an angle of about $\pi/2$ with the initial relative velocity. This phenomenon stems from the transformation between the centre of mass frame and lab frame velocities. The centre of mass travels with the lab frame velocity, v_{COM}, towards the right corner of the image in the middle panel of Figure 6.4. The lab frame velocity of the scattered NO is the sum of $\boldsymbol{v}_{\mathrm{COM}}$, and the final centre-of-mass velocity of NO, $\boldsymbol{u}'_{\mathrm{NO}}$. If $\boldsymbol{u}'_{\mathrm{NO}}$ is roughly parallel to $\boldsymbol{v}_{\mathrm{COM}}$ the particle's lab frame velocity is greater, therefore it can leave the detection volume faster. As a consequence, the probability of being ionised and detected has been reduced. Since these particles have higher speeds, this (the upper) side of the image is called fast side. On the other hand, those NO molecules which are scattered with a velocity antiparallel to the v_{COM} have smaller lab frame velocities. They spend more time in the detection volume, thus it is more likely they obtain sufficient laser power to be ionised when it fires. It follows that these molecules will be detected with a higher probability, leading to the enhancement of the instrument function in the bottom diagonal with respect to $\boldsymbol{k}$. This is referred to as the slow side.

6.3 Summary

In this chapter, the experimental methods employed in this work have been reviewed. The hexapole state selective ion-imaging apparatus enables us to investigate the rotational polarisation effects in NO(X)+Ar collisions. The outcome of the experiment is an ion-image, which both embodies intrinsic information about the molecular system, and depends on the actual circumstances of the measurement. The algorithm by means of which it is possible to extract polarisation information, namely the PDDCSs, from the ion-images will be developed in the following chapter. The experimentally retrieved alignment moments will also be shown and interpreted.

Chapter 7

Analysis of the rotational alignment effects in inelastic collisions of NO(X) and Ar

The rotational alignment effects in the inelastic NO(X)–Ar collisions have been investigated by means of a hexapole state selective velocity mapped ion imaging apparatus. The working principles and the relevant details of the experimental work were described in Chapter 6. In the case of the alignment measurements, the polarisation of the dye laser was flipped between horizontal (H) and vertical (V), with respect to the plane of the molecular beams, for subsequent images. Taking the normalised difference (V−H)/(V+H) of the ion-images collected, the degree of the rotational alignment of the molecules can be extracted. It is quantified by the renormalised polarisation dependent differential cross sections (PDDCSs), $\rho_{q\pm}^{\{k\}}$, introduced in Chapter 3.

A novel algorithm has been developed to retrieve the renormalised PDDCSs from the normalised difference images based on the Fourier moment method [142, 158]. The algorithm is universal such that it is capable of extracting both alignment and orientation PDDCSs from experimental normalised difference images recorded using, in general, any kind of elliptically polarised light. The algorithm and the formalisms, on which it is built, are discussed in this chapter.

The experimental normalised difference images were collected for the NO(X)–Ar rotationally inelastic collisions which are characterised and interpreted. The alignment po-

larisation dependent differential cross sections were extracted, and used to elucidate the underlying mechanism responsible for the observed rotational alignment. The experimental results are in line with the findings of the theoretical work, that is the rotational alignment is due to the inherently hard shell nature of the interaction potential.

The experimental ion-images were collected by Helen Chadwick and Bethan Nichols. I gratefully acknowledge their contribution to this work.

7.1 Overview

The majority of the studies concerning NO(X)–rare gas scattering have focussed on the determination of the integral cross sections [98, 102, 159–168] and differential cross-sections [43, 66, 98, 110, 134, 142, 145, 169–177]. Most of the measurements cited above were only resolved in the final Λ-doublet level. The hexapole focussing, which was discussed in detail in the previous chapter, has been used to select a particular Λ-doublet level of the NO(X) before the collision. The fully state selected integral cross sections [159, 160] and differential cross sections have been measured for the rotationally inelastic scattering of NO(X) with helium [145], neon [178] and argon [66, 142].

It has been found that the structure of the experimental DCS depends on the parity changing or conserving nature of the collision of NO(X) with rare gases [43, 66, 134, 142, 145, 169]. These results are in line with the previous theoretical studies. The parity conserving transitions have DCSs with multiple maxima, whilst those for parity changing transitions have only a single maximum for NO(X)–Ar collisions. These observations were interpreted in terms of the semiclassical formalism based on the work of Schinke [63] and Eyles [134]. The experimental DCSs were found to be in excellent agreement with the theoretical DCSs [66, 142] obtained on the potential energy surface of Alexander [102].

The rotational polarisation effects in the rotationally inelastic collisions of NO(X)–rare gas system have been studied less extensively. The collision induced alignment in the collisions NO(X)–He has been measured by Meyer [24]. He used a counterpropagating

molecular beam setup, thus the experiment was only sensitive to the alignment with respect to the initial relative veloty. The scattered NO(X) molecules were probed by (2+1) resonance enhanced multiphoton ionisation (REMPI) and the time of flight spectra were recorded. The renormalised PDDCSs were retrieved by analysing the time-of-flight profiles of the detected NO^+ ions. The $\rho_0^{\{2\}}(\theta)$ parameters were also determined for NO(X)–Ne collisions [20, 21]. The experimental alignment parameters were found to be in good agreement with those obtained from exact close-coupled quantum mechanical (CC QM) calculations [20, 21, 24, 179]. They also agreed with those predicted based on the simple classical kinematic apse model [22, 80, 143].

The collision induced rotational polarisation of NO(X) with argon has been experimentally investigated. Both rotational orientation [180] and rotational alignment have been measured by Chandler *et al.* [19, 181]. They used a crossed molecular beam apparatus coupled with velocity mapped ion imaging to record normalised difference images for a selection of spin–orbit conserving transitions. The initial quantum state of the NO(X) was not resolved in Λ-doublet levels. The rotationally excited NO(X) molecules were probed with $(1 + 1')$ REMPI on the R_{21} branch, which probes the $\epsilon' = -1, (-1)$ Λ-doublet level. The experimental geometry allowed both $\rho_0^{\{2\}}(\theta)$ and $\rho_{2+}^{\{2\}}(\theta)$ to be measured. The theoretical renormalised PDDCSs systematically overestimated the degree of polarisation for both polaristion parameters. The discrepancies between the theoretical and experimental data were more pronounced in the sideways and backward scattered regions. Therefore it was speculated that the short range, repulsive region of the V_{sum} potential, on which the spin-orbit conserving transitions primarily happen (see Chapter 2), might be slightly inaccurate.

7.2 Fano–Macek formalism

Rotational polarisation of the NO(X) molecule is parameterised in the scattering frame, which was defined in Chapter 3 and is shown in the left hand panel of Figure 7.1. It is a

right handed frame, in which the principal axis, $\hat{\boldsymbol{z}}$, is parallel to the initial relative velocity of the collision partners, $\boldsymbol{k}$. The molecule is always scattered to the $+xz$ half of the plane. It is convenient to introduce the so-called detector frame according to Fano and Macek [77] whose principal axis, $\hat{\boldsymbol{\zeta}}$, is parallel to the propagation axis of the laser which induces the $j_f \leftarrow j_i$ transition. The major component of the electric vector of this laser, $\hat{\boldsymbol{\epsilon}}$, is always parallel to the first axis, $\hat{\boldsymbol{\xi}}$. The second axis, $\hat{\boldsymbol{\eta}}$, is chosen so that the $(\hat{\boldsymbol{\xi}}, \hat{\boldsymbol{\eta}}, \hat{\boldsymbol{\zeta}})$ frame is right handed as shown in the right hand panel of Figure 7.1. Therefore the electric vector of the laser can be written as $\hat{\boldsymbol{\epsilon}} = (\cos\beta, i\sin\beta, 0)$, where β is the angle between $\hat{\boldsymbol{\xi}}$ and $\hat{\boldsymbol{\epsilon}}$. If the laser light is linearly polarised, the electric vector always lies on the $\hat{\boldsymbol{\xi}}$ axis. In the case of right or left circularly polarised light it makes an angle of $\beta = \pm\pi/4$ with the $\hat{\boldsymbol{\xi}}$ axis, respectively. In the case of elliptically polarised light, that is neither linearly nor circularly polarised light, the modulus of β is less than $\pi/4$. The scattering frame and the detector frame are related by the angles (Θ, ϕ, χ), where Θ and ϕ are the polar angle and the azimuth of $\hat{\boldsymbol{\zeta}}$ in the scattering frame, respectively. The third angle, which is required to specify the relative orientation of the two frames, is denoted by χ.

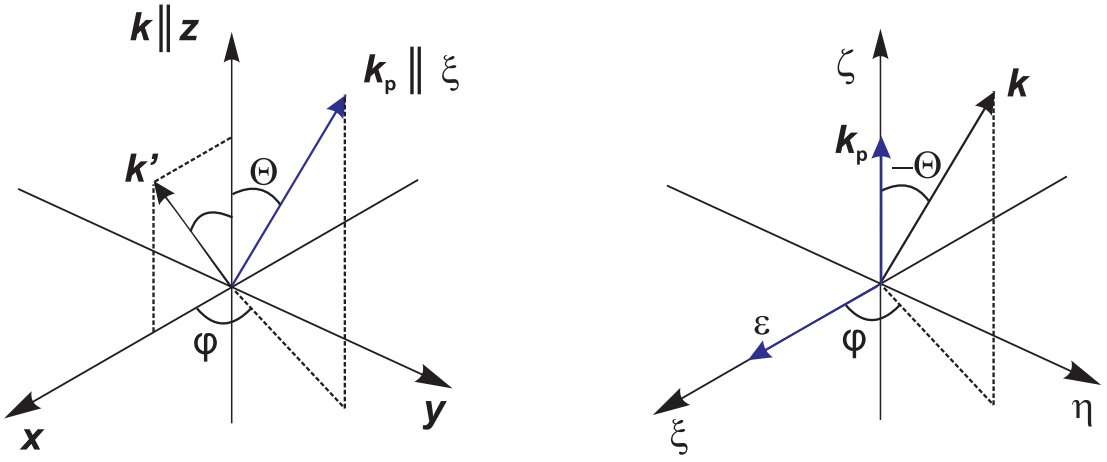

Figure 7.1: The scattering and the detector frames. The principal axis of the detector frame, $\hat{\boldsymbol{\zeta}}$, is parallel to the dye laser's propagation direction and it is related to the $\hat{\boldsymbol{z}}$ axis of the scattering frame by the angles (Θ, ϕ).

Fano and Macek derived a formula for the intensity of the $j_i \rightarrow j_f$ one photon transition

in a rotationally polarised medium [77]:

$$\begin{aligned} I &= CS\left[1+\tfrac{3}{2}h^{(1)}\left(j_i,j_f\right)O_0^{\mathrm{det}}\sin(2\beta)\right. \\ &\quad \left.-\tfrac{1}{2}h^{(2)}\left(j_i,j_f\right)A_0^{\mathrm{det}}+\tfrac{3}{2}h^{(2)}\left(j_i,j_f\right)A_{2+}^{\mathrm{det}}\cos(2\beta)\right]\,, \end{aligned} \tag{7.1}$$

where C is a constant which converts the transition probability to a power flux [77]. S is a line strength, and $h^{(k)}(j_i,j_f)$ is a line strength factor for the polarization moment of rank k, and is defined in Eq. (7.2) [77]:

$$h^{(k)}(j_i,j_f)=(-1)^{j_i-j_f}\begin{Bmatrix} j_i & j_i & k \\ 1 & 1 & j_f \end{Bmatrix}\Big/\begin{Bmatrix} j_i & j_i & k \\ 1 & 1 & j_i \end{Bmatrix}\,. \tag{7.2}$$

The first and second rank real polarisation parameters, O_0, $A_{q\pm}$ are defined in terms of the expectation values of the real combination of the spherical tensor operators, $\hat{J}_q^{(k)}$ of the angular momentum:

$$O_0^{\mathrm{det}} = \frac{\langle j_z\rangle}{\langle j^2\rangle}=\frac{\langle\hat{J}_0^{(1)}\rangle}{\langle\hat{\boldsymbol{j}}^2\rangle} \tag{7.3}$$

$$A_0^{\mathrm{det}} = \frac{\langle 3\hat{j}_z^2-\hat{j}^2\rangle}{\langle\hat{j}^2\rangle}=\sqrt{6}\frac{\langle\hat{J}_0^{(2)}\rangle}{\langle\hat{\boldsymbol{j}}^2\rangle} \tag{7.4}$$

$$A_{2+}^{\mathrm{det}} = \frac{\langle\hat{j}_x^2-\hat{j}_y^2\rangle}{\langle\hat{j}^2\rangle}=\frac{\langle J_{+2}^{(2)}+\hat{J}_{-2}^{(2)}\rangle}{\langle\hat{\boldsymbol{j}}^2\rangle}=2\frac{Re\langle\hat{J}_{+2}^{(2)}\rangle}{\langle\hat{\boldsymbol{j}}^2\rangle}\,. \tag{7.5}$$

These formulae will play a central role in developing the algorithm by means of which the orientation and alignment renormalised PDDCSs can be recovered from experimental normalised difference ion-images.

However, other authors worked out similar formulae for the polarisation dependence of electronic transitions which are also in use [79, 182–184], especially that of Suzuki and Mo [185]. The relationship between the Fano–Macek and Suzuki–Mo treatment will be derived in Appendix C.

7.3 Modelling

The algorithm developed in this work combines the formalism of Fano and Macek [77], reviewed in the previous section, and the method of fitting in Fourier moment space [134, 156, 158]. Its key concept is to factor the overall polarisation effects according to the contributions of the various renormalised PDDCSs. The renormalised PDDCSs are then expressed in terms of a series expansion which enables the construction of a basis image for an individual expansion order. The normalised difference images are obtained as a linear combination of these basis images where the expansion coefficients are identical to those of the renormalised PDDCSs. The objective of the fitting is to find the combination of these coefficients which maximises the overlap between the experimental and simulated image in Fourier space. Having accomplished this task the renormalised PDDCSs can be generated from the expansion coefficients.

7.3.1 Construction of polarisation dependent basis functions

The total intensity on a certain (x, y) pixel of the detector can be represented as a convolution of three terms as shown in Eq. (6.8) in Section 6.2.5. The intensity of a single scattering event, labelled by the index n, which impacts on the (x_n, y_n) position of the detector, $\imath_{\mathrm{V/H}}(x_n, y_n)$, can thus be given as a product of three terms,

$$\imath_{\mathrm{V/H}}(x_n, y_n) = z(x_n, y_n)\, P_{\mathrm{scat}}(\theta_n)\, P_{\mathrm{V/H}}(\theta_n; \Gamma^n_{\mathrm{V/H}})\,, \tag{7.6}$$

where $z(x_n, y_n)$ is the apparatus function for the (x_n, y_n) pixel, $P_{\mathrm{scat}}(\theta_n)$ is the angular distribution function which is proportional to the differential cross section and $P_{\mathrm{V/H}}(\theta_n; \Gamma^n_{\mathrm{V/H}})$ is the polarization dependent transition probability for the 'H' and 'V' polarisations of the dye laser. $\Gamma_{\mathrm{V/H}} = (\chi, \Theta, \phi)$ are the orientation angles which relate the detector frame to the scattering frame defined in the previous section.

Let us rewrite the Fano–Macek intensity formula [77] in terms of real polarisation

parameters [15]:

$$\begin{aligned} I &= CS\Big[1+\tfrac{3}{2}h^{(1)}\left(j_i,j_f\right)A_0^{\{1\}\mathrm{det}}\sin(2\beta)/\sqrt{j_i(j_i+1)} \\ &\quad -\tfrac{1}{2}h^{(2)}\left(j_i,j_f\right)A_0^{\{2\}\mathrm{det}}+\tfrac{\sqrt{3}}{2}h^{(2)}\left(j_i,j_f\right)A_{2+}^{\{2\}\mathrm{det}}\cos(2\beta)\Big]\,, \end{aligned} \tag{7.7}$$

where the meaning of the C, S and $h^{(k)}(j_i,j_f)$ are identical to those given previously in Section 7.2. The standard polarisation parameters are related to those of Fano and Macek with the aid of Table C.1 in Appendix C, so that $A_0^{\{2\}\mathrm{det}} \equiv A_0^{\mathrm{det}}$ and $A_{2+}^{\{2\}\mathrm{det}} \equiv A_{2+}^{\mathrm{det}} \times \sqrt{3}$, and $A_0^{\{1\}\mathrm{det}} \equiv O_0^{\mathrm{det}} \times \sqrt{j_i(j_i+1)}$, respectively. These definitions are identical to those of Fano and Macek apart from the coefficient of $1/\sqrt{3}$ in front of the parameter $A_{2+}^{\{2\}\mathrm{det}}$, due to the non-standard normalization they used for their alignment parameters [77]. The frame in which these parameters are defined is the detector frame introduced in Section 7.2 and they are referred to by the superscript 'det'. The scattering frame is related to the detector frame through a rotation by the angles $\Gamma_{\mathrm{V/H}} = (\chi,\Theta,\phi)$ for which a constructive definition was provided in Section 7.2. The superscripts 'V/H' discern between the two angles which relates the scattering frame to the detector frame when either vertically or horizontally polarised light is employed. In general, they are used to denote different laser polarisations. As our main interest lies in the alignment effects, the subscripts 'V' and 'H' will be used throughout this chapter, but they should be understood in a broader sense. The primary frame used in this thesis is the scattering frame, so the detector frame moments have to be rotated to this frame. Fano and Macek provided formulae to rotate real polarisation parameters, which are adapted to standard parameters:

$$A_0^{\{1\}\mathrm{det}} = A_{1-}^{\{1\}}\,\sin\Theta\sin\varphi \tag{7.8}$$

$$A_0^{\{2\}\mathrm{det}} = A_0^{\{2\}}\tfrac{1}{2}\left(3\cos^2\Theta-1\right)+A_{1+}^{\{2\}}\tfrac{\sqrt{3}}{2}\sin 2\Theta\cos\varphi+A_{2+}^{\{2\}}\tfrac{\sqrt{3}}{2}\sin^2\Theta\cos 2\varphi \tag{7.9}$$

$$\begin{aligned} A_{2+}^{\{2\}\mathrm{det}} &= A_0^{\{2\}}\tfrac{\sqrt{3}}{2}\sin^2\Theta\cos 2\chi \qquad (7.10)\\ &+ A_{1+}^{\{2\}}\left[\sin\Theta\cos\varphi\sin 2\chi+\sin\Theta\cos\Theta\sin\varphi\cos 2\chi\right] \\ &+ A_{2+}^{\{2\}}\left[\tfrac{1}{2}\left(1+\cos^2\Theta\right)\cos 2\varphi\cos 2\chi-\cos\Theta\sin 2\varphi\sin 2\chi\right]\,, \qquad (7.11) \end{aligned}$$

where again the $1/\sqrt{3}$ factor has been taken into account in the terms containing the $A_{1+}^{\{2\}\mathrm{det}}$ and $A_{2+}^{\{2\}\mathrm{det}}$ parameters.

Analogous relationships are readily obtained between the renormalised PDDCSs, $\rho_{q\pm}^{\{k\}}(\theta)$, and the scattering angle resolved polarisation parameters with the aid of Table C.1, where θ is the scattering angle,

$$
\begin{aligned}
A_0^{\{1\}\mathrm{det}}(\theta) &= c_1(j_i)\rho_{1-}^{\{1\}}(\theta)\sin\Theta\sin\varphi && (7.12)\\
A_0^{\{2\}\mathrm{det}}(\theta) &= c_2(j_i)\Big\{\rho_0^{\{2\}}(\theta)\tfrac{1}{2}\left(3\cos^2\Theta-1\right) && (7.13)\\
&\quad + \rho_{1+}^{\{2\}}(\theta)\tfrac{\sqrt{3}}{2}\sin 2\Theta\cos\varphi + \rho_{2+}^{\{2\}}(\theta)\tfrac{\sqrt{3}}{2}\sin^2\Theta\cos 2\varphi\Big\} && (7.14)\\
A_{2+}^{\{2\}\mathrm{det}}(\theta) &= c_2(j_i)\Big\{\rho_0^{\{2\}}(\theta)\tfrac{\sqrt{3}}{2}\sin^2\Theta\cos 2\chi && (7.15)\\
&\quad + \rho_{1+}^{\{2\}}(\theta)\left[\sin\Theta\cos\varphi\sin 2\chi + \sin\Theta\cos\Theta\sin\varphi\cos 2\chi\right]\\
&\quad + \rho_{2+}^{\{2\}}(\theta)\left[\tfrac{1}{2}\left(1+\cos^2\Theta\right)\cos 2\varphi\cos 2\chi - \cos\Theta\sin 2\varphi\sin 2\chi\right]\Big\}\,.
\end{aligned}
$$

The $c_k(j_i)$ normalisation factors serve as the proportionality constants between the polarisation parameters and the renormalised PDDCSs. Their explicit values are $c_1(j_i) = [j_i(j_i+1)]^{-1/2}$ and $c_2(j_i) = [(2j_i+3)(2j_i-1)/(j_i(j_i+1))]^{1/2}$ which can be found in Table C.1 [11, 16]. Therefore each detector frame scattering angle resolved polarisation parameter can be expressed in terms of a linear combination of the scattering frame renormalised PDDCSs, thus the polarisation dependent transition intensity itself can be written as a linear function of the orientation and alignment renormalised PDDCSs. The coefficients for a particular renormalised PDDCS of rank k and component q, $\rho_{q\pm}^{\{k\}}(\theta)$, are grouped into a function, $F_{q\pm}^{\{k\}}(\Gamma_{\mathrm{V/H}}^n,\beta)$. These functions embody all the geometrical information which is necessary to calculate the contribution of a $\rho_{q\pm}^{\{k\}}(\theta)$ to the total polarisation dependent intensity. There is one $F_{q\pm}^{\{k\}}(\Gamma_{\mathrm{V/H}}^n,\beta)$ function for the orientation and three $F_{q\pm}^{\{k\}}(\Gamma_{\mathrm{V/H}}^n,\beta)$ functions for the alignment renormalised PDDCSs. These are defined

as follows:

$$F_{1-}^{\{1\}}(\Gamma_{\mathrm{V/H}}^{n},\beta) = \frac{3}{2}h^{(1)}(j_i,j_f)c_1(j_i)\sin\Theta\sin\phi\sin(2\beta) \tag{7.16}$$

$$F_{0}^{\{2\}}(\Gamma_{\mathrm{V/H}}^{n},\beta) = \tfrac{1}{4}h^{(2)}(j_i,j_f)c_2(j_i)\left[3\sin^2\Theta_n\cos 2\chi\cos 2\beta - \left(3\cos^2\Theta_n - 1\right)\right] \tag{7.17}$$

$$F_{1+}^{\{2\}}(\Gamma_{\mathrm{V/H}}^{n},\beta) = \tfrac{\sqrt{3}}{4}h^{(2)}(j_i,j_f)c_2(j_i)\left[2\sin\Theta_n\cos\varphi_n\sin 2\chi\right. \tag{7.18}$$

$$\left. +2\left(\sin\Theta_n\cos\Theta_n\sin\varphi_n\cos 2\chi - \sin 2\Theta_n\cos\varphi_n\right)\cos(2\beta)\right] \tag{7.19}$$

$$F_{2+}^{\{2\}}(\Gamma_{\mathrm{V/H}}^{n},\beta) = \tfrac{\sqrt{3}}{4}h^{(2)}(j_i,j_f)c_2(j_i)\left[\left[\left(1+\cos^2\Theta_n\right)\cos 2\varphi_n\cos 2\chi\right.\right.$$

$$\left.\left. -\ 2\cos\Theta_n\sin 2\varphi_n\sin 2\chi\right]\cos(2\beta) - \sin^2\Theta_n\cos 2\varphi_n\right]\ . \tag{7.20}$$

The $F_{q\pm}^{\{k\}}(\Gamma_{\mathrm{V/H}}^{n},\beta)$ functions depend on the polarisation of the laser in two ways in Eqs. (7.16)–(7.20). There is an indirect dependence on β, the polarisation angle of the electric vector of the laser. It is readily seen that the rotational orientation cannot be probed by linearly polarised light when $\beta = 0$, for the $\sin(2\beta)$ factor vanishes. On the other hand, the experiment is most sensitive to the rotational orientation if circularly polarised light is employed. The polarisation also manifests itself through the $\Gamma_{\mathrm{V/H}}$ angles. Θ and ϕ are identical for a particular laser geometry since they are the orientation angles of the laser propagation axis, however, the third angle χ takes different values for alternative laser polarisations. Since usually, β can only take constant values in a particular experiment apart from negligible experimental fluctuations, the argument, β, will be supressed in the following for sake of brevity.

The Fano–Macek intensity formula in Eq. (7.1) is recast in terms of geometrical functions, where the summation runs over the non vanishing renormalised PDDCSs in Eq. (7.21). In the case of an alignment measurement, these are the $\rho_{q+}^{\{2\}}(\theta)$, and in case of the orientation measurements, also the $\rho_{1-}^{\{1\}}(\theta)$ renormalised PDDCSs.

$$P_{\mathrm{V/H}}(\theta_n;\Gamma_{\mathrm{V/H}}^{n}) = CS\left[1+\sum_{kq}\rho_{q\pm}^{\{k\}}(\theta_n)F_{q\pm}^{\{k\}}(\Gamma_{\mathrm{V/H}}^{n})\right] \tag{7.21}$$

Series expansion of the renormalised PDDCSs

In the framework of the Fourier moment method, the differential cross sections were given in terms of a series expansion [134, 156]. The expansion coefficients were retrieved by fitting experimental images by basis set images which corresponded to the various expansion orders. Having accomplished the fitting, the DCSs were reconstructed from the expansion coefficients [134, 156].

Because of the robustness and speed of this approach it is now extended to retrieve information about polarisation dependent effects. In doing so the key step is to expand the $\rho_{q\pm}^{\{k\}}$ renormalised PDDCSs:

$$\rho_{q\pm}^{\{k\}}(\theta_n) = \sum_{l=0}^{N_{q\pm}^{\{k\}}} c_{q\pm,l}^{\{k\}}\, w_l\, W_l(\theta_n)\,, \tag{7.22}$$

where $W_l(\theta_n)$ constitute a suitable set of basis functions (*e.g.*, Legendre polynomials, spherical harmonics or Gaussian functions), $c_{q\pm,l}^{\{k\}}$ are the expansion coefficients, w_l are a set of known l-dependent normalization coefficients, and $N_{q\pm}^{\{k\}}$ is the maximum expansion order for the $\rho_{q\pm}^{\{k\}}$ renormalised PDDCSs.

The basis functions either can span over the entire scattering angle region from 0 to π, or they can be localised in a particular interval. Any kind of continuous polynomials are suitable to span the unlocalised basis, which are orthogonal in the $[\cos\pi, \cos 0] = [-1, 1]$ interval. This choice has the advantage that the renormalised PDDCSs can be decomposed into a sum of elementary functions. For instance, if the Legendre polynomials are chosen, the zeroth, first and second order contributions quantify the constant, linear and quadratic behaviour of a particular $\rho_{q\pm}^{\{k\}}(\theta)$ as function of the scattering angle. A main advantage of choosing an unlocalised basis is that a relatively low number of expansion coefficients suffice to describe the overall polarisation over the entire scattering angle region. However, if the $\rho_{q\pm}^{\{k\}}(\theta)$ of interest rapidly changes with θ, a high number of basis functions are required. It also could happen that the experimental signal to noise ratio is superior for some regions in the image than in others. If an unlocalised basis is employed, these

regions may distort the retrieved renormalised PDDCSs, since the fitting algorithm tries to approximate simultaneously the polarisation effects for the whole image. This can be mediated by excluding regions of the image having low signal-to-noise ratio, at the expense of losing the possibility of gaining any polarisation information in those regions. These problems can be avoided to a greater extent with localised basis sets. The basis functions are spatially more separated. As a consequence, different regions in the image can be fitted more independently. However, the adjacent basis functions might overlap, so that their expansion coefficients are not fully independent. A drawback of the localised basis function is that they are not necessarily orthogonal, thus they may introduce some redundancy in the fitting. A sequence of Gaussian functions with fixed full width at half maxima and centres is a simple example of the localised basis sets.

Construction of the basis functions

The original expression for the intensity in Eq. (7.6) can now be factored into terms according to the various renormalised PDDCSs, which are in turn given in terms of a series expansion according to Eq. (7.22). If Eq. (7.22) is merged with Eq. (7.21) and then substituted to Eq. (7.6) the expression for the intensity assumes the following form:

$$\imath_{\mathrm{V/H}}(x_n, y_n) \;=\; CS \left[P_{\mathrm{scat}}(\theta_n)\, z(x_n, y_n) + \sum_{k,q} \sum_{l=0}^{N_{q\pm}^{\{k\}}} c_{q\pm,l}^{\{k\}} g_{q\pm,l}^{\{k\}}(x_n, y_n, \theta_n; \Gamma_{\mathrm{V/H}}^n) \right] \quad (7.23)$$

where

$$g_{q\pm,l}^{\{k\}}(x_n, y_n, \theta_n; \Gamma_{\mathrm{V/H}}^n) = w_l\, W_l(\theta_n)\, F_{q\pm}^{\{k\}}(\Gamma_{\mathrm{V/H}}^n)\, z(x_n, y_n)\, P_{\mathrm{scat}}(\theta_n)\,, \quad (7.24)$$

which are the key expressions in the development of our formalism. The total intensity in Eq. (7.23) separates into two terms. $P_{\mathrm{scat}}(\theta_n)\, z(x_n, y_n)$ is proportional to the scattering intensity in the absence of polarisation effects. It also incorporates the apparatus function. Thus knowledge of the scattering intensity, $P_{\mathrm{scatt}}(\theta)$, is required prior to construction of the basis functions, which will be addressed in the subsequent section. The second term

in the square bracket in Eq. (7.23) manifests the effect of the rotational polarisation on the transition probability. The density-to-flux effects are also accounted for in this term, and it is, in theory, also dependent of the scattering intensity, $P_{\rm scatt}(\theta)$.

The total intensity in the (x, y) position of the experimental image $I_{\rm V/H}(x, y)$ is the outcome of many individual scattering events encountered during the collection of the image. As consequence, the basis image has to be constructed using a great number of trajectories, *i.e.* it is a sum of many $z(x_n, y_n)$ and $g(\theta_n; \Gamma^n_{\rm V/H})$ functions for individual scattering events,

$$I_{\rm V/H}(x, y) \;=\; \sum_n \imath_{\rm V/H}(x_n, y_n)\,. \tag{7.25}$$

An ion hit can spread over a number of pixels in the detector which should be taken into account. A Gaussian blurring was used to simulate this effect. Both the summation of the individual intensities and the blurring are linear, thus $I_{\rm V/H}(x, y)$ in Eq. (7.25) is still linear with respect to the $c^{\{k\}}_{q\pm,l}$ expansion coefficients of the renormalised PDDCSs. The summed and blurred intensity contribution of the l-th order basis of $\rho^{\{k\}}_{q\pm}(\theta)$ is denoted by $G^{\{k\},{\rm V/H}}_{q\pm,l}(x, y)$,

$$G^{\{k\},V/H}_{q\pm,l}(x, y) \;=\; \sum_n g^{\{k\}}_{q\pm,l}(x_n, y_n, \theta_n; \Gamma^n_{\rm V/H})\,, \tag{7.26}$$

whereas the summed and convoluted apparatus function is referred to as $Z(x, y)$,

$$Z(x, y) \;=\; \sum_n z(x_n, y_n)\,. \tag{7.27}$$

At this point it is insightful to consider the meaning of the $G^{\{k\}{\rm V/H}}_{q\pm,l}$ functions which are displayed in Figure 7.2 for an ideal experiment and assuming isotropic scattering intensity.

The velocities of the NO(X) and Ar beams are 625 $\rm ms^{-1}$ and 580 $\rm ms^{-1}$, respectively. The propagation vector of the dye laser is almost perpendicular to the relative velocity and it is linearly polarised so that the electric vector lies either in the plane of the molecular beams

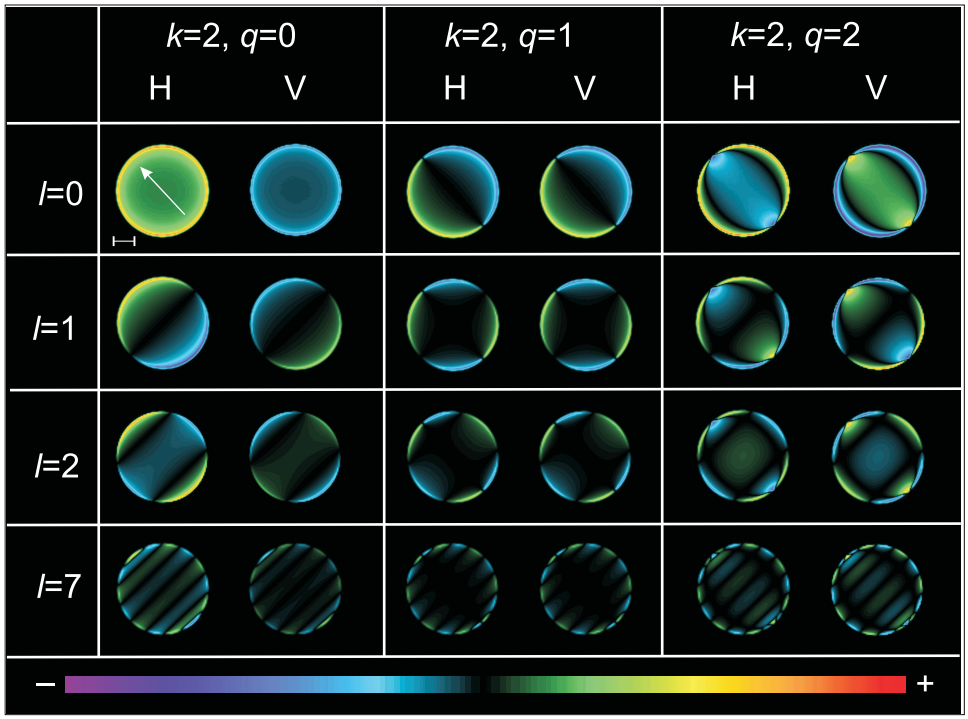

Figure 7.2: The $k = 2, q = 0$, $k = 2, q = 1$ and $k = 2, q = 2$ $G^{\{k\}\mathrm{V/H}}_{q\pm,l}$ functions for an idealised experiment are shown in the left, middle and right columns, respectively. The $l = 0, 1, 2,$ and 7-th order basis functions were chosen to demonstrate how the intensity changes across the image for horizontal (H) and vertical (V) polarisations. Note that scales of the $G^{\{2\}\mathrm{V/H}}_{1\pm,l}$ and $G^{\{2\}\mathrm{V/H}}_{1\pm,l}$ functions are multiplied by a factor of 1000.

for horizontal polarisation or perpendicular to that for vertical polarisation. The angle between the laser propagation axis and the relative velocity is approximately 92°. The $l = 0, 1, 2$ and 7 order $G^{\{k\}\mathrm{V/H}}_{q\pm,l}$ functions are shown for both polarisations in Figure 7.2. The zeroth order Legendre polynomial is unity. The Legendre polynomials of order $l > 1$ change sign $l + 1$ times which is responsible for the alternating intensity pattern along the initial relative velocity. The zeroth order functions, $G^{\{2\}\mathrm{V/H}}_{q\pm,0}$, represents the contribution of the respective renormalised PDDCSs to the total intensity, in the hypothetical case when they assume their maximum limiting value. The horizontal $k = 2$, $q = 0$ image is a constant positive function apart from the radial enhancement of the intensity due to the Abel transform. This reflects positive alignment of $\boldsymbol{j'}$ with respect to the horizontal electric vector. On the other hand, $G^{\{2\}\mathrm{V}}_{q\pm,0}$ is negative, since $\boldsymbol{j'}$ is aligned perpendicularly to the vertical electric vector. If $\hat{\boldsymbol{\xi}}$ is perfectly perpendicular to $\hat{\boldsymbol{k}}$ the experiment is insensitive to the $\rho^{\{2\}}_{1+}(\theta)$ parameter. Since $\hat{\boldsymbol{\xi}}$ is not exactly perpendicular to $\hat{\boldsymbol{k}}$ a small

contribution exists which is three orders of magnitude smaller than that of $\rho_0^{\{2\}}(\theta)$. The $G_{2+,l}^{\{2\}\mathrm{H}}$ functions exhibit a ϕ dependence, so that the variation of the intensity distribution perpendicular to $\hat{\boldsymbol{k}}$ provides information on the $\rho_{2+}^{\{2\}}$ renormalised PDDCSs. The intensity changes sign when the angle between the vertical polarisation vector and $\hat{\boldsymbol{x}}$ is $\pm 45°$. In the case of vertical polarisation the middle section of the image is positive which reflects parallel alignment of $\boldsymbol{j}$ with respect to $\hat{\boldsymbol{\epsilon}}$. The horizontal electric vector is very nearly perpendicular to the $\hat{\boldsymbol{x}}$ and $\hat{\boldsymbol{y}}$ axes, hence the $G_{2+,l}^{\{2\}\mathrm{H}}$ functions practically vanish for all order of l.

Returning to the derivation of the basis functions, the V and H images are again written as linear combinations of the $G_{q\pm,l}^{\{k\},\mathrm{V/H}}(x,y)$ and $Z(x,y)$ functions:

$$I_{\mathrm{V/H}}(x,y) = Z(x,y) + \sum_{k,q}\sum_{l} c_{q\pm,l}^{\{k\}} G_{q\pm,l}^{\{k\},\mathrm{V/H}}(x,y) \tag{7.28}$$

It is now straightforward to obtain both the sum and the difference of the V and H images with the aid of these functions. The basis set images for the (V−H)/(V+H) difference image of the l-th order expansion of $\rho_{q\pm}^{\{k\}}(\theta)$, $B_{q\pm}^{\{k\}}(x,y)$, is here defined in terms of the $G_{q\pm,l}^{\{k\},\mathrm{V/H}}(x,y)$ and $Z(x,y)$ functions

$$B_{q\pm,l}^{\{k\}}(x,y) \equiv \frac{G_{q\pm,l}^{\{k\},\mathrm{V}}(x,y) - G_{q\pm,l}^{\{k\},\mathrm{H}}(x,y)}{2P_{\mathrm{scat}}(\theta)\, Z(x,y) + \sum_{k,q}\sum_{l=0}^{N_{q\pm}^{\{k\}}} c_{q\pm,l}^{\{k\}}\left[G_{q\pm,l}^{\{k\},\mathrm{V}}(x,y) + G_{q\pm,l}^{\{k\},\mathrm{H}}(x,y)\right]} . \tag{7.29}$$

The linear combination of these $B_{q\pm,l}^{\{k\}}(x,y)$ basis set images returns the whole normalized difference image

$$\frac{(\mathrm{V}-\mathrm{H})}{(\mathrm{V}+\mathrm{H})} \equiv \frac{I_{\mathrm{V}}(x,y) - I_{\mathrm{H}}(x,y)}{I_{\mathrm{V}}(x,y) + I_{\mathrm{H}}(x,y)} = \sum_{k,q}\sum_{l}^{N_{q\pm}^{\{k\}}} c_{q\pm,l}^{\{k\}} B_{q\pm,l}^{\{k\}}(x,y) \ . \tag{7.30}$$

We have constructed a set of basis images based on the Fano–Macek formalism by means of which the experimental normalised difference images can be simulated using a known

set of $c^{\{k\}}_{q\pm,l}$ expansion coefficients. Conversely, the renormalised PDDCSs are obtained if the $c^{\{k\}}_{q\pm,l}$ expansion coefficients are determined by fitting the experimental image with the basis set images.

7.3.2 Construction of the basis images

The details of how the basis images in Eq. (7.1) were constructed are discussed in the following section. The experimental images were simulated in the same manner. In this case the formula in Eq. (7.7) was invoked, so that the series expansion was replaced by the actual value of the renormalised PDDCSs, $\rho^{\{k\}}_{q\pm}$, obtained from the quantum mechanical close-coupled calculations [55].

In the case of an ideal experiment, the molecular beams intersect each other in an infinitely small volume which lies exactly in the plane of the lasers. The duration of the interaction between the colliding partners and the lasers is the shortest possible. The velocity spread of the molecular beams is zero, thus all of the collisions happen in an identical point in the space relative to the detector. Every collision results in the same scattering (Newton) sphere. Therefore the apparatus function is the same for all collisions.

The ideal conditions enumerated above cannot be realised in a real experiment. The molecular beams and the lasers have spatial spread, thus the interaction and the detection volumes have finite extension. The general valves are open for a finite period of time during which a fraction of the scattered molecules can exit the detection volume. Both the spatial and temporal spreads were approximated by Gaussian functions. The lasers were also assumed to have Gaussian intensity profile. All of these paremeters were determined as described in Chapter 6. For each trajectory both the magnitude and the direction of the initial lab frame velocity of the NO(X) molecules were randomly sampled according to a Gaussian distribution. The time of a collision and its probability were worked out using the above distributions. The probability of the $(1+1')$ REMPI transition was calculated using the pre-defined spatial intensity profiles of the lasers. As a result the apparatus function of the actual individual trajectory, $z(x, y)$, was known. The scattering probability, $P_{\mathrm{scatt}}(\theta)$,

was assumed to be isotropic over the whole scattering angle region.

For each trajectory the orientation of the scattering frame was worked out and the Euler angles $\Gamma_{\mathrm{V/H}} = (\phi, \Theta, \chi_{V/H})$ were subsequently ascertained for both polarisations, so that the geometric functions, $F_{q\pm}^{\{k\}}(\Gamma_{\mathrm{V/H}}^{n})$ could be obtained. The basis functions or the simulated images were then constructed. In order to have smooth basis images of reliable statistics, 200,000,000 trajectories were run for each transition of interest.

The basis set program was implemented in Fortran77. The generation of a typical basis set required approximately an hour using a 2.83GHz dual core CPU.

A selection of $B_{q\pm,l}^{\{2\}}$, $q = 0, 2$ basis functions, which were employed to fit the $|0.5, 0.5, -1\rangle \rightarrow |8.5, 0.5, -1\rangle$ ion-images, are shown in Figure 7.3. The exact CC QM expansion coefficients were used to generate the denominators. Upon comparison with the ideal $G_{q\pm,l}^{\{2\}}$ functions in Figure 7.2, it is noted that the denominator is almost insensitive to the polarisation effects apart from a weak ϕ-dependence of the $k = 2, q = 0$ basis function. The features of the basis functions, though, are blurred in contrast to the sharp changes of intensity observed in Figure 7.2.

Finally, there are three points demanding further consideration. Firstly, the rotationally excited molecules may undergo rotational depolarisation before they are probed by the dye laser. The importance of this effect has to be ascertained. Secondly, it has to be pointed out, despite the normalised difference image being a linear combination of the basis images it is not linear in $c_{q\pm,l}^{\{k\}}$. This issue will be addressed in Section 7.3.3, where the concept of the iterative fitting is explained. Thirdly, the denominator includes the scattering intensity in Eq. (7.29). This quantity has to be known in order to generate the basis images $B_{q\pm,l}^{\{k\}}(x, y)$. However, it will be shown it can be neglected without any considerable loss of accuracy in Section 7.3.3. Hence, it will be omitted from the basis functions and fits unless otherwise stated.

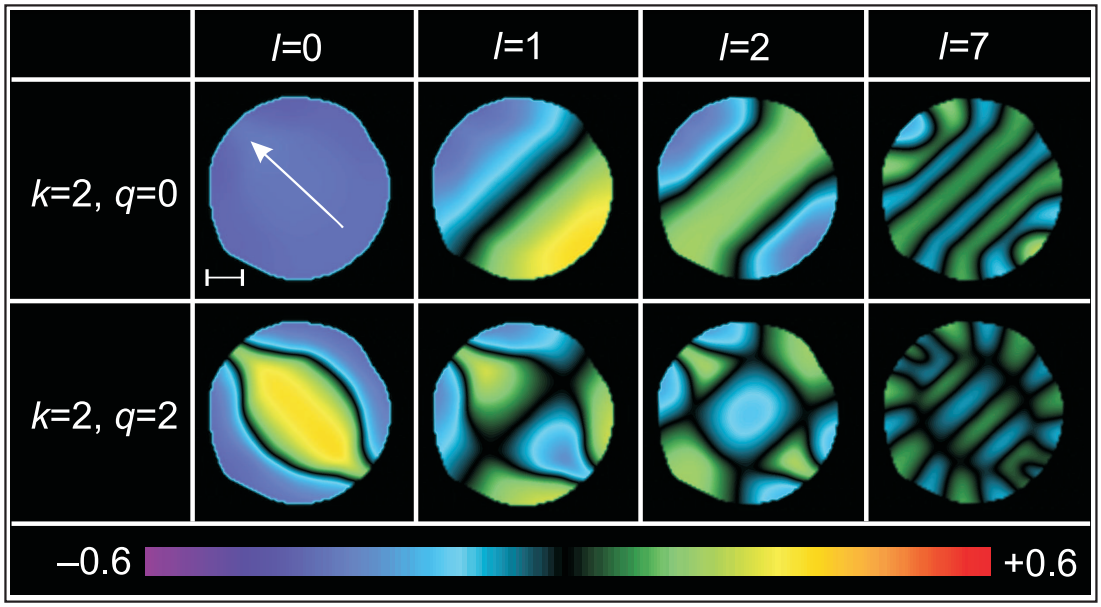

Figure 7.3: The $k = 2, q = 0$ and $k = 2, q = 2$ $B^{\{k\}}_{q\pm,l}$ functions used to fit the $|0.5, 0.5, -1\rangle \rightarrow |8.5, 0.5, -1\rangle$ (V−H)/(V+H) ion-images are shown in the top and bottom rows, respectively. The $l = 0, 1, 2,$ and 7-th order basis functions were chosen to demonstrate how the intensity changes across the basis functions (from left to right). The relative velocity, $\boldsymbol{k}$, is indicated by the white arrow. The velocity scale corresponds to 200 ms^{-1}.

Rotational depolarisation

The rotationally excited molecules generally spend some non-zero time in the interaction region before they are probed by the dye laser. As a consequence, the extent of the rotational polarisation of the NO(X) molecule may reduce in time due to the interaction with the nuclear spin of the nitrogen (the ^{16}O atom does not have nuclear spin). This is the so-called rotational depolarisation which has to be taken into account when constructing the basis sets. The period of the hyperfine beats is shorter than the average time between the collisional excitation of NO(X) and the detection. As a consequence, it is appropriate to use the time averaged depolarisation factors [72, 186]. The k-th rank depolarisation factor, $G^k(j')$ is given by

$$G^k(j') = \frac{1}{2I+1} \sum_F (2F+1)^2 \begin{pmatrix} j' & F & I \\ F & j' & k \end{pmatrix}^2 , \tag{7.31}$$

where j' is the rotational angular momentum quantum number, I is the nuclear spin and F is the total rotational quantum number. The second order depolarisation factors range between 0.8920 and 0.9672 for the minimum and maximum experimental j'-s considered in this work, namely $j' = 5.5$ and $j' = 10.5$. They can be merged with the $h^{(k)}$ line strength factors in Eqs. (7.26) and (7.29) to adjust the basis set to include these effects.

7.3.3 Fitting of the experimental normalised difference images

The objective of the fitting is to retrieve the experimental PDDCSs from the experimental images, that is to determine the $c_{q\pm l}^{\{k\}}$ expansion coefficients in Eq. (7.22). A feasible way is the direct maximisation of the overlap between the fitted image and the experimental image by varying the expansion coefficients. The overlap is calculated by comparing the images pixel-by-pixel. This method is quite time consuming and scales with the second power of the dimension of the image. Fitting in the Fourier moment space of the images has been proven to be a powerful and quick alternative [158]. In the framework of this method the Fourier transforms of the experimental and fitted (simulated) images are calculated. The aim is to maximise the overlap between the Fourier transforms for every order. The m-th order Fourier transform of the experimental image is defined in Eqs. (7.32)-(7.33).

$$F_m^{\mathrm{fit}}(r) = (2-\delta_{m0}) \int_{\tau=0}^{2\pi} I_{\mathrm{V/H}}(r,\tau)\cos(m\tau)\,\mathrm{d}\tau \quad \text{if } 0 \leq m \tag{7.32}$$

$$F_m^{\mathrm{exp}}(r) = \int_{\tau=0}^{2\pi} I_{\mathrm{V/H}}(r,\tau)\sin(m\tau)\,\mathrm{d}\tau \quad \text{if } 0 > m \tag{7.33}$$

The Fourier transform of the fitted image in Eq. (7.28) can be decomposed according to the contributing renormalised PDDCSs and their expansion orders as shown in Eq. (7.34).

$$F_m^{\mathrm{fit}}(r) = \sum_{k,q\pm} \sum_{l} c_{q\pm,l}^{\{k\}} F_{m,k,q,l}^{\mathrm{fit}}(r) \tag{7.34}$$

where $F^{\mathrm{fit}}_{m,k,q,l}(r)$ is the Fourier transform of the $B^{\{k\}}_{q\pm,l}$ basis image:

$$F^{\mathrm{exp}}_{m,k,q\pm,l}(r) = (2-\delta_{m0}) \int_{\tau=0}^{2\pi} B^{\{k\}}_{q\pm,l}(r,\tau)\cos(m\tau)\,\mathrm{d}\tau \quad \text{if } 0 \leq m \tag{7.35}$$

$$F^{\mathrm{fit}}_{m,k,q\pm,l}(r) = \int_{\tau=0}^{2\pi} B^{\{k\}}_{q\pm,l}(r,\tau)\sin(m\tau)\,\mathrm{d}\tau \quad \text{if } 0 > m \tag{7.36}$$

Since the numerator is linear with respect to the expansion coefficients $c^{\{k\}}_{q\pm,l}$ it is possible to factor them out, so to say, a linear combination of the Fourier transforms of the fitted image is fitted against the Fourier transform of the experimental image. However, the basis functions, $B^{\{k\}}_{q\pm,l}$, are still not linear in $c^{\{k\}}_{q\pm,l}$ since they build up the denominator in Eq. (7.29). This means once any of the expansion coefficients has been modified every pixel of the whole basis set has to regenerated and the Fourier moments recalculated. This slows down the optimisation and makes it cumbersome. This difficulty can be overcome by the iterative refinement of the expansion coefficients outlined below.

The sum of the H and V images are less sensitive to the polarisation effects than the difference, (V-H), image. As a consequence, variation of the expansion coefficients primarily modify the (V–H)/(V+H) normalised difference through changing the numerator. Therefore the optimisation can be split into a sequence of steps. Firstly, the basis functions are constructed using an initial guess of the expansion coefficients, and the Fourier moments are calculated. Then the coefficients are varied in the numerator, but they are left unchanged in the denominator until the error function is minimised. The basis functions are again constructed now using the optimised set of coefficients. This procedure is repeated until there is no further decrease in the error function. The computational demand regarding the basis functions is hugely reduced. The $G^{\{k\}}_{q\pm l}$ functions and the apparatus function only have to be generated once, prior to starting the optimisation. The basis functions, $B^{\{k\}}_{q\pm,l}$, have to be calculated, before each optimisation step using the latest set of expansion coefficients. This number is usually in the order of 4–6. The iterative algorithm is represented as a flow chart in Figure 7.4.

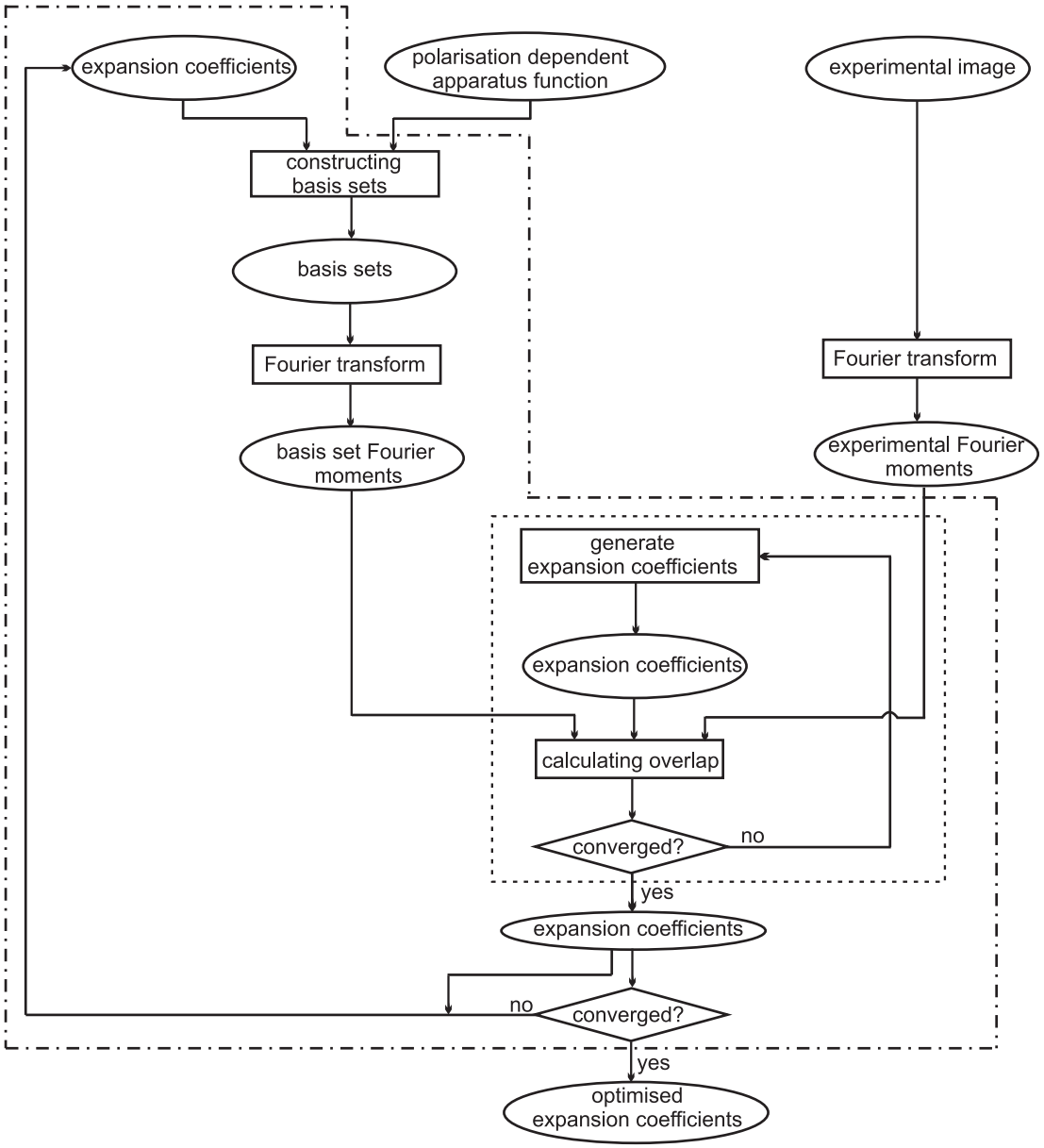

Figure 7.4: Flow chart of the iterative fitting algorithm. The expansion coefficients in the numerator are optimised using a genetic algorithm (inner loop, dashed box). Once the numerator is converged, the global convergence is checked for. The denominator is iteratively refreshed until global convergence is achieved (main loop, dash-dotted box). Note, an initial guess for the expansion coefficients has to specified prior to the first main iteration.

The exact QM expansion coefficients are chosen as the initial guess in order to reduce the number of iterations. In this manner, the first simulated image is the full QM simulation of the experimental image. These simulated images are generated using expansion coefficients instead of renormalised PDDCSs which provide a basis for comparison to the fitted images later on. There is no reference to the first set of coefficients after the sec-

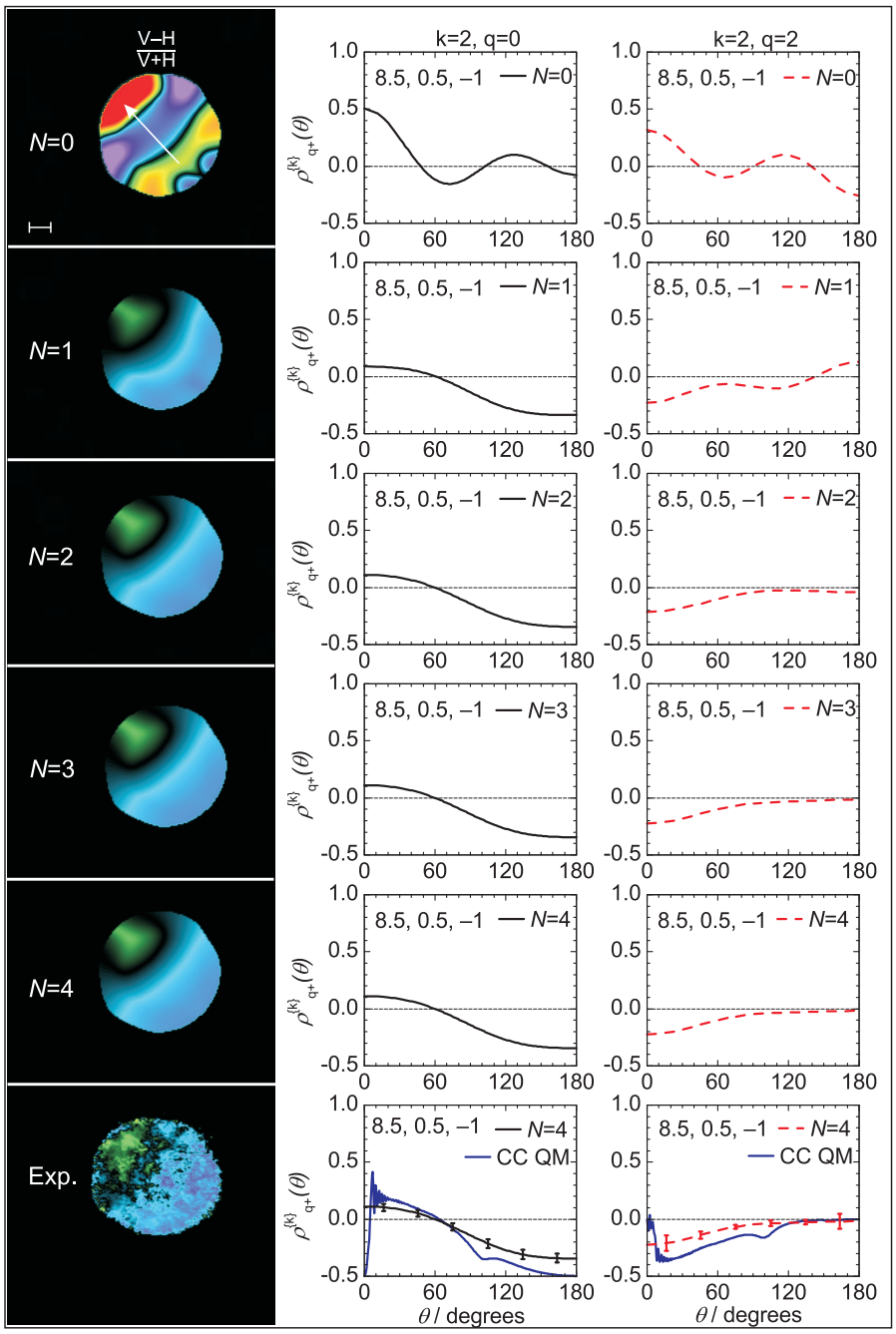

Figure 7.5: A sequence of the iteratively fitted (V−H)/(V+H) images and returned renormalised PDDCSs are shown in the left and right columns, respectively. The image and the renormalised PDDCSs which is scaled by a factor of 1/5 were generated random expansion coefficients in the top row. As the fitting progresses the experimental image is gradually recovered. The direction of the relative velocity is indicated by the white arrow. The velocity scale corresponds to 200 ms^{-1}.

ond iteration and any arbitrary set of $c^{\{k\}}_{q\pm,l}$-s lead to identical experimental renormalised PDDCSs. In order to demonstrate that the result of the fitting is independent of the input coefficients, a number of fits were carried out using randomly chosen expansion co-

efficients on input, which lead to identical results. A sequence of the iteratively fitted images are shown in Figure 7.5. The image and renormalised PDDCSs were randomly generated in the top row of Figure 7.5. Even after the first iteration, the main features of the experimental image are reproduced. The $\rho_0^{\{2\}}(\theta)$ PDDCSs are practically converged after passing two iterations, though, full convergence of the $\rho_{2+}^{\{2\}}(\theta)$ PDDCSs requires more cycles during which the denominator is refreshed. This reflects the fact that the $\rho_{2+}^{\{2\}}(\theta)$ is more sensitive to the details of the image than the $\rho_0^{\{2\}}(\theta)$ which primarily determines the overall intensity distribution along the relative velocity.

Explicit form of the error function

The target function, ε, which is minimised during the fitting is the sum of the differential overlaps, that is the integrated square modulus of the difference between the Fourier moments of the experimental image and those of the simulated image:

$$\varepsilon = \sum_{m=-M}^{M} \varepsilon_m \,. \tag{7.37}$$

The differential overlaps, ϵ_m, are calculated for every Fourier order, m, according to Eq. (7.37). The minimum and maximum order of the Fourier moments, $\pm M$, are usually set as ± 18 in order to capture the finer details of the images:

$$\begin{aligned} \varepsilon_m &= \sum_{m=-M}^{M} \int_{r=0}^{R} \left[F_m^{\mathrm{exp}}(r) - F_m^{\mathrm{fit}}(r)\right]^2 \mathrm{d}r \\ &= \int_{r=0}^{R} F_m^{\mathrm{exp}}(r)^2 \mathrm{d}r - 2 \sum_{k,q,l} c_{q\pm,l}^{\{k\}} \int_{r=0}^{R} F_{m,k,q,l}^{\mathrm{fit}}(r) F_m^{\mathrm{exp}}(r) \mathrm{d}r \\ &+ \sum_{\substack{k,q,l \\ k',q',l'}} c_{q\pm,l}^{\{k\}} c_{q'\pm,l'}^{\{k'\}} \int_{r=0}^{R} F_{m,k,q,l}^{\mathrm{fit}}(r) F_{m,k',q',l'}^{\mathrm{fit}}(r) \mathrm{d}r \,. \end{aligned} \tag{7.38}$$

The calculation of the integrals in Eq. (7.38) is the computationally most expensive step of the optimisation. They have to be evaluated every time when any of the expansion

coefficients is changed. There is a sixfold summation over the k and q indices and the l expansion orders of renormalised PDDCSs. In addition, the integration is carried out numerically which involves a summation over the pixels in one dimension of the image. This computational demand can be hugely reduced by noticing that the basis functions do not change during an optimisation cycle and the experimental image is unchanged for the whole procedure. It is possible to perform the integration of the basis function prior to each cycle, which results in the following equation:

$$\varepsilon_m = O_m^{\mathrm{exp,exp}} - 2\sum_{k,q,l} c_{q\pm,l}^{\{k\}} O_{m,k,q,l}^{\mathrm{exp,fit}} + \sum_{\substack{k\le k'\\ q\le q'\\ l\le l'}} (2-\delta_{kk',qq',ll'}) c_{q\pm,l}^{\{k\}} c_{q'\pm,l'}^{\{k'\}} O_{m,k,q,l,k',q',l'}^{\mathrm{fit,fit}}\,, \qquad (7.39)$$

where the $O^{\mathrm{x,y}}$ symbols are identified as the overlap integrals in Eq. (7.38). Considering the average radius of an ion-image is approximately 50 pixels, a reasonable acceleration is achieved by this method.

The fitting code was implemented in Fortran77 and a genetic algorithm was used to minimise the error function of Eq. (7.37). A typical fitting took 0.5–1 minutes to converge.

Error analysis

The errors of the experimental renormalised PDDCSs were estimated as follows. The horizontal and vertical ion-images used to calculate the normalised difference images were the sum of 8–10 individual ion-images. These were grouped into subsets of 3–4 images depending on the overall signal quality. Normalised-difference images were calculated from these triplets or quadruplets of H and V images. The normalised images were subsequently fitted and both renormalised PDDCSs calculated for each of these subgroups. The standard deviation of the returned $\rho_0^{\{2\}}(\theta)$ and $\rho_{2+}^{\{2\}}(\theta)$ renormalised PDDCSs were calculated with the standard formulae [187].

Role of the scattering intensity

It has been stated that the basis functions virtually do not depend on the scattering intensity, or equivalently on the DCS of the transition of interest. Formally, the basis functions, $B^{\{k\}}_{q\pm,l}$, are functions of the differential cross section in Eq. (7.29). The DCS is proportional to the scattering probability $P_{\text{scatt}}(\theta)$ which is incorporated in the $G^{\{k\}}_{q\pm,l}$ and apparatus functions of the basis functions, such that it appears both in the numerator and denominator. Because the scattering angles that contribute to a certain pixel, (x, y), on the detector are convoluted (*cf.* Eqs. (7.26) and (7.27)), it cannot be factored out in a rigorous mathematical way. However, it is found that the basis functions are essentially independent of the scattering probability, therefore it can be omitted. This stems from the fact the only a small range of scattering angles contribute to the intensity of a given pixel. As a consequence, $P_{\text{scatt}}(\theta)$ is almost constant over the scattering events for a given pixel, thus it very nearly cancels.

In order to demonstrate the validity of this assumption three simulations and fits were performed employing different basis sets which are shown in Figure 7.6. The normalised difference images were simulated for the $|0.5, 0.5, -1\rangle \rightarrow |8.5, 0.5, -1\rangle$ transition using the QM PDDCSs. In the top left panel of Figure 7.6 an ideal simulation is displayed, whilst in the middle and right panels the full simulations are shown with and without DCS weighting in the middle and left panels of the same figure. The images from the full simulations are markedly different from the ideal image which is due to the experimental circumstances discussed in Section 7.3.1 and which will be discussed in detail in the following section. The full simulated images with and without DCS weighting are virtually identical. The full simulated image containing the DCS weighting was fitted by three basis sets, the returned renormalised PDDCSs of which are shown in the bottom panels. If the ideal basis set is used, the retrieved renormalised PDDCSs are good approximations of the input CC QM ones according to the left panel. The fits with unweighted and weighted basis sets return identical PDDCSs. Therefore these observations makes it plausible to neglect the scattering intensity from the basis sets. $P_{\text{scatt}}(\theta)$ was set to unity in Eqs. (7.29) and (7.30)

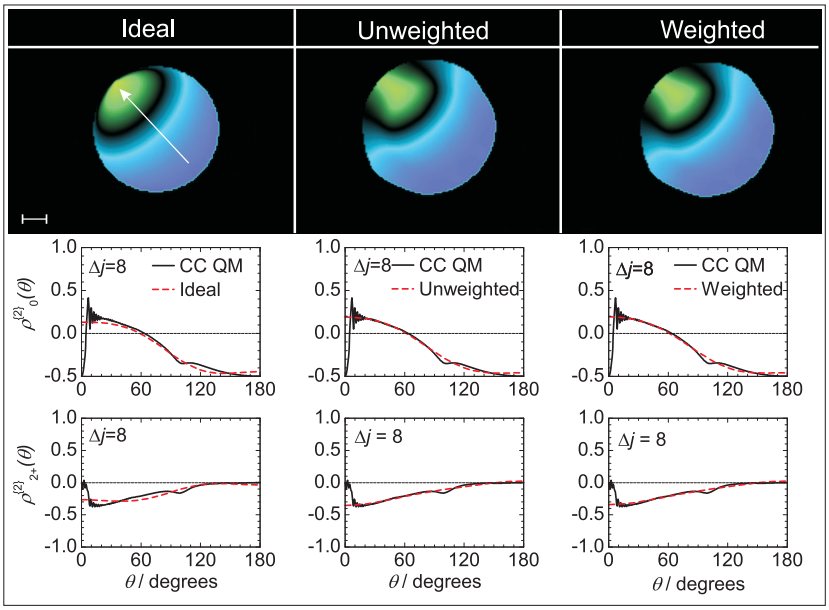

Figure 7.6: Simulations of the difference (V−H)/(V+H) ion images for $|0.5, 0.5, -1\rangle \rightarrow |8.5, 0.5, -1\rangle$ (top row). The figure shows the results of the 'ideal' simulation (left column) and the full simulation (middle column), both obtained without weighting by the DCS. The right hand column shows the results of a full simulation, this time including the weighting by DCS in the basis function generation. Second and third rows: the $\rho_0^{\{2\}}(\theta)$ and $\rho_{2+}^{\{2\}}(\theta)$ renormalized PDDCSs returned by fitting the full simulated images with the basis sets generated as indicated in the three columns. The direction of the relative velocity is indicated by the white arrow. The velocity scale corresponds to 200 ms^{-1}.

and so employed in all of the fits and simulations, unless otherwise stated.

Thresholding

Because of the spatial spread of the molecular and laser beams the collisions between the NO(X) and Ar become less frequent when moving away from the most intense parts of the image in the detector. The scattered signal becomes indistinguishable from the background and then dies off. For this reason the individual experimental H and V images were background subtracted. They were also subject to threshold criterion in order to discern the signal from incidental noise which is left after the background substraction. This sharpens both the edges and the details of the individual H and V and the normalised difference images.

A similar effect is observed in the case of the full simulation. The spatial spread of the beams theoretically extend to infinity, so that there will be finite but very small intensity

even at large distances from the intense rim of the simulated image. When calculating the normalised image, this artefact is hugely amplified and becomes more visible due to the division of the difference image by the sum image, which has very small intensities outside of the main Newton-circle. As a result, the basis set images and simulated images are distorted and have an artefact, extended fringe. This was remedied in the following way. H and V ion images were simulated using the QM renormalised PDDCSs along with the basis set images which were used to threshold the basis sets. If the intensity of a certain pixel was below a limit in the H and V images, the intensity of the corresponding basis set was set to zero. The limit was expressed in terms of percentage of the maximum intensity of the images, which was in turn chosen to match the experimental threshold.

7.4 Simulated images

Having developed the formalism to simulate and fit the experimental normalised difference images, we now turn our attention to the investigation of the alignment effects in the rotationally inelastic collisions of the NO(X)–Ar system. Firstly, the general characteristics of the normalised difference images are discussed. The ion-images were recorded for the $|0.5, 0.5, -1\rangle \rightarrow |6.5, 0.5, -1\rangle$, $|0.5, 0.5, -1\rangle \rightarrow |7.5, 0.5, -1\rangle$, $|0.5, 0.5, -1\rangle \rightarrow |7.5, 0.5, +1\rangle$, $|0.5, 0.5, -1\rangle \rightarrow |8.5, 0.5, -1\rangle$ and $|0.5, 0.5, -1\rangle \rightarrow |10.5, 0.5, -1\rangle$ spin–orbit conserving transitions and for the $|0.5, 0.5, -1\rangle \rightarrow |5.5, 1.5, +1\rangle$ and $|0.5, 0.5, -1\rangle \rightarrow |9.5, 1.5, +1\rangle$ spin–orbit changing transitions. Both ideal and full simulations have been performed in order to ascertain the effect of the experimental circumstances on the ion-image. The exact quantum mechanical renormalised PDDCSs were used in both cases. In addition, an ideal simulation was done employing the kinematic apse model (AM) renormalised PDDCSs derived in Chapter 5 for illustrative purposes. The apse model normalised difference images have already been shown and discussed in [188]. Those images were generated using the correction images for collision induced alignment which are discussed in [134], whereas the normalised difference images were obtained by direct simulations using Eq. (7.25) and the

apse model PDDCSs in the present work. Nevertheless the two procedures should produce identical results.

The spin–orbit conserving AM ideal simulations are shown in the first column of Figure 7.7. The alignment reflects collision dynamics which are due to a purely impulsive mechanism which was discussed in Chapter 5 and in [188]. The requirement that the projection of $\boldsymbol{j'}$ onto the kinematic apse should be conserved during the collision imposes a restriction on the distribution of $\boldsymbol{j'}$ thus the distribution of the transition dipole moment is restricted too, which leads to characteristic intensity patterns when the collision is probed by linearly polarised light. The spin–orbit conserving simulated ideal (V−H)/(V+H) images are compared to the AM ones in the second column of Figure 7.7. They agree well for all of the investigated states implying hard shell collision dynamics. Since the attractive well depth is about $120\,\mathrm{cm^{-1}}$ which is relatively small to compared to the collision energy of $530\,\mathrm{cm^{-1}}$, this is a plausible assumption. The spin–orbit conserving AM and QM renormalised PDDCSs were compared in Section 5.3.2. The major deviations are observed in the forwards scattered region when the effect of the attractive well is expected to be more pronounced.

The agreement between the exact quantum mechanical and apse model simulations is less good for spin–orbit changing collisions as shown in Figure 7.8. This can be attributed to the fact that these transitions primarily sample the strongly attractive V_{dif} potential defined in Chapter 2. Thus the kinematic apse model which assumes the total dominance of the repulsive forces is less applicable.

The general features of the ideal simulations are recognised in the full simulated images. However, the finer details of the intensity pattern characteristic to the ideal simulations are washed out to some extent in the full simulation. This effect is due to the finite angular resolution of the experiment, that is both the laser and molecular beams have spatial spread, and the interaction is extended over a finite period of time and space which was discussed in more details in Section 6.2.5. One of the most remarkable consequences of this blurring effect is that the sharp peak is weakened in the forward scattered region

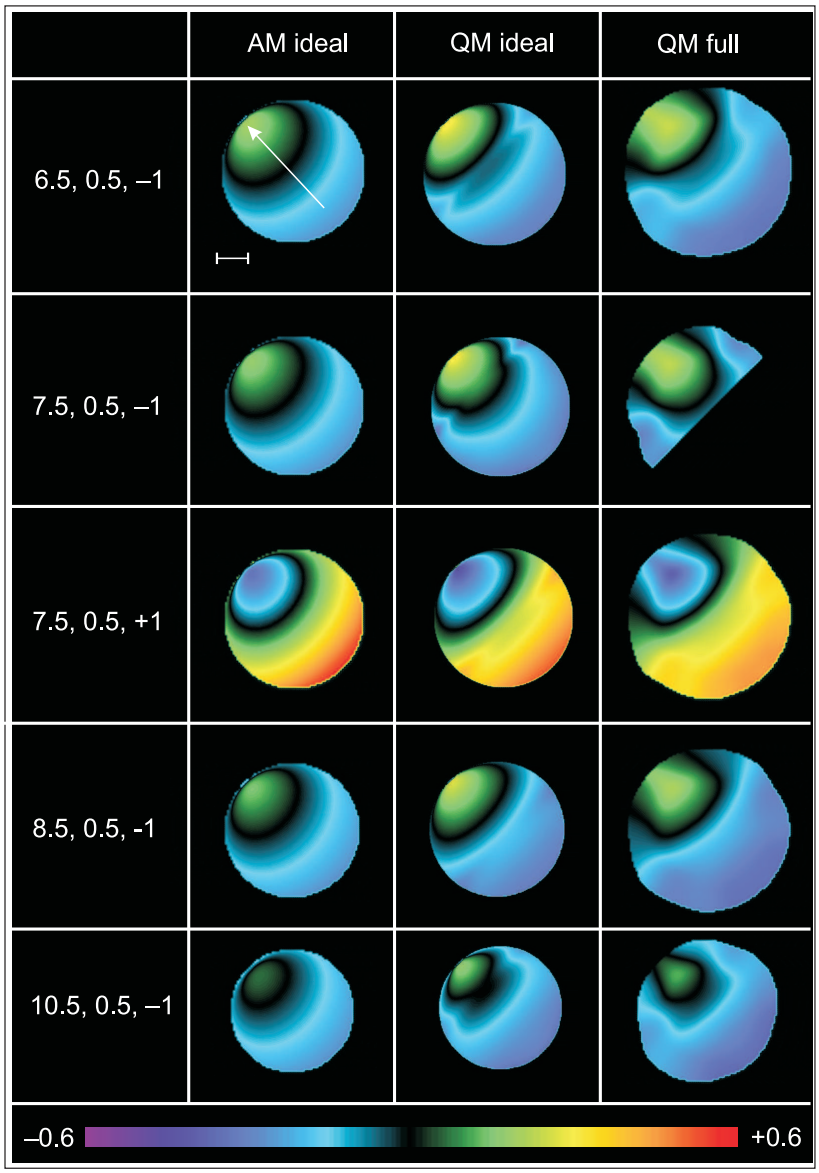

Figure 7.7: The apse model ideal (AM, left column), the exact quantum mechanical ideal (QM, middle column) and quantum mechanical full (right column) simulations of the (V−H)/(V+H) ion images for the $|0.5, 0.5, -1\rangle \rightarrow |6.5, 0.5, -1\rangle$, $|7.5, 0.5, -1\rangle$, $|7.5, 0.5, +1\rangle$, $|8.5, 0.5, -1\rangle$ and $|10.5, 0.5, -1\rangle$ spin–orbit conserving transitions from top to bottom. The direction of the relative velocity is indicated by the white arrow. The velocity scale corresponds to 200 ms^{-1}.

about $5° - 10°$ in the full simulations. This is most apparent in the simulated image for the $|9.5, 1.5, +1\rangle$ final state. In the full simulation the intensity slowly decreases to around zero, and does not take negative values. Whereas in the ideal simulation the intensity drops below zero within the first 3° in the very forward scattered region. These observations suggest that the experimental circumstances have to be accurately taken into account when fitting the experimental images.

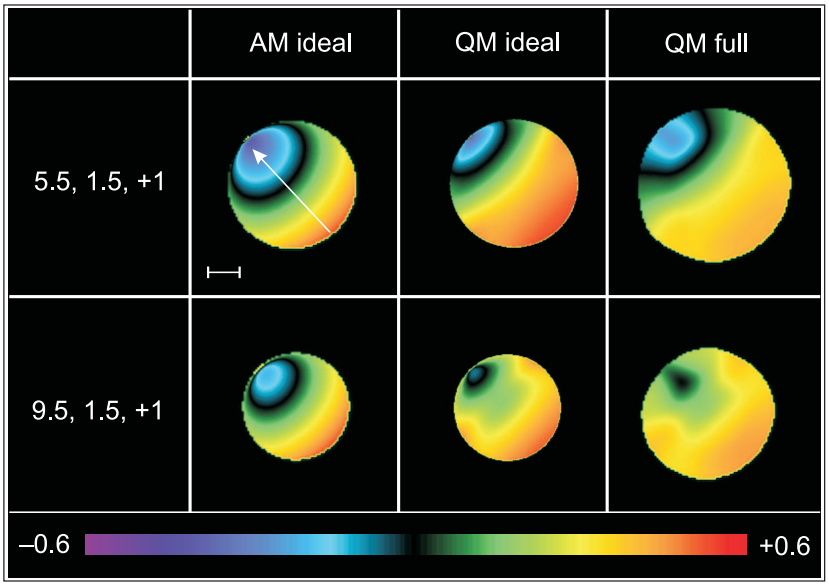

Figure 7.8: The apse model ideal (AM, left column), the exact quantum mechanical ideal (QM, middle column) and quantum mechanical full (right column) simulations of the (V−H)/(V+H) ion images for the $|0.5, 0.5, -1\rangle \rightarrow |5.5, 1.5, +1\rangle$ and $|9.5, 1.5, +1\rangle$ spin–orbit changing transitions from top to bottom. The apse model and CC QM renormalised PDDCSs were employed in the left and the middle and right columns respectively. The direction of the relative velocity is indicated by the white arrow. The velocity scale corresponds to 200 ms^{-1}.

7.5 Experimental normalised difference images

The experimental normalised difference images for the spin–orbit conserving transitions are shown in the first column of Figure 7.9, while those for the spin–orbit changing collisions are displayed in the first column Figure 7.10. The fitted images are shown in the second column of Figures 7.9–7.10. The full simulations previously discussed are compared to the experimental images in the third row and the sum of the experimental H and V images are also displayed in the rightmost column of Figures 7.9–7.10. The sum of the H and V images is mostly sensitive to the differential cross section, and less sensitive to the polarisation effects. As such, it provides information about the intensity distribution of the images independent of the alignment effects. It is expected that the signal-to-noise ratio is the highest where the sum image is the most intense, thus the sharpest features of the (V−H)/(V+H) are expected to be observed in these regions. On the other hand, the signal-to-noise ratio is slightly less good where the summed intensity is lower. Some of the (V−H)/(V+H) images are 'speckled' and the features are less sharp

in these regions. This could either result from the small values of the DCSs or from the uneven detection probability of the apparatus functions. For instance the top right diagonal of the images correspond to the fast side (*cf.* Section 6.2.5) where the detection probability is in general lower and is responsible for the bottom left diagonal of the spin–orbit conserving (V−H)/(V+H) images being smoother than the opposite diagonal. The effect of the DCS on the scattering intensity is most pronounced in the images belonging to the $|0.5, 0.5, -1\rangle \rightarrow |7.5, 0.5, -1\rangle$ transition. The DCS is strongly forward scattered with a maximum around 60°. The probability of a particle being scattered at higher angles convoluted with the apparatus function was insufficient to obtain reasonable signal-to-noise ratio, thus the angles bigger than 90° were omitted from the fitting and simulation.

It is a common attribute of the fitted images that they are less intense than the simulated ones. The experimental images have regions where the intensity rapidly changes pixel-by-pixel usually at backward scattered angles which results in the depletion of the total intensity. The lowest order Fourier moments are represented with the most weight in the fitting. They describe the overall intensity or the asymmetry in the intensity distribution in the case of zeroth order and low order moments, respectively. They are insensitive to the details of the image. As a consequence, the total intensity of the fitted image will mostly be determined by that of the experimental one. This phenomenon will also be mirrored in the values of the recovered experimental renormalised PDDCSs.

It has been experimentally shown that the parity pair transitions, which have identical initial and final parities $(-1)^{j-\epsilon/2}$ possess similar DCSs [66, 145]. The theoretical explanation of this phenomena was discussed in [134]. This observation is readily reaffirmed upon comparison of the (V+H) images for the $|0.5, 0.5, -1\rangle \rightarrow |7.5, 0.5, +1\rangle$ and $|0.5, 0.5, -1\rangle \rightarrow |8.5, 0.5, -1\rangle$ transitions in the 3rd and 4th rows of Figure 7.9 . The normalised difference images reveals a similar relationship between the renormalised PDDCSs.

Since the line strength factor, $h^{(2)}(j_i, j_f)$, is negative for R-branch transitions and unity for Q-branch transitions, the intensity of the normalized difference image is inverted when the Q-branch is used instead of the R-branch to detect the rotationally excited

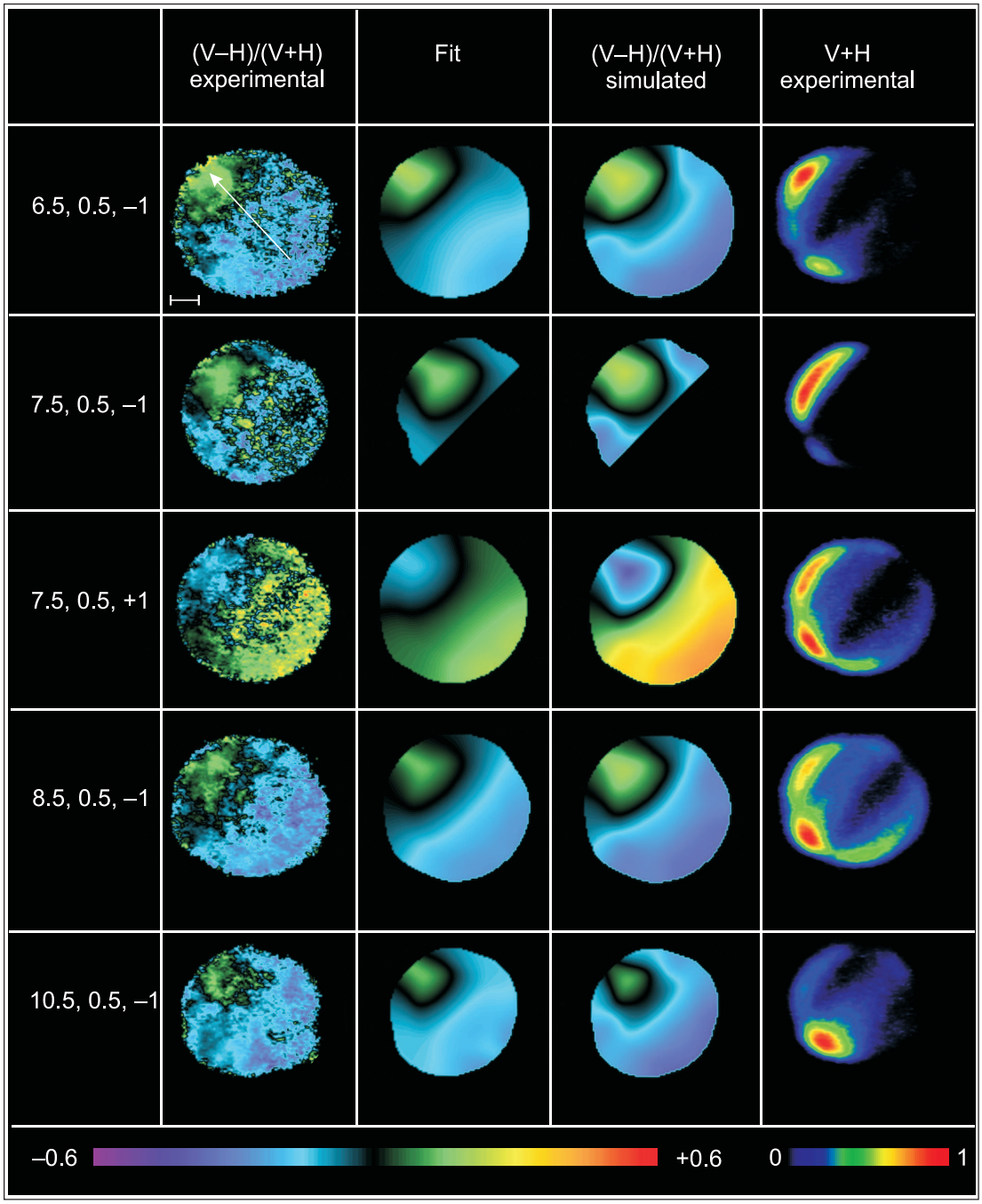

Figure 7.9: The experimental and fitted (V−H)/(V+H) ion images are shown in the first and second columns for the $|0.5, 0.5, -1\rangle \rightarrow |6.5, 0.5, -1\rangle$, $|7.5, 0.5, -1\rangle$, $|7.5, 0.5, +1\rangle$, $|8.5, 0.5, -1\rangle$ and $|10.5, 0.5, -1\rangle$ spin–orbit conserving transitions from top to bottom. The simulated images and the experimental (V+H) sum images are displayed in the third and fourth columns. Note, only the $0° - 90°$ scattering angle interval of the $|0.5, 0.5, -1\rangle|7.5, 0.5, -1\rangle$ ion image was fitted. The direction of the relative velocity is indicated by the white arrow. The velocity scale corresponds to 200 ms^{-1}.

molecules. The $|7.5, 0.5, +1\rangle$ image is the negative of the $|8.5, 0.5, -1\rangle$ up to a factor of $h^{(2)}(8.5, 9.5)/(1 - h^{(2)}(8.5, 9.5)) \approx 0.75$. This is shown in the 3rd and 4th rows of Fig. 7.9

neglecting the depolarisation factor which is about 0.92 for these states. These observations imply that the second order $\rho_0^{\{2\}}(\theta)$ and $\rho_{2+}^{\{2\}}(\theta)$ renormalized PDDCS are nearly identical for the parity conserving $|0.5, 0.5, -1\rangle \rightarrow |0.5, 7.5, +1\rangle$ and $|0.5, 0.5, -1\rangle \rightarrow |8.5, 0.5, -1\rangle$ transitions which make up a parity pair.

The normalised difference images $|0.5, 0.5, -1\rangle \rightarrow |5.5, 1.5, +1\rangle$ and $|0.5, 0.5, -1\rangle \rightarrow |9.5, 1.5, +1\rangle$ spin–orbit changing images are shown in Figure 7.10. The agreement between the experimental, fitted and simulated images is excellent.

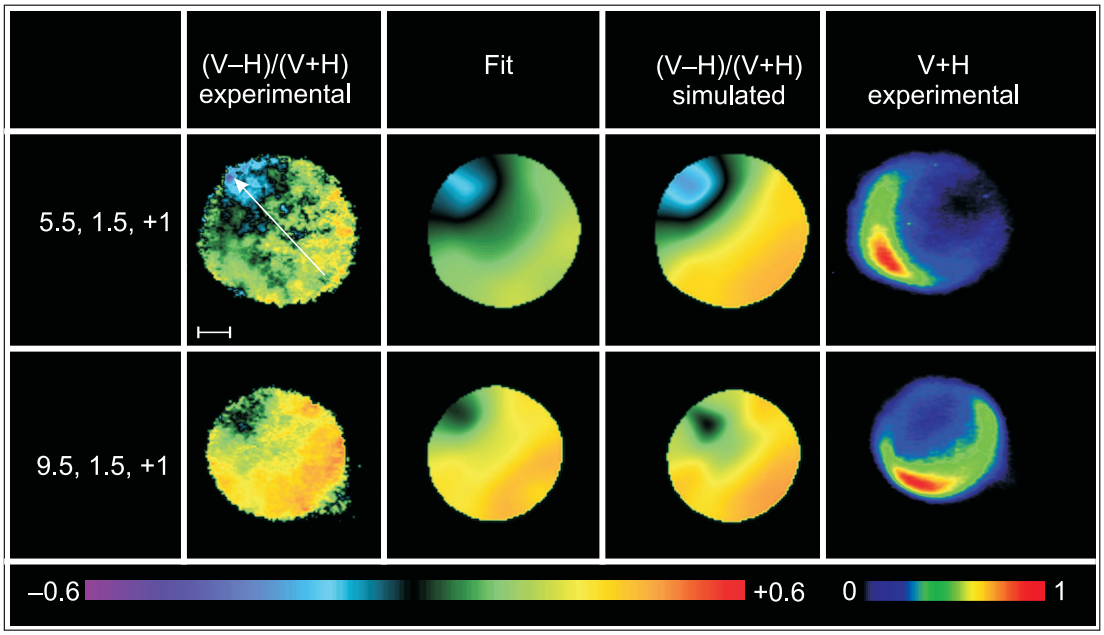

Figure 7.10: The experimental and fitted (V−H)/(V+H) ion images are shown in the first and second columns for the $|0.5, 0.5, -1\rangle \rightarrow |5.5, 1.5, +1\rangle$, $|9.5, 1.5, +1\rangle$ spin–orbit changing transitions from top to bottom. The simulated images and the experimental (V+H) sum images are displayed in the third and fourth columns. The direction of the relative velocity is indicated by the white arrow. The velocity scale corresponds to 200 ms^{-1}.

The intensity pattern of the normalised difference, (V−H)/(V+H), images can be invoked to deduce alignment information about $\boldsymbol{j'}$. The intensity of the normalised image is positive, meaning the vertical transition probability is greater than the horizontal, $I_\mathrm{V} > I_\mathrm{H}$. On the other hand, negative intensity is the consequence of the horizontal transition probability being greater than the vertical, $I_\mathrm{H} > I_\mathrm{V}$. Zero intensity corresponds to a case when the transition probabilities are roughly the same for both polarisations. Let us restrict ourselves only considering the R-branch of the NO $\mathrm{A}^2\Sigma^+ \leftarrow \mathrm{X}^2\Pi$ electronic transition.

In the classical high-j limit the transition dipole moment, $\hat{\boldsymbol{r}}$, lies perpendicular to the molecular axis, and is also perpendicular to $\boldsymbol{j'}$. The transition probability is proportional to the square modulus of the $|\langle\hat{\boldsymbol{\epsilon}}\cdot\hat{\boldsymbol{r}}\rangle|$ product, and it is thus large, if the electric vector of the laser light and the transition dipole moment are aligned parallel. It vanishes, if $\hat{\boldsymbol{\epsilon}}$ and $\hat{\boldsymbol{r}}$ are aligned perpendicular. Positive intensity, $I_{\mathrm{V}} > I_{\mathrm{H}}$, indicates that $\hat{\boldsymbol{r}}$ is more likely to be aligned parallel to the vertical polarisation axis, so that $\boldsymbol{j'}$ is preferentially confined in the scattering plane. This corresponds to a 'propeller' or 'cartwheel' motion of the scattered NO(X) depending on the direction of $\boldsymbol{k'}$ in the scattering frame. If the horizontal intensity is bigger than the vertical, $\hat{\boldsymbol{r}}$ preferentially lies in the scattering plane that is $\boldsymbol{j'}$ is perpendicular to that. If $\boldsymbol{k'}$ is aligned parallel to $\boldsymbol{k}$ this indicates a 'frisbee' like motion of the scattered NO(X).

The above qualitative arguments are helpful to interpret the experimental images. The intensity of every R-branch normalised difference images exhibits a decreasing intensity as a function of the scattering angle. The intensity is positive in the forward scattered region which rapidly lessens on moving towards bigger scattering angles leading to a region where $I_{\mathrm{V}} \approx I_{\mathrm{H}}$. Beyond this region the sideways and backward scattered sections have negative intensity. This can be expressed in terms of molecular rotational motion as follows: the scattered molecules rotate like a propeller in the forward scattered region where $\boldsymbol{k'}$ is nearly parallel to $\boldsymbol{k}$. This slowly transforms to a frisbee-like motion at larger scattering angles where the role of the repulsive forces becomes more dominant.

It is worth pointing out that the extension as well as the average modulus of the–forward scattered–positive section of the difference images reduces as j' increases from $j' = 6.5$, to $j' = 10.5$. The forward scattered molecules are less aligned. Simultaneously, the sideways and backward scattered regions of the normalised difference images become more negative with increasing rotational excitation. This means the molecules scattered towards these angles exhibit an increasing tendency to rotate in the scattering plane.

7.6 Experimental renormalised PDDCSs

The renormalised PDDCSs were retrieved from the experimental images with the algorithm introduced in Section 7.3. During the course of the fitting the $c_{0,l}^{\{2\}}$ and $c_{2+,l}^{\{2\}}$ were optimised in order to maximise the overlap between the experimental and fitted images. The finest detail that the fitted renormalised PDDCSs are able to capture depends on how many coefficients, $c_{q\pm,l}^{\{2\}}$, are included in the series expansion in Eqs. (7.22) and (7.28). The basis functions were generated using Legendre polynomials. A basis set consisting of images of higher order are more flexible than those which are made up from only low order images. As a consequence, the fitted renormalised PDDCSs are expected to approximate better the real ones, if an extended basis set is employed to fit the experimental images. In fact it is the experimental image whose intensity variation is approximated during the fitting irrespective of its origin. It might happen that those features of the image are taken into account with greater weight which are due to the locally less good signal-to-noise ratio, if high order moments are used in the fitting. In order to ascertain the possible effect of this phenomenon all of the experimental images were fit using a sequence of larger basis sets. The lowest and highest orders included were $l = 2$ and $l = 9$, respectively.

A selection of fitted images and renormalised PDDCSs obtained with increasing basis sets are shown in Figure 7.11 for the $|0.5, 0.5, -1\rangle \rightarrow |5.5, 1.5, +1\rangle$ transition. The angular dependence of $\rho_0^{\{2\}}(\theta)$ and $\rho_{2+}^{\{2\}}(\theta)$ renormalised PDDCSs can be recovered even with $N_0^{\{2\}} = 3$, $N_{2+}^{\{2\}} = 2$ maximum expansion orders which is similar to that of the calculated CC QM ones. The error function reaches a plateau, when the maximum expansion order of basis functions employed exceeds $l = 5$. The returned experimental PDDCSs assume gradually more oscillatory structure. The finer details of the experimental image are reproduced in the fitted image, including those due to the less good signal-to-noise ratio. Therefore we decided to truncate the basis set for the $\rho_0^{\{2\}}(\theta)$ parameters by setting $N_0^{\{2\}} = 5$, so that these artifacts are washed out, whilst the polarization information can still be reliably recovered. The maximum expansion order of $\rho_{2+}^{\{2\}}(\theta)$ was determined to be $N_2^{\{2\}} = 3$ since

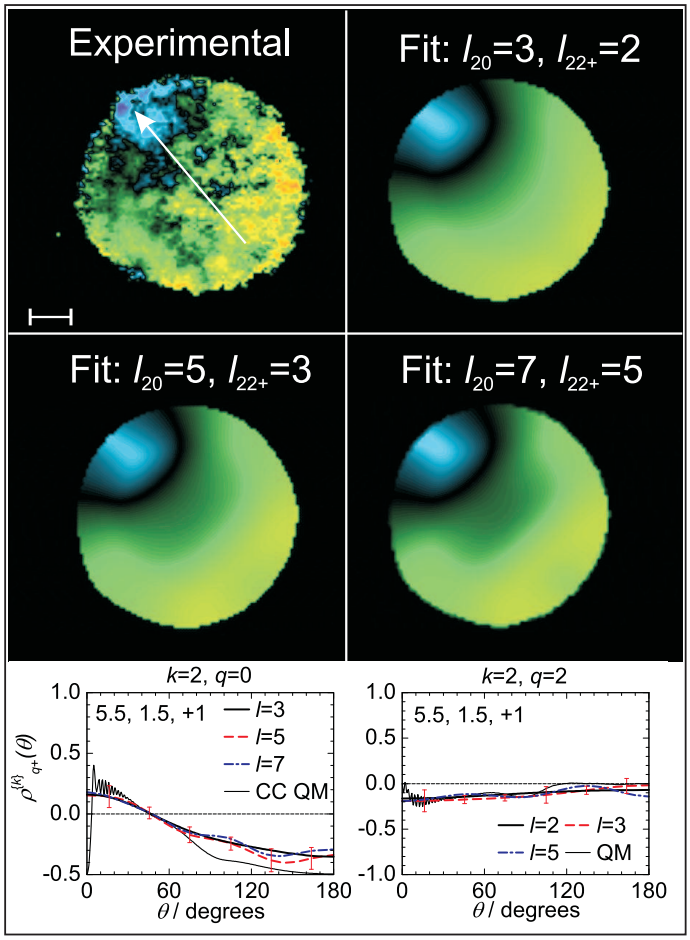

Figure 7.11: The experimental and fitted (V−H)/(V+H) ion image (top left panel) and the fitted images are shown for the $|0.5, 0.5, -1\rangle \rightarrow |5.5, 1.5, +1\rangle$ transition. The fits were carried out employing 4, 6, 8 and 3, 5, 7 basis images, $B^{\{2\}}_{q\pm,l}$, $q = 0, 2$, respectively. The extended basis sets are able to capture the finer details of the experimental image. The recovered renormalised PDDCSs are shown in the bottom panels. The direction of the relative velocity is indicated by the white arrow. The velocity scale corresponds to 200 ms^{-1}.

the experiment is less sensitive to this component of the alignment parameter.

The renormalised PDDCSs for the spin-orbit conserving and changing transitions retrieved from the experimental normalised difference images are shown in Figures 7.12 and 7.13, respectively. The corresponding CC QM renormalised PDDCSs are plotted in the same figures. The experimental DCSs and CC QM DCSs are compared in the left columns of these figures which were previously obtained and analysed [66, 156] in order to provide a more general basis for comparison. The agreement between the experimental and CC QM renormalised PDDCSs is in general excellent for both spin–orbit conserving and spin–orbit changing collisions. Another general remark is that the agreement between

the CC QM and experimental $\rho_0^{\{2\}}(\theta)$ is somewhat better than that between the CC QM and experimental $\rho_{2+}^{\{2\}}(\theta)$. The deviation between the two sets of data is more noticeable in the backward scattered region for both renormalised PDDCSs where the scattering intensity is lower.

If the dye laser's propagation axis were perpendicular to the initial relative velocity, $\boldsymbol{k}$, the normalised difference image would not have an azimuthal dependence on the $\rho_0^{\{2\}}(\theta)$ alignment parameter according to the Fano–Macek intensity formula in Eq. (7.1). Thus the value of this parameter can be inferred from the intensity variation of the stripes perpendicular to the relative velocity along its direction. Conversely, the $\rho_{2+}^{\{2\}}(\theta)$ renormalised PDDCSs is multiplied with a factor of $\cos(2\phi)$ so that the intensity contribution from this parameter depends on the azimuthal angle of the laser's propagation axis ϕ which varies over the direction perpendicular to $\boldsymbol{k}$. As a consequence, the retrieved $\rho_{2+}^{\{2\}}(\theta)$ parameter is sensitive to the intensity distribution within a stripe perpendicular to $\boldsymbol{k}$. The real experimental setup is close to the ideal one to the extent which was discussed above. Therefore it is expected that the retrieved $\rho_0^{\{2\}}(\theta)$ is mostly sensitive to the intensity variation along the symmetry axis, $\boldsymbol{k}$. On the other hand, the experimental $\rho_{2+}^{\{2\}}(\theta)$ depends more on the intensity distribution perpendicular to $\boldsymbol{k}$. The images are slightly asymmetric with respect to $\boldsymbol{k}$ due to the density-to-flux effects and have regions in which the signal-to-noise ratio is lower, which has a moderate distorting effect on the retrieved $\rho_{2+}^{\{2\}}(\theta)$ parameters. Therefore the experiment is more robust with respect to measuring the $\rho_0^{\{2\}}(\theta)$ parameters.

The experimental renormalised PDDCS data tie in with the qualitative conclusions about the angular momentum alignment deduced from the intensity distribution of the normalised difference images. They also agree well with their theoretical counterparts apart from the sudden rise in the very forward scattered region. The $\rho_0^{\{2\}}(\theta)$ renormalised PDDCSs are positive in the forward scattered region which indicate positive alignment of $\boldsymbol{j}$ with respect to $\boldsymbol{k}$. When $\boldsymbol{k}$ and $\boldsymbol{k'}$ are nearly parallel this value of the alignment refers to a propeller-like motion of the scattered NO(X) molecules. It gradually decreases at sideways and backward scattered angles taking negative values which corresponds to

perpendicular alignment of $\boldsymbol{j'}$ to $\boldsymbol{k}$. If $\boldsymbol{k}$ and $\boldsymbol{j'}$ are roughly antiparallel, a frisbee-like motion can be associated with the negative value of this alignment moment. It is also in accordance with theory that the $\rho_0^{\{2\}}(\theta)$ renormalised PDDCSs become more negative as j' increases.

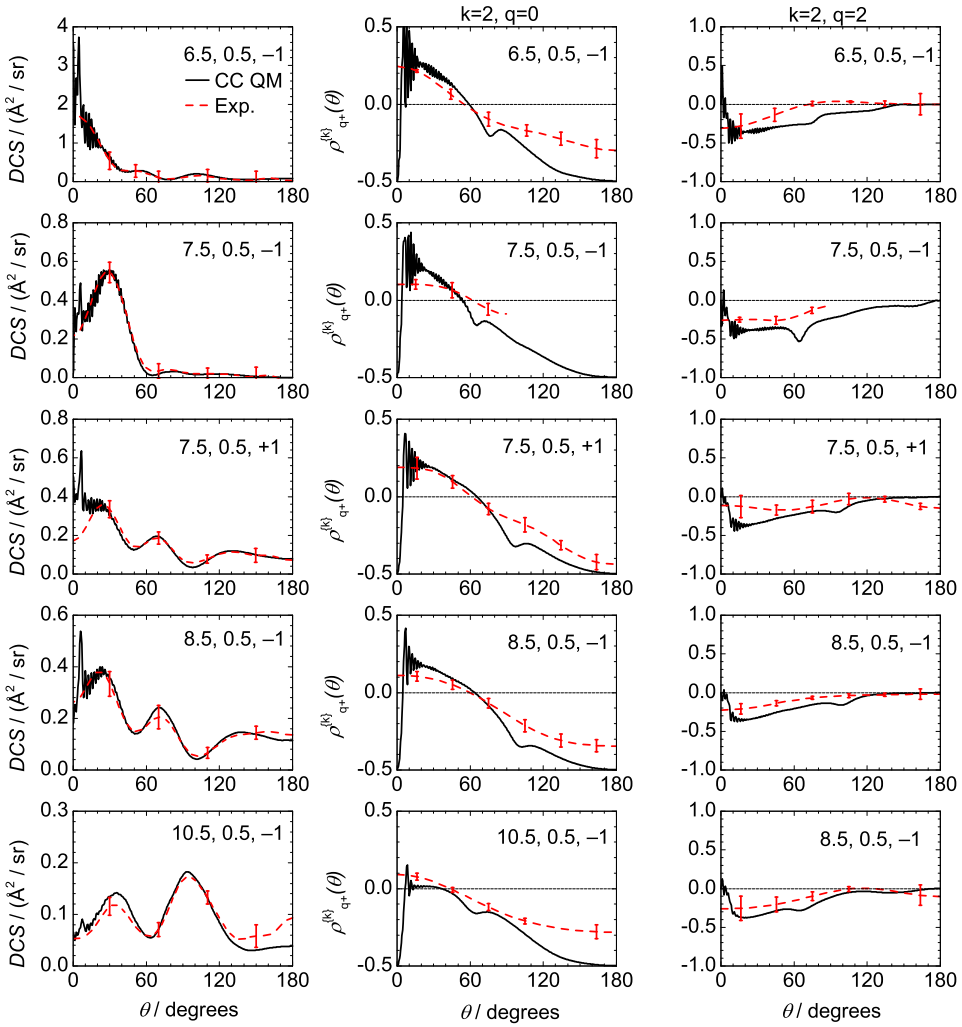

Figure 7.12: The CC QM (black solid lines) and experimental (red dashed lines) DCSs and $\rho_0^{\{2\}}(\theta)$, $\rho_{2+}^{\{2\}}(\theta)$ renormalised PDDCSs for $|0.5, 0.5, -1\rangle \rightarrow |6.5, 0.5, -1\rangle$, $|7.5, 0.5, -1\rangle$, $|7.5, 0.5, +1\rangle$, $|8.5, 0.5, -1\rangle$ and $|10.5, 0.5, -1\rangle$ spin–orbit conserving transitions from top to bottom. The DCSs were taken from [142].

The initial drop of the theoretical $\rho_{2+}^{\{2\}}(\theta)$ renormalised PDDCSs is not fully mirrored in the experimental renormalised PDDCSs which might be attributed to the blurring effect of the experimental circumstances, as was demonstrated by comparing the ideal

and full simulations of the normalised difference images. Nevertheless, these parameters are positive in the forward scattered region which implies that $\boldsymbol{j'}$ is preferentially aligned parallel to the $\hat{\boldsymbol{y}}$ axis of the scattering frame. It approaches zero towards bigger scattering angles which indicates vanishing alignment with respect to the $\hat{\boldsymbol{x}}$ and $\hat{\boldsymbol{y}}$ axes.

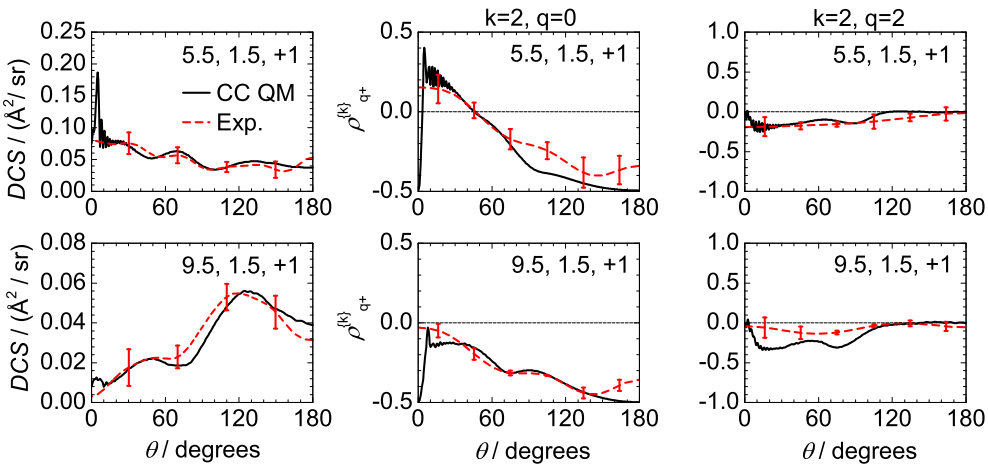

Figure 7.13: The CC QM (black solid lines) and experimental (red dashed lines) DCSs and $\rho_0^{\{2\}}(\theta)$, $\rho_{2+}^{\{2\}}(\theta)$ renormalised PDDCSs for $|0.5, 0.5, -1\rangle \rightarrow |5.5, 1.5, +1\rangle$ and $|9.5, 1.5, +1\rangle$ spin–orbit changing transitions (top and bottom rows, respectively). The DCSs were taken from [142].

The agreement between the theoretical and experimental PDDCSs is, in general, very good, although, there are some systematic discrepancies whose possible origin must be addressed. The $\rho_0^{\{2\}}(\theta)$ renormalized PDDCSs agree well with the theoretical ones in the forward scattered region, though, the deviation between them is somewhat more pronounced in the backward scattered region. The decrease of the scattering intensity might be responsible for this observation. The DCSs are especially forward and sideways scattered except for the $|0.5, 0.5, -1\rangle \rightarrow |9.5, 1.5, +1\rangle$ transition. This lessens the overall signal level as illustrated by the H+V sum images in Figure 7.9–7.10. The somewhat decreased level of signal-to-noise ratio causes 'speckles' to appear in this region which virtually reduces the degree of overall alignment seen by the detector. During the course of fitting this reduced intensity is approximated by the linear combination of the basis sets, thus the returned expansion coefficients will return less negative renormalised PDDCSs. Discrepancies with

theory are also more noticeable for the $\rho_{2+}^{\{2\}}(\theta)$ renormalized PDDCSs.

Potential sources of experimental errors could be as follows. The first step of the $(1+1')$ REMPI process can be saturated if the the dye laser is too intense. This would reduce the sensitivity to the alignment over the whole scattering angle region. However, the deviation is more pronounced at bigger scattering angles. The laser power was kept low when the images were collected in order to avoid saturation. Also, the degree of saturation was an input parameter of the fitting. It was found that setting the saturation to zero produced best agreement between the fitted and experimental images.

The second laser applied in the REMPI scheme was assumed to have enough intensity to fully saturate the ionisation process. If the power of the excimer laser is not high enough, the ionisation depends on the polarisation of the laser and of the molecular ensemble. Again, this would have equally affected the scattered molecules irrespective of which angle they departed. Therefore it was not considered as an important source of experimental error.

Stray magnetic fields could also depolarise the scattered NO(X) molecules. The longer the time that the scattered NO(X) molecules spend in the detection volume, the bigger is this effect. Thus the molecules with the smallest lab frame velocities are expected to be depolarised the most, those which are backward scattered. Although μ-metal shielding was installed around the scattering region, it is possible that the residual stray magnetic fields might play some role in the underestimation of the $\rho_0^{\{2\}}(\theta)$ moment in the backward scattered region.

Another systematic error may be due to the background scattered signal, which mainly affects the forward scattered region of the raw ion images. This is due to collisions happening in the hexapole section of the experimental apparatus and mostly affects the low j' final states [66, 142]. Therefore it is plausible to assume it only plays a negligible role in the results presented here.

Chandler and coworkers measured the Λ-doublet averaged alignment parameters [19] for the spin–orbit conserving $|0.5, 0.5\rangle \rightarrow |j', 0.5\rangle$ transitions, where $j' = 4.5, 8.5, 11.5, 12.5$

and 15.5. They found that the experimental $\rho_0^{\{2\}}(\theta)$ renormalized PDDCSs were less negative in the sideways and backward scattered regions for all of the final states. For the highest rotational state they investigated the theoretical value of $\rho_0^{\{2\}}(\theta)$ was considerably less negative than the experimental one for all scattering angles. It is assumed that Chandler used the polarisation parameters of Fano and Macek, though, the $j(j+1)$ normalisation factor was not indicated, and Eqs. (8) and (9) are misprinted in [19]. The Λ-doublet averaged $\rho_{2+}^{\{2\}}(\theta)$ renormalised PDDCSs were less negative in the forward scattered region shown in their work [19]. The agreement was good in the backward scattered region. They speculated that the innermost repulsive region of the $V_{\rm sum}$ potential might be inaccurate. However, the experimental and theoretical data presented in this work agree well, not only for the spin–orbit conserving but also for the spin–orbit changing collisions which primarily probes the $V_{\rm dif}$ potential [102]. Therefore the comparison of the experimental and theoretical results serves as an additional confirmation that the *ab initio* potential [102] is accurate.

7.7 Summary

An algorithm has been developed to retrieve polarisation dependent differential cross sections from normalised difference velocity mapped ion images. It is based on the formalism of Fano and Macek to describe transition probabilities in a rotationally polarised medium [77]. Its key concept is to obtain the experimental normalised difference image as a linear combination of basis images, where the expansion coefficients are those of the renormalised PDDCSs contributing to the observed intensity. The procedures of generating the basis sets and performing the fit were detailed. Various simulations were carried out to help to understand the observed experimental images. The algorithm was employed to extract $\rho_0^{\{2\}}(\theta)$ and $\rho_{2+}^{\{2\}}(\theta)$ renormalised PDDCSs from the experimental images for a selection of spin–orbit conserving and changing transitions in the NO(X)+Ar collisions. The agreement between CC QM and experimental data was generally very good. The

possible source of the discrepancies were also addressed. The experimental PDDCSs confirms that the collision dynamics responsible for the rotational alignment is inherently due to the hard shell-like, impulsive interaction between the NO(X) molecule and the argon atom, which was found in the theoretical Chapter 5 of this thesis.

Although, the fitting algorithm has only been employed here to extract alignment parameters, it is capable of retrieving orientation parameters from measurements using circularly polarised light.

Chapter 8

Theoretical studies of the rotational orientation effects in the inelastic collisions of NO(X) and Ar

In this Chapter, rotational orientation effects in the inelastic collisions of NO(X) and Ar are investigated. The properties of the collision system, and of the rotational orientation, will be examined in order to explain the various phenomena observed. By invoking a wide range of theoretical models, general rules will be established and used to predict the presence or absence of rotational orientation in classical atom-diatom collisions. These will be exemplified by comparing results from various classical hard shell, full potential QCT and quantum mechanical calculations. The main finding to be presented is that the rotational orientation vanishes in collisions between classical hard shells and atoms, if certain symmetry properties pertain to the system.

Contrary to this classical result, it will be shown, in general, there is rotational orientation in hard shell collisions in the framework of quantum mechanics.

The so-called orientation resolved polarisation dependent differential cross sections and polarisation dependent opacity functions will be first defined here in order to elucidate the origin of the rotational orientation.

8.1 Overview

Rotational orientation in the collisions of diatomic molecules and atoms has attracted a considerable deal of attention, though much less than the investigation of the scalar and low order vector quantities, such as integral cross sections and differential cross sections. Approaches have been made from both theoretical [44, 126, 150] and experimental points of view [181], and have resulted in a number of different explanations, each emphasising different properties and physical relationships relevant to the system of interest.

The earliest theoretical study was concerned with the left-right symmetry of the classical and semi-classical differential cross sections [189], which has implications on the rotational orientation [181]. Bosanac concluded that classically, the rotational orientation is solely due to multiple encounter impacts in the collisions of structureless atoms and hard ellipses [116]. In the present work a detailed explanation of these findings and extension to three dimensions will be given. The extra requirements and correct criteria that are needed to determine the existence of the rotational orientation in the classical hard shell collisions of atoms and diatoms will be stated.

Aoiz *et al.* carried out quasi-classical trajectory (QCT) calculations at a collision energy of 66 meV [44] using the V_{sum} potential energy surface of Alexander [102]. These results were compared to those from averaged close coupled quantum mechanical (CC QM) calculations. The agreement was reasonable between the classical and averaged quantum mechanical results, implying that the underlying mechanism can be well described by a classical mechanism. The observed trend is as follows: the orientation renormalised polarisation dependent differential cross section (renormalised PDDCS), $\rho_{1-}^{\{1\}}(\theta)$, defined in Chapter 3, is positive in the forward scattered region at low Δj transitions. It does not have a particular pattern in the case of medium rotational excitation. At high Δj $\rho_{1-}^{\{1\}}(\theta)$ predominantly takes negative values. It was pointed out by Aoiz *et al.* that this is due to the correlation between the orbital and rotational angular momenta. However, a detailed explanation for this correlation was not fully provided [44]. The integrated orientation

moments almost monotonically decrease as a function of Δj.

The quantum mechanical investigations into the nature of rotational orientation started in the second half of the 1970-s. Although these studies focussed on the effect of electron impact on an electronically excited atom [125, 190–192], many findings are general enough to be invoked in the following discussion of atom–diatom collisions. Based on experimental evidence, Kohmoto and Fano proposed that the attractive forces are more likely to cause positive orientation in the scattering frame, whilst the repulsive part of the potential might cause negative rotational orientation of the final rotational angular momentum [192]. They subsequently derived a relationship between the sign of the scattered wave's phase shifts and the sign of the rotational orientation, thus they were able to assign the attractive or repulsive nature of the potential to a particular sign of the orientation qualitatively. Herman and Hertel [190] introduced the so-called natural frame in which the quantisation axis is parallel to the $\hat{\boldsymbol{y}}$ axis of the scattering frame defined in Chapter 2, which facilitates the calculation of the orientation parameters. They explained the forward scattered orientation in terms of the grazing model [190]. Andersen [191] applied this theory to the collisions of electrons with He(^{2}P$_1$). His formalism more heavily relied on the scattering amplitudes similar to the works to be discussed in the following.

Alexander [193] investigated the necessary and sufficient conditions under which the rotational orientation vanishes in the collisions between a structureless atom and a diatomic molecule. He showed that the square moduli of the $\pm m_{j'}$ scattering amplitudes are generally not equal in the natural frame, hence the scattered product will be oriented. The actual magnitude of the scattering amplitudes are determined by the interaction potential which varies system by system. The modulus and sign of the orientation are thus hard to accurately predict without performing scattering calculations. Nevertheless, qualitative rules can still be derived. These were illustrated with the example of N_2–Ar scattering where the long range anisotropy was found to induce rotational orientation [193].

More recently, de Miranda *et al.* reformulated the problem of the rotational orientation in the collisions of open shell diatomic molecules and structureless atoms in terms of

the canonical scattering mechanism [150]. The initial, or reagent, rotational orientation is almost perfectly conserved during both parity conserving and parity changing collisions of NO(X)–Ar at a collision energy of 66 meV. If $j = 0.5$ initially, each quantum mechanical mechanism associated with a particular transition can be decomposed into the incoherent sum of two canonical mechanisms according to the total parity of the scattering wavefunction [194, 195]. The even mechanism always leads to positive final rotational orientation, whilst the odd mechanism leads to negative final rotational orientation. The total final orientation is given by the weighted sum of these two, and is determined by the angular dependence of this weight factor. In other words, the different probabilities of the even and odd transitions are responsible for the interesting behaviour of the renormalised PDDCSs. investigated. There is only a single canonical mechanism in the collisions of initially non-rotating closed shell molecules [194]. As a consequence, rotational orientation in these collisions cannot be explained in terms of a balance between various canonical mechanisms.

The $\rho_{1-}^{\{1\}}(\theta)$ was measured by Chandler *et al.* [181] for the NO(X)–Ar system. Their results were resolved only in the final Λ-doublet levels. They found that the experimental $\rho_{1-}^{\{1\}}(\theta)$ changes rapidly as a function of the scattering angle behaviour, which is markedly different for various Δj transitions. The experimental results were in good agreement with the rigorous quantum mechanical calculations [181]. However, they proposed that multiple encounter collisions are primarily responsible for the rotational orientation, which were illustrated by classical model hard shell Monte Carlo calculations. The agreement between the hard shell and experimental data were good for some of the transitions, but in general it seemed to not be better than qualitative.

8.2 Orientation resolved polarisation parameters

With classical trajectory methods it is possible to exactly calculate the physical quantities of every trajectory at any time. This quantity can, for example, be the impact parameter,

b, the scattering angle, θ, or the final rotational angular momentum, $\boldsymbol{j'}$. It is thus possible to label the trajectories according to these physical quantities. Here, we choose to the label the trajectories depending on whether the diatom has a negative or positive final rotational orientation. Therefore all of the derived functions, such as the deflection function, opacity function, the integral cross section (ICS), differential cross section (DCS), and PDDCS can be calculated with a specifically labelled subset of all trajectories. In this manner it is possible to establish whether a correlation between the final rotational orientation and initial collision geometry exists. These functions will be referred to using the prefix of orientation resolved (OR). For example, the orientation resolved histogram binned DCSs are defined as follows:

$$\frac{\mathrm{d}\sigma_{f\leftarrow i,\pm}}{\mathrm{d}\omega} = \frac{1}{2\pi\Delta\cos(\theta+\Delta\theta)} b_{max}^2 \frac{\pi N_{f\leftarrow i,\pm}}{N_i}\,, \tag{8.1}$$

where $N_{f\leftarrow i,\pm}$ is the number of trajectories ending in the final state f in the interval $\Delta\cos\theta$ and causing $(+)$ or $(-)$ rotational orientation. N_i is the total number of trajectories starting from the state i. The DCSs can also be calculated with the Legendre moment expansion method according to Eqs. (2.25)– (2.26) where the expectation value is separately calculated for the $(+)$ or $(-)$ trajectories. The OR-integral cross sections are the integrals of the OR-DCSs, and the sum of them returns the ordinary, or total, integral cross sections.

The definition of the normalised polarisation dependent differential cross sections, $n_{1-}^{\{1\}}(\theta)$, given in Chapter 3 by Eq. (3.20), is easily extended to yield the orientation resolved normalised PDDCSs, $n_{q\pm,\pm}^{\{k\}}(\theta)$:

$$n_{q\pm\pm}^{\{k\}}(\theta) = \frac{1}{2}\sum_{k_1\geq q}^{\infty}(2k_1+1)s_{q\pm,\pm k_1}^{\{k\}}C_{k_1,-q}(\theta,0)\,, \tag{8.2}$$

where $s_{q\pm,\pm k_1}^{\{k\}}$ is the expectation value provided by Eqs. (3.21)– (3.23) is calculated for those trajectories which lead to $(-)$ or $(+)$ final rotational orientation. The OR-polarisation

moments are the integrals of the normalised PDDCSs according to Eq. (8.3)

$$a^{\{k\}}_{q\pm,\pm} = \int_{-1}^{1} n^{\{k\}}_{q\pm\pm}(\theta)\mathrm{d}\cos\theta\,. \tag{8.3}$$

Obviously, the $a^{\{1\}}_{1-,+}$ and $a^{\{1\}}_{1-,-}$ moments can only be positive or negative, apart from zero, respectively. The ordinary, or total, polarisation moments are simply the sum of the OR-moments:

$$a^{\{k\}}_{q\pm} = a^{\{k\}}_{q\pm,-} + a^{\{k\}}_{q\pm,+}\,. \tag{8.4}$$

Finally, the histogram binned real OR-renormalised PDDCSs, $\rho^{\{k\}}_{q\pm,\pm}(\theta)$, are calculated as the expectation values of the appropriate Hertel–Stoll normalised conjugated modified spherical harmonics in the $(\theta + \Delta\theta)$ interval. The arguments, $\theta_{j'}$ and $\phi_{j'}$, are the polar angle and the azimuth of $\boldsymbol{j'}$ in the scattering frame, respectively.

$$\rho^{\{k\}}_{q\pm,\pm}(\theta) = \langle\, C^{\{k\}}_{q\pm,\pm}(\theta_j, \phi_j)\rangle_{(\theta+\Delta\theta)} \tag{8.5}$$

Alternatively, the OR-renormalised PDDCSs can be calculated from the expanded OR-normalised PDDCSs by dividing them by the correct angular distribution function. The ordinary, or total, renormalised PDDCSs, $\rho^{\{k\}}_{q\pm}(\theta)$, are obtained as the weighted average of the orientation resolved ones.

$$\rho^{\{k\}}_{q\pm}(\theta) = \frac{\rho^{\{k\}}_{q\pm,-} DCS_{-}(\theta) + \rho^{\{k\}}_{q\pm,+}(\theta) DCS_{,+}(\theta)}{DCS(\theta)} \tag{8.6}$$

Eq. 8.6 will be particularly important in uncovering the origin of the classical rotational orientation which is quantified by the $\rho^{\{1\}}_{1-}(\theta)$ parameter. This formalism interprets the rotational orientation as a balance between the (+) and (−) orientations belonging to different trajectories, which are presumably linked to different mechanisms.

8.2.1 Polarisation dependent and orientation resolved opacity functions

The PDDCSs quantify the final rotational polarisation in terms of a final variable, *i.e.* the scattering angle. From a mechanistic point of view it would be more meaningful to link the orientation of $\boldsymbol{j'}$ to the initial variables. The impact parameter and the initial bond axis orientation are most likely to provide information on the dynamics of the collisions. By analogy of the PDDCSs of Eq. (3.20) in Chapter 3 the probability that a trajectory having an impact parameter b leads to j' final state, when the orientation angles of $\boldsymbol{j'}$ are $(\theta_{j'}, \phi_{j'})$ is given by Eq. (8.7),

$$P\left(\widetilde{b}, \theta_{j'}, \phi_{j'}\right) = \frac{1}{4\pi} \sum_{k=0}^{\infty} (2k+1) \sum_{q=-k}^{k} b_q^{(k)}(\widetilde{b}) C_q^{(k)*}\left(\theta_{j'}, \phi_{j'}\right) , \tag{8.7}$$

where $b_q^{(k)}(\widetilde{b})$ expansion coefficient is the polarisation dependent opacity function, PDOF, of rank k and component q. $C_q^{(k)*}(\theta_j, \phi_j)$ is the complex conjugate of the modified spherical harmonic [117], and $\widetilde{b}$ is the reduced impact parameter [14, 108] defined as

$$\widetilde{b} = \frac{2b^2 - b_{\max}^2}{b_{\max}^2} \quad \text{in 3D} \tag{8.8}$$

$$\widetilde{b} = \frac{2b - b_{\max}}{b_{\max}} \quad \text{in 2D} . \tag{8.9}$$

Note, the probability function is normalised to N_f/N_i rather than unity in order to be consistent with the ordinary opacity function, $p(b)$ defined in Eq. 2.19. The sum over all of the possible final states f of the integrated opacity functions is obviously unity:

$$\begin{aligned} \sum_f & \int_{-1}^{1} \int_{0}^{2\pi} \int_{-1}^{1} P_f\left(\widetilde{b}, \theta_{j'}, \phi_{j'}\right) \mathrm{d}\cos\theta_{j'} \mathrm{d}\phi_{j'} \mathrm{d}\widetilde{b} \\ = & \sum_f \int_{-1}^{1} P_f\left(\widetilde{b}\right) \mathrm{d}\widetilde{b} = \sum_f \frac{N_f}{N_i} = 1 , \end{aligned} \tag{8.10}$$

from which the polarisation dependent opacity function, $b_q^{(k)}(\widetilde{b})$, is easily calculated using the orthogonality properties of the modified spherical harmonics,

$$b_q^{(k)}(b) = \int_{-1}^{-1} \int_{0}^{\pi} P\left(\widetilde{b}, \theta_{j'}, \phi_{j'}\right) C_q^{(k)}(\theta_{j'}, \phi_{j'}) \mathrm{d}\cos\theta_{j'} \mathrm{d}\phi_{j'} \,. \tag{8.11}$$

If this formula is specialised to the $k = 0, q = 0$ case, the ordinary opacity function is recovered:

$$b_0^{(0)}(\widetilde{b}) = p(\widetilde{b}) \,. \tag{8.12}$$

The polarisation moments are obtained as an integral over the entire impact parameter region as shown in Eq. (8.13), where the N_i/N_f factor accounts for the normalisation of the opacity function:

$$\begin{aligned} a_q^{(k)} &= \frac{N_i}{N_f} \int_{-1}^{1} b_q^{(k)}(\widetilde{b}) \mathrm{d}\widetilde{b} \\ &= \frac{N_i}{N_f} \int_{0}^{b_{\max}} \frac{\pi 4b}{b_{\max}^2} b_q^{(k)}(b) \mathrm{d}b = \int_{0}^{b_{\max}} p_q^{(k)}(b) \mathrm{d}b \,. \end{aligned} \tag{8.13}$$

The polarisation dependent partial cross section of rank k and component q, $p_q^{(k)}(b)$, PDPCS, was introduced in the bottom line. It comprises all of the integration and normalisation factors, in order that its integral results in the corresponding polarisation moment:

$$p_q^{(k)}(b) \equiv \frac{N_i}{N_f} \frac{\pi 4b}{b_{\max}^2} b_q^{(k)}(b) \,. \tag{8.14}$$

The PDOF can be given as a series expansion in terms of modified spherical harmonics according to Eq. (8.15):

$$b_{q\pm}^{\{k\}}(\widetilde{b}) = \sum_{k_1, m} P_m^{k_1}(\widetilde{b}) N_{q\pm, k_1 m}^{\{k\}} s_{q\pm, k_1 m}^{\{k\}} \,, \tag{8.15}$$

where $N^{\{k\}}_{q\pm,lm}$ is a normalisation factor, and $s^{\{k\}}_{q\pm,lm}$ is the expansion coefficient. Using the Hertel-Stoll normalised modified spherical harmonics, one may write

$$\begin{aligned} N^{\{k\}}_{q\pm,lm} s^{\{k\}}_{q\pm,lm} &= \int_{-1}^{1}\int_{0}^{2\pi}\int_{-1}^{1} P\left(\widetilde{b},\theta_{j'},\phi_{j'}\right) C^{\{k\}}_{q\pm}(\theta_{j'},\phi_{j'}) P^{l}_{m}(\widetilde{b}) \mathrm{d}\cos\theta_{j'}\mathrm{d}\phi_{j'}\mathrm{d}\widetilde{b} \\ &= \langle C^{\{k\}}_{q\pm}(\theta_{j'},\phi_{j'}) C^{l}_{m}(\widetilde{b},0)\rangle \,. \end{aligned} \tag{8.16}$$

If $k=0, q=0$, Eq. (8.16) should return the expansion of the opacity function, which is equivalent to choosing the orthogonal polynomials to be the modified spherical harmonics. The proportionality coefficients are

$$N^{\{k\}}_{q\pm,k_q} = \frac{N_f}{N_i}\frac{2l+1}{2}\,. \tag{8.17}$$

The orientation resolved (OR) polarisation dependent opacity functions, $b^{\{k\}}_{q\pm,\pm}(b)$, quantify how a particular final rotational orientation, *i.e.* clockwise or counterclockwise, depends on the initial impact parameter. The $(+/-)$ OR-PDOF are calculated on the subset of trajectories for which the final rotational angular momentum has $(+)$ or $(-)$ orientation. The integral of these quantities returns the orientation resolved polarisation moments of Eq. (8.4).

The formulae for calculating the real expansion coefficients are inherently identical to those in Eq. (8.16) and in Eqs. (3.21)–(3.23), provided the scattering angle, θ, is replaced by the reduced impact parameter, and the normalisation factor is accounted for. The above defined quantity thus may help to distinguish between various mechanisms linked to different impact parameters.

Initial bond axis orientation resolved polarisation dependent opacity function

The initial bond axis orientation resolved polarisation dependent opacity function, r-PDOF, $p^{(k)}_{q}(a^{\{1\}}_{1-}(\boldsymbol{r}))$, is defined in Eq. (8.18). It quantifies the final rotational polarisation as a function of the initial bond axis orientation. It should, however, be pointed out that

only the scalar $a_{q\pm}^{\{k\}}(\boldsymbol{r})$ moments are considered in the present work. The problem is more general and a thorough examination requires the exact treatment of the $\boldsymbol{r}-\boldsymbol{k}-\boldsymbol{k'}-\boldsymbol{j'}$ four vector correlation. $a_{1-}^{\{1\}}(r)$ is the initial bond axis orientation in the frame in which the classical hard shell and QCT calculations are initialised. Namely, its principal axis $\hat{\boldsymbol{Z}}$ is parallel to the initial relative velocity, $\boldsymbol{k}$, and the impact parameter is measured in the $+\hat{\boldsymbol{Y}}$ direction. The $\hat{\boldsymbol{X}}$ axis is chosen so that the frame is right handed.

The probability of an event that results in final rotational angular momentum, $\boldsymbol{j'}$, pointing at a direction specified by the angles $(\theta_{j'},\phi_{j'})$ and with initial bond axis orientation is $a_{1-}^{\{1\}}(\boldsymbol{r})$ is given by $P\left(a_{1-}^{\{1\}}(\boldsymbol{r}),\theta_{j'},\phi_{j'}\right)$.

$$P\left(a_{1-}^{\{1\}}(\boldsymbol{r}),\theta_{j'},\phi_{j'}\right) \;=\; \frac{1}{4\pi}\sum_{k=0}^{\infty}\sum_{q=-k}^{k}(2k+1)C_q^{(k)}(\theta_{j'},\phi_{j'})p_q^{(k)}(a_{1-}^{\{1\}}(\boldsymbol{r}))\,, \qquad (8.18)$$

where the expansion coefficients $p_q^{(k)}(a_{1-}^{\{1\}}(\boldsymbol{r}))$ are the r-PDOFs. The real, Hertel–Stoll normalised opacity function can again be given in terms of a series expansion according to Eq. (8.19):

$$p_{q\pm}^{\{k\}}(x)=\sum_{l}\frac{2k_1+1}{2}C_q^{(k_1)}(x,0)s_{q\pm,k_1}^{\{k\}}\,, \qquad (8.19)$$

where the shorthand notation x stands for $a_{1-}^{\{1\}}(\boldsymbol{r})$. The expansion coefficients are conveniently obtained as the expectation values of the product of the appropriate spherical harmonics:

$$s_{q\pm}^{\{k\}}=\int_{-1}^{1}\int_{0}^{2\pi}\int_{-1}^{1}P(x,\theta_{j'},\phi_{j'})C_{q\pm}^{\{k\}}(\theta_{j'},\phi_{j'})C_q^{(l)}(x)\mathrm{d}\cos\theta_{j'}\mathrm{d}\phi_{j'}\mathrm{d}x\,. \qquad (8.20)$$

Alternatively, the initial bond axis orientation dependent reaction probability can be determined with a histogram binning method:

$$p_{q\pm}^{\{k\}}\left(a_{1-}^{\{1\}}(r)\right)=\sum_{n}\frac{\tilde{a}_{q\pm,\pm,n}^{\{k\}}\left(a_{1-,n}^{\{1\}}(\boldsymbol{r})\right)}{N_i}\,, \qquad (8.21)$$

where the subscript 'n' refers to the n-th trajectory which ends up in the final state of interest.

The running integral of this parameter, defined in Eq. (8.22) shows how the integrated polarisation moments depend on a particular initial bond axis orientation region,

$$I_{q\pm}^{\{k\}}(s) = \int\limits_{a_{1-}^{\{1\}}(\boldsymbol{r})=-1}^{s} p_{q\pm}^{\{k\}}\left(a_{1-}^{\{1\}}(\boldsymbol{r})\right) \mathrm{d}a_{1-}^{\{1\}}(\boldsymbol{r})\,. \tag{8.22}$$

The integral of $p_{q\pm}^{\{k\}}\left(a_{1-}^{\{1\}}(r)\right)$ over all the possible bond axis orientations results in the $a_{q\pm}^{\{k\}}$ polarisation moment, that is:

$$I_{q\pm}^{\{k\}}(1) = a_{q\pm}^{\{k\}}\,. \tag{8.23}$$

The ratio of clockwise and anticlockwise polarisation is given by the $(+/-)$ orientation resolved r-PDOFs as a function of the bond axis orientation. These quantities are calculated using Eqs. (8.18)–(8.22) but considering only those trajectories that lead to (+/-) final rotational orientation. Having introduced the polarisation dependent and orientation resolved reaction probabilities we have the necessary apparatus to ascertain the origin of the classical rotational orientation.

8.3 Rotational orientation in classical hard shell collisions

Rotational orientation in the case of classical impulsive collisions will be investigated in this section. It will be shown that the rotational orientation vanishes in the collisions of NO(X)–Ar at a collision energy of 66 meV. Moreover, the absence of rotational orientation in single encounter classical hard shell collisions turns out to be a general phenomenon due to symmetry reasons.

8.3.1 Classical hard shell orientation renormalised PDDCSs

The classical heteronuclear hard shell Monte Carlo model (C-HEHS) [131, 196] detailed in Section 2.2.1 was employed to calculate the ordinary and orientation resolved $\rho_{1-}^{\{1\}}(\theta)$ renormalised PDDCSs. The collision energy was set to 66 meV, at which the contour of the full V_{sum} potential was taken. The contour and the expansion coefficients are shown in Figure 4.1 and Table 4.1, respectively.

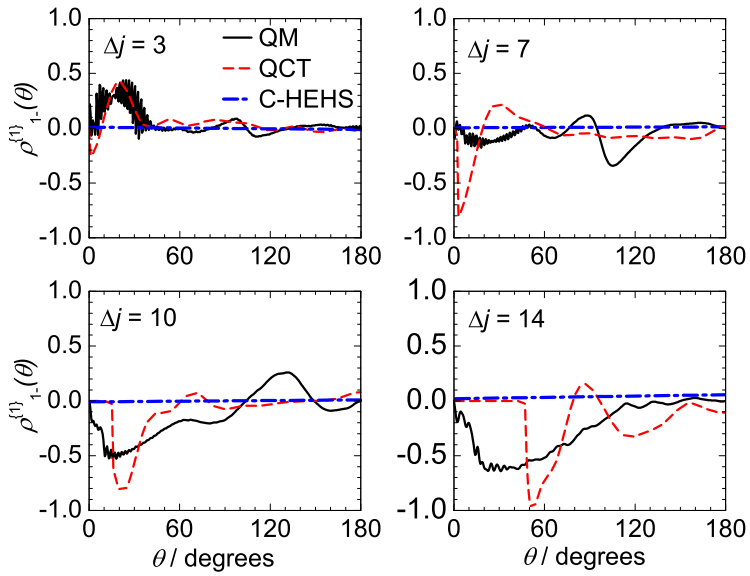

Figure 8.1: The averaged CC QM (black solid line), the QCT (red dashed line) and the classical hard shell (blue dashed-dotted line) $\rho_{1-}^{\{1\}}(\theta)$ for the $\Delta j = 3, 7, 10$ and 14 transitions from top left to bottom right. All calculations were carried out at a collision energy of 66 meV.

The $\rho_{1-}^{\{1\}}(\theta)$ renormalised PDDCSs are shown in Figure 8.1 for the $\Delta j = 3, 7, 10$ and 14 transitions, along with the QCT and averaged CC QM results. There is no rotational orientation with respect to the $\hat{\boldsymbol{y}}$ axis of the scattering frame at any scattering angles for all of the final states in the C-HEHS model. Classical calculations when the full V_{sum} potential is employed, or the exact CC QM calculations return orientation [44, 150, 181], which only disappears at certain scattering angles.

To understand the lack of orientation in the classical hard shell case, it is instructive to consider the (+) and (−) orientation resolved renormalised and normalised PDDCSs,

as shown in the top row of Figure 8.2. The (+) and (−) orientation resolved renormalised PDDCSs do not vanish in the classically allowed region and their moduli are equal, hence they should possess equal weights, as confirmed by the middle row of Figure 8.2, where the OR-normalised PDDCSs are plotted.

The moduli of the $n^{\{1\}}_{1-,+}(\theta)$ and $n^{\{1\}}_{1-,-}(\theta)$ OR-normalised PDDCSs are equal at a particular scattering angle, therefore they cancel one other out, which results in the lack of net orientation. The doubly peaked structure of the $n^{\{1\}}_{1-,\pm}(\theta)$-s reflects the angular probability distribution. Each maximum corresponds to scattering from different sides of the molecule. The forward scattered peak is due to collisions with the N-end, whilst the other peak is due to encounters on the O-end, as was discussed in Section 4.1.1. The lack of orientation

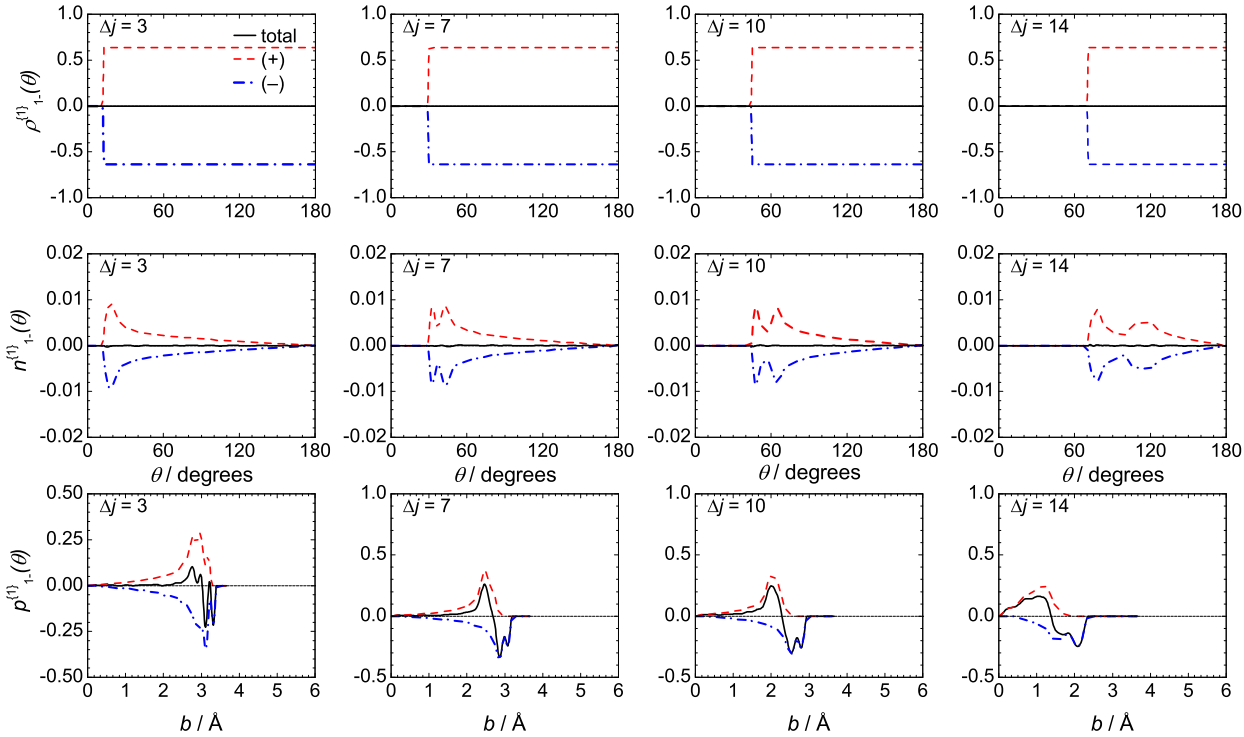

Figure 8.2: The classical hard shell total (black solid line) and orientation resolved: (+): red dashed line, (−): blue dash-dotted line renormalised PDDCSs, $\rho^{\{1\}}_{1-\pm}(\theta)$, (top row) and normalised PDDCSs, $n^{\{1\}}_{1-,\pm}(\theta)$. The corresponding total and orientation resolved PDPCSs, $p^{\{1\}}_{1-}(b)$, are shown in the bottom row, for the $\Delta j = 3, 7, 10$ and 14 transitions from top left to bottom right. All calculations were carried out at a collision energy of 66 meV.

stems from the cylindrical symmetry about the kinematic apse. It is best exemplified in the case of a 2D collision. Let us consider a single scattering event: the collision plane is defined by the $\boldsymbol{k}$ and $\boldsymbol{k'}$ vectors. The resultant rotational angular momentum, $\boldsymbol{j'}$, is solely determined by the point of contact, $\boldsymbol{R}$, the surface normal at that point, $\boldsymbol{a}$, and β, the angle between $\boldsymbol{k}$ and $\hat{\boldsymbol{a}}$ according to Eqs. (4.5)–(4.7) [115]. Since $\boldsymbol{R}$, $\boldsymbol{k}$ and $\hat{\boldsymbol{a}}$ are coplanar, $\boldsymbol{j'}$ should always be perpendicular to the scattering plane so that $\rho_{1-}^{\{1\}}(\theta)$ can only take the values of $+1$ and -1. A 2D collision is depicted in the left panels of Figure 8.3. In the top left panel $\boldsymbol{j'}$ and $\hat{\boldsymbol{y}}$ are parallel, thus $\rho_{1-}^{\{1\}}(\theta) = +1$. If another collision takes place in the same collision plane, but this time $\boldsymbol{k}$ and $\boldsymbol{a}$ make an angle of $-\beta$, the same amount of linear momentum is transferred in the same direction, thus $\boldsymbol{j'}$ will be identical to that resulting from the first collision in the lab frame. The scattering angle is also identical with that of the first encounter as shown in the bottom left panel of Figure 8.3.

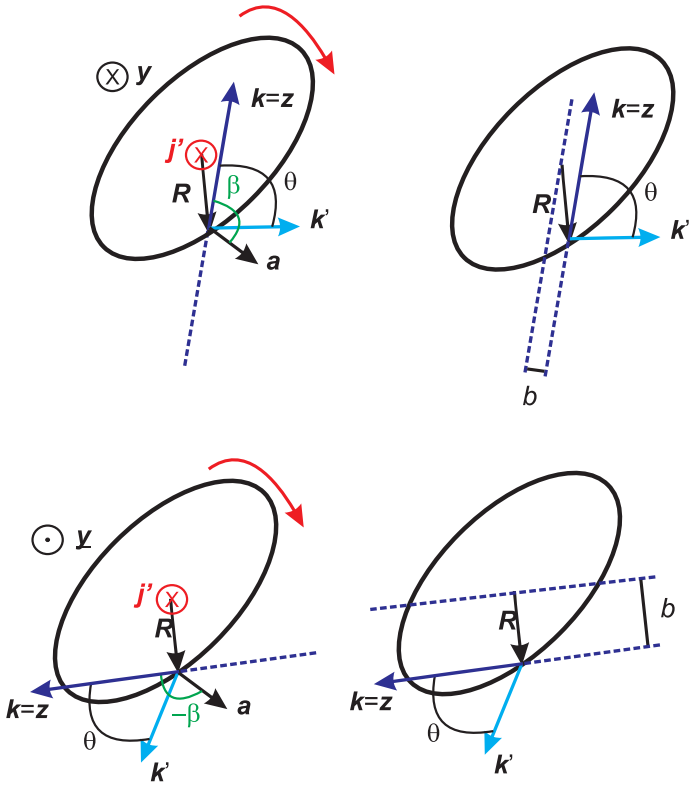

Figure 8.3: Illustration of two trajectories which lead to identical scattering angles, θ, and final rotational state, j' (left panels). The corresponding impact parameters are different for the two encounters. The small impact parameter is associated with shallow approach angle with respect to the molecular axis (right panels).

The two collisions are identical except that the handedness of the $\boldsymbol{k}$, $\boldsymbol{k'}$ and $\boldsymbol{a}$ vectors

is inverted. The new and the old scattering frames are related by a rotation about its $\hat{\boldsymbol{z}}$ axis by an angle of π. Hence, the orientation of $\boldsymbol{j'}$ in the second scattering frame will be the opposite of that in the first scattering frame. The individual rotational orientation contributions of these two collisions thus perfectly cancel each other, resulting in a lack of orientation for any particular $\boldsymbol{j'}$ state and scattering angle.

Figure 8.4 illustrates the cancellation of the individual orientations in the case of $\Delta j = 4$ and $\theta = 30°$ in terms of the initial parameters of the trajectories. If the collision is restricted to 2D, two parameters are sufficient to specify the initial geometry; the impact parameter, b, and the orientation angle of the bond axis with respect to the initial relative velocity, ϕ_r. There are eight paths which lead to identical θ and j'. Pairs of them belong to the same inter-particle distance, but to different ϕ_r and b. The individual rotational orientations of these trajectories are equal in magnitude but differ in sign as shown by Figure 8.4.

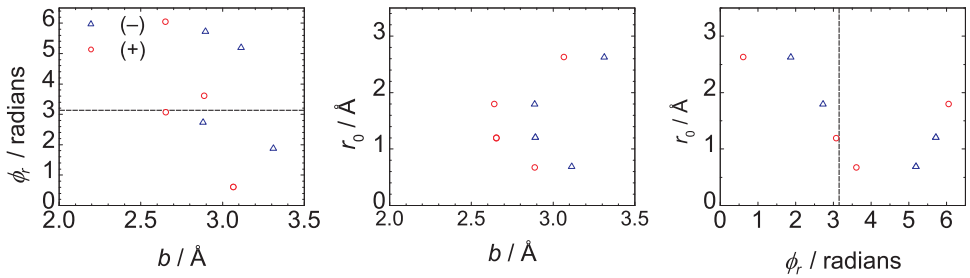

Figure 8.4: The trajectories which lead to $\theta = 30°$ and $\Delta j = 4$. There are eight paths, half of which result in +1 rotational orientation. Two points belong to a certain atom–diatom separation, $\boldsymbol{r}$, having opposite signs (middle panel). The (+) trajectories are concentrated at shallow impact angles, when the bond axis is aligned parallel to the incoming velocity. The dashed line represents $\gamma = \pi$ bond axis orientation.

If $\phi_r = n\pi$, the bond axis of the molecule is aligned parallel with respect to the incoming velocity, and if $\phi_r = \frac{2n+1}{2}\pi$, it is aligned perpendicularly. Atoms which approach the molecule at a shallow angle, with a small impact parameter will cause the molecule to rotate in clockwise sense, whilst those impinging on the hard shell with a relative velocity making an angle of about $\pi/2$ with the bond axis, and having large impact parameter induce anti-clockwise rotation of the molecule as can be read from the right panel of Figure 8.4. Again, it is important to remind ourselves both geometries belong to the same

point of contact, $\boldsymbol{R}$.

The separation of the initial configurations leading to (+) or (−) rotational orientation is greater at high Δj transitions, because the geometries in which sufficient momentum can be transferred to the rotational degree of freedom of the molecule are restricted, as discussed in Section 4.1.1.

The same argument, that pairs of encounters exist which lead to the same final state and scattering angle but with rotational orientation of opposite signs, can also be applied to three dimensional collisions. These trajectories can be transformed into each other by a rotation about $\hat{\boldsymbol{a}}$ by π, since the system is cylindrically symmetric about the kinematic apse. The individual orientation moments associated with each of the trajectories can take any value between -1 and $+1$. The classical hard shell OR-renormalised PDDCSs only assume two values in 3D, which can be calculated by integrating the projection of $\boldsymbol{j'}$ onto the $\hat{\boldsymbol{y}}$ axis:

$$\rho^{\{1\}}_{1-,\pm}(\theta) = \frac{1}{\pi}\int_{0}^{\pm\pi} \cos(\pi/2 - \phi_{\mathrm{a}})\mathrm{d}\phi_{\mathrm{a}} = \pm\frac{2}{\pi} \approx \pm 0.63\,, \tag{8.24}$$

where ϕ_a is the angle between $\boldsymbol{j'}$ and $\hat{\boldsymbol{y}}$. These values are independent of the scattering angle and the final rotational state, and it is indeed this value that is seen in Figure 8.4.

A hard shell can exhibit a preferred sense of rotation if the cylindrical symmetry of the trajectories about the kinematic apse is removed. This can happen by both spatial and temporal means. In the case of concave contours, there might be certain points on the molecular surface which are hidden by other parts of the surface, such that only one of the two supposedly equivalent trajectories can hit them. The dumbbell-shaped molecular surface is shown as an example in the left panel of Figure 8.5.

Let us assume an atom impacts on the concave middle section of the contour, and makes an angle of β with the surface normal. It could happen that the end of the molecule prevents those atoms from hitting the same point, which would otherwise make an angle of $-\beta$ with the surface normal. As a consequence, there will be net orientation. This is a purely geometrical cause of classical hard shell orientation. This type of collision requires a

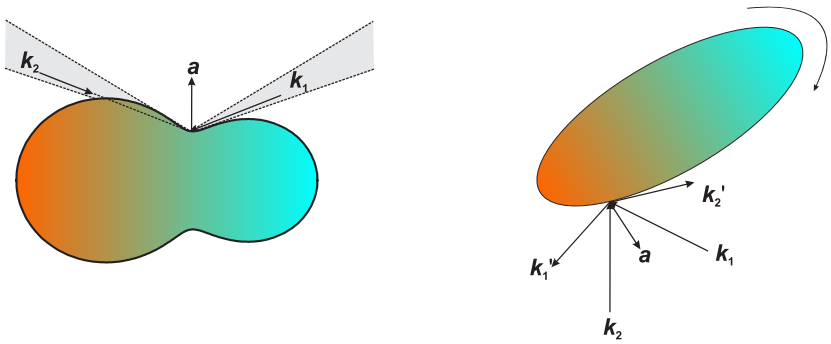

Figure 8.5: The highly anisotropic molecular shape prevents the '2' trajectory from canceling its equivalent trajectory's, '1', elementary orientation (left panel). The chattering collisions remove the temporal symmetry of the trajectories (right panel).

highly anisotropic molecular contour. It could also happen that the symmetry is lifted after the collision has occurred, *e.g.*, the free departure of the scattered atom is hindered by the now rotating molecule. This results in secondary or so-called chattering collisions [19, 116]. The probability of this event is the higher if the molecule has an elongated shape, meaning that a large amount of momentum can be transferred to the rotational degree of freedom of the molecule, slowing the atom down.

In summary, if the cylindrical symmetry of the trajectories about the kinematic apse is present, a hard shell cannot be rotationally oriented in classical collisions with structureless atoms.

8.4 Rotational orientation in classical collisions

The origin of the classical rotational orientation is investigated in this section. It is highlighted how the attractive and soft repulsive features of the interaction potential complicates the classical hard shell picture, and their exact role in the rotational orientation will be elucidated. The details of the quasi-classical trajectory, (QCT), calculations were discussed in Chapter 2. The trajectories were propagated on the $V_{\rm sum}(R,\gamma)$ surface of Alexander's PESs [102].

The QCT and averaged CC QM $\rho_{1-}^{\{1\}}(\theta)$ orientation renormalised PDDCSs were shown in the top row of Figure 8.1 for the $\Delta j = 3, 7, 10$ and 14 transitions. They were previously

characterised in Ref. [44]. As pointed out the agreement between the QCT and averaged CC QM data is generally good in the classically allowed region.

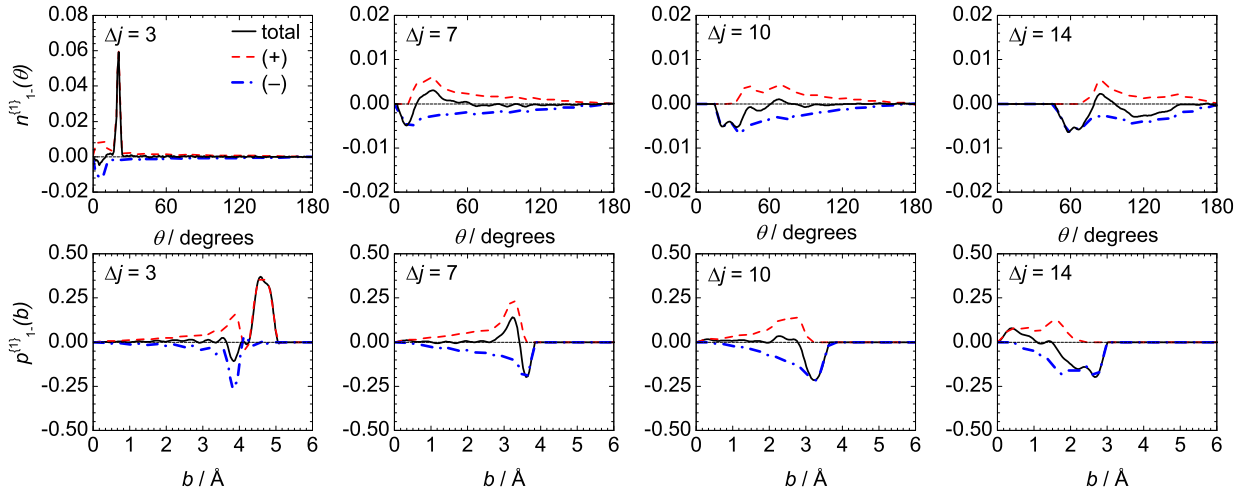

Figure 8.6: The QCT total (black solid line) and OR-normalised PDDCSs ((+) red dashed line, (−) blue dash-dotted line), $n^{\{1\}}_{1-,\pm}(\theta)$ employing the full $V_{\rm sum}$ potential are shown in the to row for the $\Delta j = 3, 7, 10$ and 14 transitions from left to right. The corresponding total and OR-PDPCSs, $p^{\{1\}}_{1-}(b)$, are shown in the bottom row. All calculations were carried out at a collision energy of 66 meV.

The orientation resolved normalised QCT PDDCSs are shown in the top row of Figure 8.6. The forward scattered positive peak is due to the attractive forces at low Δj transitions. These collisions are usually associated with large impact parameters, so the incoming atom mainly samples the long range attractive part of the potential. As the atom approaches the molecule, it is pulled towards the molecule by the long range attractive forces. The molecule starts to rotate in a direction following the atom passing by. The atom is deflected and scattered to the far side which results in positive rotational orientation. Other mechanisms can simultaneously be observed, which might lead to different, *i.e.* negative, final rotational orientation, but their weight is marginally lower as compared to that of the deflective mechanism. As Δj increases, the contribution of the deflective collisions decreases. The well depth of the potential is about 25% of the collision energy, hence orbiting collisions cannot happen. At intermediate Δj, the (+)

and (−) orientation resolved normalised PDDCSs, $n^{\{1\}}_{1-\pm}(\theta)$, are roughly equal, thus the total normalised PDDCS is close to zero as shown for the $\Delta j = 7$ and 10 transitions in the middle panels of Figure 8.6. But they are not strictly equal for all scattering angles. The classically forbidden region of the (+) OR-normalised PDDCSs is always more extended. Its maximum is shifted towards higher scattering angles, and becomes smaller compared to that of the (−) OR-normalised PDDCSs. They are only equal to each other at the backward scattered angles, but this region gradually shrinks as Δj increases. For instance, at $\Delta j = 10$, $n^{\{1\}}_{1-,+}(\theta)$ and $n^{\{1\}}_{1-,-}(\theta)$ are approximately the opposite to each other between $\theta = 100°$ and $\theta = 180°$, but at $\Delta j = 14$ this interval spans only between $\theta = 150°$ and $\theta = 180°$. The contribution of the $n^{\{1\}}_{1-,-}(\theta)$ PDDCSs exceeds that of the $n^{\{1\}}_{1-,+}(\theta)$ one, which results in negative rotational orientation.

These findings are further confirmed by the polarisation dependent partial cross sections, $p^{\{1\}}_{1-}(b)$, which are shown in the bottom panels of Figure 8.6. At $\Delta j = 3$, $p^{\{1\}}_{1-}(b)$ is comprised of two parts. The first of them spans between zero impact parameter until about $b \approx 4\,\text{Å}$, in which region the $p^{\{1\}}_{1-,-}(b)$ and $p^{\{1\}}_{1-,+}(b)$ are roughly equal, leading to the lack of orientation. The corresponding collisions mainly sample the steep repulsive wall of the interaction potential. Between $b = 3.5\,\text{Å}$ and $b = 4\,\text{Å}$ those mechanisms that lead to negative orientation are slightly more dominant.

The second main feature at large impact parameters is a broad peak. In this region, the incoming atom primarily experiences the attractive part of the potential resulting in deflective collisions of (+) orientation of $\boldsymbol{j'}$ as discussed above.

At intermediate final states, the contributions from the $p^{\{1\}}_{1-,-}(b)$ and $p^{\{1\}}_{1-,+}(b)$ are almost equal to each other, such that the overall orientation is nearly cancelled. As the degree of the excitation increases, the maximum impact parameter is reduced. It reflects the fact that the atom has to penetrate deeper into the potential in order to impart translational energy to the rotational degree of freedom of the molecule. The two orientation resolved PDPCSs become gradually more asymmetric as the degree of excitation rises as illustrated by the 2nd–4th panels of Figure 8.6. The trajectories which result in negative

final rotational orientation are more likely to be found at high impact parameters, whilst those causing $\boldsymbol{j'}$ to be positively oriented are confined to small impact parameter regions. Naïvely, it might be anticipated that as higher Δj final states are being populated, the interaction becomes more impulsive, thus the collision dynamics responsible for the rotational orientation become increasingly similar to that of the hard shell case, and the rotational orientation vanishes. However, this is not the case. As Δj increases, the degree of the negative orientation approaches then surpasses that of the positive orientation.

Rotational orientation in soft potential collisions

In order to exactly distinguish between effects arising from attraction and soft repulsion, QCT calculations have been carried out on the soft repulsive V_{sum} PES, from which the attractive part was removed according to Eqs. (4.12)–(4.13) in Chapter 4. The orientation resolved and total normalised PDDCSs are shown in the top row of Figure 8.7. At $\Delta j = 3$, the strong forward scattered positive peak is absent, and $n^{\{1\}}_{1-,+}(\theta)$ $n^{\{1\}}_{1-,-}(\theta)$ are equal with respect to their magnitudes, resembling the classical hard shell case. As a consequence, the overall rotational orientation vanishes. It is thus plausible to say that the classical orientation is almost exclusively due to the presence of the attractive forces at low Δj transitions. The number of molecules rotating anti-clockwise and clockwise is nearly equal up to about $\Delta j = 7$, above which value the negative orientation becomes preferred. If Δj is high, the soft and full potential orientation is very similar as seen by comparing Figures 8.6 and 8.7. It reveals that the soft repulsive forces are primarily responsible for removing the trajectories which would otherwise lead to positive rotational orientation.

The full or soft potential collisions can thus be viewed as distorted classical hard shell collisions. If a full potential QCT calculation is carried out where the initial parameters are not randomly sampled, but those from C-HEHS calcualtion are used which lead to inelastic collisions, the effect of the attractive and soft repulsive PESs can be further elucidated.

Four sets of ICSs were obtained, depending on final rotational orientation of the input

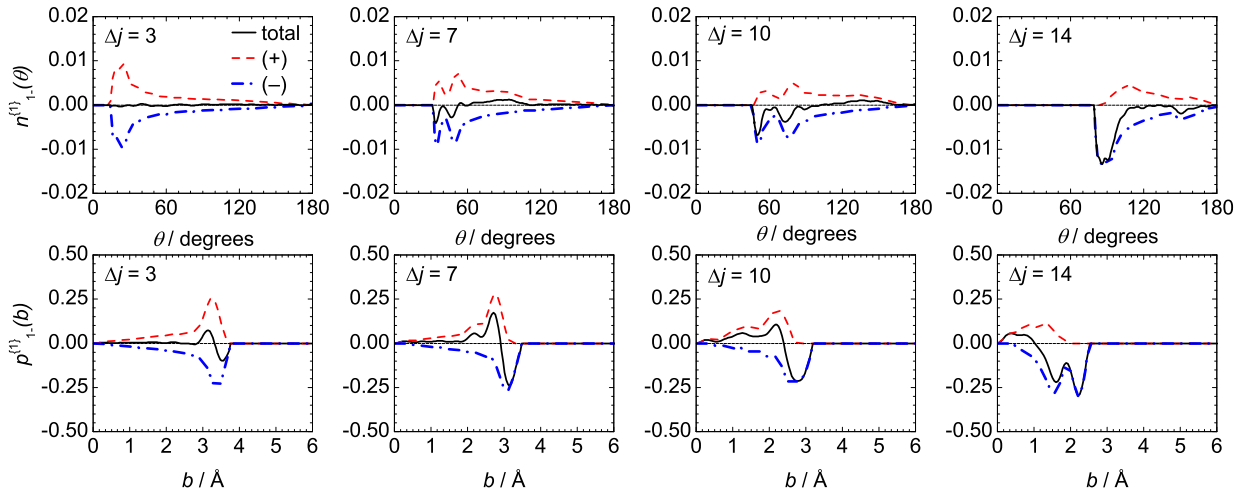

Figure 8.7: The soft potential total QCT (black solid line) and OR-normalised PDDCSs ((+) red dashed line, (−) blue dash-dotted line), $n^{\{1\}}_{1-,\pm}(\theta)$, employing the 'soft' $V_{\rm sum}$ potential are shown for the $\Delta j = 3, 7, 10$ and 14 transitions from left to right. The corresponding orientation resolved PDPCSs, $p^{\{1\}}_{1-}(b)$, are shown in the bottom row. All calculations were carried out at a collision energy of 66 meV.

C-HEHS trajectory, and on the final rotational orientation of the QCT trajectory initialised with the C-HEHS trajectory as shown Figure 8.8.

There is net rotational orientation, because the (+) and (−) ICSs are not equal. This clearly demonstrates that the full potential removes or modifies some of the C-HEHS trajectories. At low Δj transitions, there is a propensity for retaining those C-HEHS paths which lead to (+) orientation. In contrast, at high Δj transition, those C-HEHS trajectories that lead to (−) orientation are favoured. These cross sections are bigger than the ordinary ones, because they are calculated using only those trajectories which lead to inelastic collisions in the hard shell case.

The ordinary QCT and classical hard shell ICSs are compared in the left panel of Figure 8.8. For low Δj transitions, the QCT ICSs are larger than the hard shell ICSs, because the attractive and soft parts of the potential enlarges the region in which the interaction is strong enough to induce rotational transitions. The full potential reduces the degree of excitation as compared to the classical hard shell collisions at high Δj

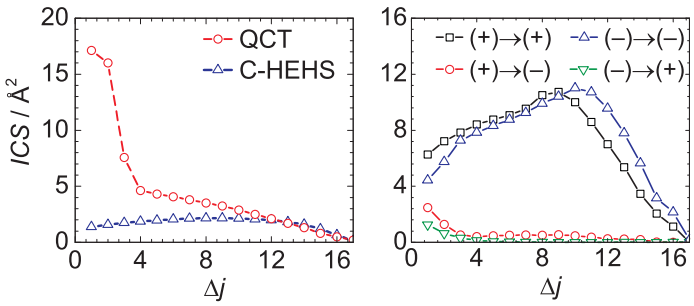

Figure 8.8: The C-HEHS and QCT ICSs (left panel) and the QCT ICSs resolved in $(+/-)$ final rotational orientation using those C-HEHS trajectories which lead to $(+/-)$ final rotational orientation. (black open squares $(+) \rightarrow (+)$, red open circles $(+) \rightarrow (-)$, blue open upward triangles $(-) \rightarrow (-)$, green open downward triangles $(-) \rightarrow (+)$).

transitions. This results in a rotationally cooler molecular ensemble. The hard shell ICSs are larger than those obtained using the full potential for high Δj transitions, because the soft repulsive parts of the potential removes some of the trajectories which otherwise would lead to transition in the case of hard shell collisions.

Role of the initial bond axis orientation

The orientation resolved initial bond axis orientation resolved polarisation dependent opacity function, OR r-PDOF, $p^{\{k\}}_{q\pm,\pm}(a^{\{1\}}_1(\mathrm{r}))$, introduced in Section 8.2.1, measures the final rotational polarisation as a function of the initial bond axis orientation. The integral of this function returns the orientation resolved polarisation moments, the sum of which gives the total polarisation moment.

If the bond axis orientation, $a^{\{1\}}_{1-}(\boldsymbol{r})$, is equal to ± 1 then the N-end or O-end of the molecule is directed towards the dimension along which the impact parameter is defined, so that the initial relative velocity is perpendicular to the initial bond axis. Conversely, $a^{\{1\}}_{1-}(\boldsymbol{r}) = 0$ means that $\boldsymbol{k}$ is parallel to $\boldsymbol{r}$.

The classical hard shell, QCT and soft QCT OR-r-PDOFs, $p^{\{1\}}_{1-,\pm}(a^{\{1\}}_1(\boldsymbol{r}))$, are shown in Figure 8.9. All of them are asymmetric with respect to $a^{\{1\}}_{1-}(r) = 0$, because the two ends of the heteronuclear molecule are not identical. At $\Delta j = 3$ the QCT $p^{\{1\}}_{1-,+}(a^{\{1\}}_1(\boldsymbol{r}))$ has a broad maximum at around $a^{\{1\}}_{1-}(r) = -0.4$, which represents a geometry where the NO molecule is tilted by an angle of about $-45°$ with respect to the initial relative velocity

and its O-end protrudes towards the incoming atom. The atom can experience the most of the attractive potential at this configuration. The maximum belonging to the N-end of the molecule is much smaller than that belonging to the O-end, meaning the orientation is greatly sensitive to the asymmetry of the attractive part of the potential.

At medium Δj transitions, the trajectories which result in positive rotational orientation are confined in the $-0.5 \lesssim a_{1-}^{\{1\}}(r) \lesssim +0.5$ regime in the case of all of the three potentials. It implies that geometries with bond axis orientation roughly parallel to the incoming velocity lead to positive orientation of $\boldsymbol{j'}$. These molecular geometries cannot result in negative orientation, thus $p_{1-,-}^{\{1\}}(a_1^{\{1\}}(\boldsymbol{r}))$ drops to zero. The preponderance of the negative rotational orientation increases with increasing Δj, as the trajectories are concentrated around the $a_{1-}^{\{1\}}(\boldsymbol{r}) = \pm 1$ endpoints.

The harder the potential, the more likely that a bond axis orientation parallel to $\boldsymbol{k}$ induces counterclockwise rotation. At $\Delta j = 10$, there is a single peak centered about $a_{1-}^{\{1\}}(\boldsymbol{r}) \approx 0$ in the case of hard shell collisions, whilst a plateau bounded by shallow peaks is observed in the case of the full potential QCT calculation. This is due to the strong correlation between the initial geometry and the kinetic energy transfer in the hard shell collisions as discussed in Section 4.1.1.

The negative rotational orientation is associated with perpendicular collision geometries for high Δj. The weight of these collisions is equal to those inducing positive orientation in the case of the hard shell collisions. By contrast, these trajectories outnumber the positive ones if the soft or full potential acts on the system. Only those trajectories in which the atom approaches at angles close to a right angle are able to transfer sufficient energy to excite the molecule to a high j' state. Those which approach the molecule at a shallow angle are deflected by the range of potential, thus they cannot bring about higher rotational excitation.

A final comparison of the three potentials is provided in Figure 8.10. The integrated r-PDOFs, $I_{1-}^{\{1\}}(a_{1-}^{\{1\}}(r))$, are shown. At $\Delta j = 3$, the hard shell and soft QCT results are virtually identical. For example, the positive slope between in the N-side, characteristic

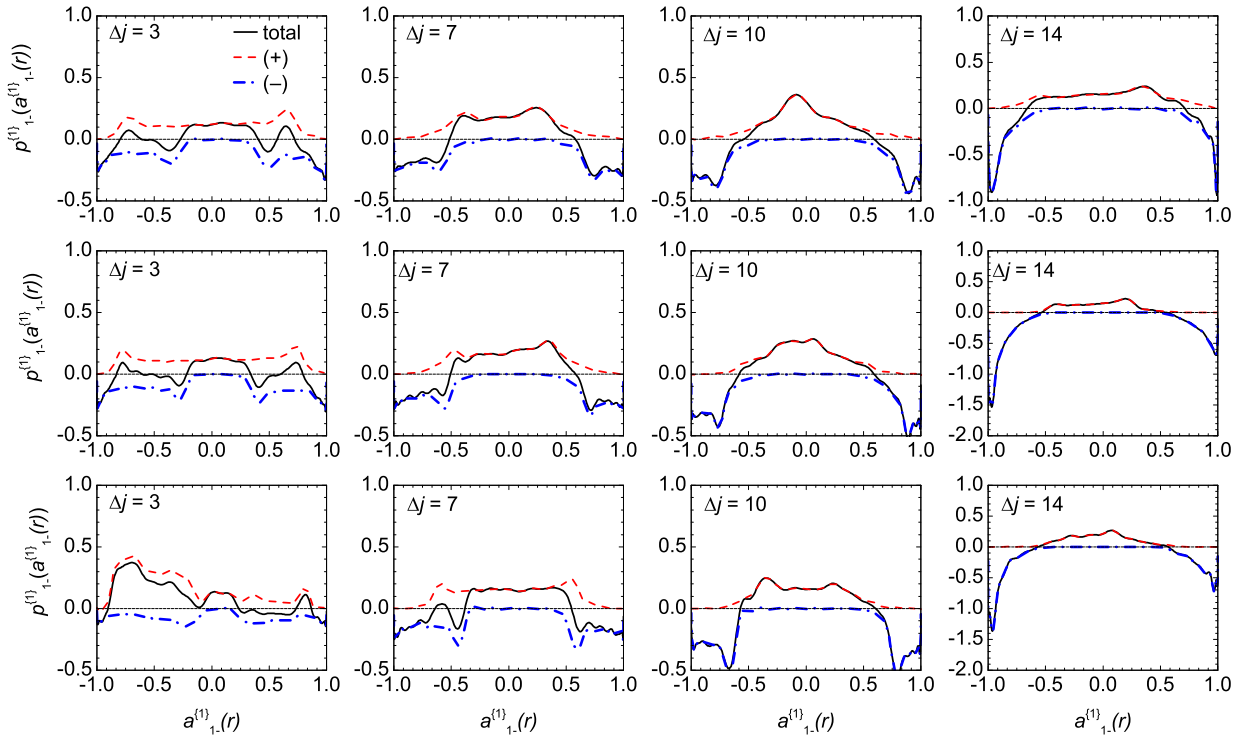

Figure 8.9: The C-HEHS (top row), soft QCT (middle row), full QCT (bottom row) total and orientation resolved r-PDCSs and orientation resolved PDPCSs, $p^{\{1\}}_{1-}(b)$, (total: black solid line, (+): red dashed line, (−): blue dashed-dotted line) for the $\Delta j = 3, 7, 10$ and 14 transitions from left to right. All calculations were carried out at a collision energy of 66 meV.

to the full potential, is absent from these data. The deviation between the hard shell and soft-QCT results becomes more pronounced as Δj increases. At $\Delta j = 14$, the soft and full potential integrated opacity functions are very similar. The C-HEHS and soft QCT orientation moments $a^{\{1\}}_{1-} = I^{\{1\}}_{1-}(1)$ vanish for low and intermediate transitions. When the excitation is high, the soft QCT $I^{\{1\}}_{1-}(1)$ is much closer to the QCT value, due to the effect of the repulsion, though they do not agree exactly, indicating that the attractive forces still play some minor role. From these graphs, it is readily seen that the lack of the integrated orientation is due to the balance between the (+) and (−) trajectories.

In the collisions of hard shells, the initial bond axis orientation is uniformly sampled establishing symmetry around the kinematic apse, leading to the lack of rotational orienta-

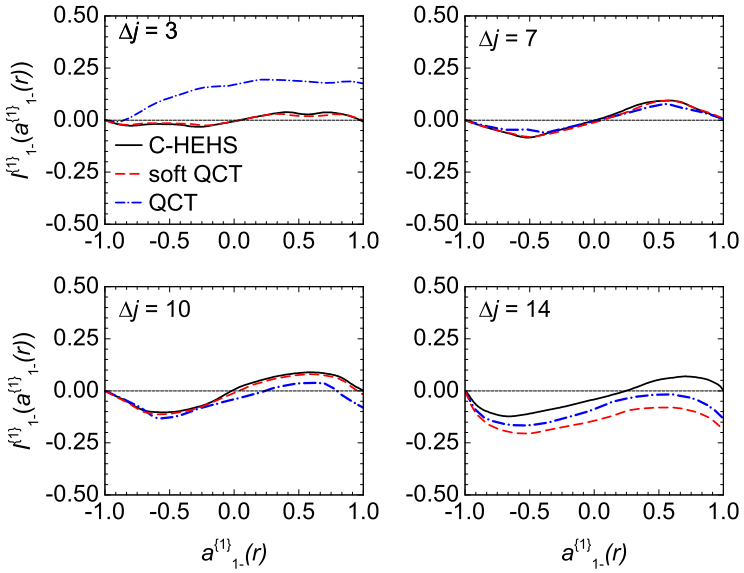

Figure 8.10: The C-HEHS: black solid line, QCT: black solid line, soft QCT: blue dash-dotted line) integrated total r-PDOFs, PDOFs, $I^{\{1\}}_{1-}(p^{\{1\}}_{1-}(\boldsymbol{r}))$, for the $\Delta j = 3, 7, 10$ and 14 transitions from top left to bottom right. All calculations were carried out at a collision energy of 66 meV.

tion. If there is a finite range of the attractive or repulsive potential, the number of initial geometries, leading to a certain final state, is restricted with respect to the hard shell case. As a consequence, the symmetry of the trajectories is lifted giving rise to rotational orientation.

Origin of classical rotational orientation

In summary, the symmetry of the single encounter hard shell trajectories can be broken in two distinct way, depending on the degree of rotational excitation.

At low Δj transitions the attractive part of the potential deflects the trajectories which have large impact parameters, resulting in positive orientation as shown in the left panel of Figure 8.11. At high Δj transitions, the atoms, which approach the molecule at shallow angles, are repelled by the soft repulsive potential, thus cannot reach the hard core. These trajectories are illustrated by the dashed arrows in the right panel of Figure 8.11.

Due to either the 'attractive' or the 'soft repulsive' mechanism some of the originally

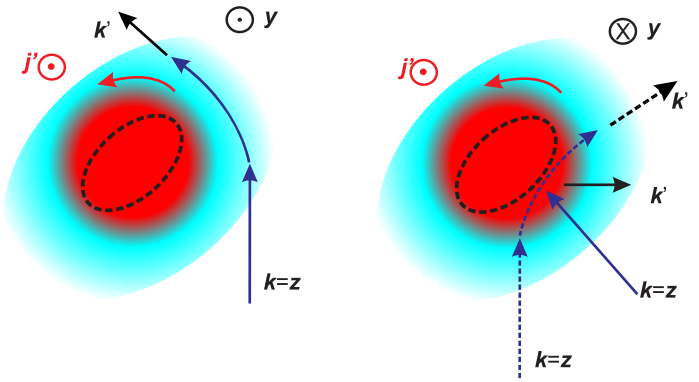

Figure 8.11: Trajectories with large impact parameters are deflected by the attractive forces (left panel). Trajectories with shallow incident angles are repelled by the repulsive forces (right panel), respectively. Hence the individual orientation moments do not cancel each other.

equivalent hard shell trajectories are removed or modified leading to rotational orientation.

Chattering collisions

A collision is called chattering if the final rotational angular momentum is smaller than its maximum achieved during the course of the collision [110]. Since the classical angular momentum is continuous, the criterium is that the quantised values of the maximum and final rotational angular momentum should differ. The ratio of the chattering collisions, f_{ch}, is defined as:

$$f_{\mathrm{ch}} = \frac{ICS_{\mathrm{ch}}}{ICS_{\mathrm{ch}} + ICS_{\mathrm{non-ch}}}, \tag{8.25}$$

where $ICS_{(\mathrm{non-})\mathrm{ch}}$ is the integral cross section of the (non-)chattering collisions. This ratio never exceeds 30% and is the largest between $\Delta j = 4$ and $\Delta j = 13$, as can be seen in the left panel of Figure 8.12. Despite the fact that the chattering collisions result in strong orientation; their weight is relatively small compared to the non-chattering collisions, so they do not have an overwhelming influence on the underlying classical orientation dynamics as justified by the right panel of Figure 8.12 where the total, chattering and non-chattering, $a_{1-}^{\{1\}}$, orientation moments are plotted together. A word of conceptual warning might be appropriate here. The term 'chattering' or 'secondary' collision was first applied to classical hard shell collisions, where there is no interaction between the two encounters. In the case of collisions taking place on the full V_{sum} PES, the atom and

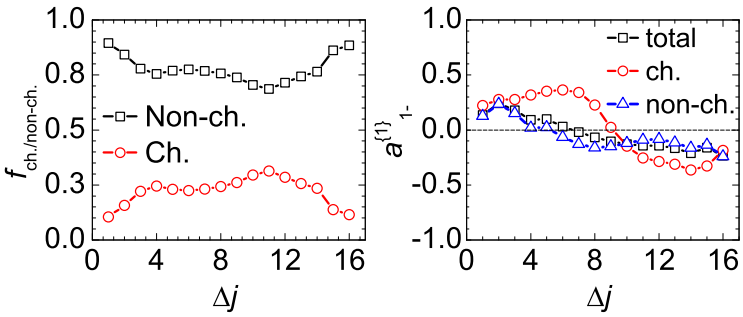

Figure 8.12: The ratio of the chattering collisions (red open circles) as a function of Δj from a QCT calculation which employs the full V_{sum} potential (left panel). The $a^{\{1\}}_{1-}$ moments are shown according to whether they belong to chattering (red open circles) or non-chattering (blue open triangles) trajectories. The ordinary $a^{\{1\}}_{1-}$ moments (black open squares) are obtained as the weighted average of the previous two (right panel).

the molecule interact continuously with each other. Therefore these collisions can better be viewed as examples of a prolonged and more complicated collision mechanism, rather than a sequence of independent scattering events.

8.4.1 Summary of classical rotational orientation

It has been shown that rotational orientation in the collisions of NO(X)–Ar is due to the interplay of attractive and repulsive forces. The cylindrical equivalence of the trajectories around the kinematic apse, which persists to the classical hard shell collisions, is the reason behind the lack of rotational orientation in those collisions. Removing this symmetry gives rise to the preferred sense of rotation. The attractive forces deflect the trajectories at low Δj transitions. The finite range of the repulsive potential repels the atoms' approach to the molecule at shallow angles from the hard core. In both cases, some of the cylindrically equivalent hard shell trajectories are removed resulting in rotational orientation.

As a final remark, it is useful to express the q-th component of k-th rank polarisation renormalised PDDCS as a sum over the classical paths, which lead to the same final state

and scattering angle.

$$\rho_{q\pm}^{\{k\}}(\theta) = \frac{\sum_{i=0}^{N_{\text{paths}}} n_{q\pm}^{\{k\},i}(\theta)}{\sum_{i=0}^{N\text{paths}} n_0^{\{0\},i}(\theta)} = \frac{1}{\sum_{i=0}^{N\text{paths}} n_0^{\{0\},i}(\theta)} \sum_{i=0}^{N\text{paths}} n_0^{\{0\},i}(\theta)\rho_0^{\{0\},i}(\theta) \tag{8.26}$$

This sum vanishes if the individual terms cancel each other. As for the orientation, in the hard shell case there are pairs of paths which are equal with respect to their moduli but differ in sign. Therefore, removal of one of them in general results in a substantial change of the orientation. Also if any of them is modified it has a profound effect on the overall orientation. On the contrary, in the case of the rotational alignment, each path of a certain pair has an identical contribution to the overall alignment. As a consequence, the alignment PDDCSs are expected to be less sensitive to the details of the potential energy surface. In fact, this observation clearly explains the different classical behaviour of the rotational orientation and alignment, which was discussed in the present chapter and in Chapter 5.

8.5 Rotational orientation in quantal systems

In this section the rotational orientation will be examined from a quantum mechanical point of view. The model systems used in the classical investigation will be applied under the rules of quantum mechanics in order to ascertain the exact role that the classical and quantal phenomena play in the rotational orientation.

8.5.1 Rotational orientation in the open shell NO(X)–Ar collisions

The exact close coupled quantum mechanical scattering calculations were carried out using the Hibridon suite of codes [55]. These calculations were previously presented and discussed by Miranda *et al.* [150]. The same results were obtained in the present work and are shown

in Figure 8.13.

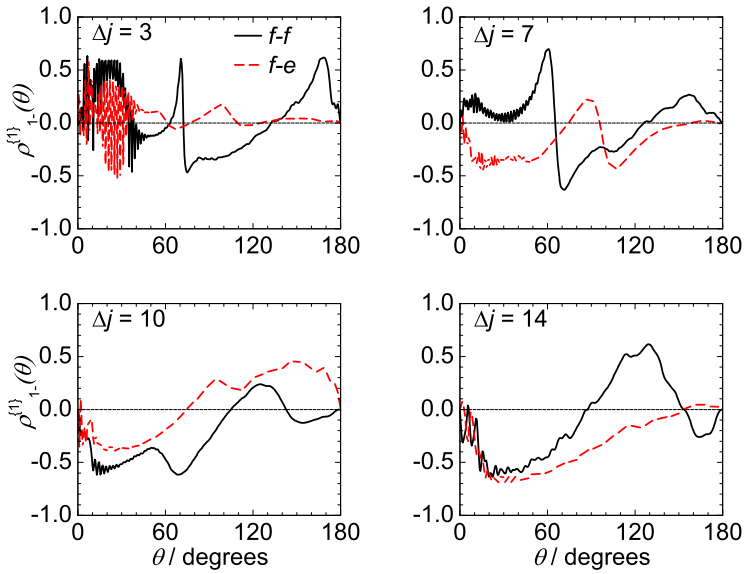

Figure 8.13: Λ-doublet resolved QM $\rho^{\{1\}}_{1-}(\theta)$ for $\epsilon' = -1$ (black solid line), $\epsilon' = +1$ (red dashed line) $|0.5, 0.5, -1\rangle \rightarrow |j', 0.5, \epsilon'\rangle$ transitions. $j' = 3.5$ (top left panel), $j' = 7.5$ (top right panel), $j' = 10.5$ (bottom left panel), $j' = 14.5$ (bottom right panel).

The $\rho^{\{1\}}_{1-}(\theta)$ orientation renormalised PDDCSs are plotted for a selection of the $|0.5, 0.5, -1\rangle \rightarrow |j', 0.5, \pm 1\rangle$ transitions. The renormalised orientation PDDCSs belonging to the same Δj transition but different final Λ-doublet levels are markedly different, unlike the alignment renormalised PDDCSs, $\rho^{\{2\}}_{q+}(\theta)$. For instance, in the case of the $|0.5, 0.5, -1\rangle \rightarrow |3.5, 0.5, \pm 1\rangle$ transitions, the $\epsilon' = +1$ $\rho^{\{1\}}_{1-}(\theta)$ rapidly oscillates between its positive and negative limiting values up to scattering angle of 40^0 beyond which it only exhibits minor undulations around zero. Its $\epsilon' = -1$ counterpart $\rho^{\{1\}}_{1-}(\theta)$ has a broad positive peak at low scattering angles superimposed with a rapidly oscillating structure. A sharp peak resembling a Fano-resonance in shape can be observed at about 70^0, beyond which it slowly increases and decreases. The parity conserving and changing renormalised PDDCSs are rather dissimilar up to high Δj transitions, where they gradually become more similar to each other, as the classical mechanism starts to dominate at these impulsive collisions.

Parity pairs can clearly be recognised among the orientation renormalised PDDCSs, as shown in Figure 8.14. However, the agreement between those $\rho^{\{1\}}_{1-}(\theta)$-s for which $j' - \epsilon\epsilon'/2$

is identical is somewhat less good than that between the alignment PDDCSs.

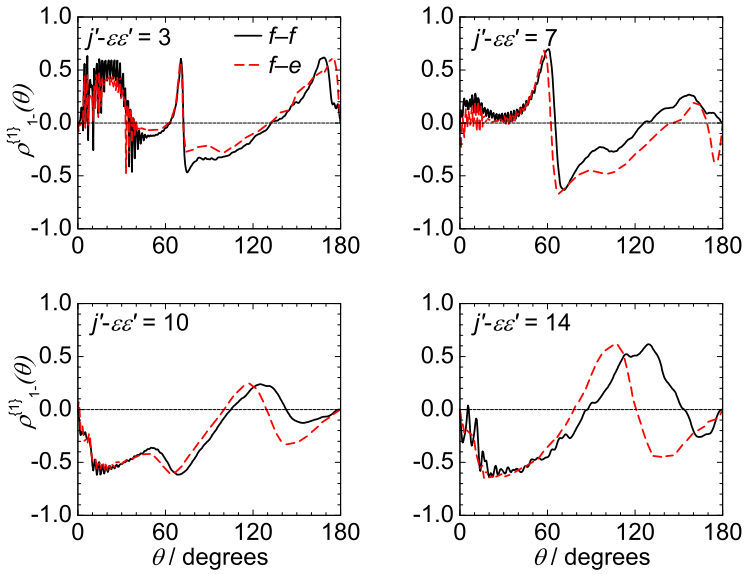

Figure 8.14: Λ-doublet resolved QM $\rho^{\{1\}}_{1-}$-s for $\epsilon' = -1$ (black solid line) and $\epsilon' = +1$ (red dashed line) $|0.5, 0.5, -1\rangle \rightarrow |j', 0.5, \epsilon'\rangle$ transitions. $j' - \epsilon\epsilon'/2 = 3$ (top left panel), $j' - \epsilon\epsilon'/2 = 7$ (top right panel), $j' - \epsilon\epsilon'/2 = 10$ (bottom left panel), $j' - \epsilon\epsilon'/2 = 14$ (bottom right panel).

The Λ-doublet resolved orientation moments, $a^{\{1\}}_{1-}$, show a decreasing trend superimposed with parity dependent oscillations, as seen in the left panel of Figure 8.15. The phase of the Λ-doublet conserving and changing oscillations are opposite of each other, such that the parity conserving moments are smaller than the adjacent ones in the case of $f \rightarrow f$ and $f \rightarrow e$ transitions as illustrated in the left panel of Figure 8.15. The hybrid orientation moments, constructed using the QCT renormalised PDDCSs, $\rho^{\{1\}}_{1-}(\theta)$ and the Λ-doublet resolved CC QM angular distribution functions, reproduce the decreasing trend, but fail to follow the oscillations.

The simple classical hard shell alignment parameters are an excellent approximation to the exact quantum mechanical hard shell ones irrespective of the change or conservation of the diatomic parity. In contrast, the quantum mechanical rotational orientation is not approximated by the classical single encounter hard shell model. Therefore a question arises regarding the nature of the rotational orientation, namely, whether there is rotational

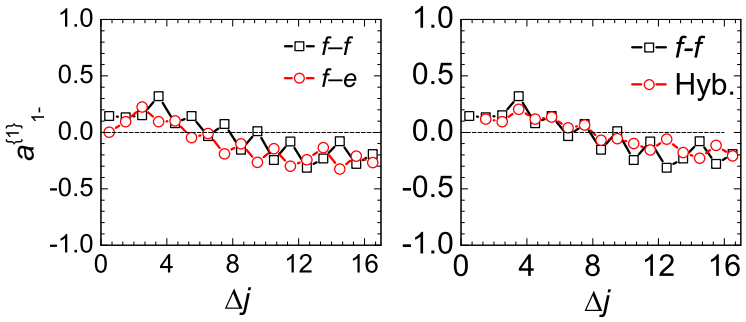

Figure 8.15: The $f \rightarrow f$ (black open squares) and $f \rightarrow e$ (red open circles) orientation moments, $a^{\{1\}}_{1-}$ (left panel). The parity dependent oscillations are out of phase for the two sets of date. The $f \rightarrow f$ (black open squares) and the QM/QCT hybrid (red open circles) orientation moments. The hybrid moments do not match the oscillations peculiar to the pure QM data.

orientation in the collision of hard shells according to quantum mechanics? The main focus of the remainder of this chapter lies in answering this question.

8.5.2 Open shell soft potential calculations

In order to ascertain the role of the attractive features of the potential energy surface a series of calculations have been carried on the soft potential PESs. These soft potential calculations also serve as an approximation to the exact quantum mechanical hard shell calculations. The $V_{\rm sum}$ and $V_{\rm dif}$ potentials were scaled according to Eqs. (4.12)–(4.13). The steepness parameters were chosen to be $\beta = 5.0\,\text{bohr}^{-1}$ (case (a)) and $10.0\,\text{bohr}^{-1}$ (case (b)), and the shift parameters were set to 1.0 bohr and 0.5 bohr, respectively. Using two differently modified PESs, the dependence of the orientation on the steepness of the repulsive wall could be determined.

A selection of open shell spin–orbit conserving differential cross sections were shown in Chapter 4. The DCSs were shifted to higher scattering angles and the forward scattered peak at low j' states disappeared due to the absence of the attractive forces in the $V_{\rm sum}$ potential. The lack of the secondary lobe of the corresponding opacity functions at high J values is also caused by the truncation of the potential. The alignment PDDCSs were less affected by modification of the PESs as discussed in 5.4.

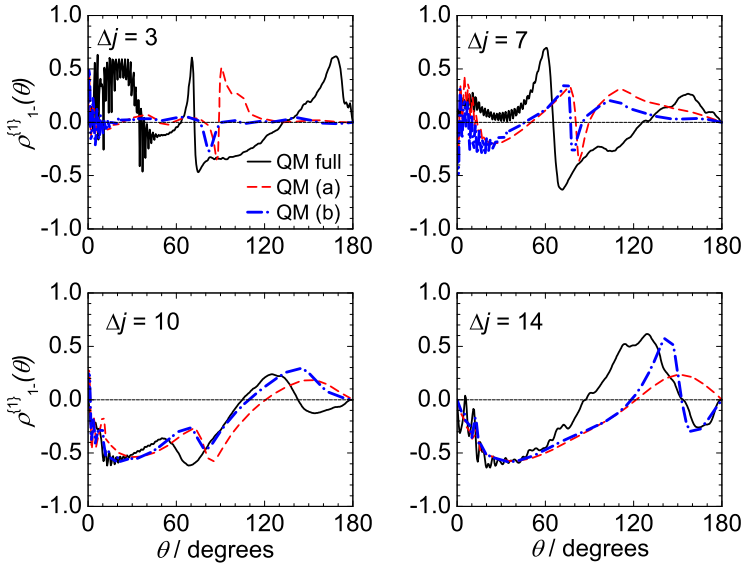

Figure 8.16: The Λ-doublet resolved orientation renormalised CC QM PDDCSs for the $|0.5, 0.5, -1\rangle \rightarrow |j', 0.5, -1\rangle$ transitions. $j' = 3$ (top left panel) transitions. $j' = 7$ (top right panel), $j' = 10$ (bottom left panel), $j' = 14$ (bottom right panel). The three data sets correspond to the full potential (black solid line), a potential scaled with $R = 1$ bohr, $\beta = 5\,\text{bohr}^{-1}$, ((a), red dashed line) $R = 0.5$ bohr, $\beta = 10\,\text{bohr}^{-1}$ ((b) blue dash-dotted line)

The $\rho^{\{1\}}_{1-}(\theta)$ renormalised PDDCSs obtained on the soft PESs are compared to those calculated employing the full PESs in Figure 8.16. The structure of $\rho^{\{1\}}_{1-}(\theta)$ is drastically changed over the entire scattering interval for the $|0.5, 0.5, -1\rangle \rightarrow |3.5, 0.5, -1\rangle$ transition. The positive peak is removed at low scattering angles. A Fano-type resonance pattern can be observed in the sideways scattered region,the only feature of the PDDCSs. This is greatly reduced when the steeper, or more repulsive, (b) potential acts on the system. At $j' = 7.5$, the full potential $\rho^{\{1\}}_{1-}(\theta)$ is shrunk and shifted towards negative values at low scattering angles, such that the sign of the original orientation is inverted. The degree of orientation is reduced at the sideways and backward scattered region. In addition its overall angular dependence has drastically changed. However, the original trend can still be recognised. The soft and the full data gradually becomes more similar to each other as j' increases, as exemplified by the $|0.5, 0.5, -1\rangle \rightarrow |j', 0.5, -1\rangle$, $j' = 7.5, 10.5$ and 14.5 transitions. The steepness of the soft potential influences to a gradually lesser extent the shape of the $\rho^{\{1\}}_{1-}(\theta)$ with increasing rotational excitation.

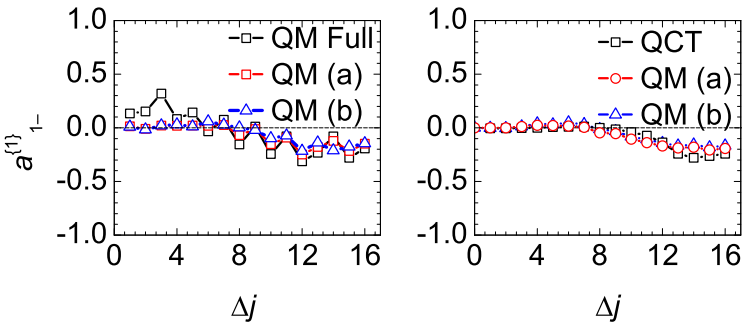

Figure 8.17: The full CC QM (black open squares), (a) soft CC QM (red open circles), (b) soft CC QM (blue open triangles) orientation moments for the $|0.5, 0.5, -1\rangle \rightarrow |j', 0.5, -1\rangle$ transitions (left panel). The soft QCT (black open squared) and the corresponding soft CC QM moments, summed over the final and averaged over the initial Λ-doublet levels are compared in the right panel.

The integrated soft potential orientation moments are compared to the full potential ones for the $|0.5, 0.5, -1\rangle \rightarrow |j', 0.5, -1\rangle$ transitions in Figure 8.17. The soft potential moments virtually vanish for low Δj transitions, though the renormalised PDDCSs are not uniformly zero throughout the entire scattering angle region as shown in Figure 8.16. The reason is that the forward scattered positive peaks are missing from both the DCSs and $\rho^{\{1\}}_{1-}(\theta)$ PDDCSs, and these contributed the most to the positive moments in the case of full potential scattering. The regions of significant scattering intensity are found where there is practically no rotational orientation. The soft potential moments start to deviate from zero at intermediate Δj transitions, exhibiting a decreasing trend superimposed with a parity dependent oscillation. The magnitude of the soft orientation moments is still less than that of the moments calculated using the full potential. The $a^{\{1\}}_{1-}$ moments obtained employing the steeper (b) surface are smaller than those obtained from the less steep (a) surface.

The averaged open shell soft CC QM and soft QCT orientation moments are in good agreement according to the right panel of Figure 8.14. Therefore, the origin of the full and soft potential average quantum mechanical orientation is can be explained in terms of the 'attractive' and 'soft repulsive' classical mechanisms.

It is worth noting, the (a) and (b) soft CC QM moments almost perfectly overlap when

they are summed over the final and averaged over the initial Λ-doublet states, which might imply that there is orientation in the hard shell limit.

8.5.3 Rotational orientation in quantum mechanical collisions of hard shells

In order to answer the question whether or not there is rotational orientation in the quantum mechanical collisions of hard shells and atoms, exact hard shell quantum mechanical calculations were carried out. Two collision energies were considered, namely 15 meV and 66 meV. The hard shell quantum mechanical (HS QM) orientation renormalised PDDCSs and moments were calculated using the contours given in Section 4.1.

Quantum mechanical rotational orientation does not generally vanish in the scattering of an atom from an infinitely repulsive non-sperical potential. This result seems to be a little counter-intuitive, when the absence of the rotational orientation is recalled in the case of classical hard shell collisions. However, this result, along with the observations regarding the QM and classical hard shell alignment, will enable us to understand better the nature of the rotational orientation.

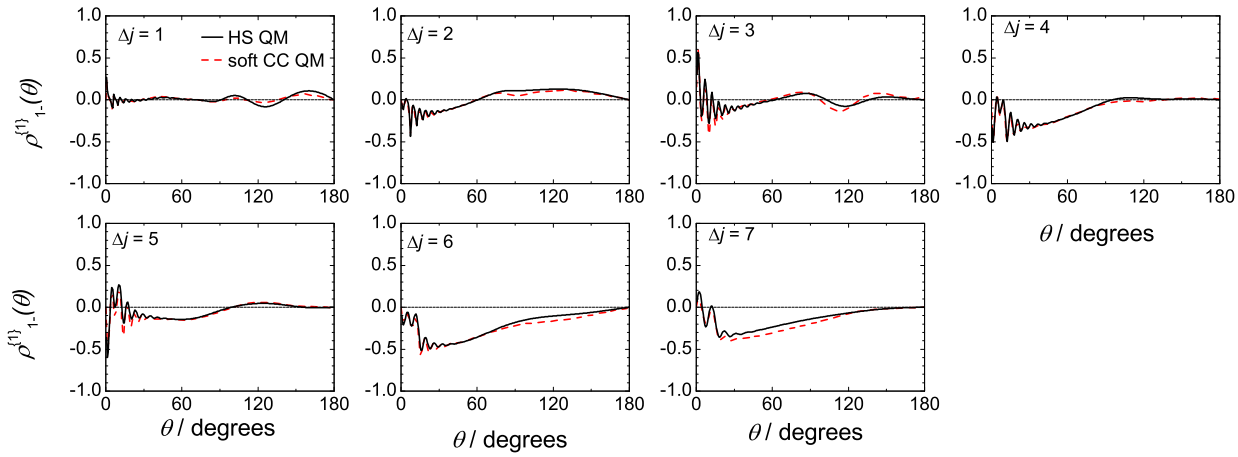

Figure 8.18: The closed shell HS QM (black solid line) and soft CC QM orientation renormalised PDDCSs, $\rho^{\{1\}}_{1-}(\theta)$ for the $|0\rangle \rightarrow |j'\rangle$, $j' = 1, 2, ..., 7$ transitions from top left to bottom right. All the calculations were carried out at a collision energy of 15 meV.

The exact HS QM results are compared to the closed shell CC QM results obtained on the steep (b) soft PES, using the Hibridon[55] suite of codes. The agreement between the CC QM and HS QM $\rho_{1-}^{\{1\}}(\theta)$ is excellent at the lower collision energy. Both the general trend and details of the exact orientation parameters are faithfully captured by the hard shell model data. However, it is worth pointing out that the agreement slightly deteriorates at higher j' final states.

At a collision energy of 15 meV, the phase and the magnitude of the rapid oscillations in the forward scattered region are accurately matched, for $\Delta j = 2$, as shown in Figure 8.18. Both $\rho_{1-}^{\{1\}}(\theta)$-s rapidly oscillate around zero below 40°, then slowly undulate for all of the final states. The value of $\rho_{1-}^{\{1\}}(\theta)$-s never exceed the limits of ± 0.3 indicating small or moderate rotational orientation, at $\Delta j = 2$ and 3. The number of nodes at which the $\rho_{1-}^{\{1\}}(\theta)$-s change sign reduces to zero as Δj increases. In the case of $\Delta j \geq 6$ the $\rho_{1-}^{\{1\}}(\theta)$ stays below zero throughout the entire scattering angle region.

The HS QM and soft CC QM orientation PDDCSs compare well at a collision energy of 66 meV as shown in Figure 8.19. The general characteristics of the two sets of data are, in general, similar. The HS QM $\rho_{1-}^{\{1\}}(\theta)$-s possess a more complicated structure at a collision energy of 66 meV than those obtained at 15 meV. They rapidly oscillate in the forward scattered region, $\theta \lessapprox 40°$, at all final states. The oscillations become gradually less rapid with increasing outgoing wavelength as Δj increases. If the degree of the rotational excitation is small, the $\rho_{1-}^{\{1\}}(\theta)$-s take small values, but their sign changes several times over the entire scattering angle interval. The parity changing ones, $(-1)^{j'}$ is odd, change their sign more times than parity conserving ones, $(-1)^{j'}$ is even, but the nodes disappear gradually, when progressing towards higher j' states. The degree of the orientation becomes greater, and mostly takes negative values as Δj increases. It is also remarkable that the parity conserving renormalised PDDCSs are greater than the parity changing ones, for $\Delta j < 8$.

The forward scattered oscillations of the HS QM and soft CC QM renormalised PDDCSs coincide for low Δj. However, some remarkable differences can be observed between the soft CC QM and hard shell data, especially in the sideways and backward scattered

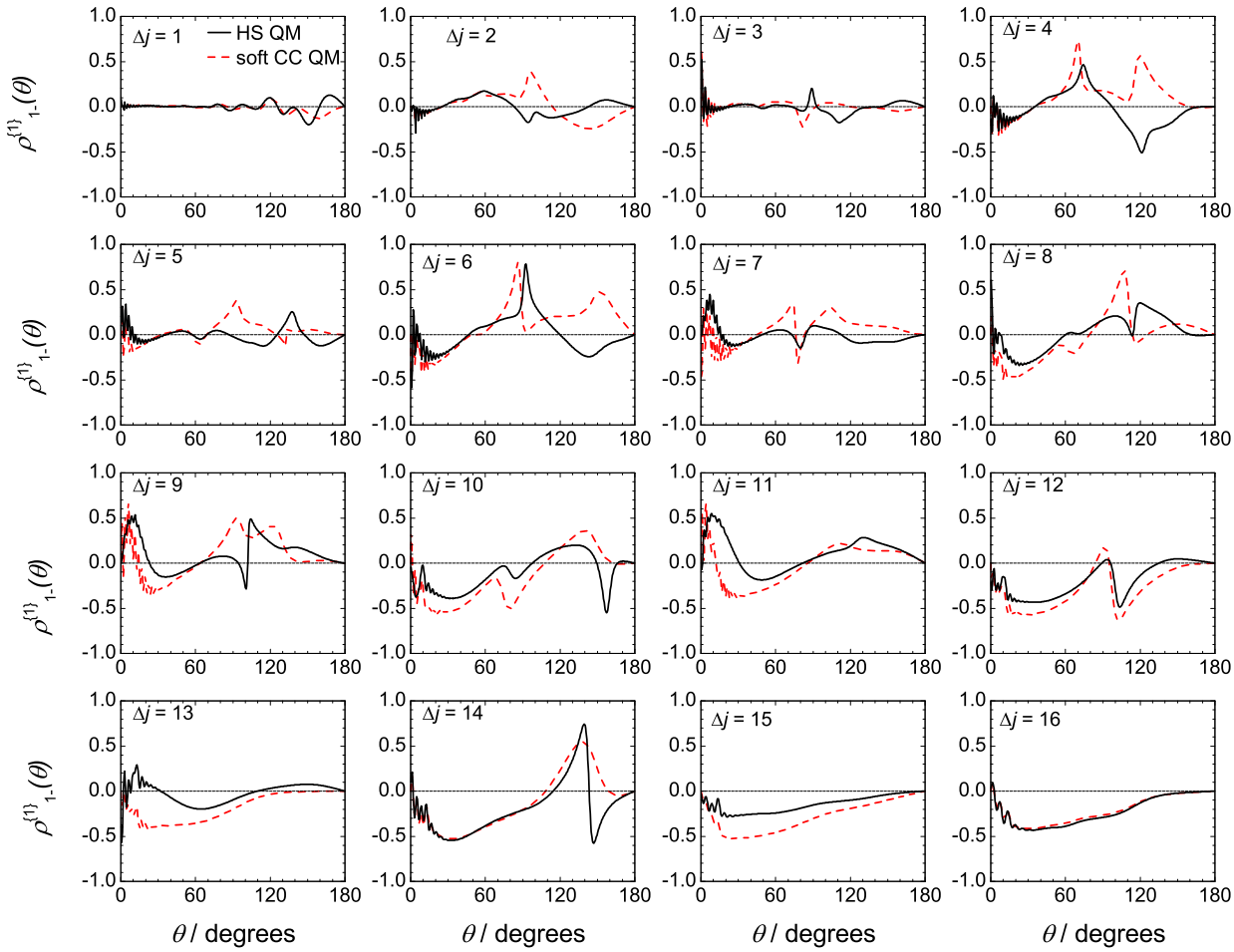

Figure 8.19: The closed shell HS QM (black solid line) and soft potential CC QM orientation renormalised PDDCSs, $\rho^{\{1\}}_{1-}(\theta)$ for the $|0\rangle \rightarrow |j'\rangle$, $j' = 1, 2, ..., 16$ transitions from top left to bottom right. All the calculations were carried out at a collision energy of 66 meV.

region. For example, the scattering angles where the derivative of the soft and HS QM $\rho^{\{1\}}_{1-}(\theta)$-s change sign, coincide, apart from for low rotational transitions. For instance, at $\Delta j = 9$, the double peak present in the HS QM data, at which $\rho^{\{1\}}_{1-}(\theta)$ plummets by a value of about 0.5, manifests itself as a much less prominent double peak in the soft potential CC QM data. Similar relationships between the two PDDCSs can be observed for most of the states.

For $\Delta j = 14$, the HS QM $\rho^{\{1\}}_{1-}(\theta)$ drops from $+0.7$ to -0.7 between 140° and 150° which means the orientation of the rotational angular momentum is almost completely

inverted. The soft $\rho_{1-}^{\{1\}}(\theta)$ has a broad peak centered around these angles. It rises from a value of about 0 to around +0.6 and returns to slightly below zero in a wider angular ranger of 30^0.

As the collision energy increases the classical turning point moves towards smaller atom–diatom distances, thus the atom – or the corresponding matter wave – penetrates deeper into the potential. As a consequence, the potential experienced by the atom is softer at higher collision energies, thus the soft shell potential becomes a less accurate approximation to the hard shell. Hence disagreement between the 'soft' CC QM and HS QM orientation renormalised PDDCSs is expected to be more pronounced at higher collision energies.

Quantum mechanical soft potential and hard shell orientation moments

The integrated orientation moments, $a_{1-}^{\{1\}}$ shown in Figure 8.20, decrease as a function of Δj. The relative magnitude of the adjacent moments changes according to whether they belong to parity changing or conserving transitions. The parity conserving $(-1)^{j'} =$ even moments are more negative than the adjacent parity changing moments, reflecting that $\boldsymbol{j'}$ is more strongly oriented in the case of parity conserving transitions.

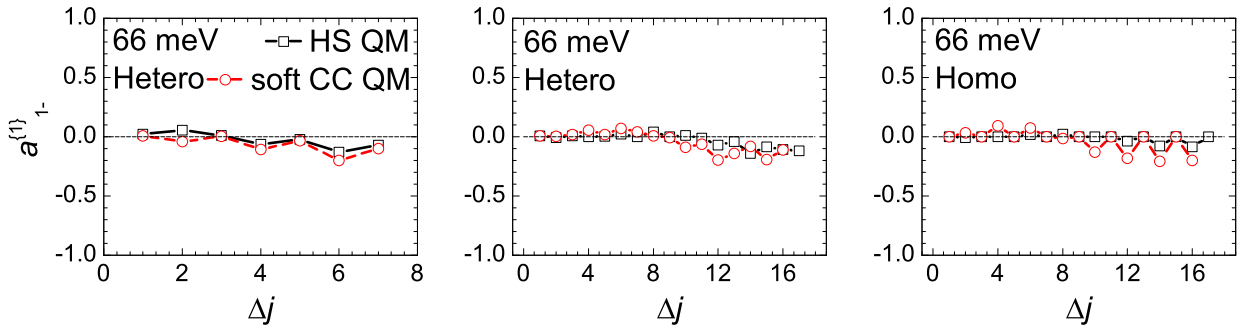

Figure 8.20: The integrated HS QM (black open squares) and CC QM (red open circles) orientation moments, $a_{1-}^{\{1\}}$, at collision energies of 15 meV (left panel) and 66 meV (middle panel). The homonuclear orientation moments, at a collisions energy of 66 meV, are shown in the right panel.

The soft shell moments have larger moduli than the hard shell moments. The effect of parity is also more pronounced when a finite range of the anisotropic repulsive potential is retained than in the case of hard shell collisions, where the potential is replaced with an infinitely steep wall.

8.5.4 Origin of the quantum mechanical hard shell orientation

The rotational orientation is absent from the single encounter classical collisions of concave hard shell molecules and atoms. Only the quantum mechanical treatment returns non-vanishing rotational orientation in the collisions of such hard shells and atoms.

Collisions of homonuclear hard shells

It was shown that the structure of DCSs in the collisions of NO(X) and Ar, can be qualitatively explained in terms of interferences between matter waves scattered from the flatter sides and the two ends of the molecule [66]. The interference depends on whether the molecule is hetero- or homonuclear and on parity changing or conserving nature of the transition.

Rotational orientation may arise from the interference between the waves scattered from the N-end, O-end and the two sides of the molecule. This effect is absent from classical mechanics and may lead to the breakdown of the symmetry about the kinematic apse. If this is the case, the orientation should vanish in the collisions of a homonuclear NO(X) molecule and Ar atoms. $\rho_{1-}^{\{1\}}(\theta)$-s were calculated in the collision of a homonuclear NO(X) molecule with Ar at a collision energy of 66 meV. The details of the contour were given in Section 4.1.

The quantum mechanical hard shell, and the soft CC QM $\rho_{1-}^{\{1\}}(\theta)$-s do not vanish, even if the molecule is homonuclear as proven by Figure 8.21. This proves that it is not the heteronuclear nature of the molecule that is responsible for the quantum mechanical orientation. However, the heteronuclear nature of the molecule is important, as homonuclear and heteronuclear renormalised PDDCSs have markedly different structures. Again, it is

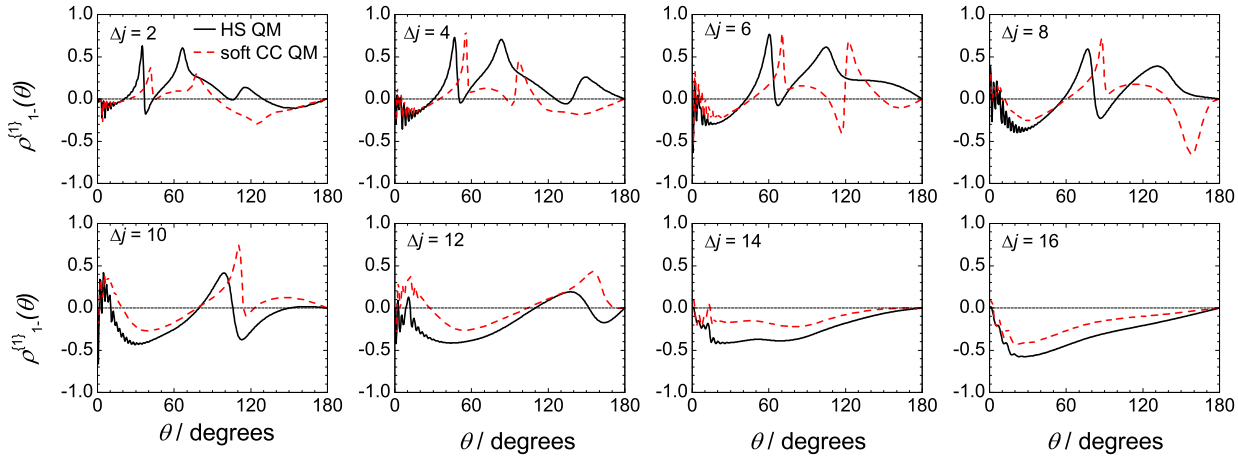

Figure 8.21: The HS QM (black solid line) and soft CC QM (red dashed line) $\rho_{1-}^{\{1\}}(\theta)$ for the $\Delta j = 2, 4, ..., 16$ transitions. Since the NO(X) molecule is treated as a homonuclear entity the parity changing, odd Δj, transition are forbidden.

worth pointing out, the structure of $\rho_{1-}^{\{1\}}(\theta)$ becomes simpler with increasing rotational excitation. It changes sign less frequently, when the final de Broglie wavelength of the system is large.

A shorter outgoing de Broglie wavelength gives rise to more intense interference between the scattered waves around the scattering centre [66], therefore the rotational orientation is expected to vary more rapidly with the scattering angle for low Δj transitions.

Random phase approximation

The role of the interference will be further investigated below. The classical DCSs and unnormalised PDDCSs are constructed as the algebraic sums of individual contributions of trajectories which end up in identical j' final state and scattering angle. In 3D there are a maximum of sixteen such trajectories (*cf.* Eq. (8.26)). Each path has a particular impact parameter which corresponds to a particular orbital angular momentum, ℓ, and total angular momentum, J, or equivalently, to a partial wave. The classical scattering angle resolved quantities are thus obtained as an incoherent sum of a selection of partial waves.

If a classical hard shell calculation is carried out with a fixed b, only certain θ-s see scattered particles, and the orientation is, in general, not zero. However, if this calculation is repeated for all b-s and the results are summed up, the orientation vanishes for all scattering angles, because all of the cylindrically equivalent trajectories have been generated.

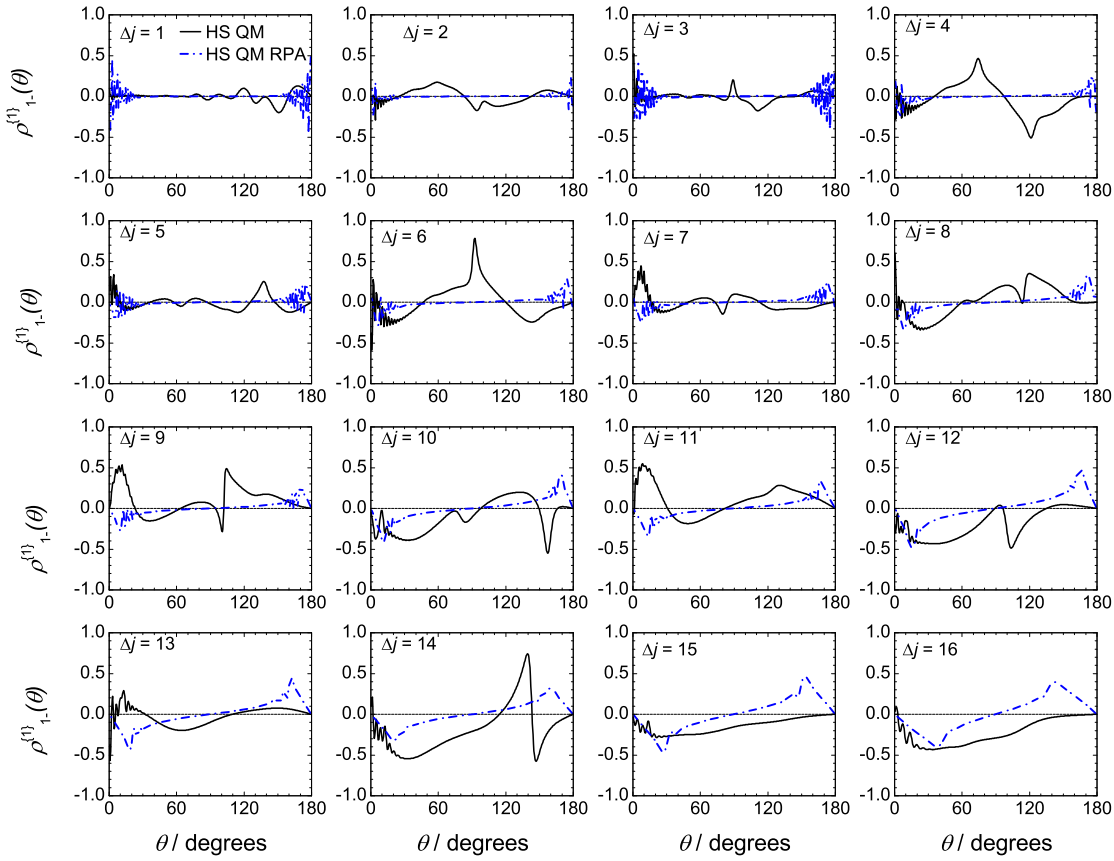

Figure 8.22: The closed shell HS QM (black solid line) and RPA HS QM (blue dashed line) orientation renormalised PDDCSs, $\rho_{1-}^{\{1\}}(\theta)$ for the $|0\rangle \rightarrow |j'\rangle$, $j' = 1, 2, ..., 16$ transitions from top left to bottom right. The orientation virtually disappears at low Δj transitions. All the calculations were carried out at a collision energy of 66 meV.

The exact quantum mechanical DCSs and PDDCSs include interference terms between different partial waves [12]. In order to ascertain to what extent the interference is responsible for the orientation the random phase approximation (RPA) [197] was invoked. According to RPA, the cross terms between different partial waves are ignored assuming the overall interference is totally destructive, so only terms diagonal in J are retained

in Eq. (8.27). The unnormalised PDDCS, $U_q^{(k)}(\theta)$, are given by Eq. (8.27) in the helicity frame [11].

$$\frac{2\pi}{\sigma}U_q^{(k)} = \frac{1}{4k_i^2}\frac{1}{2j_1+1}\sum_J (2J+1)^2 S^J_{m_2 m_1} S^{J*}_{m_{2'} m_1} d^J_{m_2 m_1}(\theta) d^J_{m_{2'} m_1}(\theta) \langle j_2 m_2, kq | j_2 m_{2'} \rangle \quad (8.27)$$

The DCS is simply the $k = 0$, $q = 0$ unnormalised PDDCS, which is an even function of the scattering angle, because the angular dependence is contained in the sum of products of identical Wigner d-matrices. On the other hand, the orientation is an odd function of θ, because the product of the Wigner d-matrices are always odd, if a pair of their indices only differ by unity. As a consequence, the renormalised orientation PDDCS is an odd function too, and the integrated orientation moment vanishes for all final states.

The HS QM RPA $\rho_{1-}^{\{1\}}$-s are shown in Figure 8.22. In general they do not vanish for all scattering angles and final states. At $\Delta j \leq 5$, $\rho_{1-}^{\{1\}}(\theta)$ is zero for almost the entire scattering interval and it rapidly oscillates around zero in the very forward and backward scattered regions. The 'endpoint' oscillations have larger amplitude and are extended over a slightly bigger range in the case of parity changing collisions. The oscillations gradually smooth out and $\rho_{1-}^{\{1\}}(\theta)$-s depart from zero as Δj increases. These findings can be explained by considering the properties of the associated Legendre polynomials and the shape of the partial cross sections. The density of the nodes of the associated Legendre polynomials quadratically increases towards ± 1 [111], therefore oscillations will be more rapid at the corresponding scattering angle regions. The parity conserving partial cross sections are multiple peaked, thus more partial waves – or spherical harmonics – are included in the summation which leads to the cancelation of the individual terms.

As j' increases, the onset of the partial cross section slowly moves towards small J values, so that a smaller number of low order spherical harmonics are included in the sum. As a consequence the frequency of the oscillations decreases and the waves are not quenched in the sideways scattered region, where the polynomials are well approximated by slightly shifted cosine waves, which add up constructively. Despite the fact that the

RPA model does not fully explain the origin of the rotational orientation in the hard shell collisions, it further highlights the dependence of the rotational orientation on the final state and parity.

In conclusion, in quantum mechanics, the incoming classical particle is replaced by series of plane waves which interacts with the surface of the molecule. As a consequence, neither the kinematic apse nor the trajectories can be exactly defined, resulting in the loss of symmetry. Therefore the quantal RPA calculations do return rotational orientation. The RPA renormalised orientation PDDCSs are not identical to the exact quantum mechanical ones, implying that the interference between the different partial waves is also important. The way in which the partial waves interact is determined by the partial cross sections. Those, in turn, depend on the parity changing or conserving nature of the collision.

Rotational orientation and the kinematic apse model

Let us assume that the projection of $\boldsymbol{j'}$ onto the kinematic apse, or equivalently, the apse frame magnetic populations are conserved in the $|0\rangle \rightarrow |j'\rangle$ transitions. Since only the $m_{\mathrm{a}} = 0$ magnetic level is occupied, there will be no orientation. However, this projection is generally not conserved in the quantum mechanical collisions of hard shells. The collision is not instantaneous, so the diatom can rotate during the collision, leading to the breakdown of the kinematic apse model as discussed in Section 5.4.

As a consequence, the projection of $\boldsymbol{j'}$ onto the kinematic apse is not in general conserved. $m_{\mathrm{a}} \neq 0$ states can be populated and rotational orientation may appear due to the coherence between the different levels. In order to illustrate this effect the apse frame HS QM alignment and orientation renormalised PDDCSs are plotted in Figure 8.23. Note, the apse frame and scattering frame $\rho_1^{\{1\}}(\theta)$-s are identical, as the apse frame y-axis, $\hat{\boldsymbol{y}}_{\mathbf{a}}$, and the scattering frame y-axis, $\hat{\boldsymbol{y}}$, are identical.

The alignment renormalised PDDCSs are less sensitive to the deviations from the kinematic apse model than the corresponding orientation renormalised PDDCSs. The

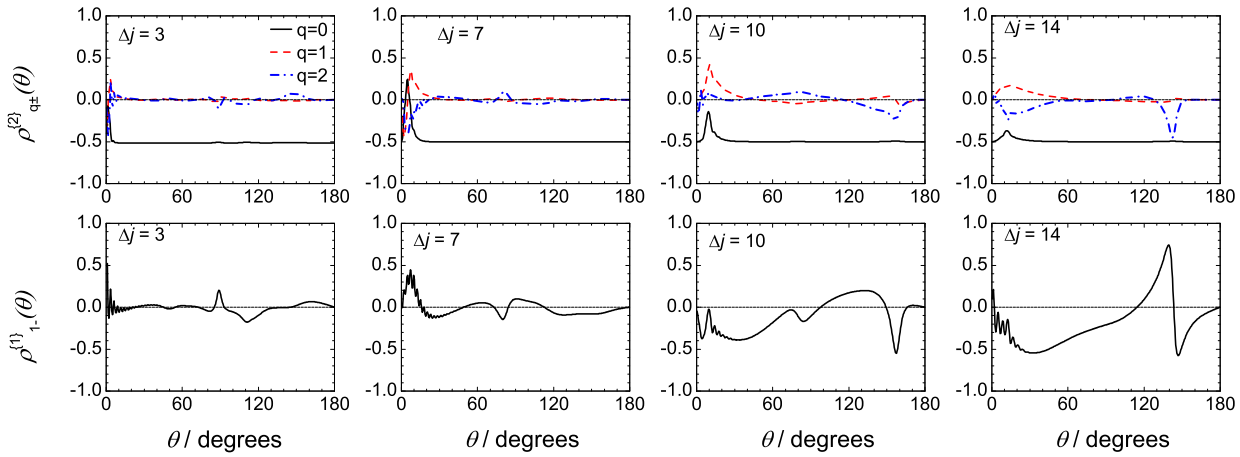

Figure 8.23: The apse frame HS QM alignment renormalised PDDCSs, $\rho^{\{2\}}_{q+}$, $q = 0$ (black solid line), $q = 1$ (red dashed line), $q = 2$ (blue dash-dotted line) for the $\Delta j = 3, 7, 10$ and 14 transitions (top row). The HS QM orientation renormalised PDDCSs for the same transitions are shown in the bottom row. The orientation is much more sensitive to the deviations from the kinematic apse model than the alignment. All the calculations were carried out at a collision energy of 66 meV.

alignment is primarily determined by the impulse of the collision, with the quantum effects appearing as small perturbations. Even small deviations from the kinematic apse model can result in strong orientation. For instance, although for $30° < \theta$ the projection of $\boldsymbol{j'}$ onto $\boldsymbol{a}$ is almost perfectly conserved as shown in Figure 8.23, the $\rho^{\{1\}}_{1-}(\theta)$ parameter takes values between -0.5 and $+0.6$. By contrast, the alignment, $\rho^{\{2\}}_{1/2+}(\theta)$, parameters never exceed the ± 0.3 limits, revealing weak alignment. This can be explained by considering the different symmetry properties of alignment and orientation. Alignment is always defined with respect to two axes, thus it has a higher order symmetry than orientation, which is defined with respect to a single axis [72] (*i.e.* an ensemble can be aligned even if it is not oriented), thus the alignment is less sensitive to the violation of the symmetry.

The consequences of finite interaction time and interaction region

As discussed above, the breakdown of the kinematic apse model may lead to rotational orientation. The kinematic apse model requires that the molecule should not rotate during

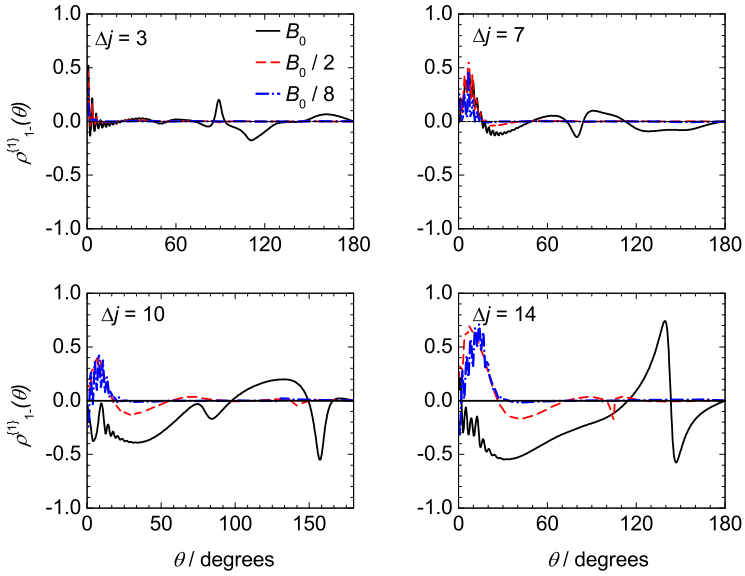

Figure 8.24: The longer rotational period reduces the degree of the rotational orientation. The HS QM $\rho_{1-}^{\{1\}}$ are shown, where the rotational constant is not scaled (black solid line), halved (red dashed line), and scaled down by a factor of eight (blue dash-dotted line) for the $\Delta j = 3, 7, 10$ and 14 transitions (top left to bottom right panels). All the calculations were carried out at a collision energy of 66 meV.

the collision, and that the interaction is confined to an infinitely small region on the surface. Semiclassically, the point-like atom is replaced by a matter wave which interacts with the molecule on a finite area in the order of the square its de Broglie wavelength. If the molecule rotates during the collision, the interaction region is extended, and the symmetry is violated. In other words, the matter wave is perturbed by the rotating molecule to a greater extent, giving rise to stronger rotational orientation.

In order to test this assumption, a set of calculations was performed using a reduced rotational constant, B_0. As the rotational constant decreases, the rotational period of the molecule increases and the projection of $\boldsymbol{j'}$ onto the kinematic apse is better conserved. This results in the reduction of the rotational orientation, as shown in Figure 8.24. $\rho_{1-}^{\{1\}}(\theta)$ nearly vanishes at $\Delta j = 3$, where the rotational period, T, is increased by a factor of eight. In this case, $T = 2.31 \times 10^{-11}$ s, and the final relative velocity is about 873 m/s, so that while the atom travels 1 Å, the molecule is only rotated by approximately 1.8°. At $\Delta j = 14$, the bond axis is rotated by 7.8°, and the relative velocity is about 839 m/s.

Therefore, the enhancement of the rotational orientation is mostly due to the displacement of the bond axis. The NO(X) molecules scattered through small angles will only have a preferred sense of rotation at high Δj transitions, in which case the interaction time is classically the longest, as illustrated by the bottom row of Figure 8.24.

The orientation is also expected to be a function of the de Broglie wavelength of the system. If the rotational motion is slow, the effects arising from the displacement of the molecular axis are suppressed, which enables us to investigate how the rotational orientation depend on the initial de Broglie wavelength of the system. The de Broglie wavelength of the NO(X)–Ar system is approximately 0.27 Å at a collision energy of 66 meV, which is very small compared to the characteristic size, twice the average of the semiaxes, 6.5 Å, of the scatterer.

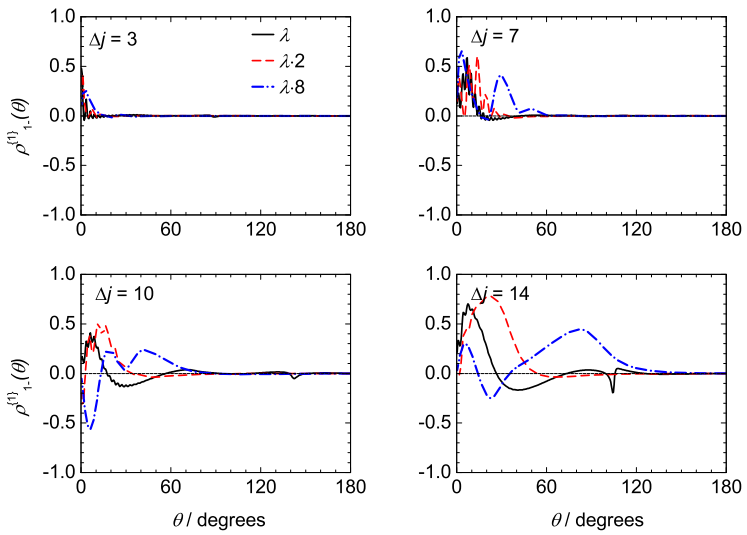

Figure 8.25: The longer de Broglie wavelength increases the degree of the rotational orientation. The HS QM $\rho^{\{1\}}_{1-}$ are shown with the original de Broglie wavelength left unchanged (black solid line), doubled (red dashed line), and multiplied by a factor of eight (blue dash-dotted line) for the $\Delta j = 3, 7, 10$ and 14 transitions (top left to bottom right panels). All the calculations were carried out at a collision energy of 66 meV.

A set of calculations was carried out where the rotational constant was halved. The reduced mass of the collision pair was divided by a factor of four and sixty-four, hence the wavelength was twice and eight times larger than the original in these calculations, respectively. The larger the de Broglie wavelength, the stronger the orientation as illus-

trated by Figure 8.25. Again, from a semiclassical point of view, a trajectory interacts with the surface in the range roughly equal to the square of its de Broglie wavelength. If λ is small, the extension of this finite region goes to zero, thus the classical hard shell case is recovered in the $\lambda \to 0$ limit (which is also equivalent to the energy sudden limit). Longer wavelengths result in a broader interaction region, which breaks down the cylindrical symmetry around the kinematic apse leading to more pronounced rotational orientation. The outgoing de Broglie wavelength also increases with larger reduced mass, giving rise to a larger 'interaction area' according to our semiclassical picture.

Quantum mechanically, the interaction time and region is always finite, even in the case of hard shell collisions, unlike the classical description. This fundamental difference lifts the cylindrical symmetry of trajectories giving rise to rotational orientation.

Orientation resolved differential cross sections

The angular dependence of the rotational orientation is addressed in this section. One can define DCSs for the clockwise and counterclockwise rotating molecules, $\sigma_-(\theta)$ and $\sigma_+(\theta)$, respectively. The sum of these two DCSs return the total DCS, whilst their normalised difference is equal to $\rho_{1-}^{\{1\}}(\theta)$:

$$\sigma_+(\theta) + \sigma_-(\theta) = \frac{\mathrm{d}\sigma}{\mathrm{d}\omega} \tag{8.28}$$

$$\frac{\sigma_+(\theta) - \sigma_-(\theta)}{\sigma_+(\theta) + \sigma_-(\theta)} = \rho_{1-}^{\{1\}}(\theta)\,. \tag{8.29}$$

The two orientation resolved DCSs, shown in Figure 8.26 are very similar to the total DCS shown in Figure 4.10. The peaks of $\sigma_+(\theta)$ and $\sigma_-(\theta)$ are positioned around the same scattering angles, and the number and positions can be explained in terms of the simple semiclassical four path model [134]. These maxima in the scattering intensity arise from the constructive interference between the matter waves scattered from the flatter sides and different ends of the NO(X) molecule [134]. The parity conserving DCSs have more peaks than the adjacent parity changing ones.

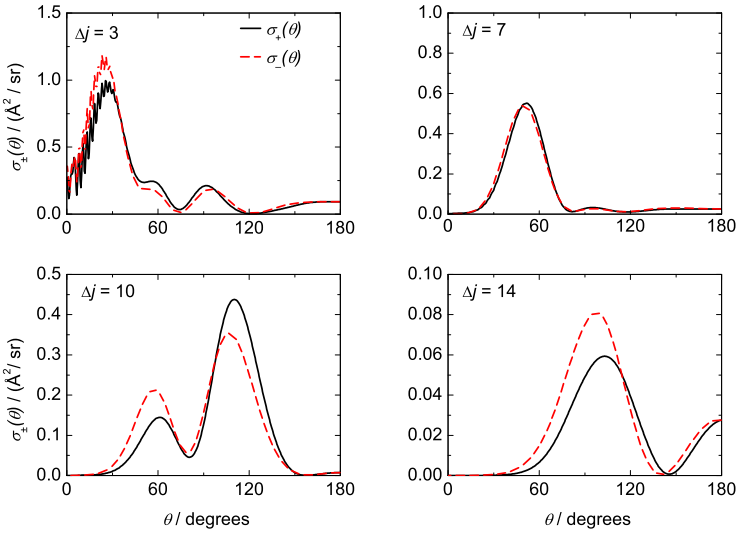

Figure 8.26: The orientation resolved HS QM DCSs, $\sigma_+(\theta)$ (black solid line) and $\sigma_-(\theta)$ (red dashed line) for the $\Delta j = 3, 7, 10$ and 14 transitions (top row). The separation between the two orientation resolved DCSs increases with increasing Δj. All the calculations were carried out at a collision energy of 66 meV.

The DCSs which correspond to (+) rotation are slightly shifted towards higher scattering angles with respect to those belonging to the (−) rotation. The bigger scattering angles are associated with smaller total angular momenta, J, or equivalently, impact parameters, as previously shown in Figures 4.7 and 4.11. Thus the main contribution to $\sigma_+(\theta)$ comes from smaller impact parameters as compared to $\sigma_-(\theta)$. In fact, the classical hard shell trajectories leading to positive rotational orientation usually belonged to the smaller impact parameters, as was shown in Figure 8.2, which is reflected in the relative positions of the $\sigma_+(\theta)$ $\sigma_-(\theta)$ differential cross sections. However, in the classical case, there is a cylindrical symmetry about the kinematic apse, so $\sigma_+(\theta)$ and $\sigma_-(\theta)$ are equal, for every scattering angle. In the QM case, this symmetry is lifted, thus the two DCS are not identical.

One can visualise the QM mechanism as if the scattering were happening simultaneously on two ellipses. One rotates in a counterclockwise sense, with which the $\sigma_+(\theta)$ is associated. The other one rotates in a clockwise sense, and its scattering intensity is given by $\sigma_-(\theta)$. The ellipse parameters are determined by the characteristic 'impact parameters', which are different for anticlockwise and clockwise rotation. The semiclassical 'four

path' DCSs are, in turn, the functions of the semiaxes of the ellipses [134]. The DCSs for anticlockwise and clockwise rotations will not generally be identical. The rotational orientation is the normalised difference of these DCSs and will not vanish. As Δj increases, gradually more distant impact parameter regions are sampled, thus the separation between $\sigma_+(\theta)$ and $\sigma_-(\theta)$ increases leading to stronger rotational orientation.

8.6 Summary

The origin of the rotational orientation in the collisions of NO(X) and Ar has been investigated in this chapter. The orientation resolved polarisation dependent differential cross sections and polarisation dependent partial cross sections have been introduced as useful tools to investigate these phenomena. Our findings rely on comparing numerous results using a variety of different model potentials. It has been established that the classical rotational orientation vanishes if there is a spatial–temporal cylindrical equivalence of the trajectories about the kinematic apse. The attractive potential removes this symmetry by means of deflective collisions which results in positive rotational orientation in the classical case. The finite range of the repulsive potential distorts the hard shell trajectories which lead to negative orientation at high Δj transitions.

The parity averaged quantum mechanical behaviour is well explained in terms of classical mechanics, if the full V_{sum} potential governs the interaction. We first demonstrated that there is a preferred sense of rotation in the quantum mechanical hard shell–atom collisions, which is a fundamental difference between classical and quantum mechanics. The point-like atom is replaced a series of partial waves which interact with the molecule on its surface. The atom–diatom interaction has a finite extension in space and time which breaks down the symmetry about the kinematic apse leading to rotational orientation. The interferences between different partial waves are also important in determining the fine details of the orientation as a function of the scattering angle.

Chapter 9

Conclusions and future plans

9.1 Conclusions

Rotational polarisation effects in the inelastic collisions of NO and Ar were investigated by means of theoretical and experimental methods. It has been found that the rotational alignment, or plane of rotation, is primarily determined by a classical impulsive mechanism of hard shells. In contrast, the rotational orientation, or sense of rotation, sensitively depends on the details of the interaction potential and on quantum mechanical effects.

The angular dependence of the rotational polarisation has previously been quantified by the polarisation dependent differential cross sections (PDDCSs) [10, 15, 16]. By introducing the orientation resolved PDDCSs and the polarisation dependent opacity functions, and other related polarisation dependent quantities, it was possible to provide a full and exact classical description of these collisions.

Comparison of classical hard shell, quasi-classical and exact quantum mechanical calculations revealed that the dynamics responsible for the rotational alignment in spin–orbit conserving transitions are inherently classically impulsive in nature, if the attractive well depth of the V_{sum} potential is small compared to the collision energy. In a purely impulsive classical collision, the projection of the rotational angular momentum onto the kinematic apse is conserved and it is cylindrically symmetric about the kinematic apse. The scattering angle dependence of the alignment renormalised PDDCSs is the consequence of this

conservation. At a collision energy of 66 meV, the attractive features of the potential and quantum effects act as a small perturbation to this underlying classical mechanism.

It has also been demonstrated that the kinematic apse model is not equivalent to the exact quantum mechanical description of hard shell collisions. Since the quantum mechanical interaction has a finite extension in space and time, the cylindrical symmetry around the apse is lifted, and the projection $\boldsymbol{j'}$ onto the apse is no longer perfectly conserved. However, the kinematic apse model provides an excellent approximation to the full exact quantum mechanical dynamics responsible for rotational alignment.

It has been established, in classical mechanics, that the rotational orientation vanishes if there is a spatial–temporal cylindrical symmetry of the trajectories about the kinematic apse. In the case of classical hard shell collisions this cylindrical symmetry is provided in the most cases. It can be removed by secondary collisions or by the highly asymmetric shape of the molecule. In the case of classical collisions taking place on the full V_{sum} potential, the attractive potential removes this symmetry by means of deflection, which results in positive rotational orientation at low Δj transitions. The finite range of the repulsive potential distorts the hard shell trajectories, which leads to negative orientation at high Δj transitions.

The closed shell and the average quantum mechanical orientation is well explained by a classical mechanism. The Λ-doublet resolved rotational orientation strongly depends on the parity conserving or changing nature of the transitions, unlike the rotational alignment.

It has been shown for the first time, that there may be a preferred sense of rotation in the quantum mechanical hard shell–atom collisions, which is a fundamental difference between the classical and quantum mechanical description of this elementary process. The quantal rotational orientation arises from the finite spatial and temporal extension of the interaction. The interference between the different scattered partial waves also plays a role in determining the scattering angle dependence of the rotational orientation.

A novel algorithm was developed, which can be used to extract the angular dependence of the rotational polarisation from the experimental ion-images. It was employed to

determine the experimental rotational alignment in the collisions of NO(X) and Ar. The measurements were realised by a hexapole state selective ion-imaging apparatus using a $(1 + 1')$ resonantly enhanced multiphoton ionisation detection scheme, which allows full initial and final state selection. As such, the rotational alignment can be investigated as a function of the scattering angle for a well defined final rotational, spin–orbit and Λ-doublet state. The experimentally determined alignment PDDCSs were in good agreement with the theoretically calculated ones. This implies that the underlying mechanism which is responsible for the rotational alignment is inherently classical and impulsive.

9.2 Future plans

9.2.1 Theoretical Aspects

The spin–orbit conserving collisions of the NO(X)–Ar system can be well explained by using a single repulsive potential. Therefore, most of the discussions builds on the results of hard shell models. The effect of the attractive forces and the finite range of the potential were considered as perturbations to the hard shell picture [126]. It would thus be interesting to consider systems with a more attractive V_{sum} potential, such as NO(X)–Kr, NO(X)–Xe, which have a well depths of 138 cm^{-1} [198] and 140 cm^{-1} [199], respectively. Furthermore, these wells have a longer range, and are more anisotropic than that of the NO(X)–Ar system. The repulsive wall is also less steep, thus the classical [25] or quantum mechanical hard shell models would be expected to give less accurate results.

The quantum mechanical hard shell model can only handle collisions between closed shell species. However, the formalism has already been extended to the collisions of open shell diatoms and closed shell atoms. The implementation of the open shell wavefunction can be helpful in further elucidating what role the parity plays in determining the rotational orientation. The coupled equations are ill-conditioned thus the accuracy of the HS-QM calculations breaks down at high partial waves. This is a well known problem in the scattering of electromagnetic waves from non-spherical particles [200, 201]. A possible

solution to this problem could be using quadruple precision arithmetics [202]. This will enable the code to calculate the T-matrix for very high partial waves, so that collisions of heavy particles can be treated.

Almost exclusively spin–orbit conserving transitions were investigated throughout this work. The rotational alignment effects were rationalised in terms various hard shell models, which were also used to gain insight on the rotational orientation. This was because the spin–orbit conserving processes primarily take place on the mainly V_{sum} PES [9, 141] in the energy range considered in the present work. The spin–orbit changing transitions primarily sample the strongly attractive V_{dif} PES. As a consequence, the hard shell models cannot be rigorously applied to this problem. Moreover,the electronic spin is involved in the scattering process as an non-spectator [203].

On the other hand, we have found that the projection of the rotational angular momentum onto the kinematic apse is conserved to a considerable extent, even in the case of spin–orbit changing transitions, (see Chapter 5) which implies there might be a possible way to extend the quantum mechanical hard shell model to handle spin–orbit changing transitions.

9.2.2 Experimental aspects

The collision induced rotational orientation can be measured using circularly polarised light in the experimental geometry shown in Figure 6.2. The orientation is very sensitive to the details of the potential, as such it serves as a test for the potential energy surface [102] and the theoretical calculations. The fitting algorithm is general, such that it is capable of simulating the experimental image and retrieving the orientation PDDCSs. The fully state resolved rotational orientation in the inelastic collisions of NO(X) and Ar and has been recently measured in our group, and the fitting algorithm was successfully used to extract the experimental orientation polarisation dependent differential cross sections [204, 205].

The effect of orienting the bond axis of the NO(X) molecule can be experimentally investigated by creating an electric field in the interaction region. By appropriately choosing

the direction of the field the NO(X) molecule can be oriented with its O-end or N-end is pointing parallel preferably to the initial relative velocity vector, so that not only the steric asymmetry factor can be determined [168], but also the differential cross sections. Using linearly or circularly polarised light the polarisation dependent differential cross sections can also be measured, which is equivalent to measuring the $\boldsymbol{k} - \boldsymbol{r} - \boldsymbol{k'} - \boldsymbol{j'}$ four vector correlation.

Diatomic molecules can be chosen as the collision partners of the NO(X) molecule. Since a diatom can also be rotationally excited which increases the number of the Newton spheres for a particular $|0.5, 0.5, -1\rangle \rightarrow |j', \Omega', \epsilon'\rangle$ transition of the NO(X) molecule. As a consequence, the corresponding ion-image might be congested, since the Newton spheres overlap. In order to separate the most intense rims of the Newton spheres, either a light molecule should be chosen, such as HD which has a large rotational constant, so that the Newton spheres are more separated. Alternatively, slice imaging [206, 207] with fast frame cameras [208] can be employed to increase the experimental resolution.

Appendix A

Glossary

Methods

HS	hard shell
C-HOHS	classical homonuclear hard shell
C-HEHS	classical heteronuclear hard shell
QCT	quasi-classical trajectory
QM	quantum mechanical
CC QM	close coupled quantum mechanical. It refers to calculations where the potential employed is smooth.
HS QM	hard shell quantum mechanical
RPA	random phase approximation

Quantities

PES	potential energy surface
ICS	integral cross section
DCS	differential cross section
PDDCS	polarisation dependent differential cross section
OR	orientation resolved
PDOF	polarisation dependent opacity function
PDPCS	polarisation dependent partial cross section
r-PDOF	initial bond axis orientation dependent polarisation dependent opacity function

Appendix B

Quantum mechanical scattering of a hard shell and a structureless atom

The total wavefunction of the hard shell atom–diatom scattering problem is derived in this Appendix. It follows the procedure of Bosanac [136], but the derivation is slightly modified in order to include the scattering problem for open shell diatomic molecules.

B.1 Angular wavefunction

The wavefunction of a closed shell diatomic rigid rotator is a spherical harmonic which is written as a D-matrix element in Eq. (B.1). The angles α and β describe the orientation of the molecular axis,

$$\sqrt{\frac{2j+1}{4\pi}} D^{j}_{m0}(\alpha,\beta,0)^{*} \ . \tag{B.1}$$

The Hund's case (a) rotational wavefunction for a Λ-doubled diatom is given by Eq. (B.2),

$$|j,m,\Omega,\epsilon\rangle = \sqrt{\frac{1}{2}}\left[\sqrt{\frac{2j+1}{4\pi}} D^{j}_{m\overline{\Omega}}(\alpha,\beta,0)^{*} + \epsilon\sqrt{\frac{2j+1}{4\pi}} D^{j}_{m-\overline{\Omega}}(\alpha,\beta,0)^{*}\right] , \tag{B.2}$$

where $\overline{\Omega} = |\Omega|$ and $\epsilon = \pm 1$ is the Λ-doublet level. The wavefunction of the orbital angular momentum, ℓ, is a spherical harmonic expressed here in terms of a Wigner D-matrix

element. The arguments, θ, ϕ are the orientation angles of the atomic collision partner,

$$Y_\ell^n(\theta,\phi) = \sqrt{\frac{2j+1}{4\pi}} D_{n0}^{\ell}(\phi,\theta,0)^* \,. \tag{B.3}$$

In the following, we will attempt to derive a suitable and convenient total wavefunction for the hard shell scattering problem. It is assumed that the diatom has a Hund's case (a) wavefunction. The uncoupled angular wavefunction is the product of the orbital angular momentum eigenfunction and the Hund's case (a) eigenfunctions:

$$\sqrt{\frac{2\ell+1}{4\pi}} D_{n0}^{\ell}(\phi,\theta,0)^* \left|j,m,\Omega,\epsilon\right\rangle. \tag{B.4}$$

It will prove to be convenient to change the (α, β) angles to those describing the relative orientation of the molecule and the atom. These angles are denoted by γ and Δ, the former being the polar angle the latter being the azimuth.

The uncoupled wavefunction of Eq. (B.4) is parametrised by the relative orientation angles:

$$\begin{aligned}&\sqrt{\frac{2\ell+1}{4\pi}} D_{n0}^{\ell}(\phi,\theta,0)^* \left|j,m,\Omega,\epsilon\right\rangle = \\ &\sqrt{\frac{2\ell+1}{4\pi}} D_{n0}^{\ell}(\phi,\theta,0)^* \sum_{m''} D_{m,m''}^{j}(\phi,\theta,0)^* \sqrt{\frac{2j+1}{8\pi}} \left[D_{m''\overline{\Omega}}^{j}(\Delta,\gamma,0)^* + \epsilon D_{m''-\overline{\Omega}}^{j}(\Delta,\gamma,0)^* \right].\end{aligned} \tag{B.5}$$

The diatomic wavefunction is not affected by the transformations apart from a $m \to m''$ substitution. However, its arguments are now the angles describing the relative orientation of the atom and the diatom, (γ,Δ). In the following the shorthand $\left|j,m'',\Omega,\epsilon\right\rangle^{\text{rel.}}$ refers to the function. The product of the two D-matrices is then decomposed using the Clebsch–Gordan series:

$$\begin{aligned}&\sqrt{\frac{2\ell+1}{4\pi}} D_{n0}^{\ell}(\phi,\theta,0)^* \left|j,m,\Omega,\epsilon\right\rangle = \\ &\sqrt{\frac{2\ell+1}{4\pi}} \sum_{J'm''} \langle \ell n, jm | J' n+m\rangle \langle \ell 0, jm'' | J' m''\rangle D_{n+m,m''}^{J'}(\phi,\theta,0)^* \left|j,m'',\Omega,\epsilon\right\rangle^{\text{rel.}}.\end{aligned} \tag{B.6}$$

The uncoupled product wavefunction of Eq. (B.6) can now be coupled:

$$\begin{aligned} Y_{JM}(j,\ell) &= \sum_n \langle \ell n, jM-n|JM\rangle \sqrt{\frac{2\ell+1}{4\pi}} D^l_{n0}\left(\phi,\theta,0\right)^* |j, M-n, \Omega\epsilon\rangle \\ &= \sqrt{\frac{2\ell+1}{4\pi}} \sum_{m''} \langle \ell 0, jm''|Jm''\rangle D^{J'}_{M,m''}\left(\phi,\theta,0\right)^* |j,m'',\Omega,\epsilon\rangle^{\text{rel.}} . \end{aligned} \tag{B.7}$$

The bottom line of (B.7) is the total coupled angular wavefunction for the Hund's case (a) scattering problem. However, it is more convenient, if the function consists of a single term rather than a sum. Any linear combination of these functions is a proper eigenfunction. Multiplying by $\langle \ell 0, jm'|J-m'\rangle$ and summing over ℓ results in a correct wavefunction of simpler form, since only those terms where $m' = m''$ are retained:

$$\begin{aligned} &\sum_{\ell m''} \langle \ell 0, jm'|J-m'\rangle \langle \ell 0, jm''|Jm''\rangle \sqrt{\frac{2\ell+1}{4\pi}} D^{J'}_{M,m''}\left(\phi,\theta,0\right)^* |j,m'',\Omega,\epsilon\rangle^{\text{rel.}} \\ &= \sum_{\ell m''} \frac{2J+1}{\sqrt{2\ell+1}} (-1)^{j-m''}(-1)^{j-m'} \langle J-m', jm'|\ell 0\rangle \langle J-m'', jm''|\ell 0\rangle \\ &\times \sqrt{\frac{2\ell+1}{4\pi}} D^{J'}_{M,m''}\left(\phi,\theta,0\right)^* |j,m'',\Omega,\epsilon\rangle^{\text{rel.}} \\ &= \frac{2J+1}{\sqrt{4\pi}} D^{J'}_{M,m'}\left(\phi,\theta,0\right)^* |j,m',\Omega,\epsilon\rangle^{\text{rel.}} . \end{aligned} \tag{B.8}$$

After some rearranging, Υ^{JM}_{jm}, a good angular wavefunction is given by Eq. (B.9).

$$\begin{aligned} &\Upsilon^{JM}_{jm} = D^{J'}_{M,m'}\left(\phi,\theta,0\right)^* |j,m',\Omega,\epsilon\rangle^{\text{rel.}} = \\ &\frac{\sqrt{4\pi}}{2J+1} \sum_{\ell m''} \sqrt{2\ell+1} \langle J-m', jm'|\ell 0\rangle \langle \ell 0, jm''|Jm''\rangle \sqrt{\frac{2\ell+1}{4\pi}} D^{J'}_{M,m''}\left(\phi,\theta,0\right)^* |j,m'',\Omega,\epsilon\rangle^{\text{rel.}} . \end{aligned} \tag{B.9}$$

B.2 Total wavefunction

The incident wavefunction assumes the following form:

$$\Psi_{\rm inc} = \frac{i}{2k_{j_0\Omega_0\epsilon_0}} \sum_{J,m} D^J_{m_0 m}\left(\phi,\theta,0\right)^* \left|j_0, m, \Omega_0, \epsilon_0\right\rangle \sum_{\ell} (2\ell+1) i^\ell j_\ell^{(1)}(k_{j_0} R) \langle \ell 0, j_0 m_0 | J m_0\rangle \langle \ell 0, j_0 m | J m\rangle \,. \tag{B.10}$$

The scattered wavefunction involves a sum over the total angular momentum and its projection, J and M, respectively. There is also a sum over all of the final rotational, magnetic, spin–orbit and Λ-doublet states of the diatom, which are denoted by j', m', Ω' and ϵ', respectively:

$$\Psi_{\rm sca} = \frac{1}{R} \sum_{JM} \frac{1}{2J+1} \sum_{j,m\Omega,\epsilon} F^{JM}_{jm\Omega\epsilon, j_0 m_0 \Omega_0 \epsilon_0} \sum_{m'} D^J_{Mm'}\left(\phi,\theta,0\right)^* \left|j, m', \Omega, \epsilon\right\rangle \sum_{\ell} (2\ell+1) i^{\ell+1} h_\ell^{(1)}(k_j R) \langle \ell 0, jm | J m\rangle \langle \ell 0, jm' | J m'\rangle \,, \tag{B.11}$$

where the $F^{JM}_{jm\Omega\epsilon, j_0 m_0 \Omega_0 \epsilon_0}$ partial scattering amplitudes determine the probability of the $jm\Omega\epsilon \leftarrow j_0 m_0 \Omega_0 \epsilon_0$ transition for a particular J, M state. Propagation methods cannot be employed in order to obtain the partial scattering amplitudes, because the the potential is infinite within the hard shell.

However, the total wavefunction should vanish on every point on the surface of the hard shell, which enables us to construct a set of linear equations:

$$\Psi = \Psi_{\rm inc} + \Psi_{\rm sca} = 0 \Leftrightarrow \Psi_{\rm inc} = -\Psi_{\rm sca} \,. \tag{B.12}$$

The first step is to equate Eq. (B.10) to the negative of Eq. (B.11), and subsequently multiply both sides by $D^{J''}_{M''m''}\left(\phi,\theta,0\right)$, and integrate over the angles θ and ϕ. As a result, the summation over J, m and J, M, m' collapses for the incident and scattered waves, respectively. In addition, it is required that $M'' = m_0$:

$$
\begin{aligned}
r.h.s &= \frac{i}{2k_{j_0}}|j_0, m'', \Omega_0, \epsilon_0\rangle \sum_{\ell}(2\ell+1)i^{\ell} j_{\ell}^{(1)}(k_{j_0}R) && \text{(B.13)}\\
&\times \langle \ell 0, j_0 m_0 | J m_0\rangle \langle \ell 0, j_0 m'' | J m''\rangle \\
l.h.s. &= \frac{1}{R}\frac{1}{2J''+1}\sum_{j,m\Omega,\epsilon} F^{J'' m_0}_{jm\Omega\epsilon, j_0 m_0 \Omega_0 \epsilon_0}|j, m'', \Omega, \epsilon\rangle && \text{(B.14)}\\
&\times \sum_{\ell}(2\ell+1)i^{\ell} h_{\ell}^{(1)}(k_j R)\langle \ell 0, jm | J'' m\rangle \langle \ell 0, jm'' | J'' m''\rangle \,.
\end{aligned}
$$

Both sides are then multiplied by the diatomic rotational wavefunction $|j', m', \Omega', \epsilon'\rangle^*$ and integrated over the angles Δ and γ. R is a function of γ but independent of Δ because of the cylindrical symmetry of the diatom. This has two consequences: (i) m'' should be equal to m', (ii) the (big) D-matrix elements can be replaced by the (small) d-matrix elements in the wavefunction $|j', m', \Omega', \epsilon'\rangle$. Also, the $J'' \to J$ substitution can be performed:

$$
\begin{aligned}
r.h.s &= \frac{i}{2k_{j_0}}\sum_{\ell}(2\ell+1)\langle \ell 0, j_0 m_0 | J m_0\rangle \langle \ell 0, j_0 m' | J m'\rangle \left[\frac{(2j_0+1)(2j'+1)}{64\pi}\right]^{1/2} && \text{(B.15)}\\
&\times \int_0^{\pi} \sin\gamma \mathrm{d}\gamma \left[d^{j'}_{m'\overline{\Omega}'}(\gamma) + \epsilon' d^{j'}_{m'-\overline{\Omega}'}(\gamma)\right] i^{\ell} j_{\ell}^{(1)}(k_{j_0}R(\gamma)) \left[d^{j_0}_{m'\overline{\Omega_0}}(\gamma) + \epsilon_0 d^{j_0}_{m'-\overline{\Omega_0}}(\gamma)\right] \\
l.h.s &= \frac{1}{R}\frac{1}{2J+1}\sum_{j,m,\Omega,\epsilon} F^{Jm_0}_{jm\Omega\epsilon, j_0 m_0 \Omega_0 \epsilon_0} && \text{(B.16)}\\
&\times \sum_{\ell}(2\ell+1)\langle \ell 0, jm | J m\rangle \langle \ell 0, jm' | J m'\rangle \left[\frac{(2j+1)(2j'+1)}{64\pi}\right]^{1/2} \\
&\times \int_0^{\pi} \sin\gamma \mathrm{d}\gamma \left[d^{j'}_{m'\overline{\Omega}'}(\gamma) + \epsilon' d^{j'}_{m'-\overline{\Omega}'}(\gamma)\right] i^{\ell} h_{\ell}^{(1)}(k_j R(\gamma)) \left[d^{j}_{m'\overline{\Omega}}(\gamma) + \epsilon d^{j}_{m'-\overline{\Omega}}(\gamma)\right] .
\end{aligned}
$$

In a more condensed form:

$$
-\frac{i(2J+1)}{2k_{j_0\Omega_0\epsilon_0}} X^{J}_{j'm'\Omega'\epsilon', j_0 m_0 \Omega_0 \epsilon_0} = \sum_{jm} W^{J}_{j'm'\Omega'\epsilon', jm\Omega\epsilon} F^{Jm_0}_{jm\Omega\epsilon, j_0 m_0 \Omega_0 \epsilon_0} \qquad \text{(B.17)}
$$

which should be solved for $F^{Jm_0}_{jm\Omega\epsilon, j_0 m_0 \Omega_0 \epsilon_0}$, the partial scattering amplitude. The

$W^J_{j'm'\Omega'\epsilon',jm\Omega\epsilon}$ matrix is the coupling matrix. For the scattered wave one has:

$$W^J_{j'm'\Omega'\epsilon',jm\Omega\epsilon} \equiv \sum_\ell (2\ell+1)\langle \ell 0, jm|Jm\rangle\langle \ell 0, jm'|Jm'\rangle B^{(\ell)}_{jm'\Omega\epsilon,j'm'\Omega'\epsilon'}\,, \tag{B.18}$$

where

$$B^{(\ell)}_{jm'\Omega\epsilon,j'm'\Omega'\epsilon'} \equiv \langle j'm'\Omega'\epsilon'|i^\ell h^{(\ell)}_{k_{jm\Omega\epsilon}}|jm\Omega\epsilon\rangle\,. \tag{B.19}$$

The overlap integral, $B^{(\ell)}_{jm'\Omega\epsilon,j'm'\Omega'\epsilon'}$, between the initial and final wavefunctions determines the probability of the transition. As such, it is the analogue of the potential, or coupling, matrix, $\langle j''\ell'', JM|V|JM, j'\ell'\rangle$, in the case of finite range potential scattering introduced in the close–coupled equations in Eq. (2.41).

Appendix C

Equivalence of the Fano–Macek and Suzuki–Mo line strength factors

C.1 Overview of the polarisation parameters

The quantum mechanical polarisation parameters which are used throughout this work were defined in Eq. (C.1):

$$a_q^{(k)} = (-1)^q \frac{2j+1}{2k+1} \langle T_{-q}^{(k)}(j)^\dagger \rangle \,. \tag{C.1}$$

The polarisation parameters have been defined by several authors often using notations and normalisations which are slightly different to each other. Table C.1 provides a compilation of the most frequently referenced polarisation moments. The moments included in the first column of Table C.1 are the *real* Fano–Macek moments. Their orientation and alignment moments are denoted by $O_{q\pm}$ and $A_{q\pm}$, respectively [125]. $\mathcal{A}_{\pm q}^{(k)}$ and $\mathcal{A}_{q\pm}^{\{k\}}$ are the *complex* and *real* polarisation parameters of Orr-Ewing and Zare [15]. The *complex* and *real* polarisation moments of Aoiz and de Miranda defined in Eqs. (C.1) and (3.17)–(3.19) in Chapter 3 are denoted by $a_{\pm q}^{(k)}$ and $a_{q\pm}^{\{k\}}$, respectively. It will be helpful to give the definition of the standard (complex) polarisation parameters, $\mathcal{A}_{q\pm}^{(k)}$, for the further development of calculation of line strength factors. These parameters are expressed in terms of the

Macek and Fano [77]	Orr-Ewing [15]	Hertel-Stoll [125]	de Miranda [11] [11]	de Miranda [11] ⋆
real	*real*	*real*	*complex*	*real*
O_0	$c_1(j)\mathcal{A}_0^{\{1\}}$	$c_1(j)A_0^{\{1\}}$	$c_1(j)a_0^{(1)}$	$c_1(j)a_0^{\{1\}}$
A_0	$\mathcal{A}_0^{\{2\}}$	$A_0^{\{2\}}$	$c_2(j)a_0^{(2)}$	$c_2(j)a_0^{\{2\}}$
A_{1+}	$\frac{1}{\sqrt{3}}\mathcal{A}_{1+}^{\{2\}}$	$\frac{1}{\sqrt{3}}A_{1+}^{\{2\}}$	$\frac{2}{\sqrt{6}}c_2(j)a_{\pm1}^{(2)}$	$\frac{1}{\sqrt{3}}c_2(j)a_{1+}^{\{2\}}$
A_{2+}	$\frac{1}{\sqrt{3}}\mathcal{A}_{2+}^{\{2\}}$	$\frac{1}{\sqrt{3}}A_{2+}^{\{2\}}$	$\frac{2}{\sqrt{6}}c_2(j)a_{\pm2}^{(2)}$	$\frac{1}{\sqrt{3}}c_2(j)a_{2+}^{\{2\}}$

$$c_1(j) = [j(j+1)]^{-1/2}\,, \quad c_2(j) = [(2j+3)(2j-1)/(j(j+1))]^{1/2}\ .$$

Table C.1: The relationship between the most commonly used polarization moments and alignment parameters.
*In the case of the differential polarization moments, dependent on the scattering angle θ, the $a_{q\pm}^{\{k\}}$ parameters in this column should be replaced by the renormalized PDDCS, $\rho_{q\pm}^{\{k\}}(\theta)$, used in this work.

adjunct of the state multipoles, $\langle T_q^{(k)}\rangle$, as discussed in Section 3.2.2 [15, 72]:

$$\mathcal{A}_q^{(k)} = \frac{c(k)}{\langle jm|\boldsymbol{J}^2|jm\rangle^{k/2}}\,\langle T_q^{(k)}(j)\rangle\,, \tag{C.2}$$

$$\mathcal{A}_q^{(k)} = \frac{c(k)}{\langle jm|\boldsymbol{J}^2|jm\rangle^{k/2}}\,\frac{\langle j||J^{(k)}||j\rangle}{\sqrt{2k+1}}\,\langle T_q^{(k)}(j)\rangle\,. \tag{C.3}$$

The state multipoles are related to the multipole moments of the spherical tensor operators, $\langle J_q^{(k)}\rangle$, of the rotational angular momentum, $\boldsymbol{j}$ [15]:

$$\langle T_q^{(k)}(j)\rangle = \frac{\sqrt{2k+1}}{\langle j||J^{(k)}||j\rangle}\langle J_q^{(k)}\rangle\,, \tag{C.4}$$

and are equal to $(-1)^q\rho_{-q}^{(k)}(j)$ parameters of Orr-Ewing [15] and $(-1)^q\rho_{-q}^{(k)}$ parameters of Mo *et al.* [185]. The role of the $c(k)$ normalization constants in Eqs. (C.2) and (C.3) is to match the limiting values of the quantum mechanical $\mathcal{A}_0^{(k)}$ alignment parameters to those of the classical ones in the high-j limit. Their explicit values are $c(0) = 1$, $c(1) = 1$, and $c(2) = \sqrt{6}$ [16]. The relationship between the *complex* $a_{\pm q}^{(k)}$ polarisation moments and the

standard polarisation parameters can then be formulated as:

$$\mathcal{A}^{(k)}_{\pm q} = \frac{c(k)}{\langle jm|\boldsymbol{J}^2|jm\rangle^{k/2}} \frac{\langle j||J^{(k)}||j\rangle}{\sqrt{2j+1}}\, a^{(k)}_{\pm q}\,. \tag{C.5}$$

C.2 Equivalence between the Fano–Macek and Suzuki–Mo intensity formulae

The data analysis which was introduced in Chapter 7 relies on the Fano–Macek description of the one photon induced transition intensities in a rotationally polarised medium [77]. Their formula for the the $j_i \rightarrow j_f$ one photon transition reads as,

$$\begin{aligned} I \;\; = \;\; & CS\left[1 + \tfrac{3}{2}h^{(1)}\left(j_i, j_f\right) O_0^{\mathrm{det}} \sin(2\beta)/\right. \\ & \left. -\tfrac{1}{2}h^{(2)}\left(j_i, j_f\right) A_0^{\mathrm{det}} + \tfrac{3}{2}h^{(2)}\left(j_i, j_f\right) A_{2+}^{\mathrm{det}} \cos(2\beta)\right]\,, \end{aligned} \tag{C.6}$$

where C is a constant which converts the transition probability to a power flux [77]. S is a line strength, and $h^{(k)}(j_i, j_f)$ is a line strength factor for the polarization moment of rank k, and is defined in Eq. (C.7) [77]:

$$h^{(k)}(j_i, j_f) = (-1)^{j_i - j_f} \begin{Bmatrix} j_i & j_i & k \\ 1 & 1 & j_f \end{Bmatrix} \Big/ \begin{Bmatrix} j_i & j_i & k \\ 1 & 1 & j_i \end{Bmatrix}\,. \tag{C.7}$$

However, more recently Mo and Suzuki [185] developed a formalism alternative to that of Fano and Macek for the two photon transitions, based on the work of Docker [209], Kummel, Sitz and Zare [79] and Case and Herschbach [210].

The Mo–Suzuki type intensity formula for a one photon induced transition can be written as [185]:

$$I = c \sum_k P_k\left(j_i, j_f\right) \langle T_0^{(k)\mathrm{PR}}(j_i)^\dagger\rangle\,, \tag{C.8}$$

where $\langle T_0^{(k)\mathrm{PR}}(j_i)^\dagger\rangle$ is the k-th rank state multipole [72], c is a constant [185] and $P_k\left(j_i, j_f\right)$

is a geometric factor defined as:

$$P_k(j_i, j_f) = \sum_{m_i, m_f} (-1)^{j_i - m_i} \sqrt{2k+1} \begin{pmatrix} j_i & k & j_i \\ -m_i & 0 & m_i \end{pmatrix} |\langle \psi_i | \hat{\boldsymbol{r}} \cdot \hat{\boldsymbol{\epsilon}} | \psi_f \rangle|^2 \,, \tag{C.9}$$

where $\hat{\boldsymbol{r}}$ is the dipole moment operator of the diatom whose initial and final wavefunctions are denoted by $|\psi_i\rangle$ and $|\psi_f\rangle$, respectively. The superscript 'PR' refers to the probe frame of Mo and Suzuki, in which the state multipoles are defined. The Suzuki–Mo probe frame is constructed in a different way from that of Fano and Macek [185]. Its principal axis, $\hat{\boldsymbol{Z}}$, is parallel to the laser propagation axis in the case of circularly polarised light. In the case of linearly polarised light, it is assumed to be parallel to the polarisation vector of the laser, $\hat{\boldsymbol{\epsilon}}$. The detector frame of Fano and Macek will be denoted by the superscript 'det' in order to distinguish between the probe frame of Mo and Suzuki. Only the $q = 0$ moments are included in Eq. (C.8) since cylindrical symmetry pertains to the system with respect to the $\hat{\boldsymbol{Z}}$ axis.

C.2.1 Derivation of intermediate Hund's case (a) and Hund's case (b) line strength factors

In the following, line strength factors will be obtained for a one photon transition between initial and final states described by intermediate Hund's case (a) and Hund's case (b) coupling scheme. We will proceed in a way similar to that of Suzuki and Mo derived in Appendix A of Ref. [185]. The initial and final wavefunctions are denoted by $|\psi_i\rangle$ and $|\psi_f\rangle$, respectively. Both of them are expanded in terms of Hund's case (a) wavefunctions [144, 185] in Equation (C.10). The wavefunction of the initial and final states are

$$\begin{aligned} |\psi_i\rangle &= \sum_{\Omega_i} C^{(i)}_{\Omega_i} |n_i \Lambda_i S \Sigma_i, J_i M_i \Omega_i\rangle \\ |\psi_f\rangle &= \sum_{\Omega_f} C^{(f)}_{\Omega_f} |n_f \Lambda_f S \Sigma_f, J_f M_f \Omega_f\rangle \,. \end{aligned} \tag{C.10}$$

The matrix elements of the transition operator, $\boldsymbol{\epsilon}\cdot\boldsymbol{r}$ is calculated as shown in Equation (C.11):

$$\langle\psi_f|\hat{O}|\psi_i\rangle = |\langle\psi_f|\boldsymbol{\epsilon}\cdot\boldsymbol{r}|\psi_i\rangle|^2 = \langle\psi_f|\boldsymbol{\epsilon}\cdot\boldsymbol{r}|\psi_i\rangle\langle\psi_f|\boldsymbol{\epsilon}\cdot\boldsymbol{r}|\psi_i\rangle^* . \tag{C.11}$$

Upon substituting the expansion of the initial and final wavefunctions in Eq. (C.10) into Eq. (C.11) one has:

$$\langle\psi_f|\hat{O}|\psi_i\rangle = \sum_{\Omega_i,\Omega_f} C^i_{\Omega_i} C^{f*}_{\Omega_f} \langle n_f\Lambda_f S\Sigma_f, J_f M_f\Omega_f|\boldsymbol{\epsilon}\cdot\boldsymbol{r}|n_i\Lambda_i S\Sigma_i, J_i M_i\Omega_i\rangle \tag{C.12}$$
$$\left(\sum_{\Omega_{i'},\Omega_{f'}} C^i_{\Omega_{i'}} C^{f*}_{\Omega_{f'}} \langle n_f\Lambda_f S\Sigma_f, J_f M_f\Omega_{f'}|\boldsymbol{\epsilon}\cdot\boldsymbol{r}|n_i\Lambda_i S\Sigma_i, J_i M_i\Omega_{i'}\rangle\right)^* .$$

Our aim is to simplify Eq. (C.12). This may achieved *via* the following steps, which is practically identical with section III. B of Ref. [185]:

- The dot product, $\hat{\boldsymbol{\epsilon}}\cdot\hat{\boldsymbol{r}}$, can be expressed in terms of the spherical components of the $\hat{\boldsymbol{\epsilon}}$ and $\hat{\boldsymbol{r}}$ operators [99] which is preferable over the Cartesian representation.

- If the dipole moment operator, $\hat{\boldsymbol{r}}$, is rotated to the body fixed frame (in which the bond axis is taken as the principal axis) the calculation of the matrix elements is significantly simplified.

- The terms of the product spherical operators are separated according to their effect on the rotational wavefunction.

- The resultant integral over the product of the Wigner D-matrices is evaluated invoking the appropriate closure relations.

The transition operator can be expressed as a tensorial product of the laser polarisation vector and the dipole moment of the molecule. The probe frame (PR) dipole momentum operator can be obtained by rotating to the body frame (BF) dipole momentum operator

as shown in Eq. (C.13):

$$\boldsymbol{\epsilon}\cdot\boldsymbol{r} = (-1)^s \epsilon^{(1)}_{-s} r^{(1)}_s \,(PR) = (-1)^s \epsilon^{(1)}_{-s} \sum_{q_1=-1}^{1} D^{1*}_{sq_1}\,(\alpha,\beta,\gamma)\, r^{(1)}_{q_1}(BF)\,. \tag{C.13}$$

Let us consider a matrix element of the transition operator:

$$\begin{aligned}(-1)^s \epsilon^{(1)}_{-s} \sum_{q_1=-1}^{1} \langle n_f \Lambda_f S\Sigma_f, J_f M_f \Omega_f | D^{1*}_{sq_1}\,(\alpha,\beta,\gamma)\, r^{(1)}_{q_1}(BF) | n_i \Lambda_i S\Sigma_i, J_i M_i \Omega_i\rangle = \\ (-1)^s \epsilon^{(1)}_{-s} \sum_{q_1=-1}^{1} \langle n_f \Lambda_f S\Sigma_f | r^{(1)}_{q_1}(BF) | n_i \Lambda_i S\Sigma_i\rangle \langle J_f M_f \Omega_f | D^{1*}_{sq_1}\,(\alpha,\beta,\gamma)\,|J_i M_i \Omega_i\rangle\,.\end{aligned} \tag{C.14}$$

The product of three rotation matrices is readily recognised in the second term of the product, and can then be evaluated using Eq. (3.114) in Ref. [93]:

$$\begin{aligned}&\langle J_f M_f \Omega_f | D^{1*}_{sq_1}\,(\alpha,\beta,\gamma)\,|J_i M_i \Omega_i\rangle = \\ &\left[\frac{2J_i+1}{8\pi^2}\right]^{1/2}\left[\frac{2J_f+1}{8\pi^2}\right]^{1/2}\left(\langle D^{J_f}_{M_f\Omega_f} D^{1*}_{sq_1} D^{J_i*}_{M_i\Omega_i}\rangle^*\right)^* = \\ &\left[\frac{2J_i+1}{8\pi^2}\right]^{1/2}\left[\frac{2J_f+1}{8\pi^2}\right]^{1/2}\langle D^{J_f*}_{M_f\Omega_f} D^{1}_{sq_1} D^{J_i}_{M_i\Omega_i}\rangle^* = \\ &\left[\frac{2J_i+1}{8\pi^2}\right]^{1/2}\left[\frac{2J_f+1}{8\pi^2}\right]^{1/2}\frac{8\pi^2}{2J_f+1}\langle J_f M_f, 1s | J_i M_i\rangle\langle J_f\Omega_f, 1q_1 | J_i\Omega_i\rangle = \\ &\left[\frac{2J_i+1}{2J_f+1}\right]^{1/2}\langle J_f M_f, 1s | J_i M_i\rangle\langle J_f\Omega_f, 1q_1 | J_i\Omega_i\rangle\,.\end{aligned} \tag{C.15}$$

Thus we have:

$$\begin{aligned}&\langle n_f \Lambda_f S\Sigma_f, J_f M_f \Omega_f | \boldsymbol{\epsilon}\cdot\boldsymbol{r} | n_i \Lambda_i S\Sigma_i, J_i M_i \Omega_i\rangle = \\ &(-1)^s \epsilon^{(1)}_{-s} \sum_{q_1=-1}^{1} G^f_i\,(r_{q_1})\left[\frac{2J_i+1}{2J_f+1}\right]^{1/2}\langle J_f M_f, 1s | J_i M_i\rangle\langle J_f\Omega_f, 1q_1 | J_i\Omega_i\rangle\,,\end{aligned} \tag{C.16}$$

where the $G^f_i\,(r_{q_1}) \stackrel{def.}{=} \langle n_f \Lambda_f S\Sigma_f | r^{(1)}_{q_1}(BF) | n_i \Lambda_i S\Sigma_i\rangle$ was used.

The $\langle n_f \Lambda_f S\Sigma_f | r^{(1)}_{q_1}(BF) | n_i \Lambda_i S\Sigma_i\rangle$ matrix element can be valuated using the Wigner–Eckart theorem. Substituting Eq. (C.16) into Eq. (C.12) one has:

$$\left(\sum_{\Omega_f,\Omega_i} C^i_{\Omega_i} C^{f*}_{\Omega_f} \sum_{q_1=-1}^{1} G^f_i\left(r_{q_1}\right)\left[\frac{2J_i+1}{2J_f+1}\right]^{1/2} \langle J_f M_f, 1s|J_i M_i\rangle \langle J_f\Omega_f, 1q_1|J_i\Omega_i\rangle\right) \tag{C.17}$$

$$\left(\sum_{\Omega_{f'},\Omega_{i'}} C^i_{\Omega_{i'}} C^{f*}_{\Omega_{f'}} \sum_{q_2=-1}^{1} G^{f'}_{i'}\left(r_{q_2}\right)\left[\frac{2J_i+1}{2J_f+1}\right]^{1/2} \langle J_f M_f, 1s|J_i M_i\rangle \langle J_f\Omega_{f'}, 1q_2|J_i\Omega_{i'}\rangle\right)^* =$$

$$\langle J_f M_f, 1s|J_i M_i\rangle^2 \left[\frac{2J_i+1}{2J_f+1}\right] \sum_{q_1,q_2} G^f_i\left(r_{q_1}\right) G^{f'}_{i'}\left(r_{q_2}\right)$$

$$\sum_{\Omega_f,\Omega_i,\Omega_{f'},\Omega_{i'}} C^i_{\Omega_i} C^{f*}_{\Omega_f} C^{i*}_{\Omega_{i'}} C^f_{\Omega_{f'}} \langle J_f\Omega_f, 1q_1|J_i\Omega_i\rangle \langle J_f\Omega_{f'}, 1q_2|J_i\Omega_{i'}\rangle =$$

$$\frac{2J_f+1}{2J_i+1}\langle J_f M_f, 1s|J_i M_i\rangle^2 E^f_i = \frac{(2J_f+1)^2}{2J_i+1}\begin{pmatrix} J_f & 1 & J_i \\ M_f & s & -M_i \end{pmatrix}^2 E^f_i, \text{ where}$$

$$E^f_i \overset{def.}{=} \sum_{q_1,q_2} G^f_i\left(r_{q_1}\right) G^{f'}_{i'}\left(r_{q_2}\right) \sum_{\Omega_f,\Omega_i,\Omega_{f'},\Omega_{i'}} C^i_{\Omega_i} C^{f*}_{\Omega_f} C^{i*}_{\Omega_{i'}} C^f_{\Omega_{f'}} \langle J_f\Omega_f, 1q_1|J_i\Omega_i\rangle \langle J_f\Omega_{f'}, 1q_2|J_i\Omega_{i'}\rangle\,.$$

C.2.2 Factorisation of P_k

The P_k factors of Suzuki and Mo are defined by Eq (C.18), according to Eq. (6b) of Ref. [185].

$$P_k = \sum_{M_i,M_f} (-1)^{J_i-M_i}\sqrt{2k+1}\begin{pmatrix} J_i & k & J_i \\ -M_i & 0 & M_i \end{pmatrix} |\langle\psi_i|\boldsymbol{r}\cdot\boldsymbol{\epsilon}|\psi_f\rangle|^2 \tag{C.18}$$

If the transition matrix elements, $|\langle\psi_i|\boldsymbol{r}\cdot\boldsymbol{\epsilon}|\psi_f\rangle|$, derived in Eq. (C.17) are substituted into the above definition, a sum over a product of three $3j$-symbols appear which is written out below:

$$\sum_{M_i,M_f} (-1)^{J_i-M_i}\begin{pmatrix} J_f & 1 & J_i \\ M_f & s & -M_i \end{pmatrix}\begin{pmatrix} J_f & 1 & J_i \\ M_f & s & -M_i \end{pmatrix}\begin{pmatrix} J_i & k & J_i \\ M_i & 0 & -M_i \end{pmatrix}. \tag{C.19}$$

Some simple algebraic manipulation has to be done in order to evaluate this expression:

$$\begin{pmatrix} J_f & 1 & J_i \\ M_f & s & -M_i \end{pmatrix} = \begin{pmatrix} 1 & J_f & J_i \\ -s & -M_f & +M_i \end{pmatrix} , \tag{C.20}$$

where identities from Appendix I. of Ref. [99] (and of [93] Chapter 3.) were used. Phase factors can be introduced without changing the overall phase of the expression in Eq. (C.18) when taking to account the triangle condition, $M_f + s = M_i$:

$$\begin{aligned} 1 = (-1)^{J_i}(-1)^{-J_i} = (-1)^{J_i}(-1)^{-J_i}(-1)^{J_f-M_f}(-1)^{M_f-J_f} = \\ (-1)^{J_i}(-1)^{-J_i}(-1)^{J_f-M_f}(-1)^{M_i-s-J_f} = (-1)^{J_i-M_i}(-1)^{J_f-M_f}(-1)^{J_i-J_f-s} . \end{aligned} \tag{C.21}$$

Eq. (C.19) can then be factored into a product $6j$- and $3j$-symbols according to Eq. 7.35 in Ref. [99]:

$$\begin{aligned} &(-1)^{J_i-J_f-s} \sum_{M_i,M_f} (-1)^{J_i-M_i}(-1)^{J_i-M_i}(-1)^{J_f-M_f} \\ &\begin{pmatrix} 1 & J_f & J_i \\ -s & -M_f & +M_i \end{pmatrix} \begin{pmatrix} J_f & 1 & J_i \\ M_f & s & -M_i \end{pmatrix} \begin{pmatrix} J_i & k & J_i \\ M_i & 0 & -M_i \end{pmatrix} = \\ &(-1)^{J_i-J_f-s} \begin{pmatrix} 1 & 1 & k \\ -s & s & 0 \end{pmatrix} \begin{Bmatrix} 1 & 1 & k \\ J_i & J_i & J_f \end{Bmatrix} . \end{aligned} \tag{C.22}$$

The line strength factor, P_k is recovered, if Eq. (C.22) is inserted to Eq. (C.17):

$$P_k = \frac{(2J_i+1)^2}{2J_f+1}\sqrt{2k+1}(-1)^{J_f-J_i+s}\begin{pmatrix} 1 & 1 & k \\ -s & s & 0 \end{pmatrix}\begin{Bmatrix} 1 & 1 & k \\ J_i & J_i & J_f \end{Bmatrix} E_i^f = \tag{C.23}$$

$$\frac{(2J_i+1)^2}{2J_f+1}(-1)^{1+s}\sqrt{2k+1}\begin{pmatrix} 1 & 1 & k \\ -s & s & 0 \end{pmatrix}(-1)^{J_f-J_i+1}\begin{Bmatrix} 1 & 1 & k \\ J_i & J_i & J_f \end{Bmatrix} E_i^f =$$

$$\frac{(2J_i+1)^2}{2J_f+1}(-1)^{J_f-J_i+1}\rho_0^{(k)}(\boldsymbol{\epsilon})\begin{Bmatrix} 1 & 1 & k \\ J_i & J_i & J_f \end{Bmatrix} E_i^f\,.$$

Having noted the intensity formula of Mo and Suzuki in Eq. (C.8) can be reformulated with the aid of the above expression for the line strength factor, $P_k(j_i, j_f)$ the total intensity can be written as:

$$I = c\sum_k \frac{(2j_i+1)^2}{2j_f+1}(-1)^{j_f-j_i+1}\langle T_0^{(k)}(\boldsymbol{\epsilon})^\dagger\rangle\begin{Bmatrix} 1 & 1 & k \\ j_i & j_i & j_f \end{Bmatrix} E_i^f\langle T_0^{(k)\mathrm{PR}}(j_i)^\dagger\rangle\,, \tag{C.24}$$

where the electric state multipoles, $\langle T_0^{(k)}(\hat{\boldsymbol{\epsilon}})^\dagger\rangle$, can be expressed in terms of a $3j$-symbol as shown in Eq. (C.25):

$$\langle T_0^{(k)}(\boldsymbol{\epsilon})^\dagger\rangle = (-1)^{1+s}\sqrt{2k+1}\begin{pmatrix} 1 & 1 & k \\ -s & s & 0 \end{pmatrix}\,. \tag{C.25}$$

If the state multipoles are expressed in term of Fano–Macek polarisation parameters and using their line strengths factors given in Eq. (C.7), the intensity can be written as

$$\begin{aligned} I &= \frac{1}{3}cS\left\{1 - \frac{3}{\sqrt{2}}\langle T_0^{(1)}(\boldsymbol{\epsilon})^\dagger\rangle h^{(1)}(j_i,j_f)\frac{A_0^{(1)\,\mathrm{PR}}}{\sqrt{j(j+1)}}\right. \\ &- \left.\frac{3}{\sqrt{6}}\langle T_0^{(2)}(\boldsymbol{\epsilon})^\dagger\rangle h^{(2)}(j_i,j_f)A_0^{(2)\,\mathrm{PR}}\right\}\,, \end{aligned} \tag{C.26}$$

where

$$S = (-1)^{2j_i} \frac{(2j_i+1)^{3/2}}{2j_f+1} E_i^f \,. \tag{C.27}$$

This key results allows as to find the relationship between the $h^{(k)}(j_i, j_f)$ factors of Fano and Macek and the $P_k(j_i, j_f)$ factors of Suzuki and Mo:

$$P_k(j_i, j_f) \frac{[j_i(j_i+1)]^{k/2}}{c(k)} \frac{\sqrt{2k+1}}{\langle j_i || J_i^{(k)} || j_i \rangle} = SN(k) \langle T_0^{(k)}(\boldsymbol{\epsilon})^\dagger \rangle h^{(k)}(j_i, j_f) \,, \tag{C.28}$$

where the $N(k)$ normalisation factors for first and second rank moments are

$$N(1) = \frac{3}{\sqrt{2}}, \; N(2) = \frac{3}{\sqrt{6}}. \tag{C.29}$$

C.2.3 Rotation to the Fano–Macek reference frame

Eq. (C.26) is still defined in the probe frame of Mo and Suzuki. The last remaining step is to transform the polarisation parameters in Eq. (C.28) to the detector frame of Fano and Macek. Since they are tensorial quantities, this transformation should be carried out with the Wigner rotation matrices [99]. The two frames are identical in the case of circularly polarised light, thus no rotation is required. In the case of linearly polarised light, the angles of rotation for rotating from the Mo–Suzuki frame to the Fano–Macek frame are $(\pi, \pi/2, 0)$. Using the definition of the rotation matrices given in Ref. [99], the transformation can be written as

$$a_q^{(k)\mathrm{PR}} = \sum_{q'} (-1)^{q'} d^k_{q'q}(\tfrac{\pi}{2}) a_{q'}^{(k)\,\det} \,, \tag{C.30}$$

from which it follows the probe frame alignment paremeter is equal to

$$A_0^{(2)\mathrm{PR}} = -\tfrac{1}{2} A_0^{\{2\}\det} + \tfrac{\sqrt{3}}{2} A_{2+}^{\{2\}\det} \,. \tag{C.31}$$

If the Fano–Macek frame polarisation parameters of Eq.(7.3) are substituted into Eq. (C.31), and are used to express the intensity for linearly or circularly polarised light, by choosing the appropriate value of the electric field state multipoles, $\langle T_0^{(k)}(\epsilon)^\dagger\rangle$, [182], the original Fano–Macek formula can be recovered:

$$I = \frac{1}{3}cS\left\{1+\tfrac{3}{2}h^{(1)}(j_i,j_f)O_0^{\rm det}\sin(2\beta)-\tfrac{1}{2}h^{(2)}(j_i,j_f)A_0^{\rm det}+\tfrac{3}{2}h^{(2)}(j_i,j_f)A_{2+}^{\rm det}\cos 2\beta\right\}\ .$$

Bibliography

[1] M. Brouard and C. Vallance, *Tutorials in Molecular Reaction Dynamics*, Royal Society of Chemistry, Cambridge, 2010.

[2] F. Fleming Crim, *PNAS*, **105**, 12654 (2008).

[3] T. Odiorne, P. Brooks, and J. V. V. Kasper, *J. Chem. Phys.*, **55**, 1980 (1971).

[4] M. Y. Hayes, M. P.Deskevich, D. J. Nesbitt, K. Takahashi, and R. T. Skodje, *J. Phys. Chem. A*, **110**, 436 (2006).

[5] J.M. Alvari no and A. Laganà, *Chemical Physics Letters*, **144**, 558 (1988).

[6] C. Cohen-Tannoudji, B. Diu, and F. Laloe, *Quantum Mechanics*, Wiley, 1977.

[7] G. A. Worth and L. S. Cederbaum, *Annu. Rev. Phys. Chem.*, **55**, 127 (2004).

[8] D. R. Yarkony, *Rev. Mod. Phys. Phys.*, **68**, 985 (1996).

[9] M. H. Alexander, *J. Chem. Phys.*, **76**, 5974 (1982).

[10] F. J. Aoiz, M. Brouard, and P. A. Enriquez, *J. Chem. Phys.*, **105**, 4964 (1996).

[11] M. P. de Miranda, F. J. Aoiz, L. Bañares, and V. Sáez Rábanos, *J. Chem. Phys.*, **111**, 5368 (1999).

[12] M. S. Child, *Molecular Collision Theory*, Dover Publications Inc., 1996.

[13] L. S. Rodberg and R. M. Thaler, *The Quantum Theory of Scattering*, Academic Press, 1967.

[14] Richard B. Bernstein (Ed.), *Atom-Molecule Scattering*, Plenum, 1979.

[15] A. J. Orr-Ewing and R. N. Zare, *Annu. Rev. Phys. Chem.*, **45**, 315 (1994).

[16] N. E. Shafer-Ray, A. J. Orr-Ewing, and R. N. Zare, *J. Phys. Chem.*, **99**, 7591 (1995).

[17] M. Brouard, H. Chadwick, C. J. Eyles, B. Hornung, B. Nichols, and S. Stolte, *To be submitted.*

[18] K. T. Lorenz, D. W. Chandler, J. W. Barr, W. Chen, G. L. Barnes, and J. I. Cline, *Science*, **293**, 2063 (2001).

[19] E. A. Wade, K. T. Lorenz, D. W. Chandler, J. W. Barr, G. L. Barnes, and J. I. Cline, *Chem. Phys.*, **301**, 261 (2004).

[20] Y. Kim and H. Meyer, *Chem. Phys. Lett.*, **387**, 339 (2004).

[21] Y. Kim and H. Meyer, *Chem. Phys.*, **301**, 273 (2004).

[22] V. Khare, D. J. Kouri, and D. K. Hoffman, *J. Chem. Phys.*, **74**, 2275 (1981).

[23] V. Khare and D. J. Kouri, *J. Chem. Phys.*, **76**, 4493 (1982).

[24] H. Meyer, *J. Phys. Chem.*, **99**, 1101 (1995).

[25] S. Marinakis, B. J. Howard, F. J. Aoiz, and J. Kłos, *Chem. Phys. Lett.*, **512**, 161 (2011).

[26] J. D. Steill, J. J. Kay, G. Paterson, T. R. Sharples, J. Kłos, M. L. Costen, K. E. Strecker, K. G. McKendrick, M. H. Alexander, and D. W. Chandler, *J. Chem. Phys. A*, **117**, 8163 (2013).

[27] P. J. Dagdigian and M. H. Alexander, *J. Chem. Phys.*, **130**, 094303 (2009).

[28] A. J. McCaffery, *J. Phys. Chem.*, **91**, 5451 (1987).

[29] M. L. Costen, R. Livingstone, K. G. McKendrick, G. Paterson, M. Brouard, H. Chadwick, Y.-P. Chang, C. J. Eyles, F. J. Aoiz, and J. Kłos, *J. Phys. Chem. A*, **113**, 15156 (2009).

[30] G. Paterson, M. L. Costen, and K. G. McKendrick, *Int. Rev. Phys. Chem.*, **31**, 69 (2012).

[31] M. Brouard, H. Chadwick, Y.-P. Chang, R. Cireasa, C. J. Eyles, A. O. La Via, N. Screen, F. J. Aoiz, and J. Kłos, *J. Chem. Phys.*, **131**, 104307 (2009).

[32] M. Brouard, A. Bryant, Y.-P. Chang, R. Cireasa, C. J. Eyles, A. M. Green, S. Marinakis, F. J. Aoiz, and J. Kłos, *J. Chem. Phys.*, **130**, 044306 (2009).

[33] M. Brouard, H. Chadwick, Y.-P. Chang, C. J. Eyles, F. J. Aoiz, and J. Kłos, *J. Chem. Phys.*, **135**, 084306 (2011).

[34] G. Paterson, A. Relf, M. L. Costen, K. G. McKendrick, M. H. Alexander, and P. J. Dagdigian, *J. Chem. Phys.*, **135**, 234304 (2011).

[35] R. N. Porter, *Ann. Rev. Phys. Chem.*, **25**, 317 (1974).

[36] H. Eyring and M. Polanyi, *Z. Phys. Chem. B*, **12**, 279 (1931).

[37] F. T. Wall, L. A. Hiller, and J. Mazur, *J. Chem. Phys.*, **28**, 255 (1958).

[38] F. T. Wall, L. A. Hiller, and J. Mazur, *J. Chem. Phys.*, **35**, 1284 (1961).

[39] G. D. Barg, G. M. Kendall, and J. P. Toennies, *Chem. Phys.*, **16**, 243 (1976).

[40] R. A. Budde and R. B. Bernstein, *J. Chem. Phys.*, **55**, 5499 (1971).

[41] R. A. Budde and R. B. Bernstein, *J. Chem. Phys.*, **59**, 3691 (1973).

[42] J. M. Bowman and G. C. Schatz, *Ann. Rev. Phys. Chem.*, **46**, 169 (1995).

[43] F. J. Aoiz, M. Brouard, C. J. Eyles, J. Kłos, and M. P. de Miranda, *J. Chem. Phys.*, **130**, 044305 (2009).

[44] F. J. Aoiz, V. J. Herrero, V. S. Rábanos, and J. E. Verdasco, *Phys. Chem. Chem. Phys.*, **6**, 4407 (2004).

[45] N. C. Blais and D. G. Truhlar, *J. Chem. Phys.*, **67**, 1540 (1977).

[46] J. C. Tully and R. K. Preston, *J. Chem. Phys.*, **55**, 562 (1971).

[47] J. C. Tully, *Farad. Disc.*, **110**, 407 (1998).

[48] W. H. Miller, *Adv. Chem. Phys.*, **25**, 69 (1974).

[49] J. J. Sakurai and J. Napolitano, *Modern Quantum Mechanics*, Pearson, 2010.

[50] A. M. Arthurs and A. Dalgarno, *Proc. R. Soc. Lond.*, **256**, 540 (1960).

[51] W. N. Sams and D. J. Kouri, *J. Chem. Phys.*, **51**, 4815 (1969).

[52] B. L. Johnson and D. Secrest, *J. Math. Phys.*, **7**, 2187 (1966).

[53] B. L. Johnson, *J. Comp. Phys.*, **13**, 445 (1973).

[54] D. E. Manolopoulos, *J. Chem. Phys.*, **85**, 6425 (1986).

[55] HIBRIDON is a package of programs for the time-independent quantum treatment of inelastic collisions and photodissociation written by M. H. Alexander, D. Manolopoulos, H. -J. Werner, and B. Follmeg, with contributions by P. F. Vohralik, D. Lemoine, G. Corey, R. Gordon, B. Johnson, T. Orlikowski, A. Berning, A. Degli-Esposti, C. Rist, P. Dagdigian, B. Pouilly, G. van der Sanden, M. Yang, F. de Weerd, S. Gregurick, and J. Kłos.

[56] J. M. Hutson and S. Green, MOLSCAT computer code, version 14 (1994), distributed by Collaborative Computational Project No. 6 of the Science and Engineering Research Council (UK).

[57] G. Herzberg, *Molecular Spectra and Molecular Structure, Volume I, Spectra of diatomic molecules, 2nd edition*, D. Van Nostrand Company, 1950.

[58] M. Jacob and G. C. Wick, *Annals. Phys.*, **7**, 404 (1959).

[59] M. S. Child, *Semiclassical Mechanics with Molecular Applications*, Clarendon Press, 1991.

[60] W. H. Miller, *J. Chem. Phys.*, **53**, 1949 (1970).

[61] W. H. Miller, *Chem. Phys. Lett.*, **7**, 431 (1970).

[62] W. H. Miller, *J. Chem. Phys.*, **54**, 5386 (1971).

[63] R. Schinke, *Chem. Phys.*, **34**, 65 (1978).

[64] R. Schinke and H. J. Korsch, *Chem. Phys. Lett.*, **74**, 449 (1980).

[65] R. Schinke and J. M. Bowman, *Molecular collision dynamics*, Springer-Verlag, Heidelberg, 1982.

[66] C. J. Eyles, M. Brouard, C.-H. Yang, J. Kłos, F. J. Aoiz, A. Gijsbertsen, A. E. Wiskerke, and S. Stolte, *Nature Chemistry*, **3**, 597 (2011).

[67] Radoslaw Uberna, Robert D. Hinchliffe, and Joseph I. Cline, *J. Chem. Phys*, **105**, 9847 (1996).

[68] G. Scoles, *Atomic and Molecular Beam Methods, Volume 1*, Oxford University Press, New York, USA, 1988.

[69] G. Scoles, *Atomic and Molecular Beam Methods, Volume 2*, Oxford University Press, New York, USA, 1988.

[70] G. Hall, K. Liu, M. J. McAuliffe, C. F. Giese, and W. R. Gentry, *J. Chem. Phys.*, **78**, 5260 (1983).

[71] M. L. Costen, S. Marinakis, and K. G. McKendrick, *Chem. Soc. Rev.*, **37**, 732 (2008).

[72] K. Blum, *Density Matrix Theory and Applications, 2nd Ed.*, Plenum Press, New York, 1996.

[73] A. Gijsbertsen, H. V. Linnartz, C. A. Taatjes, and S. Stolte, *J. Am. Chem. Soc.*, **128**, 8777 (2006).

[74] A. Gijsbertsen, *Towards a Better Understanding of Inelastic Atom-Molecule Collisions*, PhD Thesis, Vrije Universiteit, Amsterdam, 2006.

[75] M. G. Tenner, E. W. Kuipers, W. Y. Langhout, A. W. Kleyn, G. Nicolasen, and S. Stolte, *Surface Science*, **236**, 151 (1990).

[76] M. N. R. Ashfold and J. D. Howe, *Annu. Rev. Phys. Chem.*, **45**, 57 (1994).

[77] U. Fano and J. H. Macek, *Rev. Mod. Phys.*, **45**, 553 (1973).

[78] C. H. Greene and R. N. Zare, *J. Chem. Phys.*, **78**, 6741 (1983).

[79] A. C. Kummel, G. O. Sitz, and R. N. Zare, *J. Chem. Phys.*, **85**, 6874 (1986).

[80] A. J. McCaffery, M. J. Proctor, and B. J. Whitaker, *Annu. Rev. Phys. Chem.*, **37**, 223 (1986).

[81] H. Katô, S. R. Jeyes, A. J. McCaffery, and M. D. Rowe, *Chem. Phys. Lett.*, **39**, 573 (1976).

[82] S. R. Jeyes, A. J. McCaffery, and M. D. Rowe, *Mol. Phys.*, **36**, 845 (1978).

[83] S. R. Jeyes, A. J. McCaffery, and M. D. Rowe, *Mol. Phys.*, **36**, 1865 (1978).

[84] E. A. Brinkman and D. R. Crosley, *J. Phys. Chem. A*, **108**, 8084 (2004).

[85] R. T. Carter and J. R. Huber, *Chem. Soc. Rev.*, **29**, 305 (2000).

[86] M. Brouard, A. Bryant, I. Burak, S. Marinakis, F. Quadrini, I. Anton Garcia, and C. Vallance, *Mol. Phys.*, **103**, 1693 (2005).

[87] H. J. Crichton, M. L. Costen, and K. G. McKendrick, *J. Chem. Phys.*, **119**, 9461 (2003).

[88] M. L. Costen, H. J. Crichton, and K. G. McKendrick, *J. Chem. Phys.*, **120**, 7910 (2004).

[89] M. L. Costen and K. G. McKendrick, *J. Chem. Phys.*, **122**, 164309 (2005).

[90] G. Paterson, S. Marinakis, M. L. Costen, K. G. McKendrick, J. Kłos, and R. Toboła, *J. Chem. Phys.*, **129**, 074304 (2008).

[91] G. Paterson, S. Marinakis, M. L. Costen, and K. G. McKendrick, *Phys. Chem. Chem. Phys.*, **11**, 8813 (2009).

[92] K. P. Huber and G. Herzberg, *Molecular Spectra and Molecular Structure, Volume IV, Constants of diatomic molecules*, D. Van Nostrand Company, 1979.

[93] R. N. Zare, *Angular Momentum, Understanding Spatial Aspects in Chemistry and Physics*, John Wiley and Sons, 1988.

[94] C. Amiot, R. Bacis, and G. Guelachvili, *Can. J. Phys.*, **56**, 251 (1978).

[95] C. A. Burrus and W. Gordy, *Phys. Rev.*, **92**, 1437 (1953).

[96] W. L. Meerts and A. Dymanus, *J. Mol. Spectrosc.*, **44**, 320 (1972).

[97] J. M. Brown, J. T. Hougen, K.-P. Huber, J. W. C. Johns, I. Kopp, H. Lefebvre-Brion, A. J. Merer, D. A. Ramsey, J. Rostas, and R. N. Zare, *J. Mol. Spectrosc.*, **55**, 500 (1975).

[98] M. H. Alexander, *J. Chem. Phys.*, **99**, 7725 (1993).

[99] D. M. Brink and G. R. Satchler, *Angular Momentum, 2nd Ed.*, Clarendon Press, Oxford, 1975.

[100] M. H. Alexander, *J. Chem. Phys.*, **81**, 4510 (1984).

[101] G. C. Nielson, G. A. Parker, and R. T. Pack, *J. Chem. Phys.*, **66**, 1396 (1977).

[102] M. H. Alexander, *J. Chem. Phys.*, **111**, 7426 (1999).

[103] P. J. Knowles, C. Hampel, and H-J. Werner, *J. Chem. Phys.*, **99**, 5219 (1993).

[104] Y. Sumiyoshi and Y. Endo, *J. Chem. Phys.*, **127**, 184309 (2007).

[105] M. Lemeshko, *The Vector Correlations in Rotationally Inelastic Molecular Collisions*, PhD Thesis, Technical University of Berlin, 2011.

[106] E. T. Whittaker, *A Treatise on the Analytical Dynamics of Particles and Rigid Bodies*, Cambridge University Press, Cambridge, 1999.

[107] M. Karplus, R. N. Porter, and R. D. Sharma, *J. Chem. Phys.*, **43**, 3259 (1965).

[108] F. J. Aoiz, V. J. Herreo, and V. Saez Rabanos, *J. Chem. Phys.*, **97**, 7423 (1992).

[109] F. J. Aoiz, M. Brouard, C. J. Eyles, J. F. Castillo, and V. Sáez Rábanos, *J. Chem. Phys.*, **125**, 144105 (2006).

[110] F. J. Aoiz, J. E. Verdasco, V. J. Herrero, V. S. Rábanos, and M. H. Alexander, *J. Chem. Phys.*, **119**, 5860 (2003).

[111] M. Abramowitz and I. A. Stegun, *Handbook of Mathematical Functions, 9th printing*, Dover, 1972.

[112] F. J. Aoiz, L. Bañares, and V. J. Herrero, *J. Chem. Soc. Faraday. Trans.*, **94**, 2483 (1998).

[113] N. M. J. Woodhouse, *Introduction to Analytical Dynamics*, Oxford Science Publications, 1987.

[114] U. Buck, F. Huisken, and J. Schleusener, *J. Chem. Phys.*, **68**, 5654 (1978).

[115] T. G. Kreutz and G. W. Flynn, *J. Chem. Phys.*, **93**, 452 (1990).

[116] S. D. Bosanac, *Phys. Rev. A*, **22**, 2617 (1980).

[117] D. A. Varsholovich, A. N. Moskalev, and V. K. Khersonskii, *Quantum Theory of Angular Momentum*, World Scientific, Singapore, 1988.

[118] M. H. Alexander and S. L. Davis, *J. Chem. Phys.*, **78**, 6754 (1983).

[119] M. H. Alexander and D. E. Manolopoulos, *J. Chem. Phys.*, **86**, 2044 (1987).

[120] P. McGuire and D. J. Kouri, *J. Chem. Phys.*, **60**, 2488 (1974).

[121] D. Secrest, *J. Chem. Phys.*, **62**, 710 (1975).

[122] R. B. Walker and J. C. Light, *Chem. Phys.*, **7**, 84 (1975).

[123] D. J. Kouri and T. G. Heil, *J. Chem. Phys.*, **65**, 1462 (1976).

[124] T. S. Tsien and R. T. Pack, *Chem. Phys. Lett.*, **6**, 54 (1970).

[125] I. V. Hertel and W. Stoll, *Adv. At. Mol. Phys*, **13**, 113 (1978).

[126] M. Brouard, H. Chadwick, C. J. Eyles, B. Hornung, B. Nichols, F. J. Aoiz, P. G. Jambrina, S. Stolte, and M. P. de Miranda, *J. Chem. Phys.* (2013).

[127] J. Aldegunde, *Stereodynamics of elementary reactions: Effect of the reagent's rotational angular momentum polarisation*, PhD Thesis, University of Salamanca, 2007.

[128] J. Aldegunde, F. J. Aoiz, and M. P. de Miranda, *Phys. Chem. Chem. Phys.*, **10**, 1139 (2008).

[129] M. P. de Miranda and F. J. Aoiz, *Phys. Rev. Lett.*, **93**, 083201 (2004).

[130] J. Z. H. Zhang and W. H. Miller, *J. Chem. Phys.*, **91**, 1528 (1989).

[131] M. Brouard, H. Chadwick, C. J. Eyles, B. Hornung, F. J. Aoiz, P. G. Jambrina, S. Stolte, and M. P. de Miranda, *J. Chem. Phys.* (2013).

[132] P. C. Jurs, *Computer Software Applications in Chemistry*, Wiley-Interscience, 1990.

[133] H. J. Korsch and R. Schinke, *J. Chem. Phys.*, **75**, 3850 (1981).

[134] C. J. Eyles, M. Brouard, H. Chadwick, F. J. Aoiz, J. Kłos, A. Gijsbertsen, X. Zhang, and S. Stolte, *Phys. Chem. Chem. Phys.*, **14**, 5420 (2012).

[135] S. D. Bosanac, *Phys. Rev. A*, **26**, 816 (1982).

[136] S. D. Bosanac and N. Petrovic, *Phys. Rev. A*, **41**, 5909 (1990).

[137] S. D. Bosanac and J. N. Murrell, *J. Chem. Phys.*, **94**, 1167 (1991).

[138] J. C. Belchior, J. N. Murrell, and S. D. Bosanac, *Mol. Phys.*, **77**, 727 (1992).

[139] J. C. Belchior and J. P. Braga, *J. Chem. Phys.*, **105**, 5792 (1996).

[140] E. Anderson, Z. Bai, C. Bischof, S. Blackford, J. Demmel, J. Dongarra, J. Du Croz, A. Greenbaum, S. Hammarling, A. McKenney, and D. Sorensen, *LAPACK Users' Guide*, Society for Industrial and Applied Mathematics, Philadelphia, PA, third ed., 1999.

[141] M. H. Alexander, *J. Chem. Phys.*, **111**, 7435 (1999).

[142] C. J. Eyles, M. Brouard, H. Chadwick, B. Hornung, B. Nichols, C.-H. Yang, J. Kłos, F. J. Aoiz, A. Gijsbertsen, A. E. Wiskerke, and S. Stolte, *Phys. Chem. Chem. Phys.*, **14**, 5403 (2012).

[143] D. K. Hoffman, J. W. Evans, and D. J. Kouri, *J. Chem. Phys.*, **80**, 144 (1984).

[144] M. H. Alexander, *J. Chem. Phys.*, **77**, 5974 (1855).

[145] A. Gijsbertsen, H. Linnartz, G. Rus, A. E. Wiskerke, S. Stolte, D. W. Chandler, and J. Kłos, *J. Chem. Phys.*, **123**, 224305 (2005).

[146] M. Lemeshko and B. Friedrich, *Phys. Rev. A*, **129**, 024301 (2008).

[147] M. Lemeshko and B. Friedrich, *Phys. Rev. A*, **79**, 12718 (2010).

[148] U. Fano and J. H. Macek, *J. Chem. Phys.*, **81**, 559 (1984).

[149] M. Lemeshko, P. G. Jambrina, M. de Miranda, and B. Friedrich, *J. Chem. Phys.*, **132**, 161102 (2010).

[150] P.G. Jambrina, J. Kłos, F.J. Aoiz, and M.P. de Miranda, *Phys. Chem. Chem. Phys.*, **14**, 9826 (2012).

[151] Y. Kim, H. Meyer, and M. H. Alexander, *J. Chem. Phys.*, **121**, 1339 (2004).

[152] J. J. Kay, G. Paterson, M. L. Costen, K. E. Strecker, K. G. McKendrick, and D. W. Chandler, *J. Chem. Phys.*, **134**, 091101 (2011).

[153] R. W. Anderson, *J. Phys. Chem. A*, **101**, 7664 (1997).

[154] H. G. Bennewitz, W. Paul, and C. Schlier, *Z. Phys.*, **141**, 6 (1955).

[155] D. H. Parker and A. T. J. B. Eppink, *J. Chem. Phys.*, **107**, 2357 (1997).

[156] C. J. Eyles, *An Experimental and Theoretical Study of the Dynamics of Atom-Molecule Scattering*, DPhil Thesis, University of Oxford, 2010.

[157] A. G. Suits and R. E. Continetti, *Imaging in Chemical Dynamics*, American Chemical Society, Washington D.C., 2000.

[158] M. J. Bass, M. Brouard, A. P. Clark, and C. Vallance, *J. Chem. Phys.*, **117**, 8723 (2002).

[159] M. J. L. de Lange, S. Stolte, C. A. Taajtes, J. Kłos, G. C. Groenenboom, and A. van der Avoird, *J. Chem. Phys.*, **121**, 11691 (2004).

[160] M. J. L. de Lange, M. Drabbels, P. T. Griffiths, J. Bulthuis, S. Stolte, and J. G. Snijders, *Chem. Phys. Lett.*, **313**, 491 (1999).

[161] J. J. van Leuken, J. Bulthuis, S. Stolte, and J. G. Snijders, *Chem. Phys. Lett.*, **260**, 595 (1996).

[162] A. Gijsbertsen, M. J. de Lange, A. E. Wiskerke, H. Linnartz, M. Drabbels, J. Kłos, and S. Stolte, *Chem. Phys.*, **301**, 293 (2004).

[163] P. Andreson, H. Joswig, H. Pauly, and R. Schinke, *J. Chem. Phys.*, **77**, 2204 (1982).

[164] C. R. Bieler, A. Sanov, and H. Reisler, *Chem. Phys. Lett.*, **235**, 175 (1995).

[165] G. C. Corey and M. H. Alexander, *J. Chem. Phys.*, **85**, 5652 (1986).

[166] M. Yang and M. H. Alexander, *J. Chem. Phys.*, **103**, 6973 (1995).

[167] T. Orlikowski and M. H. Alexander, *J. Chem. Phys.*, **79**, 6006 (1983).

[168] J. J. van Leuken, F. H. W. van Ameron, J. Bulthuis, J. G. Snijders, and S. Stolte, *J. Phys. Chem.*, **99**, 15573 (1995).

[169] J. Kłos, F. J. Aoiz, J. E. Verdasco, M. Brouard, S. Marinakis, and S. Stolte, *J. Chem. Phys.*, **127**, 031102 (2007).

[170] A. G. Suits, L. S. Bontuyan, P. L. Houston, and B. J. Whitaker, *J. Chem. Phys.*, **96**, 8618 (1992).

[171] M. S. Elioff and D. W. Chandler, *J. Chem. Phys.*, **117**, 6455 (2002).

[172] M. S. Westley, K. T. Lorenz, D. W. Chandler, and P. L. Houston, *J. Chem. Phys.*, **114**, 2669 (2001).

[173] P. Casavecchia, A. Laganà, and G. G. Volpi, *Chem. Phys. Lett.*, **112**, 445 (1984).

[174] S. D. Jons, J. E. Shirley, M. T. Vonk, C. F. Giese, and W. R. Gentry, *J. Chem. Phys.*, **97**, 7831 (1992).

[175] S. D. Jons, J. E. Shirley, M. T. Vonk, C. F. Giese, and W. R. Gentry, *J. Chem. Phys.*, **105**, 5397 (1996).

[176] L. S. Bontuyan, A. G. Suits, P. L. Houston, and B. J. Whitaker, *J. Phys. Chem.*, **97**, 6342 (1993).

[177] H. Kohguchi, T. Suzuki, and M. H. Alexander, *Science*, **294**, 832 (2001).

[178] M. Brouard, H. Chadwick C. J. Eyles, B. Hornung, B. Nichols, J. M. Scott, F. J. Aoiz, J. Kłos, S. Stolte, and X. Zhang, *Mol. Phys.* (2013).

[179] PhD thesis.

[180] K. T. Lorenz, D. W. Chandler, J. W. Barr, W. Chen, G. L. Barnes, and J. L. Cline, *Science*, **293**, 2063 (2001).

[181] J. I. Cline, K. T. Lorenz, E. A. Wade, J. W. Barr, and D. W. Chandler, *J. Chem. Phys.*, **115**, 6277 (2001).

[182] D. A. Case and D. R. Herschbach, *Mol. Phys.*, **30**, 1537 (1975).

[183] G. O. Sitz and R. L. Farrow, *J. Chem. Phys.*, **101**, 4682 (1994).

[184] A. C. Kummel, G. O. Sitz, and R. N. Zare, *J. Chem. Phys.*, **88**, 7357 (1988).

[185] Y. Mo, H. Katanayagi, and T. Suzuki, *J. Chem. Phys.*, **110**, 2029 (1999).

[186] M. Rutkowski and H. Zacharias, *Chem. Phys.*, **301**, 189 (2004).

[187] W. H. Press, S. A. Teukolsky, W. T. Vetterling, and B. P. Flannery, *Numerical Recipes in Fortran 90*, Cambridge University Press, 1996.

[188] H. Chadwick, *Angular Momentum Polarisation Effects in Inelastic Scattering*, DPhil Thesis, University of Oxford, 2012.

[189] S. D. Bosanac, *Phys. Rev. A*, **22**, 816 (1980).

[190] H. W. Herman and I. V. Hertel, *J. Phys. B*, **13**, 4285 (1980).

[191] N. Andresen, I. H. Hertel, and H. Kleinoppen, *J. Phys. B*, **17**, 901 (1984).

[192] M. Kohmoto and U. Fano, *J. Phys. B*, **14**, 447 (1981).

[193] M. H. Alexander, *J. Chem. Phys.*, **67**, 2703 (1977).

[194] J. Aldegunde, F. J. Aoiz, V. Saez-Rabanos, B. K. Kendrick, and M. P. de Miranda, *Phys. Chem. Chem. Phys.*, **9**, 5794 (2007).

[195] M. P. de Miranda and B. K. Kendrick, *J. Chem. Phys.*, **113**, 14943 (2009).

[196] D. Beck and U. Ross, *Z. Phys.*, **293**, 541 (1979).

[197] E. J. Rackman, T. Gonzales-Lezena, and D. E. Manolopoulos, *J. Chem. Phys.*, **119**, 12895 (2003).

[198] B. Wen, H. Meyer, J. Kłos, and M. H. Alexander, *J. Phys. Chem. A*, **113**, 7366 (2009).

[199] J. Kłos, *Private communication*, 2011.

[200] F. M. Kahnert, *J. Quant. Spec. Rad. Trans.*, **79**, 775 (2003).

[201] M. I. Mishchenko and L. D. Travis, *J. Quant. Spectroc. Radiat. Transfer*, **60**, 309 (1998).

[202] M. I. Mishchenko, *Appl. Optics*, **39**, 1026 (2000).

[203] M. H. Alexander and P. J. Dagdigian, *J. Chem. Phys.*, **83**, 2191 (1985).

[204] M. Brouard, H. Chadwick, S. D. S. Gordon, B. Nichols, and S. Stolte, *To be published.*

[205] M. Brouard, H. Chadwick, S. D. S. Gordon, B. Nichols, and S. Stolte, *To be published.*

[206] M. L. Lipciuc, A. J. van den Brom, L. Dinu, and M. H. Janssen, *Rev. Sci. Instrum.*, **76**, 123103 (2005).

[207] M. L. Lipciuc and M. H. M. Janssen, *Phys. Chem. Chem. Phys.*, **8**, 3007 (2006).

[208] A.T. Clark, J.P. Crooks, I. Sedgwick, R. Turchetta, J.W.L. Lee, J. John John, E.S. Wilman, L. Hill, E. Halford, C.S. Slater, B. Winter, W.-H. Yuen, S.H. Gardiner, M.L. Lipciuc, M. Brouard, A. Nomerotski, and C. Vallance, *J. Phys. Chem. A*, **116**, 10897 (2012).

[209] M. P. Docker, *Chem. Phys.*, **125**, 185 (1988).

[210] D. A. Case, G. M. McClelland, and D. R. Herschbach, *Mol. Phys.*, **35**, 541 (1978).